



TECHNISCHE  
UNIVERSITÄT  
WIEN  
Vienna University of Technology

# Spin–Orbit Interaction in Optical Imaging

## DISSERTATION

zur Erlangung des akademischen Grades

### Doktor/in der technischen Wissenschaften

eingereicht von

**Stefan Walser**

Matrikelnummer 416864

Steinbauergasse 23 / 13, 1120 Wien

an der  
Fakultät für Physik der Technischen Universität Wien

Betreuung: Prof. Dr. Arno Rauschenbeutel, E141 – Atominstitut

Diese Dissertation haben begutachtet:

---

(Prof. Dr. Arno  
Rauschenbeutel)

---

(Prof. Dr. Vahid Sandoghdar)

---

(Prof. Dr. Harald Giessen)

Wien, 05.04.2019

---

(Stefan Walser)



# Spin–Orbit Interaction in Optical Imaging

## DISSERTATION

submitted in partial fulfillment of the requirements for the degree of

**Doktor/in der technischen Wissenschaften**

by

**Stefan Walser**

Registration Number 416864

Steinbauergasse 23 / 13, 1120 Wien

to the Faculty of Physics  
at the TU Wien

Advisor: Prof. Dr. Arno Rauschenbeutel, E141 – Atominstitut

The dissertation has been reviewed by:

---

(Prof. Dr. Arno  
Rauschenbeutel)

---

(Prof. Dr. Vahid Sandoghdar)

---

(Prof. Dr. Harald Giessen)

Wien, 05.04.2019

---

(Stefan Walser)



# Abstract

Light is an electromagnetic wave that is described by Maxwell's equations and can feature an angular momentum. This angular momentum can be decomposed into a spin and orbital part, which can be associated with the light's polarization and spatial profile, respectively. In light fields that feature a strong transversal gradient, spin and orbital angular momentum are coupled, which is referred to as spin-orbit interaction of light. This causes a number of astonishing phenomena, such as, the directional emission of light into nano-phonic waveguides.

In this thesis, I study the consequences of spin-orbit interaction on free-space scattering of light. I show that it leads to the situation that light emitted by a nano-scale particle can seem to originate from a position that is offset from the particle, if the emitted light field features orbital angular momentum. This effect can be understood when considering that imaging the particle can be interpreted as a measurement of the mean momentum of the light at the aperture of the imaging system used to observe the particle. The presence of transverse momentum directly relates to orbital angular momentum and gives rise to a tilt of the wave fronts. Thus, the light seems to originate from a different position. The resulting apparent displacement is typically on the order of the optical wavelength and depends on the polarization of the emitter and the numerical aperture.

I experimentally investigate this effect in two different experimental setups. In the first experiment a sub-wavelength diameter optical waveguide is used to mount and illuminate a single gold nanoparticle. By imaging the particle, I observe an apparent displacement of the particle that depends on the polarization state of the emitter. Since the waveguide only provides the possibility to excite the particle with three different polarization states, a second experimental setup was designed in which the nanoparticle and the waveguide were placed in a microscopic gap between two half sphere lenses which subsequently was filled with index matching fluid. This prevents any reflections from the waveguide and realizes the situation found in a typical immersion microscope. I measured the apparent displacement of the particle as a function of the ellipticity of the polarization of the illuminating light and observed a total displacement up to the optical wavelength in good agreement with the theoretical models.

The polarization dependent position shift could potentially have a large influence on the accuracy of position determination in super-resolution microscopy. For this reason, I theoretically investigated how one can make use of the fact that the displacement of the emitter is accompanied by a deformation of the point spread function in order to simultaneously identify the emitter's position and polarization. The results show that it is in principle possible to account for this effect, however, depending on the desired resolution, this requires a many orders of magnitude better signal to noise ratio.



# Kurzfassung

Licht ist eine elektromagnetische Welle, die durch die Maxwell Gleichungen beschrieben wird, und kann einen Drehimpuls besitzen. Dieser Drehimpuls setzt sich aus einem Spin- und Bahndrehimpuls zusammen, welche mit der Polarisation des Lichtes und seinem räumlichen Profil assoziiert werden. In Lichtfeldern mit starkem transversalen Gradienten sind der Spin- und Bahndrehimpuls gekoppelt, was als Spin–Bahn Kopplung von Licht bezeichnet wird. Diese führt zu diversen erstaunlichen Phänomenen, wie zum Beispiel zur direktionalen Emission von Licht in nanophotonische Wellenleiter.

In dieser Arbeit untersuche ich die Konsequenzen der Spin–Bahn Kopplung beim Streuen von Licht in den freien Raum. Die Arbeit zeigt, dass es beim optischen Abbilden von Nanoteilchen zu Situationen kommen kann, in der das vom Nanoteilchen emittierte Licht, seinen Ursprung nicht am Ort des Teilchens zu haben scheint. Dieser Effekt tritt ein wenn das emittierte Lichtfeld am Ort der Apertur des Abbildungssystems einen Bahn-Drehimpuls besitzt, zum Beispiel wenn das Nanoteilchen elliptisch polarisiert ist. Der scheinbare Versatz ist typischer Weise in der Größenordnung der optischen Wellenlänge und ist abhängig von der Polarisation des Emitters und der Numerische Apertur des Abbildungssystems.

Dieser Effekt wird in zwei verschiedenen experimentellen Aufbauten untersucht. Im ersten Experiment wird ein Wellenleiter verwendet, der einen Durchmesser kleiner als die Wellenlänge des geführten Lichtes hat, um ein einzelnes Gold Nanoteilchen zu halten und zu beleuchten. Beim Abbilden des Partikels kann ein scheinbarer Versatz beobachtet werden, welcher vom Polarisationszustand des Emitters abhängt. Da der Wellenleiter nur drei verschiedenen Polarisationszustände ermöglicht mit denen der Partikel angeregt werden kann wurde ein zweites Experiment entworfen, in dem das Nanoteilchen und der Wellenleiter in dem mikroskopischen Spalt zwischen zwei Halbkugellinsen positioniert werden, welcher dann mit Immersionsflüssigkeit aufgefüllt wird. Dies verhindert Reflexionen an dem Wellenleiter und stellt ein typisches Immersions-Mikroskopie Verfahren dar. Der scheinbare Versatz des Partikels wurde als Funktion der Elliptizität der Polarisation des anregenden Lichtes vermessen und es konnte eine gute Übereinstimmung mit den theoretischen Modellen beobachtet werden.

Die polarisationsabhängige Abweichung von der realen Position kann potentiell großen Einfluss auf die Genauigkeit der Positionsbestimmung in super-auflösender Mikroskopie haben. Daher habe ich untersucht ob mittels der Verformung der Punktspreizfunktion, welche mit einem scheinbaren Versatz einher geht, die Position und Polarisation eines Emitters identifiziert werden kann. Die Ergebnisse zeigen, dass es zwar möglich ist diesen Effekt zu berücksichtigen, dafür aber um einige Größenordnung besseres Signal zu Rauschen Verhältnis notwendig ist.



# List of Publications

Parts of the results presented in this thesis have been published in the following article:

G. Araneda, S. Walser, Y. Colombe, D. B. Higginbottom, J. Volz, R. Blatt and A. Rauschenbeutel,  
Wavelength-scale errors in optical localization due to spin-orbit coupling of light.  
*Nature Physics*, 2018.



# Contents

<b>1</b>	<b>Introduction</b>	<b>1</b>
<b>2</b>	<b>Spin-orbit interaction in optical imaging</b>	<b>5</b>
2.1	Fundamental properties of light fields . . . . .	5
2.1.1	Momentum density of light fields . . . . .	5
2.1.2	Momentum density and the Poynting vector . . . . .	9
2.1.3	Wave fronts . . . . .	10
2.2	Spin-orbit interaction effects in the optical imaging process . . . . .	11
2.2.1	Elliptically polarized dipoles . . . . .	11
2.2.2	Momentum and wave fronts in the field of elliptically polarized dipoles	12
2.2.3	Displacement due to transverse linear momentum . . . . .	16
2.2.4	Fourier optics . . . . .	22
2.3	Summary . . . . .	28
<b>3</b>	<b>Measurement of apparent displacement due to SOI</b>	<b>29</b>
3.1	Introduction . . . . .	29
3.2	Preparing a single nanoparticle . . . . .	30
3.2.1	Selecting a suitable emitter . . . . .	31
3.2.2	Preparing a single gold nanoparticle . . . . .	32
3.2.3	Nanofiber based spectroscopy . . . . .	34
3.3	Illuminating the nanoparticle via the nanofiber . . . . .	37
3.3.1	Experimental setup . . . . .	38
3.3.2	Directional emission and defocussing error . . . . .	43
3.3.3	Experimental results . . . . .	45
<b>4</b>	<b>Measurement of polarization dependent apparent displacement</b>	<b>53</b>
4.1	Experimental setup . . . . .	53
4.1.1	Half sphere lenses alignment and illumination beams . . . . .	55
4.1.2	Imaging system and magnification . . . . .	57
4.1.3	Flat field correction . . . . .	57
4.1.4	Polarization alignment and data acquisition sequence . . . . .	58
4.2	Experimental results . . . . .	59
4.2.1	Focus determination . . . . .	59

4.2.2	Main results . . . . .	60
4.2.3	Defocussing errors . . . . .	64
4.3	Data analysis . . . . .	68
4.3.1	Experimental point spread function fitting . . . . .	69
<b>5</b>	<b>Consequences of spin-orbit interaction in super-resolution microscopy</b>	<b>75</b>
5.1	A precision limit in position determination of elliptically polarized emitters . .	76
5.1.1	Sum of squared difference - a measure to compare images . . . . .	77
5.1.2	Comparing noisy images . . . . .	80
5.1.3	The precision limit . . . . .	85
5.2	Optimal pixel size . . . . .	88
<b>6</b>	<b>Summary and Outlook</b>	<b>91</b>
6.1	Summary . . . . .	91
6.2	Outlook . . . . .	92
<b>A</b>	<b>Appendix</b>	<b>93</b>
A.1	Induced resonant dipole as momentum probe . . . . .	93
A.2	Momentum density of light fields - details . . . . .	93
A.2.1	Center of mass and relative coordinates . . . . .	94
A.2.2	Vector identities I . . . . .	94
A.2.3	Momentum absorbed by a dipole . . . . .	94
A.2.4	Vector identities II . . . . .	97
A.3	Decomposition of the Poynting vector . . . . .	97
A.3.1	Spin density of a light field . . . . .	97
A.3.2	Orbit and spin part of the Poynting vector . . . . .	99
A.3.3	Consistency check of momentum and spin density . . . . .	101
A.4	The dipole polarization ratio . . . . .	102
A.5	Wave fronts . . . . .	102
A.6	Displacement determined from wave fronts . . . . .	104
A.7	Modification of dipole fields by a lens . . . . .	106
A.8	Determination of mean momentum . . . . .	107
A.9	Angular momentum of photons . . . . .	109
A.9.1	Weak value of orbital angular momentum . . . . .	110
A.9.2	Displacement and momentum density . . . . .	112
A.10	Polarization of the evanescent field . . . . .	113
A.11	Determining the magnification of the immersion microscope . . . . .	115
A.12	Linear polarization under imaging conditions . . . . .	116
A.13	Other error sources in super-resolution microscopy . . . . .	118
	<b>Bibliography</b>	<b>119</b>

# Introduction

Light as electromagnetic radiation is described by Maxwell's equations which were first described by James Clerk Maxwell in 1865 and established in their today known form in the end of the 19th century. Maxwell's equations describe electromagnetic transversal waves which oscillate in the plane perpendicular to the propagation direction. They are characterized by scalar quantities like energy and vectorial quantities like linear and angular momentum, which all are conserved quantities in non-interacting and freely propagating waves. The existence of linear momentum of light gives rise to radiation pressure, which was already known to Maxwell himself [1]. Several years later the angular momentum of light was described [2]. It can *e.g.* be observed by transferring it to small particles, which are then subject to an optically induced torque [3]. The angular momentum carried by light can be decomposed into an internal, so called spin angular momentum (SAM) and an orbital angular momentum (OAM), which are determined by the polarization and the spatial degrees of freedom of the light [4]. The OAM can be associated with twisted or helical wave fronts where the light field dynamical rotates around the main beam axis, while SAM is associated with the dynamical rotation of the electromagnetic field, which occurs for instance when light is circularly polarized, as first described by Poynting [5]. In a well collimated beam of light, which is described by the paraxial approximation, the electromagnetic field oscillates orthogonal to the propagation direction and spin and the spatial degrees of freedom in such beams are independent quantities.

In light fields that exhibit a strong field gradient in direction transverse to its propagation direction, which *e.g.* occurs in the focal region of a beam that is strongly focused by a lens with high numerical aperture (NA), longitudinal field components parallel to the propagation direction can appear in addition to the field components that oscillate transverse to the propagation direction. The longitudinal field components are out of phase with the transverse components, which causes the light field to be locally elliptically polarized [6–10] in a plane which contains the propagation direction. The ellipticity of the local elliptical polarization is dependent on the spatial extension of the beam. When one considers the situation under time reversal, the propagation direction of the light, as well as the sense of rotation of the elliptical polarization components of the light field are inverted. This illustrates an inherent dependence of the lo-

cal polarization on the propagation direction. The coupling of the SAM (spin properties) and the OAM (spatial properties) is referred to as spin-orbit interaction (SOI) or spin-orbit coupling [11]. In macroscopic optics the transversal field gradients are small in the used light fields, therefore the SOI phenomena can typically be neglected, but it can become prominent in systems where the light field is confined on a microscopic scale and thus its components feature a large gradient. Consequences of SOI can for instance be seen in evanescent fields [12, 13] and nano-photon wave-guides [14–17], where the light fields are usually confined on length scales which are in the order of the optical wavelength. In recent years, a vast interest in SOI has developed [11, 18–20] due to the increasing importance of research fields like nano-optics and nano-photon structures, biosensing and near-field microscopy and the spatial controlling of atoms, molecules and nano-structures.

Remarkable phenomena appear in the context of SOI like the spin-Hall effect of light [21–24] where *e.g.* depending on the SAM of light a wavelength-scale displacement of reflected or refracted laser beams at a planar interface can be observed. This effect leads to specific polarization dependent aberrations at optical interfaces. Using nano-scale structures it is possible to investigate the SAM and OAM in strongly focussed beams [24–27]. Among these studies were the first experimental demonstrations of freely propagating light beams which carry purely transverse angular momentum, which results from an electric field which is spinning around an axis which is orthogonal to the propagation direction of the beam. This polarization components can play a key role in super-resolution microscopy and in light scattering behaviour of media and nano-structures.

In nano-scale wave-guides SOI results in a coupling between the local polarizations and the spatial properties like propagation direction and transversal gradient of the evanescent field. This strong coupling has important consequences for many applications such as the trapping and manipulation of atoms in the evanescent field close to the surface of sub-wavelength diameter optical wave-guides [28–30]. Furthermore, SOI changes the physics of light-matter interaction and gives rise to the new paradigm of chiral quantum optics [20]. This can be used to break the mirror symmetry of the scattering process of light into dielectric [31–42] and plasmonic [43–45] nano-photon wave guides by nano-scale emitters like nanoparticles or atoms. It also enables the realization of novel, spin-based non-reciprocal devices [46–48].

Until now, most experiments that studied the effect of SOI in light-matter interaction, investigated the situation when the emitters were coupled to the (evanescent) field of micro- or nano-scale optical wave guides. There exist theoretical predictions of the influence of SOI on the free space emission of small particles [49, 50], which show that the field lines of the Poynting vector of the electromagnetic field emitted by the particle leave the particle on spiral paths in the near field, if the light emitted by the particle exhibits angular momentum. In the far field, these field lines asymptotically approach straight lines which seem to not origin from the emitter. This leads to the impression that the emitter is located at a position where it is not. This apparent shift is in the order of the optical wavelength and is dependent on the SAM and OAM of the light field emitted by the particle. First experimental observations on how the polarization of emitted light can result in an apparent shift have been reported [51], analysing the light scattered from a polystyrene sphere with a diameter of about  $10 \lambda$ . In this thesis, we study the influence of SOI on the scattering properties of point-like dipole emitters in a free-space, microscope imaging

---

setting.

The possibility of the presence of an apparent shift of emitters in the order of the optical wavelength potentially affects optical imaging techniques in which the position of emitters is determined with an accuracy far exceeding the optical wavelength. The most prominent member of such imaging techniques is super-resolution microscopy, which is a fast evolving field that revolutionized traditional optical microscopy [52–57]. In 2014 it was honored with the Nobel price in chemistry which was awarded to Eric Betzig, Stefan W. Hell and William E. Moerner for the development of super-resolved fluorescence microscopy. Using different techniques, these approaches enhance the precision of optical microscopy significantly beyond the standard diffraction limit of  $\lambda/\text{NA}$  and routinely reach resolutions of a few nanometers [58–60]. Even resolutions in the sub-nanometer regime are reported [61]. While in some of these novel methods the imaging process differs from the one in classical microscopy, like for instance STED [62], other methods gain their outstanding precision from techniques using classical microscope imaging. This is for instance realized in PALM [63] and STORM [64], which make use of the fact, that despite the standard diffraction limit, the position of point-like emitters can in principle be measured with arbitrary precision [65, 66]. The basic idea of these approaches is to prepare and control their samples in such a way that only a few, well-separated emitters scatter light at a given time. Thus in a diffraction limited area only one emitter is emitting light within the exposure time of a single image and it is possible to precisely determine the position of all emitters in a set of images.

In this thesis I present in chapter 2 theoretical models which show that the presence of OAM in the light field emitted by a small dipole emitter, can lead to a deviation of the propagation direction of the light with respect to the radial direction when the light passes an aperture. Studying this effect in the context of optical imaging, we find a shift of the emitters image that depends on the overall angular momentum of the light emitted by the particle and the numerical aperture of the imaging system. The apparent displacement of the emitter is typically on the order of the wavelength but, under certain circumstances, can even reach arbitrary large values. In chapter 3 and 4 I present two experiments which were performed to observe and quantify the predicted effect by imaging a 100 nm diameter gold nano-sphere, where we found excellent agreement of the measured data with the theoretical models.

This polarization dependent position shift could potentially have a large influence on the imaging process in super-resolution microscopy. In chapter 5 we investigate the consequence of this effect on super-resolution microscopy. We discuss how well one can compensate for this effect by analysing the polarization dependent point spread function and determine the noise limited position accuracy in position determination and compare it to established models for noise dependent accuracy.



# Spin-orbit interaction in optical imaging

In this chapter, the origin of the displacement of the centroid of the far field image of an elliptically polarized emitter will be discussed. In the beginning, we determine the linear momentum density of a light field which is the fundamental property providing information about the local propagation direction of light fields. It directly relates to the orbital angular momentum. Using the momentum density we then study the wave fronts of the field emitted by a small dipole emitter which will provide an illustrative graphical explanation of the centroid's shift. A quantitative determination of the shift of the centroid is going to be performed with two different approaches, from which we derive the same analytic expression. First, we investigate the overall momentum of the light passing an imaging system, which features a small transverse momentum leading to a transverse displacement of the image while passing the imaging system. Second, we discuss a Fourier optics approach to determine the far field image. Finally, we will apply alternative position determination methods to the calculated images.

## 2.1 Fundamental properties of light fields

In this section we will determine the momentum density of a light field and then study its relation to the Poynting vector. After that we will use both of these fundamental properties to define wave fronts of light fields in a different approach than common definitions.

### 2.1.1 Momentum density of light fields

To derive the linear momentum density of a light field we use an operational approach in which we first determine the momentum transfer from the light field onto a dipolar test particle. From the momentum transfer it is then possible to conclude the momentum density of the exciting light field. The test particle is assumed to be a dipole which is induced by the exciting light

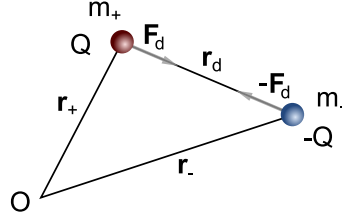


**Figure 2.1: Electric dipole.** An electric dipole consisting of the charge  $Q$  with mass  $m_+$  at position  $\mathbf{r}_+$  and the charge  $-Q$  with mass  $m_-$  at position  $\mathbf{r}_-$  with respect to the origin  $O$ . The binding force between the two charges is given by  $\mathbf{F}_d$  which is parallel to the relative distance between the two charges, given by  $\mathbf{r}_d$ . Such an dipole would for instance be realized by a hydrogen atom.

field an to be resonant with the exciting light field.<sup>1</sup> Following [67, 68] we model the dipole by two charges  $Q$  with mass  $m_+$  and  $-Q$  with mass  $m_-$  at the positions  $\mathbf{r}_+$  and  $\mathbf{r}_-$  with a relative separation of  $\mathbf{r}_d = \mathbf{r}_+ - \mathbf{r}_-$ , as shown in Figure 2.1. The forces acting on the individual charges in the external electromagnetic field are the sum of the Coulomb force, the Lorentz force and the binding force  $\mathbf{F}_d$  between the two charges, which is a function of their distance  $r_d = \|\mathbf{r}_d\|$ .<sup>2</sup> The overall forces on the charges are given by

$$\mathbf{F}_+ = Q(\mathcal{E}(\mathbf{r}_+, t) + \dot{\mathbf{r}}_+ \times \mathcal{B}(\mathbf{r}_+, t)) + \mathbf{F}_d \quad (2.1)$$

$$\mathbf{F}_- = -Q(\mathcal{E}(\mathbf{r}_-, t) + \dot{\mathbf{r}}_- \times \mathcal{B}(\mathbf{r}_-, t)) - \mathbf{F}_d. \quad (2.2)$$

The expression  $\mathcal{E}(\mathbf{r}, t)$  denotes the full real valued external electric field which is applied on the particle. It is possible to write the electric field as a sum of complex valued fields,

$$\mathcal{E}(\mathbf{r}, t) = \frac{1}{2}(\mathbf{E}(\mathbf{r}, t) + \mathbf{E}^*(\mathbf{r}, t)), \quad (2.3)$$

where  $\mathbf{E}^*$  is the complex conjugate of  $\mathbf{E}$ . In the same way the magnetic field  $\mathcal{B}(\mathbf{r}, t)$  can be written as

$$\mathcal{B}(\mathbf{r}, t) = \frac{1}{2}(\mathbf{B}(\mathbf{r}, t) + \mathbf{B}^*(\mathbf{r}, t)). \quad (2.4)$$

In order to determine the overall force  $\mathbf{F} = \mathbf{F}_+ + \mathbf{F}_-$  acting on the dipole we rewrite the positions  $\mathbf{r}_\pm$  using the center of mass coordinate  $\mathbf{R}$  and the relative coordinate  $\mathbf{r}_d$ , with

$$\mathbf{R} = \frac{m_-}{m}\mathbf{r}_+ + \frac{m_+}{m}\mathbf{r}_-, \quad (2.5)$$

where  $m = m_+ + m_-$  denotes the overall mass of the dipole. The positions of the two charges can be expressed as<sup>3</sup>

$$\mathbf{r}_\pm = \mathbf{R} \pm \frac{m_\mp}{m}\mathbf{r}_d. \quad (2.6)$$

<sup>1</sup>A short justification why we chose a dipole which is induced and resonant to the exciting field can be found in the appendix A.1

<sup>2</sup>Here,  $\|\cdot\|$  denotes the standard norm on a  $n$ -dimensional vector space.

<sup>3</sup>This decomposition is shown in the appendix A.2.1.

The overall forces acting on the charges can then be written as<sup>4</sup>

$$\mathbf{F}_{\pm} = \pm Q \left( \mathcal{E}(\mathbf{R} \pm \frac{m_{\mp}}{m} \mathbf{r}_d) + (\dot{\mathbf{R}} \pm \frac{m_{\mp}}{m} \dot{\mathbf{r}}_d) \times \mathcal{B}(\mathbf{R} \pm \frac{m_{\mp}}{m} \mathbf{r}_d) \right) \pm \mathbf{F}_d. \quad (2.7)$$

We now do a classical dipole approximation assuming that the size  $r_d$  of the dipole is much smaller than the optical wavelength  $\lambda = 2\pi c/\omega$  of the exciting light field, like it is *e.g.* the case for atoms. Therefore we approximate the electric and magnetic field up to the first order of the Taylor series of the fields. The Taylor series of a function  $\mathbf{f} : \mathbb{R}^3 \rightarrow \mathbb{R}^3$  at the position  $\mathbf{r}_0$  is given by [69]

$$\mathbf{f}(\mathbf{r}_0 + \mathbf{r}) = \sum_{n=0}^{\infty} \frac{1}{n!} (\mathbf{r} \cdot \vec{\nabla})^n \mathbf{f}(\mathbf{r}_0). \quad (2.8)$$

The first order approximation of the electric and magnetic field is then given by<sup>5</sup>

$$\mathcal{E}(\mathbf{R} \pm \frac{m_{\mp}}{m} \mathbf{r}_d) = \mathcal{E}(\mathbf{R}) \pm \frac{m_{\mp}}{m} (\mathbf{r}_d \cdot \vec{\nabla}) \mathcal{E}(\mathbf{R}) \quad (2.9)$$

$$\mathcal{B}(\mathbf{R} \pm \frac{m_{\mp}}{m} \mathbf{r}_d) = \mathcal{B}(\mathbf{R}) \pm \frac{m_{\mp}}{m} (\mathbf{r}_d \cdot \vec{\nabla}) \mathcal{B}(\mathbf{R}). \quad (2.10)$$

Now using the electric dipole moment  $\boldsymbol{\mu} = Q \cdot \mathbf{r}_d$  the overall force  $\mathbf{F}$  acting on the dipole can be written as

$$\begin{aligned} \mathbf{F} &= Q \left[ \mathcal{E}(\mathbf{R}) + \frac{m_-}{m} (\mathbf{r}_d \cdot \vec{\nabla}) \mathcal{E}(\mathbf{R}) + \left( \dot{\mathbf{R}} + \frac{m_-}{m} \dot{\mathbf{r}}_d \right) \times \left( \mathcal{B}(\mathbf{R}) + \frac{m_-}{m} (\mathbf{r}_d \cdot \vec{\nabla}) \mathcal{B}(\mathbf{R}) \right) \right. \\ &\quad \left. - \mathcal{E}(\mathbf{R}) + \frac{m_+}{m} (\mathbf{r}_d \cdot \vec{\nabla}) \mathcal{E}(\mathbf{R}) - \left( \dot{\mathbf{R}} - \frac{m_+}{m} \dot{\mathbf{r}}_d \right) \times \left( \mathcal{B}(\mathbf{R}) - \frac{m_+}{m} (\mathbf{r}_d \cdot \vec{\nabla}) \mathcal{B}(\mathbf{R}) \right) \right] \\ &= (\boldsymbol{\mu} \cdot \vec{\nabla}) \mathcal{E}(\mathbf{R}) + \dot{\boldsymbol{\mu}} \times \mathcal{B}(\mathbf{R}) \\ &\quad + \dot{\mathbf{R}} \times \left( (\boldsymbol{\mu} \cdot \vec{\nabla}) \mathcal{B}(\mathbf{R}) \right) + \dot{\boldsymbol{\mu}} \times \left( (\boldsymbol{\mu} \cdot \vec{\nabla}) \mathcal{B}(\mathbf{R}) \right) \frac{m_-^2 + m_+^2}{Qm^2} \end{aligned} \quad (2.11)$$

We now assume the exciting light field to be monochromatic, meaning that the complex valued fields  $\mathbf{E}$  and  $\mathbf{B}$  can be written as

$$\mathbf{E}(\mathbf{r}, t) = \mathbf{E}_0(\mathbf{r}) e^{-i\omega t} \quad \text{and} \quad \mathbf{B}(\mathbf{r}, t) = \mathbf{B}_0(\mathbf{r}) e^{-i\omega t}. \quad (2.12)$$

In order to derive the momentum density of the light field we consider the dipole to be induced by the exciting light field and the dipole oscillation to be resonant with the exciting light field. Consequently the dipole is only exposed to the radiation pressure [70] and not to a gradient

<sup>4</sup>In order to maintain readability in the following the time dependence of  $\mathcal{E}$ ,  $\mathbf{E}$ ,  $\mathcal{B}$  and  $\mathbf{B}$  will not be written down explicitly.

<sup>5</sup>It is common to write the first order approximation of a vector valued function  $\mathbf{f}$  as  $\mathbf{f}(\mathbf{r}_0 + \mathbf{r}) \approx \mathbf{f}(\mathbf{r}_0) + J_{\mathbf{f}}(\mathbf{r}_0)\mathbf{r}$ , where  $J_{\mathbf{f}}(\mathbf{r}_0)$  is the Jacobi matrix evaluated at  $\mathbf{r}_0$ . The expression  $J_{\mathbf{f}}(\mathbf{r}_0)\mathbf{r}$  is identical with  $(\mathbf{r} \cdot \vec{\nabla}) \mathbf{f}(\mathbf{r}_0)$ , see appendix A.2.2

force [71, 72]. The gradient force acts in direction of the intensity gradient of the light field, which is for instance used in optical tweezers. We describe the dipole as a Lorentz oscillator which is resonant to the light field. The dipole moment  $\boldsymbol{\mu}_L$  of a Lorentz oscillator is in general given by [68]

$$\boldsymbol{\mu}_L = \frac{1}{2} |\alpha| (e^{-i\varphi} \mathbf{E} + e^{i\varphi} \mathbf{E}^*) \quad \text{with} \quad \alpha = -\frac{Q^2}{\tilde{m}} \frac{1}{\omega^2 - \omega_0^2 - i\gamma\omega}, \quad (2.13)$$

$\varphi = \arg(\alpha)$  and  $\tilde{m} = (m_+ m_-)/(m_+ + m_-)$  the reduced mass. On resonance, meaning  $\omega = \omega_0$ , the dipole moment of the Lorentz oscillator can be written as

$$\bar{\boldsymbol{\mu}}_L = \frac{1}{2} |\alpha| \left( e^{i\frac{\pi}{2}} \mathbf{E} + e^{-i\frac{\pi}{2}} \mathbf{E}^* \right) = \frac{i}{2} \text{Im}(\alpha) (\mathbf{E} - \mathbf{E}^*). \quad (2.14)$$

The third term in the force  $\mathbf{F}$ , see expression 2.11, acting on the resonant Lorentz oscillator is dependent on the velocity  $\dot{\mathbf{R}}$  of its center of mass. This term stems from the Lorentz force and is proportional to the velocity of the center of mass of the Lorentz oscillator. To find the momentum density of a light field we need to fix the probe dipole at a certain point in space, meaning  $\dot{\mathbf{R}} = 0$ . Otherwise the velocity of a moving dipole would modify the intrinsic force acting on the dipole at a certain position. The force  $\mathbf{F}_0$  acting on this spatial fixed and resonant Lorentz oscillator is given by

$$\mathbf{F}_0 = \left( \bar{\boldsymbol{\mu}}_L \cdot \vec{\nabla} \right) \mathcal{E}(\mathbf{R}) + \dot{\bar{\boldsymbol{\mu}}}_L \times \mathcal{B}(\mathbf{R}) + \dot{\bar{\boldsymbol{\mu}}}_L \times \left( \left( \bar{\boldsymbol{\mu}}_L \cdot \vec{\nabla} \right) \mathcal{B}(\mathbf{R}) \right) \frac{m_-^2 + m_+^2}{Qm^2}. \quad (2.15)$$

The next step to determine the momentum density of the light field is to derive the momentum  $\mathbf{P}$  which is transferred to the resonant dipole by the light field. Therefore we average over the terms oscillating at the light frequency by integrating the force  $\mathbf{F}_0$  over one oscillation period  $2\pi/\omega$ . While the first two terms in 2.15 are partly nonzero when averaged over one oscillation period of the light field, the third term vanishes. The corresponding momentum  $\mathbf{P}$  gained by the dipole is then given by

$$\begin{aligned} \mathbf{P} &= \int_0^{\frac{2\pi}{\omega}} \mathbf{F}_0 dt \\ &= \frac{\pi}{\omega} \text{Im}(\alpha) \text{Im} \left( \left( \mathbf{E}_0^* \cdot \vec{\nabla} \right) \mathbf{E}_0 + \mathbf{E}_0^* \times \left( \vec{\nabla} \times \mathbf{E}_0 \right) \right). \end{aligned} \quad (2.16)$$

This derivation is performed in detail in A.2.3. Using the vector identity  $\left( \mathbf{E}_0^* \cdot \vec{\nabla} \right) \mathbf{E}_0 + \mathbf{E}_0^* \times \left( \vec{\nabla} \times \mathbf{E}_0 \right) = \left( \vec{\nabla} \otimes \mathbf{E}_0 \right) \mathbf{E}_0^*$ , which is proven in A.2.4, the momentum absorbed by the dipole can finally be written as

$$\mathbf{P} = \frac{\pi}{\omega} \text{Im}(\alpha) \text{Im} \left( \left( \vec{\nabla} \otimes \mathbf{E}_0 \right) \mathbf{E}_0^* \right) \quad (2.17)$$

where  $\vec{\nabla}$  acts only on  $\mathbf{E}_0$  and not on  $\mathbf{E}_0^*$ . Now in order to determine the momentum density of the light field, the amount of light absorbed by the dipole needs to be evaluated. This is done via

the absorption cross section  $\sigma_{\text{Abs}}$  [73, 74] of the Lorentz oscillator. The absorption cross section is given by the ratio of the frequency dependent absorbed power  $\mathcal{P}$  of an Lorentz oscillator and the intensity  $\mathcal{I}$  of the exciting light field<sup>6</sup>, with

$$\mathcal{P} = \frac{\omega}{2} \text{Im}(\alpha) |\mathbf{E}_0|^2 \quad \text{and} \quad \mathcal{I} = \frac{1}{2} c \epsilon_0 |\mathbf{E}_0|^2. \quad (2.18)$$

Here it is assumed, that the electric field can be considered as a plane wave over the elongation of the area in which the absorption process of the dipole takes place. This was with  $r_d \ll \lambda$  a major assumption of the past derivations. The absorption cross section is then given by

$$\sigma_{\text{Abs}} = \frac{\mathcal{P}}{\mathcal{I}} = \frac{2\pi}{\epsilon_0 \lambda} \text{Im}(\alpha), \quad (2.19)$$

with  $\omega = 2\pi c/\lambda$ . The momentum density  $\rho_{\mathbf{P}}$  of the light field is then given by the ratio of the momentum absorbed by the dipole and the volume which can be assigned to the energy absorbed by the dipole. It is given by the absorption cross section times the wavelength, which in turn corresponds to the time over which the momentum transfer was averaged. The momentum density can then be written as

$$\rho_{\mathbf{P}} = \frac{\mathbf{P}}{\lambda \sigma} = \frac{\epsilon_0}{2\omega} \text{Im} \left( (\vec{\nabla} \otimes \mathbf{E}_0) \mathbf{E}_0^* \right). \quad (2.20)$$

Since the momentum density determines the momentum absorbed by a dipolar test particle and therefore the direction of the motion of the test particle it also defines the local propagation direction of a light field.

With the linear momentum density the angular momentum density  $\rho_{\mathbf{L}}$  can be defined as

$$\rho_{\mathbf{L}}(\mathbf{r}) = \mathbf{r} \times \rho_{\mathbf{P}}(\mathbf{r}). \quad (2.21)$$

The angular momentum density is only dependent on the momentum transverse to the radial direction.

### 2.1.2 Momentum density and the Poynting vector

In light propagation, an important characteristic is the Poynting vector [68], which represents the energy flux of an electromagnetic field. The cycle-averaged Poynting vector  $\mathcal{S}_0$  is given by

$$\mathcal{S}_0 = \frac{1}{2} \text{Re} (\mathbf{E}_0^* \times \mathbf{H}_0), \quad (2.22)$$

where  $\mathbf{H}_0$  is a complex valued time independent component of the magnetic field strength  $\mathcal{H}$ .<sup>7</sup> It is possible to decompose  $\mathcal{S}_0$  into a part which is proportional to the momentum density  $\rho_{\mathbf{P}}$ , the so called orbital part  $\mathcal{S}_0^{\text{orb}}$  and a part which is proportional to the curl of the spin angular

<sup>6</sup>Note that both, the absorbed power and the intensity are averaged over one oscillation period of the field. The absolute square of  $\mathbf{E}_0$  is given by  $|\mathbf{E}_0|^2 = \mathbf{E}_0 \cdot \mathbf{E}_0^*$

<sup>7</sup>The magnetic field strength can be written in the same way as the electric and magnetic fields as  $\mathcal{H} = (\mathbf{H}_0 e^{-i\omega t} + \mathbf{H}_0^* e^{i\omega t})/2$

momentum density  $\rho_S$  of the light field, the so called spin part of the Poynting vector  $\mathcal{S}_0^{\text{spin}}$  [75, 76]. The spin angular momentum density, or just spin density  $\rho_S$  is given by

$$\rho_S = \frac{\epsilon_0}{2\omega} \text{Im}(\mathbf{E}_0^* \times \mathbf{E}_0). \quad (2.23)$$

It is derived by averaging the overall torque applied by the Coulomb and Lorentz force on a small dipolar test particle over one oscillation period of the exciting light field. This derivation is shown in detail in appendix A.3.1.

The decomposition [75, 76]

$$\mathcal{S}_0 = \mathcal{S}_0^{\text{orb}} + \mathcal{S}_0^{\text{spin}} \quad (2.24)$$

of the mean Poynting vector with

$$\mathcal{S}_0^{\text{orb}} = \frac{\epsilon_0 c^2}{2\omega} \text{Im} \left( (\vec{\nabla} \otimes \mathbf{E}_0) \mathbf{E}_0^* \right) = c^2 \cdot \rho_P \quad (2.25)$$

and

$$\mathcal{S}_0^{\text{spin}} = \frac{\epsilon_0 c^2}{2\omega} \text{Im} \left( \vec{\nabla} \times (\mathbf{E}^* \times \mathbf{E}) \right) = \frac{1}{2} c^2 \cdot (\vec{\nabla} \times \rho_S) \quad (2.26)$$

is shown in detail in the appendix A.3.2. The consequence of this decomposition is that the Poynting vector does in general not give the local propagation direction of a light field. Only in the case of a vanishing spin density the local propagation direction of the field coincides with the Poynting vector.

### 2.1.3 Wave fronts

A physical suitable definition for wave fronts of a light field can be made using the linear momentum density, which represents the local propagation direction of the light field. In particular the wave front can be defined as a surface of which the tangential plane is in every point orthogonal to the local propagation direction of the field. Such a wave front can be determined using the projection of the local time dependent orbital part of the Poynting vector A.27 onto the local propagation direction given by the linear momentum density  $\rho_P$ . At every point in the light field the projection of the time dependent orbital part of the Poynting vector onto the momentum density is a scalar which can be written as

$$\mathcal{S}_0^{\text{orb}}(\mathbf{r}, t) \cdot \rho_P(\mathbf{r}) = A_0(\mathbf{r}) + A(\mathbf{r}) \sin(2\omega t + \varphi(\mathbf{r}))^2. \quad (2.27)$$

This scalar is composed of a time independent part and a part which oscillates with twice the frequency  $\omega$  of the light field. We now define a wave front as a surface in which every point exhibits the same phase  $\varphi(\mathbf{r})$  of the oscillating part.<sup>8</sup>

---

<sup>8</sup>There exist singular points where  $\mathcal{S}_0^{\text{orb}}(\mathbf{r}, t)$  is constant in time and consequently  $A(\mathbf{r}) = 0$  in 2.27. At this points the definition of the wave fronts does not provide a clear defined wave front. Such points are for instance the rotation axis of a rotating dipole.

Note that this definition of the wave fronts is different from the more common way to define wave fronts as surfaces of constant phase of the emitted electric field [70]. This definition applies to special cases like for instance plane- or spherical waves, where the wave fronts are then orthogonal to the local propagation direction. But in general it is not possible to define a phase of the local field, which is independent from the coordinate system describing the field. This applies when the light field exhibits nonzero spin density.

## 2.2 Spin-orbit interaction effects in the optical imaging process

In this section we investigate the influence of the local linear momentum in a light field in the optical imaging process. It is most relevant when imaging elliptically polarized dipole emitters, which will be introduced first. We will then study the wave fronts of such emitters. From the wave fronts we will already be able to tell, that in certain regions in the light field emitted by an elliptically polarized emitter the local momentum leads to the impression that the light does not originate from the emitter. This effect will then be studied in a more quantitative way, with the outcome, that the center of mass of the intensity distribution of an image does in general not coincide with the position of the emitter. In the end of the section we will derive analytic expressions for the images of elliptically polarized emitters, giving us the opportunity to use other position determination methods than the center of mass.

### 2.2.1 Elliptically polarized dipoles

In this section the term elliptically polarized dipole will be defined within the framework of this thesis. The electric field emitted by an arbitrarily polarized optical dipole emitter located at the origin, which oscillates with an angular frequency  $\omega$ , is given by [77]:

$$\mathbf{E}_{\text{full}}(\mathbf{r}, t) = \frac{\omega^3}{4\pi\epsilon_0 c^3} \left[ (\mathbf{n} \times \boldsymbol{\mu}) \times \mathbf{n} \frac{1}{u} + (3\mathbf{n}(\mathbf{n} \cdot \boldsymbol{\mu}) - \boldsymbol{\mu}) \left( \frac{1}{u^3} - \frac{i}{u^2} \right) \right] e^{i(kr - \omega t)}, \quad (2.28)$$

where  $\boldsymbol{\mu}$  denotes the complex valued dipole moment, which describes the polarization of the dipole,  $r = \|\mathbf{r}\|$ ,  $u = kr$ ,  $k = \lambda/(2\pi)$  with the wavelength  $\lambda$  of the emitted light and  $\mathbf{n} = \mathbf{r}/r$ .<sup>9</sup> In the far field ( $r \gg \lambda$ ) the terms containing  $1/u^2$  and  $1/u^3$  can be neglected against the  $1/u$  term. The far field expression of the electric field can thus be written as

$$\mathbf{E}(\mathbf{r}, t) = \frac{\omega^2}{4\pi\epsilon_0 c^2} \frac{1}{r} e^{i(kr - \omega t)} (\mathbf{n} \times \boldsymbol{\mu}) \times \mathbf{n}. \quad (2.29)$$

In order to describe the electric field emitted by an elliptically polarized dipole it is suitable to decompose its field into a superposition of three fields with the elementary linear polarization states  $\boldsymbol{\mu}_{D^x} = \mathbf{e}_x$ ,  $\boldsymbol{\mu}_{D^y} = \mathbf{e}_y$  and  $\boldsymbol{\mu}_{D^z} = \mathbf{e}_z$ .<sup>10</sup> The field emitted by a dipole in polarization

<sup>9</sup>Note that this field is not the full real valued electric field emitted by a dipole but corresponds to the fields used in the decomposition 2.3 of the real valued field. This applies to all other electric fields presented in this section.

<sup>10</sup>Note that the dipole moment is not a unitless quantity, but has the unit Coulomb times length. To be more specific one could write the dipole moment as  $\boldsymbol{\mu}_{D^i} = \|\boldsymbol{\mu}_{D^i}\| \cdot \mathbf{e}_i$ . Since the absolute value of the dipole moment would only be a prefactor to the electric field, which is not important for the spatial field distribution we assume it without loss of generality to be one.

state  $\boldsymbol{\mu}_{D^i}$  will be denoted as  $\boldsymbol{E}_{D^i}$ , with  $i \in \{x, y, z\}$ . Without loss of generality we define an elliptically polarized emitter via the dipole moment

$$\boldsymbol{\mu}_{\text{ell}} = \frac{1}{N_\epsilon} (\boldsymbol{e}_x + i \epsilon \boldsymbol{e}_y) \quad \text{with} \quad N_\epsilon = \sqrt{1 + |\epsilon|^2}, \quad (2.30)$$

which means that the dipole emitter is rotating in the  $xy$ -plane.<sup>11</sup> The field of an elliptically polarized emitter is then given by

$$\boldsymbol{E}_{\text{ell}} = \frac{1}{N_\epsilon} (\boldsymbol{E}_{D^x} + \epsilon \cdot i \cdot \boldsymbol{E}_{D^y}), \quad (2.31)$$

where we denote the complex valued amplitude ratio  $\epsilon$  as the *dipole polarization ratio*. The field of any elliptically polarized dipole is fully described by  $\epsilon$ . The case  $\epsilon = 0$  corresponds to the field of a dipole which is linearly polarized along the  $x$ -axis,  $\epsilon = \pm 1$  corresponds to the fields of counter clockwise and clockwise circularly polarized dipoles, also referred to as  $\sigma^\pm$  polarized and  $\epsilon = \infty$  to the field of a dipole which is linearly polarized along the  $y$ -axis. Further considerations of  $\epsilon$  and the fields of elliptically polarized emitters described by  $\epsilon$  can be found in the appendix A.4

### 2.2.2 Momentum and wave fronts in the field of elliptically polarized dipoles

Using the linear momentum density we can determine the orbital angular momentum density  $\boldsymbol{\rho}_L$  in the light field of an elliptically polarized emitter, which we defined as

$$\boldsymbol{\rho}_L(\boldsymbol{r}) = \boldsymbol{r} \times \boldsymbol{\rho}_P(\boldsymbol{r}), \quad (2.32)$$

while the emitter is placed at the origin at  $\boldsymbol{r} = 0$ . The on the local intensity 2.18 normalized angular momentum density  $\bar{\boldsymbol{\rho}}_L$  and spin angular momentum density  $\bar{\boldsymbol{\rho}}_S$  are given by

$$\bar{\boldsymbol{\rho}}_L = \frac{|\epsilon| \sin(\theta)}{(1 + \epsilon^2) \cos(\theta)^2 + \sin(\theta)^2 (\epsilon^2 \cos(\phi)^2 + \sin(\phi)^2)} C \quad (2.33)$$

and

$$\bar{\boldsymbol{\rho}}_S = \frac{2 |\epsilon| |\cos(\theta)|}{(1 + \epsilon^2) \cos(\theta)^2 + \sin(\theta)^2 (\epsilon^2 \cos(\phi)^2 + \sin(\phi)^2)} C, \quad (2.34)$$

where  $\theta$  and  $\phi$  are spherical coordinates and  $C$  a constant factor. For the case of a  $\sigma^+$  polarized dipole the normalized orbital and spin angular momentum densities are plotted in Figure 2.2a. One can see, that along the rotation axis of the dipole emitter the field exhibits only spin angular momentum and no orbital angular momentum while the situation in the plane in which the dipole rotates is reversed. There the light features only orbital angular momentum and no spin angular momentum and is therefore linearly polarized. Similar results can be found in [78, 79]. This effect is the so called spin-orbit interaction or spin-orbit coupling of light [11, 18–20]. The ratio

---

<sup>11</sup>This is not a loss of generality since the coordinate system in which a rotating dipole is described can always be chosen such that the  $xy$ -plane coincides with the plane in which the emitter rotates.

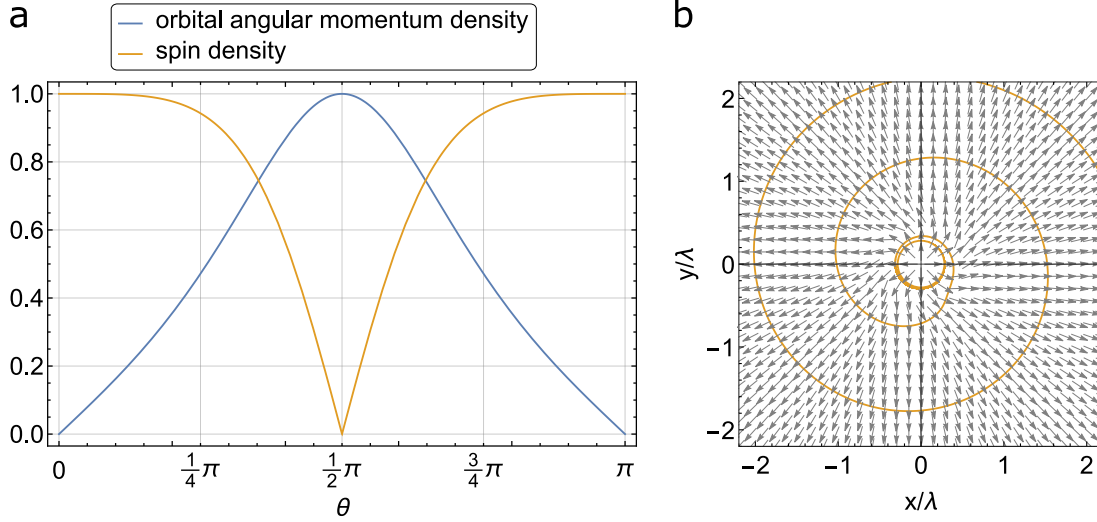


**Figure 2.2: Momentum in the light field of a circularly polarized emitter.** **a**, The on the local intensity normalized orbital angular momentum density  $\bar{\rho}_L$  (blue) and spin angular momentum density  $\bar{\rho}_S$  (yellow) of the light field of a  $\sigma^+$  polarized dipole plotted as a function of the polar angle  $\theta$ . While along the  $z$ -axis ( $\theta = 0, \pi$ ) the light features only spin angular momentum and no orbital angular momentum the situation in the equatorial plane ( $\theta = \pi/2$ ) is reversed. There the light features only orbital angular momentum and no spin angular momentum and is therefore linearly polarized. **b**, The local propagation direction given by the normalized linear momentum density  $\rho_P$  is shown as vector plot for the field emitted by a  $\sigma^+$  polarized dipole. For this plot the full field was used and not the far field approximation. The yellow curve is a wave front according to the definition that it is in every point orthogonal to the local propagation direction. For  $r \ll \lambda$  the local propagation direction coincides with the radial direction. At the transition to the far field at about  $0.4 \lambda$  the propagation direction is counter clockwise twisted. This twist decreases for  $r > \lambda$  but does not vanish completely. The wave front was derived numerically in an incremental process from a position  $r \gg \lambda$  towards the origin and forms a circle at about  $0.3 \lambda$ . This circle appears since the local propagation direction matches at this radius perfectly the radial direction.

between orbital angular momentum and spin angular momentum is coupled to the position in the light field.

We now study the wave fronts of elliptically polarized dipole emitters. As defined in section 2.1.3 a wave front is a surface which is in every point orthogonal to the local propagation direction. In Figure 2.2b a wave front in the  $xy$ -plane is plotted for the case of a  $\sigma^+$  polarized emitter. It was numerically determined as the path which is orthogonal to the local propagation direction, given by the normalized linear momentum density, which is shown as vector plot. For the determination of the linear momentum density the full electric field of a dipole emitter was used and not only the far field approximation. Therefore the transition from the near field to the far field can be seen. In the near field the local propagation direction coincides with the radial

direction and is then counter clockwise twisted at the transition to the far field. In the far field this twist is decreased but does not vanish. Consequently the wave front forms a spiral in the far field.

In the following an analytic expression for the wave fronts in the light field of an elliptically polarized emitter will be derived. Thereby we focus on polarization states with a real valued  $\epsilon$ <sup>12</sup> only and restrict the determination of the wave fronts to the  $xy$ -plane and the far field approximation. The wave front of the light field is given by a path of which the tangent is in every point orthogonal to the local momentum density. This path can be derived using the feature, that the light emitted by the elliptically polarized dipole is in the  $xy$ -plane solely linearly polarized. In particular we make use of the fact, that in the  $xy$ -plane the electric field has two zero crossings due to the linear polarization. This derivation is discussed more detailed in the appendix A.5.

The wave front of an elliptically polarized dipole is in the  $xy$ -plane given by the parametric expression

$$\mathbf{R}_{\text{ell}}(\phi, t, \epsilon, \phi_0) = R_{\text{ell}}(\phi, t, \epsilon, \phi_0) \begin{pmatrix} -\text{sgn}(\epsilon) \cos(\phi) \\ \sin(\phi) \end{pmatrix} \quad (2.35)$$

with

$$R_{\text{ell}}(\phi, t, \epsilon, \phi_0) = \frac{\lambda}{2\pi} \left( \text{sgn}(\epsilon) \phi_0 + \text{sgn}(\epsilon) \frac{2\pi}{\lambda} ct + \arctan \left( \frac{1}{\epsilon} \tan(\phi) \right) + \text{sgn}(\epsilon) \frac{n\pi}{2} \right) \quad (2.36)$$

where  $\text{sgn}(\epsilon)$  gives the sign of  $\epsilon$  and  $n \in \mathbb{N}_0$ . The parameter  $\phi_0 \in (0, 2\pi]$  defines the phasing of the wave front within one oscillation period of the light field, where the cases  $\phi_0 = 0$  and  $\phi_0 = \pi$  correspond to zero amplitude and the cases  $\phi_0 = \pi/2$  and  $\phi_0 = 3\pi/2$  to the positive respectively the negative amplitude maxima. To obtain a continuous curve from this expression several cases of  $n$  and the domain of  $\phi$  need to be considered and are dependent on  $t$  and  $\phi_0$ . For  $t = 0$  and  $\phi_0 = n_\phi \pi/2$  with  $n_\phi \in \{1, 2, 3\}$  a set  $\mathbf{R}_{\text{ell}}^0(\epsilon, n_\phi)$  of functions is given in the appendix A.49, which describes continuous wave fronts which correspond to the positive and negative maxima of the field amplitude and the two zero crossings.

For the case of a dipole emitter which is linearly polarized along the  $x$ - or  $y$ -axis, *i.e.*  $\epsilon = 0$  or  $\epsilon = \infty$  the wave fronts for  $t = 0$  are given by

$$\mathbf{R}_{\text{D}^x}^0(\phi, \phi_0) = \frac{\lambda}{2\pi} \left( \phi_0 + \frac{(n+1)\pi}{2} \right) \begin{pmatrix} -\cos(\phi) \\ \sin(\phi) \end{pmatrix} \quad (2.37)$$

$$\mathbf{R}_{\text{D}^y}^0(\phi, \phi_0) = \frac{\lambda}{2\pi} \left( \phi_0 + \frac{n\pi}{2} \right) \begin{pmatrix} \cos(\phi) \\ \sin(\phi) \end{pmatrix}. \quad (2.38)$$

In Figure 2.3a the wave fronts for the positive (red) and negative (blue) amplitude maxima of the field of an dipole which is oscillating along the  $x$ -axis are plotted together with the norm of the corresponding real valued emitted electric field. The wave fronts are given by a set of circles around the position which are separated by half the the wavelength  $\lambda$ . In particular the upper

<sup>12</sup>This is not a loss of generality, since this only fixes the angle between the coordinate system and the major and minor axis of the polarization ellipse to zero, see A.4. To generalize this case one just needs to rotate the coordinate system.

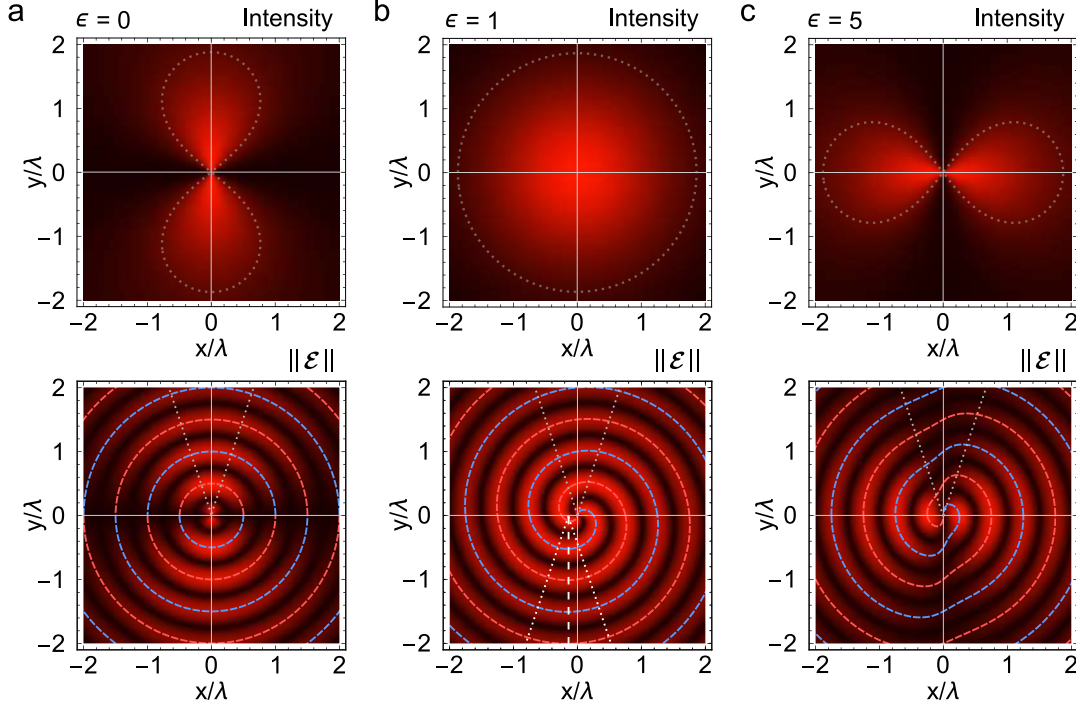


**Figure 2.3: Wave fronts.** Every subfigure shows in the upper part the intensity distribution of the radiation pattern of a dipole for different values of  $\epsilon$ , which correspond to linearly, circularly and elliptically polarized dipoles. In addition a contour line (gray, dotted) is plotted. In the lower parts of the subfigures the norm of the real valued electric fields are plotted together with wave fronts. The red wave fronts correspond to the positive maximum of the electric field and the blue wave fronts to the negative maximum. **a**, The shape of the contour line in the intensity plot is well known for the emission pattern of a linearly polarized dipole. The dotted lines in the plot of the electric field indicates the part of the wave fronts that is imaged when using an imaging system with  $\text{NA} = 0.3$ . Along the optical axis of such an imaging system one could approximate the local wave fronts with plane waves perpendicular to the optical axis. **b**, In the lower plot one would approximate the wave fronts within an aperture centered at the positive  $y$ -axis with plane waves which are tilted with respect to the optical axis and therefore estimate the position of the emitter to the right of its real position. The optical axis of a second imaging system in the lower part of the image was aligned such that the local approximation to the wave fronts is again orthogonal to the optical axis. The distance from this optical axis to the  $y$ -axis gives the apparent displacement of the emitter. **c**, The intensity distribution of this elliptically polarized dipole is very similar to the one of a linearly polarized emitter, as shown in subfigure **a**, which is clearly indicated by the contour line. Along the  $y$ -axis in the lower plot the wave fronts show a kink which tilts them stronger than in the case of the circularly polarized dipole. An approximation with plane waves would lead to the guess, that the emitter is located far right of its actual position.

half of a wave front circle corresponds to one field maxima, either positive or negative, while the lower half of the circle corresponds to the other maxima. This behaviour alternates from one wave front circle to the next. Note that there seems to exist a discontinuity of the wave fronts on the  $x$ -axis, but since the field is always zero along the  $x$ -axis, there are no wave fronts defined along the  $x$ -axis.

For the case of a  $\sigma^\pm$  ( $\epsilon = \pm 1$ ) polarized dipole the wave fronts for  $t = 0$  are Archimedean spirals given by

$$\mathbf{R}_{\sigma^+}^0(\phi, \phi_0) = +\frac{\lambda}{2\pi} \left( \phi_0 + \phi + \frac{n\pi}{2} \right) \begin{pmatrix} -\cos(\phi) \\ \sin(\phi) \end{pmatrix} \quad (2.39)$$

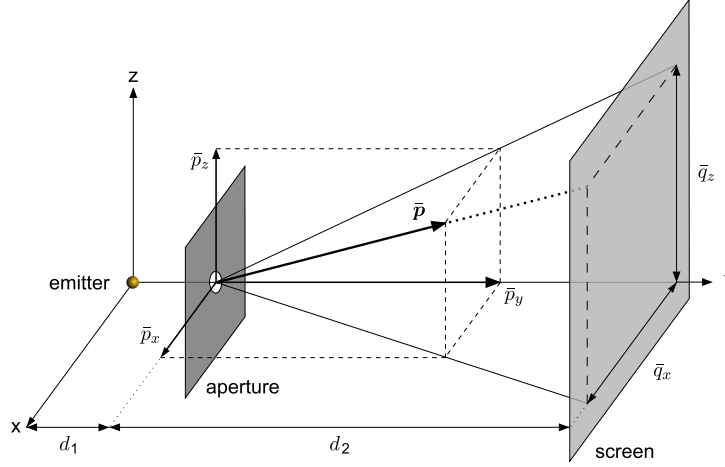
$$\mathbf{R}_{\sigma^-}^0(\phi, \phi_0) = -\frac{\lambda}{2\pi} \left( \phi_0 + \phi + \frac{n\pi}{2} \right) \begin{pmatrix} \cos(\phi) \\ \sin(\phi) \end{pmatrix}. \quad (2.40)$$

Figure 2.3b shows wave fronts of a  $\sigma^+$  polarized dipole. While the wave fronts of the linearly polarized emitter seem to be orthogonal to the  $y$ -axis at their intersections with the  $y$ -axis the wave fronts of the circularly polarized emitter are clearly tilted and not orthogonal to the  $y$ -axis at the corresponding intersections. This means that light at this positions is not propagating in radial direction, since the normal to the wave fronts corresponds to the local propagation direction of the light.

In Figure 2.3c wave fronts in the field of an elliptically polarized emitter with  $\epsilon = 5$  are shown. There the tilt of the wave fronts at the intersections with the  $y$ -axis is increased with respect to the circular polarized dipole, due to a strong kink of the wave fronts close to the  $y$ -axis. This means that the local propagation direction of the light is even more tilted with respect to the radial direction.

### 2.2.3 Displacement due to transverse linear momentum

From the wave fronts of an elliptically polarized dipole one can estimate, that the local propagation direction of the light might lead to errors in position determination, like it was already pointed out in Figure 2.3. We now investigate the consequences of the presence of a transverse momentum in the simplest imaging process, which uses only an aperture and a screen to image an elliptically polarized dipole emitter. This imaging system is shown in Figure 2.4 and assumed to be aligned along the  $y$ -axis, where the aperture is placed at a distance  $d_1$  from the emitter and the screen is placed at a distance  $d_2$  from the aperture. The linear momentum  $\bar{\mathbf{p}}$  of the light emitted by the dipole averaged over the aperture is composed by the longitudinal momentum  $\bar{p}_y$  and the two transverse linear momenta  $\bar{p}_x$  and  $\bar{p}_z$ . This transverse momenta cause the tilt of the local propagation direction of the light, with respect to the optical axis of the imaging system. Along the way to the screen the light which passed the aperture increase its distance to the optical axis due to the tilt of the mean propagation direction after the aperture. This results in a displacement of the center of mass of the image on the screen. Consequently one would estimate the light to originate from a position which is offset to the emitters position. Charles G. Darwin, grandson of the famous naturalist Charles Darwin, predicted this effect already more than 80 years ago [80]. Similar findings were made by Xin Li and Henk F. Arnoldus [49, 50, 81, 82].



**Figure 2.4: Transverse linear momentum.** An aperture is placed at a distance  $d_1$  from an emitter and the light passing the aperture is imaged on a screen at a distance  $d_2$  from the aperture. The linear transverse momentum at the position of the aperture leads to a tilt of the mean propagation direction of the light. Along the way to the screen the light which passed the aperture increase its distance to the optical axis due to the tilt of the mean propagation direction after the aperture. This results in a displacement of the center of mass of the image on the screen.

To find the mean momentum  $\bar{\mathbf{p}}$  of the light passing the aperture the momentum density  $\rho_{\mathbf{P}}$  introduced in 2.1.1 needs to be integrated over the volume inside the aperture:

$$\bar{\mathbf{p}} = \int_{\mathcal{A}} \int_{d_1}^{d_1+d_y} \rho_{\mu} dy dA, \quad (2.41)$$

where  $\mathcal{A}$  denotes the area of the aperture and  $d_y$  is much smaller than the radial elongation of the aperture. The position  $(\bar{q}_x, \bar{q}_z)$  of the center of mass in the image at the screen can then be derived from the relations

$$\frac{\|\bar{\mathbf{p}}_x\|}{\|\bar{\mathbf{p}}_y\|} = \frac{\bar{q}_x}{d_2} \quad \text{and} \quad \frac{\|\bar{\mathbf{p}}_z\|}{\|\bar{\mathbf{p}}_y\|} = \frac{\bar{q}_z}{d_2}. \quad (2.42)$$

This equations clearly show, that the image of the emitter is only shifted when the light field at the aperture exhibits a mean transverse momentum, *i.e.* an orbital angular momentum. This conditions are only fulfilled for dipole emitters which are elliptically polarized, which can already be seen in the wave fronts.

In the case of a vanishing aperture the linear momentum of the light passing the aperture can be approximated with the linear momentum in the center of the aperture,

$$\rho_{\mathbf{P}}(d_1 \mathbf{e}_y) = \frac{1}{d_1^2(1 + |\epsilon|^2)} \begin{pmatrix} -\frac{\text{Re}(\epsilon)}{d_1} \\ \frac{2\pi}{\lambda} \\ 0 \end{pmatrix}. \quad (2.43)$$

The displacement of the center of mass of the image at the screen can then be evaluated to

$$\bar{q}_x = -M \frac{\lambda}{2\pi} \operatorname{Re}(\epsilon) \quad \text{and} \quad \bar{q}_z = 0 \quad (2.44)$$

with the magnification  $M = d_2/d_1$ . The apparent displacement  $\Delta x$  in the object plane is then given by<sup>13,14</sup>

$$\Delta x = \frac{\lambda}{2\pi} \operatorname{Re}(\epsilon). \quad (2.45)$$

The apparent displacement increases linearly with the real part of  $\epsilon$  and can become arbitrary large. Although this is an interesting finding, this case is not relevant for common imaging and microscopy methods. The introduced setup to image with only an aperture with vanishing diameter and a screen is for instance realized by a pinhole camera. In general this is not an imaging method that would be used to image sub-wavelength emitters. Therefore we study in the next section the apparent displacement in an imaging system which is more related to common microscopy and optical imaging setups.

### 2.2.3.1 Transverse momentum and displacement in optical imaging systems

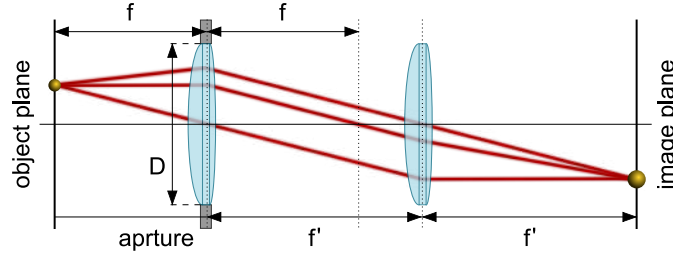


**Figure 2.5: Imaging system.** An emitter is in the object plane at a distance  $f$  from a lens with focal length  $f$  and aperture diameter  $D$ . At a distance  $f'$  from the first lens a second lens is placed with focal length  $f'$ , which forms an image of the emitter in the image plane at a distance  $f'$ . This image is magnified by the factor  $M = f'/f$ .

In order to model a more complex microscopy setup we use two lenses and place the first lens with focal length  $f$  and aperture diameter  $D$  at the distance  $f$  from the emitter, which is located in the origin. The second lens with focal length  $f'$  is placed at the distance  $f'$  from the first lens and the emitter is imaged on a screen at a distance  $f + 2f'$  from the origin, see Figure 2.5. The magnification of this imaging system is given by  $M = f'/f$  and the optical axis is the  $y$ -axis of the coordinate system. While the first lens applies a phase transformation to the light which passes the aperture, in a way that spherical waves originating from a single point in the

<sup>13</sup>Note that the switch of the sign between the real displacement of the center of mass of the image at the screen and the apparent displacement in the object plane is caused by a flip of the image in the particular imaging process.

<sup>14</sup>For a circularly polarized dipole the displacement can be geometrically determined from the spiral wave fronts, see appendix A.6

focal plane are converted into plane waves after the lens, the second lens focuses the light onto the screen. Thereby the average wave vector and thus the average linear transverse momentum is conserved [70,83]. We assume the dipole emitter to be elliptically polarized as defined in section 2.2.1. The situation with which we will deal in this subsection is sketched out for a  $\sigma^+$  polarized dipole in Figure 2.6. The spiral wave fronts, derived in section 2.2.2, which are emitted by the dipole can be approximated by spherical wave fronts at the position of the lens. However, the origin of this spherical waves lies in the object plane but not on the optical axis, as shown in Figure 2.6. Consequently they are transferred to plane waves by the first lens, while the tilt of the average momentum  $\bar{\mathbf{p}}$  at the position of the aperture is conserved, meaning the plane waves do not propagate along the optical axis of the imaging system. The second lens focusses this plane waves onto the focal plane. Due to the tilt of the plane waves they are not focused onto the optical axis [70, 83], instead the image is formed at a position offset to the optical axis.

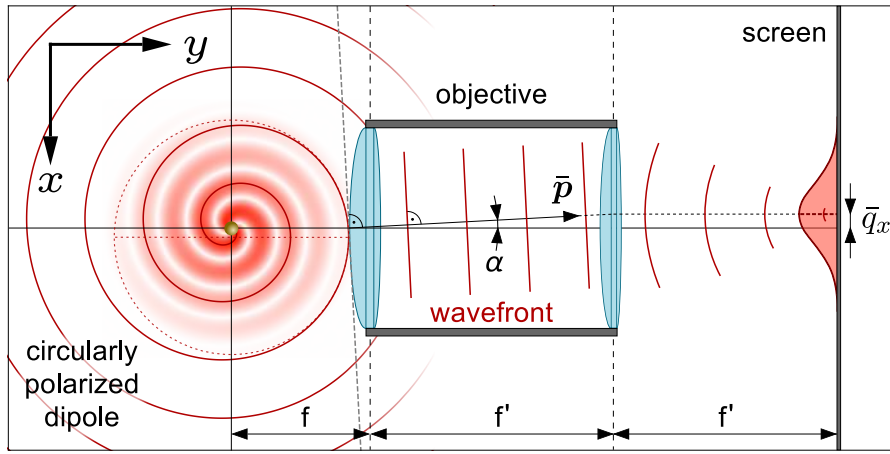


**Figure 2.6: Imaging a circularly polarized dipole.** A  $\sigma^+$  polarized dipole at the origin of the coordinate system emits a spiral wave front. At a distance  $f$  these spiral wave fronts are transformed to plane waves by a lens with the focal length  $f$ . Due to an linear transverse momentum of the light at the position of the aperture, these plane waves are tilted with respect to the optical axis by the angle  $\alpha$ , which also applies for the local momentum  $\bar{\mathbf{p}}$  averaged over the aperture. At a distance  $f'$  from the first lens the plane waves are focused by a second lens with focal length  $f'$  onto a screen in a distance  $f'$ . Due to the tilt of the plane wave fronts they are focused on a point offset to the optical axis. The image of the circularly polarized emitter is displaced in the image plane by  $\bar{q}_x$ , which leads to the assumption that the emitter is displaced in the object plane.

### 2.2.3.2 Mean linear momentum in imaging system

In order to determine the mean value  $\bar{\mathbf{p}}$  of the linear momentum of the light that passed a lens and was emitted by an elliptically polarized dipole emitter we use the decomposition of the electric field into the two fields emitted by dipoles with the two orthogonal polarization states  $D^x$  and  $D^y$  as introduced in 2.2.1. The fields emitted by the linearly polarized dipoles are after the lens

given by

$$\mathbf{E}_{D^x}^{\text{lens}}(\rho, \phi) = \frac{1}{f} \mathbf{e}_x e^{iky} C_E \quad (2.46)$$

$$\mathbf{E}_{D^y}^{\text{lens}}(\rho, \phi) = -\frac{\rho}{f^2} \mathbf{e}_\rho e^{iky} C_E. \quad (2.47)$$

with  $\mathbf{e}_\rho = \cos(\phi)\mathbf{e}_x + \sin(\phi)\mathbf{e}_z$  and  $C_E$  is constant in  $\mathbf{r}$ , but includes the time dependence of the fields. Here  $(\rho, \phi)$  are polar coordinates within the plane orthogonal to the imaging axis, with  $x = \rho \cos(\phi)$  and  $z = \rho \sin(\phi)$ . The complete derivations of the fields after the lens are shown in appendix A.7.

The electric field of an elliptically polarized emitter is after the lens given by the superposition  $\mathbf{E}_{\text{ell}}^{\text{lens}} = (\mathbf{E}_{D^x}^{\text{lens}} + i\epsilon\mathbf{E}_{D^y}^{\text{lens}})/N_\epsilon$ . Using expression 2.41 we can determine the mean momentum of the light which passed the lens. In the approximation  $D \ll f$  we can identify  $D/(2f)$  with the numerical aperture NA of the imaging system. Note that this aperture is the geometrical aperture and thus does not depend on the refractive index. The mean momentum is then given by

$$\begin{aligned} \bar{\mathbf{p}} &= \int_f^{f+d_y} \int_0^{2\pi} \int_0^{D/2} \frac{\epsilon_0}{2\omega} \text{Im} \left( \left( \vec{\nabla} \otimes \mathbf{E}_{\text{ell}}^{\text{lens}} \right) \left( \mathbf{E}_{\text{ell}}^{\text{lens}} \right)^* \right) \rho d\rho d\phi dy = \\ &= \frac{\epsilon_0 |C_E|^2}{2\omega} \frac{\text{NA}^2 d_y}{(1 + |\epsilon|^2)} \begin{pmatrix} -\frac{1}{f} \pi \text{Re}(\epsilon) d_y \\ k\pi(1 + |\epsilon|^2) \frac{\text{NA}^2}{2} d_y \\ 0 \end{pmatrix} \end{aligned} \quad (2.48)$$

This determination is performed in detail in appendix A.8. A dipole emitter which is linearly polarized along the  $x$ -,  $y$ - or  $z$ -axis, *i.e.*  $\epsilon = 0$  does not feature any linear transverse momentum, see A.8.

### 2.2.3.3 Displacement of the center of mass of an image

Now with the mean momentum of the light which was emitted by an elliptically polarized emitter and which passed the first lens of the imaging system, it is possible to determine the displacement of the center of mass with respect to the optical axis in the image using expressions 2.42. Since the second lens of the imaging system transforms the plane waves which do not propagate along the optical axis again into spherical waves which form an image on the screen offset of the optical axis the center of mass displacement does not change beyond the second lens. Therefore, the length  $d_2$  in the expressions 2.42 needs to be replaced with  $f'$ , resulting in

$$\bar{q}_x = -M \frac{\lambda}{2\pi} \frac{\text{Re}(\epsilon)}{1 + |\epsilon|^2 \frac{\text{NA}^2}{2}} \quad (2.49)$$

and

$$\bar{q}_z = 0, \quad (2.50)$$

with  $k = 2\pi/\lambda$ . Since  $\bar{q}_z = 0$  there is no displacement in  $z$ -direction.

As pointed out in appendix A.4 the field of an arbitrarily elliptically polarized dipole can always be decomposed into the fields of an optical-axis-oriented elliptically polarized dipole<sup>15</sup>, characterized by  $\text{Re}(\epsilon)$  plus a residual field of a linearly polarized dipole, characterized by  $\text{Im}(\epsilon)$ . The shift of the center of mass in the image is solely caused by the optical-axis-oriented elliptically polarized dipole, while the residual linearly polarized dipole decreases the displacement.

The shift of the center of mass of the image in on the screen consequently leads to an apparent shift of the emitter in the object plane given by

$$\Delta x = \frac{\lambda}{2\pi} \frac{\text{Re}(\epsilon)}{1 + |\epsilon|^2 \frac{\text{NA}^2}{2}}. \quad (2.51)$$

Here, the switching of the sign is caused by the fact that the imaging process provides an image of the scenery in the object plane which is inverted. In Figure 2.9 the apparent displacement in the object plane  $\Delta x$  is plotted for real valued  $\epsilon$ . The shift appears along an axis parallel to the projection of the average momentum  $\bar{\mathbf{p}}$  of the light field into the image plane. The case  $\epsilon = 0$  respectively  $\epsilon = \infty$  results in the displacement being zero, as one would expect when imaging purely linearly polarized dipoles. In the following we focus on real valued  $\epsilon$ , which gives the largest shifts. Assuming that the numerical aperture and  $|\epsilon|$  are small,  $\epsilon^2 \text{NA}^2 \ll 1$ , and the center of mass shift can be approximated by

$$\Delta x \approx \epsilon \frac{\lambda}{2\pi}, \quad (2.52)$$

Consequently, for small  $\epsilon$ , the center of mass of the far field image, *i.e.* the apparent shift of the emitter in the object plane, increases linearly in  $\epsilon$ . The same apparent displacement as function of  $\epsilon$  was obtained by determining the local tilt of the wave fronts along the optical axis, which corresponds to an imaging setup with vanishing aperture. For  $\epsilon = \pm 1$ , which corresponds to a  $\sigma^\pm$  polarized dipole, the apparent shift of the emitter in the object plane is then given by  $\Delta x \approx \pm \lambda/(2\pi)$ . For  $\epsilon = \pm \sqrt{2}/\text{NA}$  the maximum displacement is reached, given by

$$\Delta x_{max} = \pm \frac{\lambda}{2\pi} \frac{1}{\sqrt{2} \text{NA}}, \quad (2.53)$$

meaning that for vanishing NA the shift of the center of mass can get arbitrary large, which is quite an extraordinary result. For  $\text{NA} = 0.225$  and  $\epsilon = 6.3$  the distance between the positive and negative maximum displacement equals  $\lambda$  and for  $\text{NA} = 0.11$  and  $\epsilon = 12.6$  the distance between the emitter's real and apparent position equals  $\lambda$ . In this regime the polarization of the emitter is almost linear along the optical axis.

While the displacement of the center of mass of the image of an elliptically polarized dipole was determined with classical physics the same derivation can be performed in a quantum mechanically approach using the wave function of the photons emitted by the dipole. In an operational approach one can identify the local transversal linear momentum of the light at an

<sup>15</sup>As defined in appendix A.4 the major or minor axis of the polarization ellipse of an optical-axis-oriented elliptically polarized dipole coincide with the optical axis of the imaging system, which is used to image the dipole emitter.

aperture by determining the weak value [84–86] of the orbital angular momentum of the photon wave function. With the local transverse linear momentum it is then possible to determine the displacement of the centre of mass of the image, in the same way it was performed in this section. Moreover, it is in principle possible to derive the momentum density using this approach. The quantum mechanically determination of the apparent displacement is presented in the appendix A.9 and leads to the same results as they are obtained in this section.

### 2.2.4 Fourier optics

In the previous section we derived the center of mass shift of a far field image of an elliptically polarized emitter via the mean value of the linear momentum of the emitted light averaged over the aperture of the used imaging system. Unfortunately this derivation only investigates mean quantities of the wave functions and does not yield information on the spatial intensity distribution of the image. As this is of vital importance for many applications and position determination methods we will provide an approach based on Fourier optics that allows us to derive an analytical expression for this intensity distributions.

For an imaging system consisting of two lenses we already determined the electric field of an emitter after collimating the field with a lens in the small NA approximation. We now want to investigate the evolution of this field for a typical imaging configuration, where a second lens focuses the collimated field to form a real image of the emitter. This can be done within the framework of Fourier optics. The fundament of Fourier optics is the conclusion that the Fraunhofer diffraction, which describes the diffracted field at a long distance from the diffracting object [83], is given by the Fourier transform of the diffracting object. The assumption that the diffracting object is much smaller than the distance at which we determine the diffracted field, which is made in the Fraunhofer diffraction, matches the assumptions we made in our imaging system, where the diameter of the aperture of the lenses is much smaller than their focal length.

In order to determine the evolution of the field emitted by an elliptically polarized dipole emitter it is convenient to decompose it into two orthogonal linearly polarized components. For the setup we make the same assumptions as in the previous section 2.2.3. The elliptically polarized emitter rotating in the  $xy$ -plane is located at the origin and imaged along the  $y$ -axis. The diameter of the aperture  $D$  is considered to be much smaller than the focal lengths  $f$  and  $f'$  of the first and second lens in the imaging system. The lenses are placed at a distance  $f$  and  $f + f'$  from the emitter, see Figure 2.5. As outlined in appendix A.7, after the first lens, we obtain the field distributions  $\mathbf{E}_{D^x}^{\text{lens}}$  and  $\mathbf{E}_{D^y}^{\text{lens}}$  (see expressions 2.46 and 2.47). While  $\mathbf{E}_{D^x}^{\text{lens}}$  gives the field of a dipole which is linearly polarized orthogonal to the imaging axis,  $\mathbf{E}_{D^y}^{\text{lens}}$  gives the field of a dipole linearly polarized along the optical axis of our considered imaging system. According to Fourier-optics [83] the complex valued electric field in the image plane  $\mathbf{E}^{\text{ip}}$  is given by the Fourier transform of the field in the plane of the lens:

$$\mathbf{E}^{\text{ip}}(\rho, \phi) = \int_0^{2\pi} \int_0^{D/2} \mathbf{E}^{\text{lens}}(\rho', \phi', f') e^{-i \frac{k}{f'} \rho \rho' \cos(\phi - \phi')} \rho' d\phi' d\rho'. \quad (2.54)$$

The intensity distribution in the image plane averaged over one oscillation period of the field is given by

$$\mathcal{I} = \frac{1}{2} c \epsilon_0 \left| \mathbf{E}_0^{\text{ip}} \right|^2. \quad (2.55)$$

In order to evaluate the fields  $\mathbf{E}_{D^x}^{\text{lens}}$  and  $\mathbf{E}_{D^y}^{\text{lens}}$  at the position of the second lens their phase  $e^{iky}$  needs to be evaluated at the position  $f'$  of the second lens. The fields of the linearly polarized dipoles in the image plane are given by

$$\mathbf{E}_{D^x}^{\text{ip}}(\rho, \phi) = \int_0^{2\pi} \int_0^{D/2} \mathbf{E}_{D^x}^{\text{lens}}(\rho', \phi', f') e^{-i \frac{k}{f'} \rho' \cos(\phi - \phi')} \rho' d\phi' d\rho' \quad (2.56)$$

$$\mathbf{E}_{D^y}^{\text{ip}}(\rho, \phi) = \int_0^{2\pi} \int_0^{D/2} \mathbf{E}_{D^y}^{\text{lens}}(\rho', \phi', f') e^{-i \frac{k}{f'} \rho' \cos(\phi - \phi')} \rho' \cos(\phi - \phi') d\phi' d\rho'. \quad (2.57)$$

The factor  $\cos(\phi - \phi')$  stems from the vector nature of the light fields and describes the polarization overlap  $\mathbf{e}_\rho \mathbf{e}_{\rho'} = \cos(\phi - \phi')$ . Solving these integrals, the fields in the image plane are then given by

$$\mathbf{E}_{D^x}^{\text{ip}}(\rho, \phi) = \frac{J_1\left(\frac{Dk}{2f'}\rho\right)}{\rho} \mathbf{e}_x \frac{Df'\pi}{fk} e^{ikf'} C_E \quad (2.58)$$

$$\mathbf{E}_{D^y}^{\text{ip}}(\rho, \phi) = \frac{J_2\left(\frac{Dk}{2f'}\rho\right)}{\rho} \mathbf{e}_\rho \frac{Df'\pi}{fk} e^{ikf'} \cdot \frac{iD}{2f} C_E, \quad (2.59)$$

where  $J_1$  and  $J_2$  denote the first and second order Bessel functions of first kind. With the magnification  $M = f'/f$ , the numerical aperture  $\text{NA} = D/(2f)$  given in the approximation  $D \ll f$ , and  $k = 2\pi/\lambda$ , the two fields can be written as

$$\mathbf{E}_{D^x}^{\text{ip}}(\rho, \phi) = \frac{J_1\left(\frac{2\pi}{\lambda} \frac{\text{NA}}{M} \rho\right)}{\rho} \mathbf{e}_x C_E \quad (2.60)$$

$$\mathbf{E}_{D^y}^{\text{ip}}(\rho, \phi) = \frac{J_2\left(\frac{2\pi}{\lambda} \frac{\text{NA}}{M} \rho\right)}{\rho} \mathbf{e}_\rho \cdot i \text{NA} C_E. \quad (2.61)$$

Note that the NA in these fields, as it was already stated in section 2.2.3.2, corresponds to the geometrical NA and thus does not depend on the refractive index. The constant factors that appear in both dipole fields are absorbed into the constant  $C_E$ , which will not be pointed out explicitly by a different notation in the following.

The field of an arbitrarily elliptically polarized dipole rotating in the  $x$ - $y$ -plane can be decomposed into fields of two orthogonal linearly polarized dipoles as it was presented earlier, see expression 2.31. Following this decomposition we obtain for the field in the image plane

$$\mathbf{E}_{\text{ell}}^{\text{ip}}(\rho, \phi) = \frac{1}{N_\epsilon} \left( \mathbf{E}_{D^x}^{\text{ip}} + i \cdot \epsilon \mathbf{E}_{D^y}^{\text{ip}} \right), \quad (2.62)$$

## 2. SPIN-ORBIT INTERACTION IN OPTICAL IMAGING

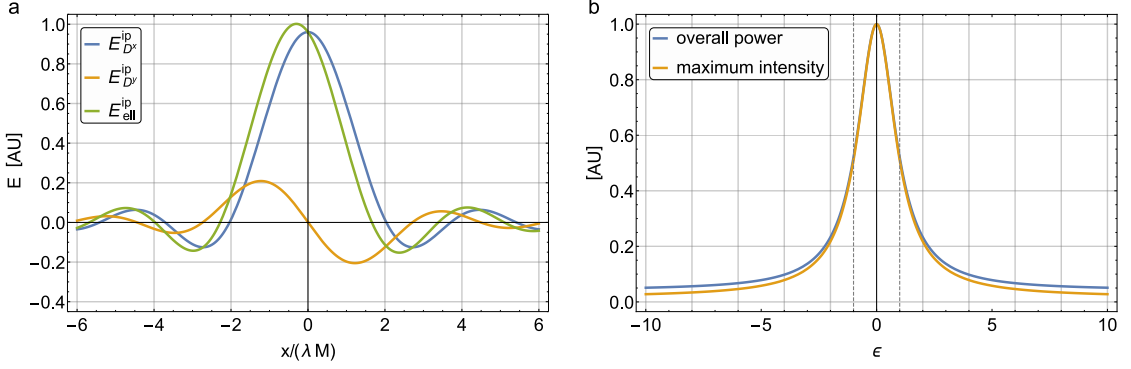


**Figure 2.7: Electric field in the image plane.** **a**, The  $x$ -component of the electric field in the image plane emitted by an elliptically polarized dipole (green) with  $\epsilon = 2$  plotted along the  $x$ -axis. The assumed imaging system has an aperture of  $\text{NA} = 0.3$ . Along the  $x$ -axis the other field components are zero. Additionally the decomposition of the field of the elliptically polarized dipole in the two fields of linearly polarized dipoles oscillating along the  $x$ - and  $y$ - axis are plotted (blue and yellow). One can see that while the field of the dipole which is linearly polarized along the  $x$ -axis is symmetric with respect to  $x = 0$ , the field of the dipole which is linearly polarized along the  $y$ -axis is antisymmetric with respect to  $x = 0$ . This leads to constructive interference on one, and destructive interference on the other side, which in turn leads to a shift of the global maximum of the electric field, *i.e.* the intensity. Consequently the centroid of the image is displaced. **b**, The overall power of a dipole emitter radiated onto the image plane (blue) and the maximum intensity (yellow) plotted as a function of  $\epsilon$ , The considered imaging system has an aperture of  $\text{NA} = 0.3$ . For increasing  $|\epsilon|$  both quantities decrease due to the decreasing relative amplitude of the dipole which is linearly polarized along the  $x$ -axis, which composes together with the dipole which is linearly polarized along the  $y$ -axis the field of the elliptically polarized dipole. For  $\epsilon = 0$  the fraction of the power emitted by the emitter across the aperture is maximal. For  $|\epsilon| = \infty$  the fraction of the power emitted across the aperture is minimal but still nonzero as long the aperture diameter is nonzero. For circularly polarized emitters ( $\epsilon = \pm 1$ , indicated by the dashed lines) the overall power and the maximum intensity already drop to half of their maximal values.

with the normalization factor  $N_\epsilon$  as defined in 2.31.

Using the decomposition 2.62 of the field which was emitted by an elliptically polarized dipole with real valued  $\epsilon$  in the image plane and in the object plane, one notices that the two composing linear dipole fields are out of phase by  $\pi/2$  at the lens, while they are in phase after a second lens in the image plane. This means that the two composing fields do not interfere at the lens, but feature constructive and destructive interference in the image plane. The field  $\mathbf{E}_{\text{ell}}^{\text{ip}}$  and the composing components  $\mathbf{E}_{D^x}^{\text{ip}}$  and  $\mathbf{E}_{D^y}^{\text{ip}}$  are plotted along the  $x$ -axis of the image plane in Figure 2.7a, for the exemplary parameters  $\epsilon = 2$  and  $\text{NA} = 0.3$ . Along the  $x$ -axis of the image plane, the polarization vectors of both fields are parallel to the  $x$ -axis. While  $\mathbf{E}_{D^x}^{\text{ip}}$  is symmetric with respect to the  $x = 0$ ,  $\mathbf{E}_{D^y}^{\text{ip}}$  is antisymmetric, leading to constructive interference on one

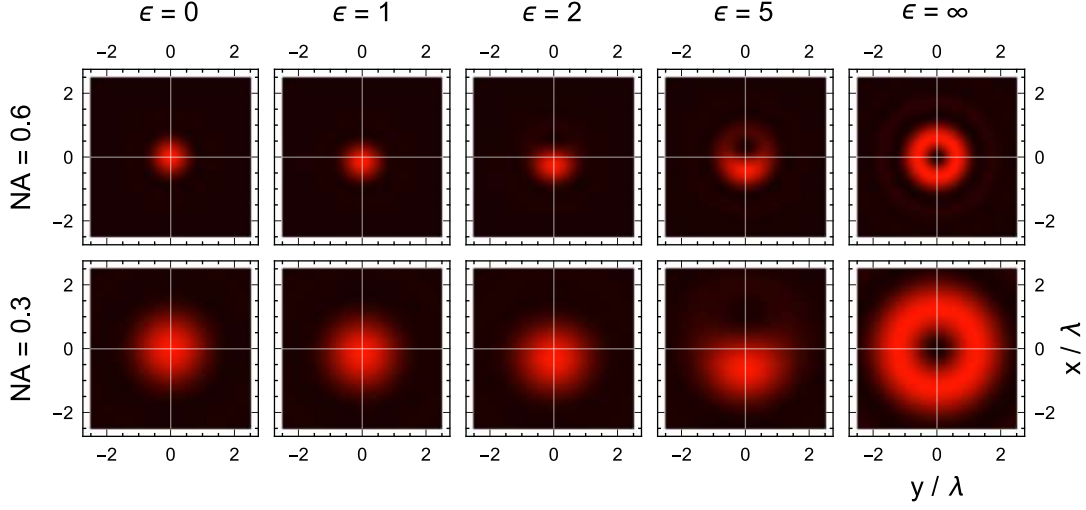


**Figure 2.8: Images of elliptically polarized dipoles.** Calculated images of an elliptically polarized dipole are shown for different values of  $\epsilon$  and the two apertures  $\text{NA} = 0.6$  and  $\text{NA} = 0.3$ . The increasing apparent displacement of the emitter can be seen, as well as the evolution of the shape of the images. This figure nicely illustrates why there is a maximum displacement which can not be exceeded. As the displacement stems from the interference of the spot like image at  $\epsilon = 0$  with the ring structure at  $\epsilon = \infty$  the apparent displacement can never exceed the radius of the ring.

side of the optical axis and destructive interference on the other side. This interference leads to a shift of the peak as well as of the center of mass of the intensity distribution of the image, giving rise to an apparent shift of the emitter’s position.

The overall power emitted by the dipole stays the same when changing  $\epsilon$ , but the power collected with the imaging system decreases with increasing  $\epsilon$ . For  $\epsilon \ll 1$  most of the collected light comes from  $\mathbf{E}_{D^x}^{\text{ip}}$ , which features a maximum of emission along the imaging axis, see Figure 2.3a and b. In contrast, for  $\epsilon \gg 1$ , most of the collected light comes from  $\mathbf{E}_{D^y}^{\text{ip}}$ , which exhibits a minimum of emission along the imaging axis. The resulting decrease of the overall power collected by the imaging system and the maximum of intensity in the taken images with increasing  $\epsilon$  is plotted in Figure 2.7b.

Figure 2.8 shows a set of images calculated for different values of  $\epsilon$  for the two numerical apertures 0.3 and 0.6. There the increasing apparent displacement of the emitter can be seen, as well as the evolution of the shape of the images. For small  $\epsilon$  the image is a circular spot. Intermediate values of  $\epsilon$  lead to some kidney shaped structure. Finally when one images a dipole which is linearly polarized along the optical axis, *i.e.*  $\epsilon = \infty$  the image is given by ring structure. This figure nicely illustrates why there is a maximum displacement which can not be exceeded. As the displacement stems from the interference of the spot like image ( $\mathbf{E}_{D^x}^{\text{ip}}$ ) with the ring structure ( $\mathbf{E}_{D^y}^{\text{ip}}$ ) the apparent displacement can never exceed the radius of the ring.

### 2.2.4.1 Apparent displacement

We now investigate how the change of the point spread function with respect to  $\epsilon$  affects different position determination methods. First we compare the center of mass obtained from the image with the results from section 2.2.3.3. Then the effects of the image distortions caused by an elliptically polarized dipole on other position determination methods will be briefly discussed.

The center of mass of an image is given by

$$\bar{q}_j = \frac{\int q_j \mathcal{I}(q_j) dA}{\int \mathcal{I}(\mathbf{q}) dA}, \quad (2.63)$$

for  $j \in \{x, z\}$ . The integral is taken over the whole image plane. In general for an elliptically polarized dipole the intensity of the elliptical field in the image plane is given by

$$\mathcal{I}_{\text{ell}}(\rho, \phi) = \frac{c\epsilon_0 |C_E|^2}{2(1 + |\epsilon|^2)\rho^2} \left( J_1(\tilde{\rho})^2 + |\epsilon|^2 \text{NA}^2 J_2(\tilde{\rho})^2 - 2 \text{Re}(\epsilon) \text{NA} \cos(\phi) J_1(\tilde{\rho}) J_2(\tilde{\rho}) \right) \quad (2.64)$$

with  $\tilde{\rho} = \rho \cdot 2\pi \text{NA} / (\lambda M)$ . Now when determining  $\bar{q}_x$ , the integrals in equation 2.63 consist of the three terms in equation 2.64 multiplied by  $q_x$ . As  $J_n^2$  is a rotationally symmetric function, the first two parts of 2.64 describe images which are rotationally symmetric with respect to the origin. Consequently their center of mass lies at the origin and they do not contribute to any nonzero  $\bar{q}_x$ . The only remaining nonzero part is therefore given by<sup>16</sup>

$$\bar{q}_x = - \frac{2 \text{Re}(\epsilon) \text{NA} \int_0^{2\pi} \int_0^\infty J_1\left(\frac{2\pi}{\lambda} \frac{\text{NA}}{M} \rho\right) J_2\left(\frac{2\pi}{\lambda} \frac{\text{NA}}{M} \rho\right) \cos(\phi)^2 d\rho d\phi}{2\pi \int_0^\infty \frac{1}{\rho} \left( J_1\left(\frac{2\pi}{\lambda} \frac{\text{NA}}{M} \rho\right)^2 + |\epsilon|^2 \text{NA}^2 J_2\left(\frac{2\pi}{\lambda} \frac{\text{NA}}{M} \rho\right)^2 \right) d\rho}. \quad (2.65)$$

Solving this integral leads to a center of mass along the  $x$ -axis of

$$\bar{q}_x = -M \frac{\lambda}{2\pi} \frac{\text{Re}(\epsilon)}{1 + |\epsilon|^2 \frac{\text{NA}^2}{2}}. \quad (2.66)$$

In the integral to evaluate  $\bar{q}_z$  the  $\cos(\phi)^2$  is exchanged by  $\cos(\phi) \sin(\phi)$ . Therefore the center of mass along the  $z$ -axis is zero. Consequently, the apparent displacement in the object plane for the center of mass estimate is given by

$$\Delta x = \frac{\lambda}{2\pi} \frac{\text{Re}(\epsilon)}{1 + |\epsilon|^2 \frac{\text{NA}^2}{2}}, \quad (2.67)$$

which is the same result as the one obtained in 2.51.

<sup>16</sup>With  $\rho_x = \rho \cos(\phi)$  and  $dA = \rho d\rho d\phi$

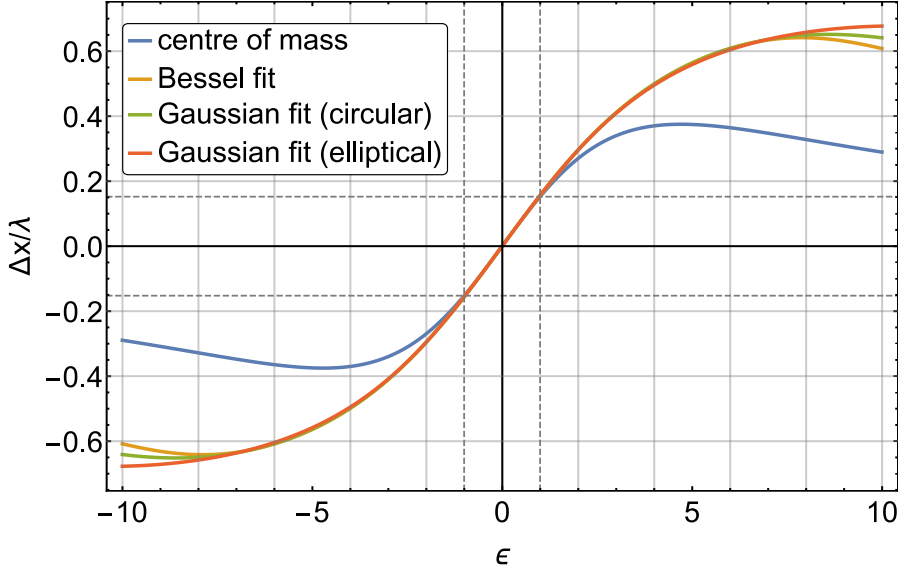


**Figure 2.9: Position determination.** The apparent displacement  $\Delta x$  plotted as a function of  $\epsilon$ . An imaging system with an aperture of  $\text{NA} = 0.3$  was assumed to calculate the images in which the apparent position was measured. The used position determination methods are the centre of mass estimate (blue), a fit of the theoretical point spread function (Bessel function) of an emitter with  $\epsilon = 0$  (yellow), a fit of a circularly shaped Gaussian function (green) and a fit of an elliptically shaped Gaussian function (red). The dashed vertical lines indicate the circular polarization states  $\epsilon = \pm 1$  and the horizontal dashed lines the displacement  $\Delta x = \lambda/(2\pi)$ . For  $|\epsilon| \leq 1$  all position determination methods lead to the same apparent displacement. For  $|\epsilon| > 1$  the centre of mass method shows a much smaller displacement than the other three methods, which lead to roughly the same displacement. Also they lead to a maximum displacement which is much higher than the one of the centre of mass method and the maximal overall displacement even exceeds the optical wavelength.

With the knowledge of the intensity distribution  $\mathcal{I}_{\text{ell}}(\rho, \phi, \epsilon)$  in the image plane, it is now possible to use other methods to determine the position of the emitter other than the center of mass estimate.

We now focus on the offset between the emitter's real and its apparent position when using other methods for position determination than the center of mass estimate.<sup>17</sup> A very prominent method to localize emitters by their images is the Gaussian fit, which is known to be a very reliable tool in position determination [87]. A more precise method is to fit the known point spread function of the imaging system to the measured intensity distributions, where the point spread function can either be theoretically or experimentally determined. In the framework of this section it is given by expression 2.64 with  $\epsilon$  being solely imaginary valued for a solely

<sup>17</sup>Thereby we neglect any knowledge of the apparent displacement of the emitter and try to measure an emitters position assuming it is linearly polarized orthogonal to the optical axis. We do this to get an estimate of the apparent displacement one would measure when not aware of the effects presented in this thesis.

linearly polarized dipole.

Figure 2.9 shows the apparent shifts of the particle's position caused by fitting the theoretical point spread function of a linearly polarized dipole and two Gaussian based fitting functions (circular and elliptical) plotted as a function of the real valued  $\epsilon$ . For  $|\epsilon| < 1$  these methods give the same apparent position. While the center of mass starts to separate at  $|\epsilon| > 1$ , the other position determination methods still give a very similar apparent displacement, which is larger than the one obtained by the center of mass estimate.

A major consequence of this study is, that although one might intuitively think so, the centroid of an elliptically polarized dipole does not coincide with its real position and that more sophisticated methods are required to determine the position of an emitter with unknown polarization state (see chapter 5).

### 2.3 Summary

In this chapter we showed that the local linear momentum of the light emitted by a dipole can feature transverse components, which causes a tilt of the local propagation direction with respect to the radial direction. The local linear momentum averaged over an aperture gives rise to a displacement of the center of mass of the image of the emitter, which in turn leads to the assumption that the emitter is at an apparent position, where in fact it is not.

In order to investigate the effect of elliptically polarized dipoles on other position estimation methods than the center of mass estimate, we determined the image formed by a two lens system with Fourier optics. With an analytical expression for the image of an elliptically polarized dipole formed in the image plane it was possible to study different position determination methods. Moreover it was possible to reproduce the shift of the center of mass of the images.

Both methods used to determine the displacement of the center of mass in the image of an elliptically polarized emitter lead to the same analytical expression and concludingly to the same apparent displacement of the emitter. This is an outstanding result since both methods used quite different approaches.

# Measurement of apparent displacement due to SOI

## 3.1 Introduction

In this chapter, an experimental setup will be presented, in which the spin-orbit coupling of light emitted by a spherical gold nanoparticle manifests as a mismatch between the measured position of the emitter determined in images which are taken for different polarization states of the nanoparticle. Therefore, the particle is deposited on a sub wavelength diameter waveguide, realized by an optical nanofiber and illuminated by the evanescent field of the latter (see Figure 3.1). This evanescent field features locally linearly polarized light and almost circularly polarized light, depending on the azimuthal position with respect to a quasilinear polarization in the nanofiber. Using light of different polarizations in the fiber, it is thereby possible to illuminate the nanoparticle with linearly and circularly polarized light, which then, due to its properties, defines the particle's polarization state. Images taken of the linearly polarized particle act as a reference of the particles real position and images taken of the circularly polarized particle reveal that it seems to have been displaced. While using nanoparticle-nanofiber samples with different particle and fiber diameter, which leads to different elliptical polarizations at the position of the particle on the fiber surface, we could not only measure different apparent positions due to the spin-orbit coupling, but also observed the effect of an apparent displacement when defocusing the imaging system. The reason for this effect in this particular setup is that the field emitted by the particle is a superposition of the directly emitted and on the fiber reflected field, which features a strong anisotropy along the aperture of the imaging system.

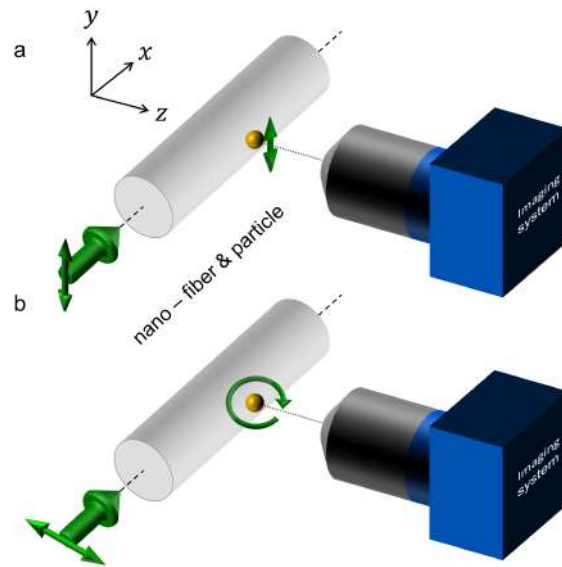


**Figure 3.1: Experimental setup.** **a**, A nanofiber oriented along the  $x$ -axis with a nanoparticle on its surface which faces towards an imaging system. Light which is linearly polarized along the  $y$ -axis is coupled into the nanofiber and causes the evanescent field at the position of the nanoparticle to be also vertically linearly polarized. This polarization configuration is used to take images from the nanoparticle in which its real position is determined. **b**, The same setup where light which is linearly polarized along the  $z$ -axis is coupled into the nanofiber. The corresponding evanescent field is at the position of the nanoparticle elliptically polarized. In images the particle now appears to be displaced with respect to the reference images.

### 3.2 Preparing a single nanoparticle

In order to quantitatively investigate the effects of spin-orbit coupling on position measurements using far field optical imaging, it is necessary to find a suitable sub-wavelength sized emitter which provides the possibility to arbitrarily control its polarization state. Also, it needs to maintain this property in the experimental environment over the time scale of the experiment and should not change any characteristics, such as shape or chemical composition which might change its polarizability. Another necessity of the emitter is the possibility to deposit it on a substrate, where it stays in place, which makes it much easier to measure an apparent position with respect to its real position, since short term drifts, as one would have to deal with if the emitter is in a liquid solution, are ruled out.

Within the experimental procedure, it is a very important task to image only one single emitter within the diffraction limited range of the resolution of the imaging system. Otherwise, interference of the emitted light from two or more emitters could modify the single emitter emission pattern, thereby disturbing the predicted apparent shift. Moreover, collective effects of the emitters could change their emission behaviour in general if they are very close together or even touch each other.

We found that the properties of spherical gold nanoparticles match our experimental needs. To assure that we image a single emitter, we deposited a gold nanoparticle on a nanofiber, which provides a handy tool to prove the presence of a single particle via absorption spectroscopy.

### 3.2.1 Selecting a suitable emitter

The above requirements are fulfilled, for instance, by metal nanoparticles or metal-coated nanoshells with a dielectric core. Due to oscillations of the electrons near the surface driven by an external electromagnetic field, such particles emit light of the same wavelength as the illuminating light field. These collective oscillations are called surface plasmons [88] of which the resonance lies often in the visible spectra. The optical properties of these emitters are highly dependent on their shape [88–91]. While a nanorod has a dipole moment which is dominant along its elongated axis, a nanosphere has in any spatial direction the same dipole moment. As a result of the spherical shape these particles can be considered ideal, rotationally symmetric, dipole emitters that copy the polarization state of the illuminating light field [92, 93], which is sometimes described as polarization maintaining. In summary, these nanospheres fulfil our experimental needs. Furthermore, the surface plasmon resonances for spherical metal nanoparticles are quite broad, up to several nanometers, and depend on the radius of the sphere. For metal nanoparticles, they lie within the visible spectra. Thus, spherical metal nanoparticles are very well suited for our experimental purposes. Gold and silver are typical materials used to produce such nanoparticles which feature for a diameter of 100 nm a surface plasmon resonance with a wavelength of about 550 nm.

For our experiments we choose spherical gold nanoparticles with diameters in the range of 80 nm to 125 nm which have a absorption maximum at a wavelength of about 535 nm to 590 nm when surrounded by water. Gold nanoparticles have evolved to be a widely used tool [91, 94] in research and medicine where they are deployed for sensing, labeling and imaging in biotechnology [95–97], or in cancer treatment [90]. Moreover, gold nanoparticles are used in super-resolution microscopy where accuracies in finding particles positions below 10 nm are stated [60, 98–101]. Since they consist of a noble metal, gold nanoparticles provide an excellent chemical stability. However, this chemical stability is not sustainable when going to very small particle sizes. Below diameters of 10 nm gold particles lose some of their noble metal properties [102]. In terms of mechanical stability, gold nanoparticles are slightly harder and more elastic than the bulk material [103]. It is known that for very small particle sizes, the melting point of gold decreases [104], but this happens far in the sub nanometre regime, where the melting temperature is reduced by a factor of two at a particle diameter of about 5 nm. However, when illuminating gold nanoparticles with high intensity light fields it is still possible to melt the particle, which was shown by [105] where an intensity of  $8 \cdot 10^9 \text{W/m}^2$  melts an 80 nm diameter gold nanoparticle.

The presented properties make spherical gold nanoparticles highly suitable for measurements of a shift of the particles position dependent on their polarization within the planned experiment. The mentioned drawbacks of very small particle sizes do not affect the particles we want to use since their size is well above the threshold of 10 nm and consequently the chemical, mechanical, and thermal stabilities are granted.

### 3.2.2 Preparing a single gold nanoparticle

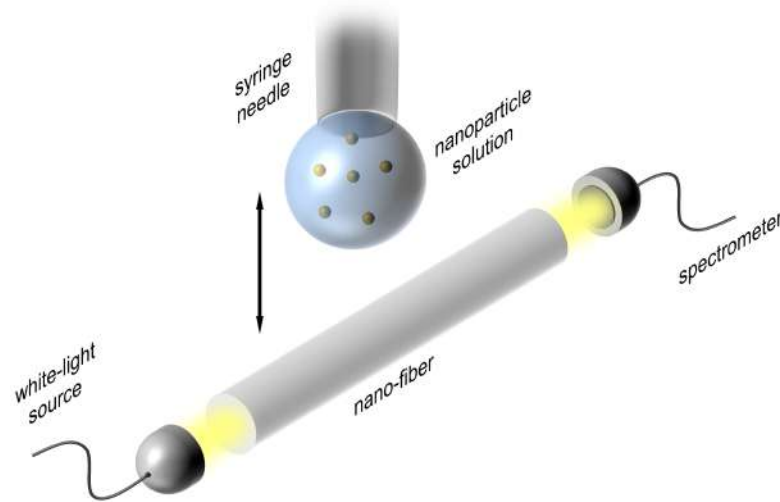


**Figure 3.2: Deposition of a nanoparticle on a nanofiber.** Using a syringe needle, small droplets of a suspension containing nanoparticles are prepared. These droplets are brought in contact with the horizontally aligned nanofiber. This process is done with a three axis translation stage and monitored with a microscope. One end of the nanofiber is attached to a white light source and the other end to a spectrometer recording the spectra of the white light source. An individual nanoparticle which is deposited onto the nanofiber is recognized by a characteristic absorption peak in the transmitted spectra

To assure to image a single nanoparticle, we use a technique which was developed in earlier experiments [35, 106]. In this technique, we deposit a single gold nanoparticle on a sub-wavelength diameter optical waveguide, realized by a nanofiber [107, 108] which we produce from standard single mode optical fibers in a heat and pull process. Through the evanescent field, these nanofibers provide a strong light–matter interaction between the light guided by the fiber and objects close to the surface. The evanescent field decays exponentially over a few hundred nanometres above the surface of the nanofiber. This strong interaction allows us to detect individual nanoparticles using an absorption spectroscopy measurement via the nanofiber, which is described in the next subsection (3.2.3). The deposition of single nanoparticles onto the nanofiber is done by directly touching the nanofiber with a droplet of a suspension containing the nanoparticles. The nanoparticles are fabricated by BBI Solutions and Nanopartz and are suspended in deionized water. Using a syringe with a very thin needle, we can prepare small droplets of nanoparticle suspension which can be positioned by a three axis translation stage along the nanofiber, see Fig. 3.2. This process is monitored with a standard optical microscope. We vertically approach the nanofiber with the droplet until they are in contact. The point where the nanofiber and the droplet are in contact can be live monitored by measuring the absorption of the light guided through the nanofiber, since the droplet scatters a lot of light from the evanescent

field. Moreover, it is possible to see the light scattered by the droplet in the microscope image. After a few seconds in which the droplet remains in contact with the fiber, the droplet is removed again. If a nanoparticle was successfully deposited on the nanofiber can be examined with the absorption spectroscopy, where the presence of a nanoparticle manifests as a characteristic absorption peak. Additionally, it is possible to conclude from the absorption spectra if one or more particles were deposited and if they are clustered [106]. When no nanoparticle was deposited on the nanofiber, the transmission is unchanged and the whole process of bringing the fiber in contact with the droplet is repeated. By sending laser light through the fiber which is roughly resonant with respect to the surface plasmon resonance any nanoparticles on the fiber surface are illuminated by the evanescent field and can be imaged with the microscope. This provides additional optical evidence of a successful deposition and is a supplementary method to distinguish between separated or clustered particles. Numerous sample preparations have shown that it is unlikely to deposit more than one nanoparticle within this setup and procedure and that the probability for a successful deposition is highly dependent on the density of nanoparticles in the suspension. Figure 3.3a shows a microscopy image of the nanofiber with three gold nanorods on the surface of the fiber. The same fiber is shown in Figure 3.3b after an additional deposition attempt of spherical nanoparticles with the droplet visible in the upper part of the image and a spherical nanoparticle with a diameter of 100 nm located a few microns right of the nanorods, which were already on the fiber. This nanoparticle is much brighter than the single nanorods. The corresponding absorption spectra is shown in Figure 3.5b. In general, repeating the above described procedure until the characteristic change in the transmission through the nanofiber is observed allows depositions of a single gold nanoparticle onto a nanofiber with a success probability close to one.

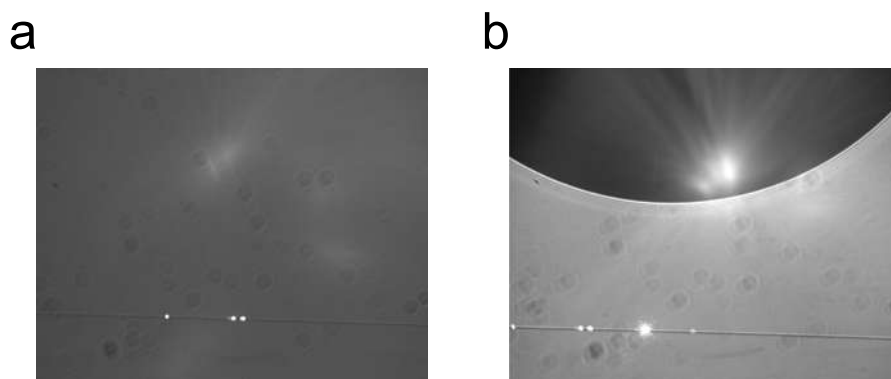


**Figure 3.3: Microscopy images of the deposition process.** **a**, Shows the nanofiber in the lower part of the image with three nanorods on it. The width of the image is about  $500 \mu\text{m}$ . **b**, Shows the same fiber after an additional deposition attempt where the droplet provided by a syringe needle with a diameter of  $400 \mu\text{m}$  is still visible in the upper part of the image. About  $80 \mu\text{m}$  right of the two nanorods, which are close together, a gold nanoparticle with a diameter of 100 nm was deposited which scatters much more light of the evanescent field of the fiber than the nanorods. This nanoparticle was used for all measurements presented in chapter 4. Its absorption spectra is shown in Figure 3.5b.

### 3.2.3 Nanofiber based spectroscopy

In order to detect nanoparticles on the surface of a nanofiber, we do an absorption spectroscopy measurement through the fiber [109,110]. A detailed description of the theory and the deposition process of a single gold nanoparticle on a nanofiber can be found in [106]. When spectral broad light is sent through the nanofiber, every scatterer on the fiber surface will interact with this light, which consequently modifies the spectra due to the scattering or absorption of light from the evanescent field. The modification of the light's spectra is caused by the physical properties of the scatterer. A gold nanoparticle causes a different change in the transmitted spectra than a dust particle. In principle there are two processes that reduce the transmission through the nanofiber, which are the scattering into free space or in opposite propagation direction of the fiber and absorption in combination with non-radiative decay, which causes the nanoparticle to heat up.

To describe the change in the transmitted spectra it is common to use a quantity called absorbance, which is defined as

$$\mathcal{A} = -\log_{10}(T), \quad (3.1)$$

where  $T$  is the power transmission given by

$$T = \frac{P_0 - P_{\text{ext}}}{P_0}. \quad (3.2)$$

Here  $P_0$  corresponds to the transmitted power through the nanofiber before a nanoparticle has been deposited on the fiber surface and  $P_0 - P_{\text{ext}}$  corresponds to the transmitted power after the deposition, while  $P_{\text{ext}}$  describes the power which is extinguished by the nanoparticle. In general the interaction between the gold nanoparticle and the evanescent field of the nanofiber is dependent on the radius of the nanoparticle  $R_{\text{NP}}$ , the radius of the nanofiber  $R_{\text{Fib}}$  and the polarization and the wavelength  $\lambda$  of the guided mode in the fiber and the respective angular position of the nanoparticle on the nanofiber surface. We now consider a quasi-unpolarized light source which, can be approximated by an incoherent, equal superposition of two orthogonal fundamental fiber modes propagating in the same direction. Since the nanofibers used in our experiments are single mode, this is an appropriate model and therefore it is not necessary to take the nanoparticles angular position into account. The extinguished power is the sum of the scattered and absorbed power. Therefore, the absorbance can be decomposed into an absorption induced ( $\mathcal{A}_{\text{abs}}$ ) and a scattering induced ( $\mathcal{A}_{\text{sca}}$ ) fraction.

$$\mathcal{A}(\lambda, R_{\text{Fib}}, R_{\text{NP}}) = \mathcal{A}_{\text{abs}}(\lambda, R_{\text{Fib}}, R_{\text{NP}}) + \mathcal{A}_{\text{sca}}(\lambda, R_{\text{Fib}}, R_{\text{NP}}) \quad (3.3)$$

with

$$\mathcal{A}_{\text{abs}}(\lambda, R_{\text{Fib}}, R_{\text{NP}}) = -\log_{10} \left( 1 - \frac{P_{\text{abs}}(\lambda, R_{\text{Fib}}, R_{\text{NP}})}{P_0(\lambda, R_{\text{Fib}})} \right), \quad (3.4)$$

$$\mathcal{A}_{\text{sca}}(\lambda, R_{\text{Fib}}, R_{\text{NP}}) = -\log_{10} \left( 1 - \frac{P_{\text{sca}}(\lambda, R_{\text{Fib}}, R_{\text{NP}})}{P_0(\lambda, R_{\text{Fib}})} \right), \quad (3.5)$$

where  $P_{\text{abs}}$  denotes the absorbed power and  $P_{\text{sca}}$  the scattered power. The absorbed and scattered power can be described via the free-space absorption and scattering cross sections  $\sigma_{\text{abs}}$  and  $\sigma_{\text{sca}}$ , times the local intensity of the evanescent field at the position of the nanoparticle,  $\mathcal{I}(\lambda, R_{\text{Fib}}, R_{\text{NP}})$ . Therefore the absorbance can then be written as

$$A_{\text{abs}}(\lambda, R_{\text{Fib}}, R_{\text{NP}}) = -\log_{10} \left( 1 - \sigma_{\text{abs}} \frac{\mathcal{I}(\lambda, R_{\text{Fib}}, R_{\text{NP}})}{P_0(\lambda, R_{\text{Fib}})} \right), \quad (3.6)$$

$$A_{\text{sca}}(\lambda, R_{\text{Fib}}, R_{\text{NP}}) = -\log_{10} \left( 1 - \sigma_{\text{sca}} \frac{\mathcal{I}(\lambda, R_{\text{Fib}}, R_{\text{NP}})}{P_0(\lambda, R_{\text{Fib}})} \right). \quad (3.7)$$

The absorption and scattering cross sections of a gold nanoparticle can be determined via Mie theory [111], in which Gustav Mie described the absorption and scattering of spherical objects with a diameter on the order of the wavelength in 1908. A full description of how to determine the absorption and scattering cross section of spherical metal nanoparticles can be found in [112] and [113]. In combination with the intensity distribution of the nanofiber mode [14], it is possible to estimate the transmission change of the light guided through the fiber due to the presence of a nanoparticle on the fiber surface.

For the two most frequently used combinations of nanoparticle diameter and nanofiber diameter in the experiments, the calculated absorbances are plotted in Fig. 3.4a and b. In both cases, the extinction of the fiber guided light due to absorption is higher than due to scattering. The transmission for the two combinations of nanoparticle and fiber diameter are plotted in Fig. 3.4c. It is shown that a single gold nanoparticle extinguishes up to 7% of the guided power in the nanofiber at its surface plasmon resonance, which underlines the strong light matter interaction of nanofibers. Figure 3.4c shows the absorbance of a nanoparticle with a diameter of 100 nm and a nanofiber with a diameter of 410 nm and, for comparison, the absorbance if the diameter of the particle or fiber is changed by  $\pm 10$  nm.

Figure 3.5 shows the experimentally obtained absorbance for different nanoparticle and nanofiber diameters together with the corresponding theoretically predicted absorbance. In each subfigure, three measured absorption spectra are shown, which originate from three individual nanoparticles. From each presented set of absorption spectra one of the corresponding nanoparticles were used for further measurements which will be presented in this and the next chapter. While in figure a and b the measured wavelength of maximal absorbance fits quite well to the theoretical prediction, one observes substantial differences between the theoretical predicted and the experimental measured absorbance in Figure 3.5c. Since the absorption spectra are very similar, these three samples are very likely featuring the same nanoparticle and nanofiber diameter. The mismatch of the theoretical prediction and the experiment might stem from a wrong nanoparticle diameter.<sup>1</sup> According to the theory, a nanoparticle diameter, which is increased by 25% would fit much better to the measured absorption spectra. However, it is likely that for this particle size the theory enters a regime where it no longer provides a good prediction for the absorbance as our theory is limited on the dipole moment of the emitter and neglects higher

<sup>1</sup>All the 125 nm nanoparticles were taken from the same package but their diameter was not verified by us. Since the presented absorption spectra were recorded with several weeks in between the individual measurements and the diameter of our nanofibers is regularly checked it is very unlikely that the mismatch between theory and experiment is caused by a wrongly assumed nanofiber diameter.

### 3. MEASUREMENT OF APPARENT DISPLACEMENT DUE TO SOI

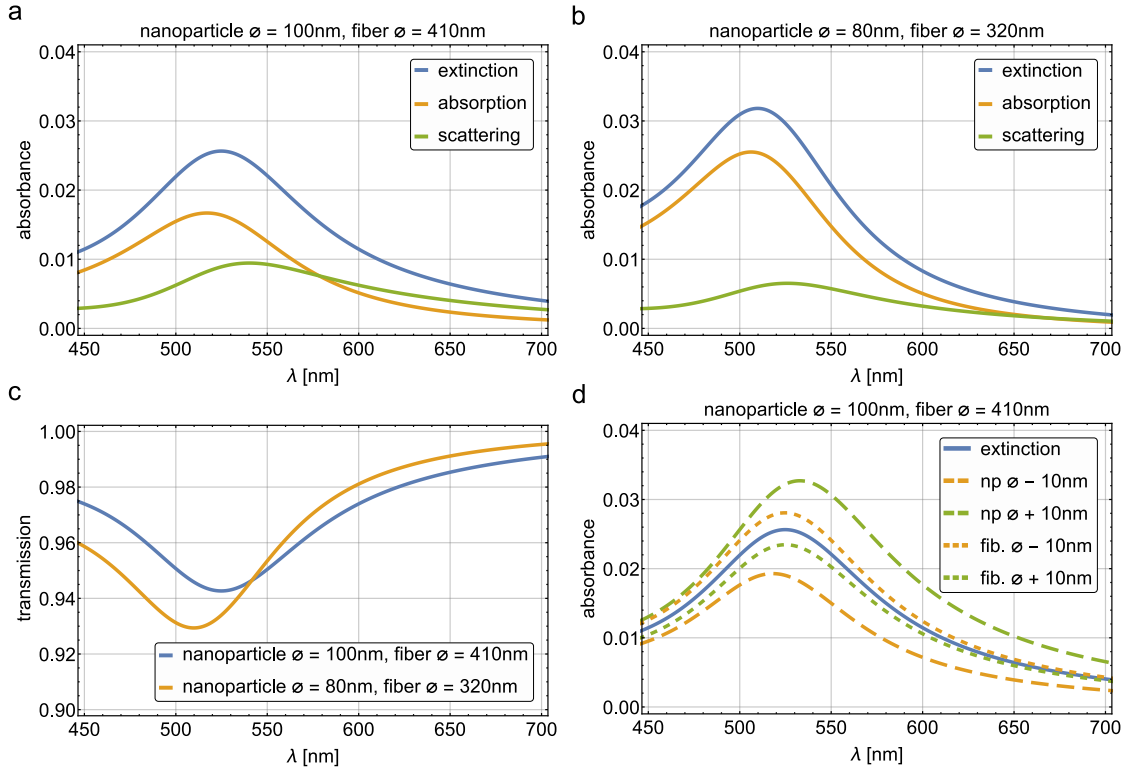


**Figure 3.4: Calculated absorbance and transmission.** **a** and **b**, Show the absorption by a nanoparticle of light guided in a nanofiber for two different sets of particle and fiber diameters. Beside the overall extinction (blue), the composing absorption induced (yellow) and scattering induced (green) fractions are plotted. **c**, Shows the remaining transmission of the fiber guided light for the two sets of nanoparticle and nanofiber diameters. **d**, Compares the absorbance of nanoparticle with a diameter of 100 nm and a nanofiber with a diameter of 410 nm with the absorbance if the diameter of the particle or fiber is changed by  $\pm 10$  nm.

order momenta. Apart from the shift of the resonance for large (125 nm) diameter nanoparticles the measured absorbance data fits well to the theoretically predicted values and together with electron microscope measurements [106], we can conclude these spectra stem from single gold nanoparticles sitting on the surface of the nanofibers.

The presented derivation of the absorbance ignores the fact that the presence of the nanofiber influences the free space scattering of the nanoparticle. While a nanoparticle in free-space would scatter light accordingly to its polarization state, the nanofiber changes the mode density of the electromagnetic field around the particle and therefore changes the intensity distribution of the emitted light. Moreover, the guided fiber modes provide additional radiation channels for the nanoparticle, see [114]. While the enhanced free-space radiation and the light scattered in backward directed fiber modes (towards the light source) decrease the transmitted power, light scattered into forward fiber modes again increases the transmitted power, which needs to be taken

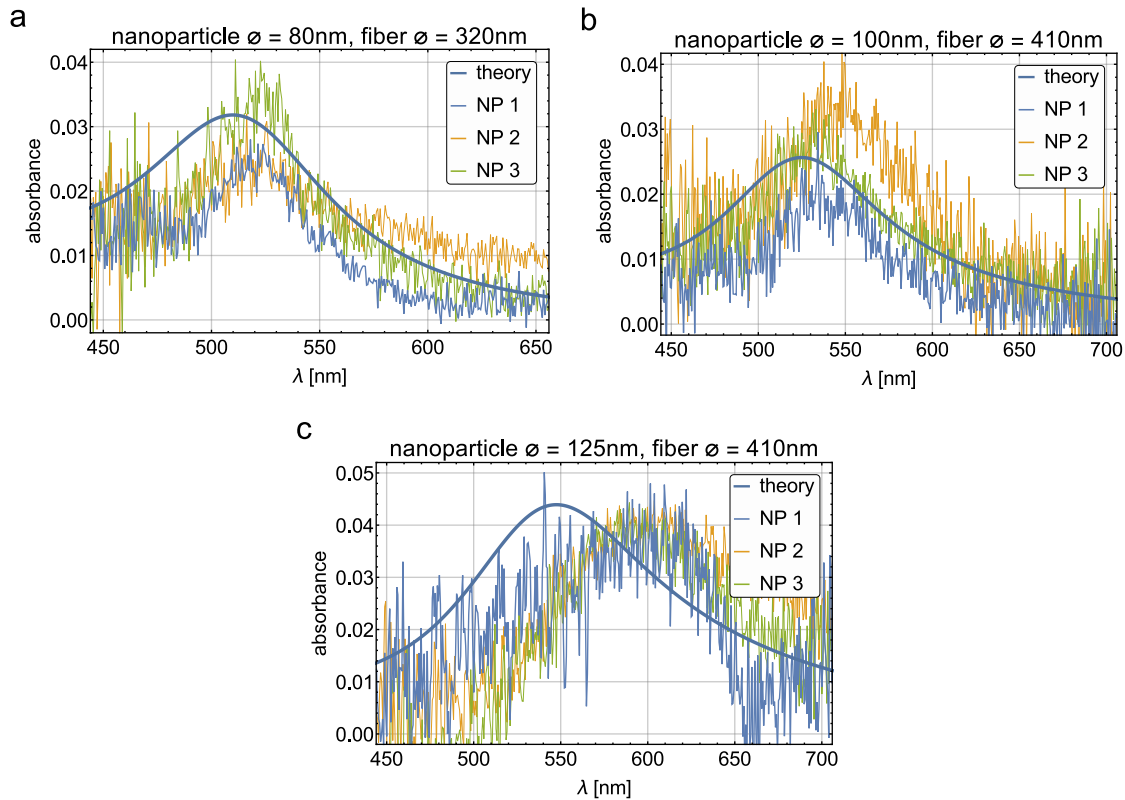


**Figure 3.5: Measured absorption spectra.** **a**, **b** and **c** show each three measured absorption spectra, while every subfigure corresponds to a different combination of nanoparticle and nanofiber diameter. In every subfigure the spectra NP 1 belongs to a nanoparticle which was used for further measurements which are going to be presented in this and the following chapter. Besides the experimentally measured spectra the theoretical determined absorbance is plotted.

into account for a more accurate description. Also, the absorption of light by the nanoparticle is influenced by the nanofiber since the presence of the fiber changes the surrounding of the nanoparticle which now does not exhibit a homogeneous refractive index, but a highly inhomogeneous one. The refractive index of the medium surrounding the nanoparticle is an important parameter when determining the absorption and scattering cross section of the particle. An inhomogeneous refractive index surrounding the nanoparticle leads to a modification of its absorption properties.

### 3.3 Illuminating the nanoparticle via the nanofiber

With a gold nanoparticle sitting on the surface of a nanofiber, it is possible to illuminate the particle with linearly and elliptically polarized light via the evanescent field of the nanofiber, see Figure 3.1. In the evanescent field, the elliptical polarization rotates in a plane of which the

surface normal is orthogonal to the propagation direction, *i.e.* the fibers roll axis, which is in contrast to elliptically polarized beams, where the field rotates in a plane which is perpendicular to the propagation direction. The polarization state at the position of the nanoparticle is thereby dependent on the polarization of the light in the nanofiber. Therefore the azimuthal position of the nanoparticle on the nanofiber needs to be measured. When imaging the nanoparticle while it is illuminated with linearly polarized light, its real position can be determined from the corresponding image. Afterwards, the nanoparticle is imaged while being illuminated with elliptically polarized light and an apparent displacement with respect to the measured real position can be found. In order to be able to switch fast between the different polarized illuminating light fields, a specific laser setup was build.

#### 3.3.1 Experimental setup

In order to image a nanoparticle which is illuminated via the evanescent field of the nanofiber, the latter is mounted horizontally and a microscope is placed such that the optical axis of the imaging system is orthogonal to the fiber axis, see Figure 3.1. The imaging system is used to monitor the deposition process, which was also done in this setup.

Several investigations of a nanofiber and nanoparticle sample in a scanning electron microscope showed that the deposited nanoparticles sit most likely on the top region of the nanofiber and rarely on the side. A nanoparticle which got somehow stuck to the nanofiber on the bottom region was never observed. Within the measurements of the particles real and apparent position, it was desirable to have the nanoparticle facing exactly towards the imaging system in order to be able to illuminate it via the evanescent field with light fields which are either linearly polarized orthogonal to the imaging axis or elliptically polarized. To adjust the azimuthal position of the nanoparticle with respect to the optical axis of the imaging system, the fiber was attached to a rotation mount which gave the possibility to rotate the nanofiber around its roll axis. The measurement and adjustment of the azimuthal position of the nanoparticle is presented in the next subsection 3.3.1.1.

After the deposition and azimuthal position measurement the two ends of the fiber which were first used for the fiber based absorption spectroscopy (see 3.2.3) were connected to the laser setup, which is described in subsection 3.3.1.3. It provides for each fiber end two arbitrarily adjustable, but orthogonal polarized modes. Their polarization was aligned to be orthogonal and parallel to the imaging axis, which caused the evanescent field at the position of the nanoparticle to be linearly and elliptically polarized.

##### 3.3.1.1 Azimuthal position of the nanoparticle

To find the azimuthal position of the nanoparticle on the nanofiber with respect to the optical axis of the imaging system, we made use of the modification of the free space emission pattern of the nanoparticle by the presence of the nanofiber. For this purpose, we look into the electric field close to the nanofiber when it is illuminated by a plane wave. Due to refraction and lens effects, the incident plane wave gets modified near the nanofiber [106, 115]. The intensity distribution of the resulting field is plotted in Figure 3.6a for the two cases of incident plane waves that are linearly polarized along the  $y$ - and  $z$ -axis. In both cases, there exists a maximum of intensity

behind the fiber, with respect to the incoming plane wave, and a minimum of intensity in front of the fiber.

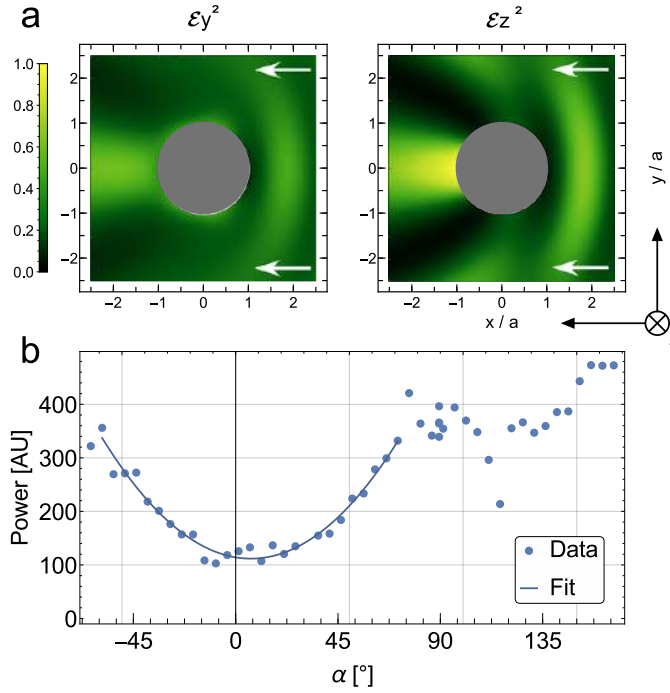


**Figure 3.6: Azimuthal position of the nanoparticle.** **a**, Modification of plane waves close to a nanofiber. The plan waves have a wavelength of 523 nm and are linearly polarized along the  $y$ - and  $z$ -axis. The nanofiber has a diameter of 320 nm. Due to refraction and lens effects, a maximum of intensity appears behind the fiber and a local minimum in front of it in the modified fields  $\mathcal{E}_y$  and  $\mathcal{E}_z$ . The propagation direction of the incident plane waves is along the  $x$ -axis as indicated by the white arrows. The intensity plots are normalized to the maximum of  $\mathcal{E}_z^2$ . **b**, The power radiated from the nanoparticle measured with a microscope by summing up the photon numbers in a certain area around the image of the nanoparticle on the CCD chip, plotted with respect to the rotation angle of the nanofiber. The deposition process of the nanoparticle was done while the fiber was at a rotation angle of  $\alpha = 90^\circ$ , where the nanoparticle is assumed to be deposited roughly on top of the fiber. Subfigure **a** indicates that when the fiber is rotated such that the nanoparticle is behind the fiber with respect to the imaging system it emits more light towards the imaging system than when the particle is placed in front of the fiber. This can be seen in the experimental data as it features a minimum of measured power at about  $\alpha \approx 0^\circ$  and a maximum at  $\alpha \approx 180^\circ$ . A simple polynomial fit of the data around  $\alpha = 0^\circ$  reveals that the nanoparticle was not deposited perfectly on top of the fiber but with an offset of  $6.7^\circ$  towards the back of the fiber. Note that due to the geometry of the nanofiber mount (fiber holder) it was not possible to image the nanoparticle under all rotation angles of the fiber.

Analogically a nanoparticle which is illuminated by the fiber guided light and placed behind the fiber will emit more power towards the imaging system than a particle which is placed

in front of the fiber. Thus, measuring the brightness of the nanoparticle with the microscope allows detection of its position along the circumference of the nanofiber. In order to prevent any influence of the polarization of the illuminating light on the particle's emission pattern, the nanoparticle should be illuminated by unpolarized light. The quasi unpolarized light was realized by sending a superposition of two orthogonal polarized fiber modes, which were slightly frequency shifted by an electro-optic modulator. When imaging the nanoparticle illuminated with the quasi unpolarized light, the local polarization of the light at the position of the nanoparticle will rotate along a great circle on the Poincarre-sphere and, thus, on average, the light emitted by the nanoparticle will have no net polarization. The power emitted by the particle towards the imaging system was measured by summing up the total number of photon counts in a certain region of the images taken of the nanoparticle. This was done for different rotation angles of the fiber. Figure 3.6b shows the data of such a measurement for a fiber with a diameter of 320 nm, a nanoparticle with a diameter of 80 nm and a laser used to illuminate the nanoparticle with  $\lambda = 532$  nm. At the time of the deposition of the nanoparticle the rotation angle of the fiber was  $\alpha = 90^\circ$ . Assuming the particle is deposited roughly on top of the fiber, a local minimum of the measured power should be visible at  $\alpha \approx 0^\circ$  and a maximum at  $\alpha \approx 180^\circ$ , which is indeed the case. Note, that due to the geometry of the nanofiber mount (fiber holder) it was not possible to image the nanoparticle under all rotation angles of the fiber. A simple polynomial fit was used to determine the minimum of the measured power. This measurement indicates that the nanoparticle was not deposited perfectly on top of the fiber, but with an offset of  $6.7^\circ$  towards the back of the fiber. After this measurement and the analysis it was possible to rotate the fiber such that the nanoparticle pointed directly towards the imaging system.

#### 3.3.1.2 Imaging system, magnification

The imaging system consists of an infinity corrected objective by Mitutoyo (20X Mitutoyo Plan Apo SL Infinity-Corrected Objective), an infinity tube with a lens which forms an image at a CCD camera (Matrix Vision mvBlueFOX3-1013G-2212) with a pixel size of  $5.3 \mu\text{m} \times 5.3 \mu\text{m}$ . The objective has a NA of 0.28, a working distance of 30.5 mm, a nominal magnification of 20 and an effective focal length of 10 mm. In order to experimentally determine the magnification of the overall imaging system, we used a piezo driven translation stage which moves the whole imaging system orthogonal to the optical axis. To rule out errors from hysteresis or similar effects of the piezo element, a feedback element was used which returns a voltage dependent on the distance the piezo was moved. This system has been calibrated via an optical interferometer. To measure the magnification of the imaging system, the movement of the nanoparticle is monitored when the piezo moves the imaging system for a few microns orthogonal to the optical axis. For this purpose, the nanoparticle is illuminated via the evanescent field of the nanofiber with linearly polarized light. In the different images, the position of the nanoparticle is fit with a two dimensional Gaussian fit, see 4.3. The magnification can then be determined by the product of the distance between the two measured positions in pixels and the pixel size of the CCD chip, divided by the distance for which the imaging system was translated. This measurement is done 20 times in a row to check its reproducibility and to obtain with the mean value of this measurements a statistically significant value for the magnification. From this we obtain for two different realizations of of the imaging system magnifications of  $M = 71.6(1)$

and  $M = 13.92(0.1)$ . The presented error is the standard error of the mean value of the 20 determined magnifications, given by  $\sigma/\sqrt{N}$ , where  $\sigma$  is the standard deviation and  $N$  the number of measurements. In order to reduce the size of the imaging system the length between the lens of the infinity tube and the CCD chip was reduced which therefore decreased the magnification.

### 3.3.1.3 Illumination setup

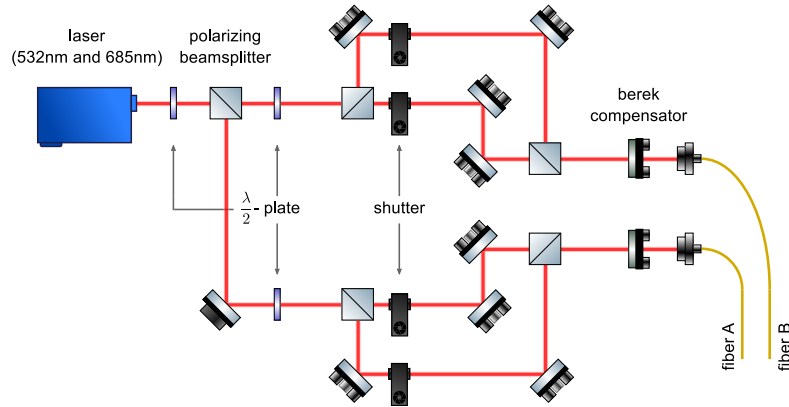


**Figure 3.7: Illumination setup.** A initial linearly polarized laser beam is split up by a polarizing beam splitter, where it is possible to change the power in the split up beams with a half wave plate in front of the beam splitter. Both beams are again split up in the same procedure, but then recombined via additional polarizing beam splitters. Before the two pairs of orthogonally linearly polarized beams are coupled into a fiber they pass a Berek compensator. This allows to arbitrarily adjust the polarization of the light fields in the fiber to correct for birefringence, while the orthogonality is conserved. Mechanical shutters provide the possibility to switch fast between the orthogonal fields in the output fibers.

In order to measure an apparent shift of the position of a gold nanoparticle on a nanofiber, we want to illuminate it via the evanescent field of the nanofiber with light fields, which are linearly and circularly polarized. Since an image of the linearly polarized particle reveals its real position and an image of the circularly polarized particle should show a displacement, it is desirable to quickly switch between these light fields. This rules out long term drifts and we can measure the apparent displacement more precisely. The corresponding light fields in the nanofiber which feature linear and circular polarization in the evanescent field at the position of the nanoparticle are orthogonally polarized inside of the nanofiber (see 3.3.1.4). When changing the propagation direction of the light fields in the nanofiber the sense of rotation of the circularly polarized field is changed, which can be used to measure the same apparent displacement in opposite directions. Therefore, it is convenient to have a illumination setup which provides orthogonally polarized light fields inherently, of which the polarization is adjustable without destroying the orthogonality.

For this purpose, a setup was designed which is shown in Figure 3.7. We used a laser diode module from Thorlabs with a wavelength of  $\lambda = 532$  nm and a DLC TA pro by Toptica laser

with a wavelength of  $\lambda = 685$  nm as light source for illuminating the nanoparticle. The initial linearly polarized beam is divided by a polarizing beam splitter cube, where it is possible to adjust the power of the two outcome beams via a half wave plate in front of the cube. These two beams are again split up by polarizing beam splitter cubes with the same possibility to adjust each beam's power. After passing a mechanical shutter, the two beam pairs are recombined via polarizing beam splitter cubes. Consequently, the two resulting beam pairs contain orthogonal linear polarizations. Before coupling into a fiber, both beam pairs pass a Berek compensator which allows to adjust their polarizations and to compensate in this way the birefringence of the fiber. This setup provides two sources of light with an arbitrary set of two orthogonal polarization states, which are sent along the two directions of the nanofiber. With the use of the mechanical shutters it is possible to quickly switch between the different light fields.

#### 3.3.1.4 Polarization alignment and data acquisition sequence

In this measurement the nanofiber is not only used as a mount for an individual gold nanoparticle, but also to illuminate it with light of different polarizations to measure an apparent position of the nanoparticle. Therefore we make use of the evanescent field of nanofibers which features, depending on the polarization of the light in the fiber, either linearly polarized or almost circularly polarized light [14], see appendix A.10.

We now consider the experimental setup which is depicted in Figure 3.1. A nanofiber is oriented along the  $x$ -axis and a gold nanoparticle deposited on its surface faces towards an imaging system of which the optical axis equals the  $z$ -axis. When light quasi linearly polarized<sup>2</sup> along the  $y$ -axis is guided in the fiber, the evanescent field is also linearly polarized along the  $y$ -axis at the position of the nanoparticle, see Figure 3.1a. On the other hand, when light which is quasi linearly polarized along the  $z$ -axis is guided in the fiber, the evanescent field at the position of the nanoparticle is almost circularly polarized, see Figure 3.1b. In contrast to a circularly polarized beam, where the light field rotates in a plane that is perpendicular to the propagation direction, the strong transverse field gradients in the nanofiber give rise to elliptically polarized light fields rotating in a plane of which the surface normal can be fully perpendicular to the propagation direction. When flipping the propagation direction of the light field in the nanofiber, the sense of rotation of the elliptically polarized light is changed.

In order to illuminate the nanoparticle with linearly and elliptically polarized light, it is necessary to align the polarization of the fiber guided light linear along the  $z$ - and  $y$ -axis. This was done by adding a linear polarizer just in front of the first lens of the imaging system. This polarizer is aligned such that the transmitted light is linearly polarized parallel to the nanofiber. If the nanoparticle is illuminated by vertically linearly polarized light, its scattered light field is almost solely vertically linearly polarized at the position of the polarization filter (see appendix A.7) and thus blocked by the latter. This allows one to adjust the polarization of the evanescent field with the use of the Berek compensator from the illumination setup by minimizing the power measured from the emitting nanoparticle. This alignment procedure automatically adjusts

---

<sup>2</sup>When linearly polarized light is coupled into a nanofiber the strong confinement gives rise to field components which are longitudinal to the propagation direction of the fiber. Only in the center of the fiber the light is solely linearly polarized.

the polarization of the second light field, which features the orthogonal polarization state to the initial one, to be quasi linearly polarized along the  $z$ -axis, which exhibits elliptical polarization at the position of the nanoparticle. The adjustment procedure was done for both arms of the illumination setup such that it was possible to send light with the described polarization states from both fiber ends to the nanoparticle. We now label the fiber modes propagating from left to right (as seen from the imaging system)  $P_1^E$  and  $P_1^L$  and the corresponding counter propagating modes as  $P_2^E$  and  $P_2^L$ . The indices E and L indicate the elliptical and linear polarization at the position of the nanoparticle of the respective modes. With these four light fields it is possible to measure the real position of the nanoparticle using  $P_1^L$  and  $P_2^L$ . The corresponding images from which the particles real position is measured will be called reference images in the following. When illuminating the nanoparticle with the elliptically polarized fields we expect a displacement of the images where for  $P_1^E$  the particle will appear shifted to the right (positive  $x$  direction) with respect to its real position and to the left (negative  $x$  direction) when illuminated with  $P_2^E$ .

Within one experimental run, four images were taken. In each image, the nanoparticle was illuminated by one of the four fiber modes  $P_{1,2}^E, P_{1,2}^L$ . Images in which we await to see a displacement of the particles position were alternatingly taken with the reference images. This was done to minimize the time between a measurement of the particles apparent and real position in order to keep the impact of mechanical or thermal drifts as small as possible. To accumulate reasonable statistics up to 500 such experimental runs were performed in a row.

### 3.3.2 Directional emission and defocussing error

When calculating the expected displacement of the nanoparticle we expect some deviations from the free-space situation as the presence of the nanofiber modifies the emission of the nanoparticle. The light emitted by the particle is reflected by the fiber and, therefore, it interferes with itself. This has two major impacts on the measurement of the particles apparent position. First the local dipole polarization ratio  $\epsilon$  is modified and second the emitted field features a directional emission [116] which gives rise to another apparent displacement when the imaging system is not properly focused.

To estimate these effects, we consider the simplified situation where the nanoparticle is located on a dielectric interface. In this case, the field emitted by the particle into the  $xz$ -plane can be calculated by superimposing it with the field of a mirror particle. This mirror particle is located directly below the interface and emits light with a relative power given by the reflectivity of the interface of  $R = 3.5\%$ , which corresponds to the reflectivity the nanofiber. Using a constant reflectivity is only valid for small angles with respect to the optical axis ( $z$ -axis). Within an aperture of  $\text{NA} = 0.28$  the reflectance varies only by about 5% and is therefore approximated by the reflectance for perpendicular incident. The emitted field can then be determined by adding to the complex dipole moment  $\mu = (I \epsilon e_x + e_z) / \sqrt{1 + \epsilon^2}$  of the free space particle the reflected amplitude  $\mu_{\text{Ref}} = \sqrt{R}(-I \epsilon e_x + e_z) / \sqrt{1 + \epsilon^2} e^{ikd_z}$  of the mirror particle where  $e^{ikd_z}$  gives the phase shift of the field of the mirror particle with respect to the real particle at a distance  $d_z$  which is given by the nanoparticle diameter. From this two amplitudes we obtain a new effective

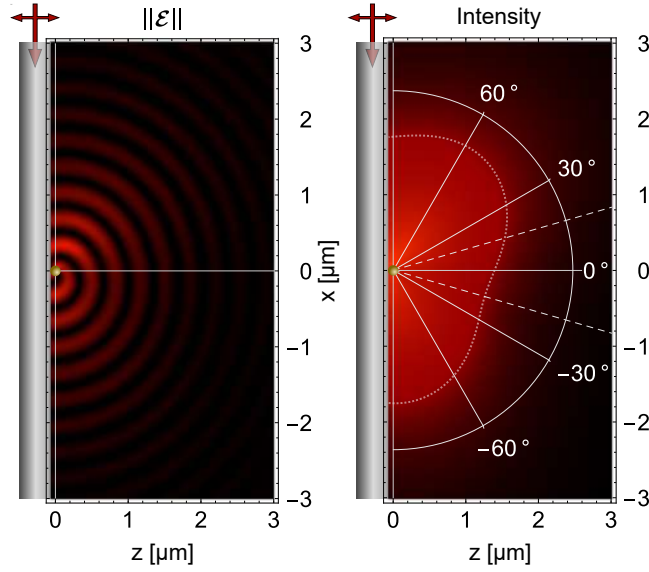


**Figure 3.8: Directional emission.** **a**, A density plot of the norm of the real part of the electric field caused by a elliptically polarized nanoparticle sitting on the surface of a nanofiber, which is due to reflections on the fiber surface different to the one of a free space particle. The nanoparticle is illuminated by the nanofiber with a fiber mode quasi linearly polarized along the  $z$ -axis which causes the evanescent field at the position of the nanoparticle to be elliptically polarized. The plotted field is a superposition of the field emitted by a free space particle and the field of a mirror particle with a relative power 0.035 which corresponds to the reflectivity of the fiber. This field was calculated for a nanoparticle with a diameter of 125 nm and a nanofiber with a diameter of 410 nm. The illuminating light has a wavelength of 685/nm. **b** A density plot of the intensity distribution of the same field. The white dotted curve shows the path of constant intensity. The anisotropic emission pattern along the aperture of  $NA = 0.28$ , which is indicated by the dashed lines is clearly visible.

dipole polarization ratio

$$\tilde{\epsilon} = \epsilon \cdot \frac{1 - \sqrt{R} e^{ikd_x}}{1 + \sqrt{R} e^{ikd_x}}. \quad (3.8)$$

In addition to changing the effective dipole polarization ratio  $\epsilon$  of the emitted light, the interference of the field emitted by the nanoparticle with the field of its mirror image also gives rise to a directional emission pattern such that the intensity distribution of the light is no longer symmetric with respect to the  $z$ -axis.

Figure 3.8 shows the field emitted by a nanoparticle sitting on the surface of a nanofiber, where in subfigure a the norm of the real valued electric field is plotted and in subfigure b the intensity distribution. The corresponding fiber mode is linearly polarized along the  $z$ -axis and propagates in  $-x$  direction. One can clearly see the anisotropic emission along the aperture of  $NA = 0.28$ , which is indicated by the dashed lines.

This anisotropy can also lead to an additional apparent displacement of the particle when the imaging system is out of focus. It is well known, that in the imaging process of linearly polarized dipoles an apparent displacement can occur, when the polarization axis is not parallel or orthogonal to the optical axis of the imaging system and when the imaging system is slightly out of focus [117, 118]. A lot of effort was put into the development of techniques to avoid this error source [119–122] which can cause localization errors up to about 100 nm. The anisotropic illumination of such tilted dipole emitters leads to a linear growth of the apparent displacement with respect to the defocusing for small defocusing lengths [121, 122]. The main difference to the polarization dependent apparent displacement presented in chapter 2 is, that while the focus dependent displacement vanishes for perfect focusing in ideal optical imaging systems, the polarization dependent displacement is still present. However, the polarization dependent displacement stems from the fundamental scattering process of a dipole emitter.

### 3.3.3 Experimental results

Within the presented experimental setup, we used two different nanofiber - nanoparticle systems. In a first experimental realization, a nanofiber with a diameter of 320 nm was used. A nanoparticle with a diameter of 80 nm was deposited on that fiber. Figure 3.5a shows the corresponding absorption spectra. The magnification of the imaging system was calibrated with the procedure presented in section 3.3.1.2 to  $M \approx 71.6(1)$ . In order to find the azimuthal position of the nanoparticle on the nanofiber, the measurement discussed in section 3.3.1.1 was performed for this nanofiber - nanoparticle system.

When using the fiber modes  $P_{1,2}^E$  with a wavelength of 532 nm the local elliptical polarization at the position of the nanoparticle has a dipole polarization ratio of  $\epsilon = \pm 1.73$  ( $\tilde{\epsilon} = \pm 1.33 \mp 0.42 i$ ). In combination with the aperture of the used objective of  $\text{NA} = 0.28$ , the theoretical predicted displacement including the effect from reflections of the nanofiber is given by  $\Delta x_t = \pm 105 \text{ nm}$ .<sup>3</sup> In one experimental imaging sequence, the nanoparticle is successively illuminated with the fiber modes  $P_1^E, P_1^L, P_2^E, P_2^L$ , while for every illuminating mode one image is taken. In this measurement, the imaging sequence was repeated 500 times and the positions of the nanoparticle in every image determined with a two-Dimensional Gaussian fit (see 4.3). All measured positions are shown in Figure 3.9, where they are plotted with respect to an origin which is given by the mean of all positions measured in all reference images. Subfigure a shows the  $x$  positions obtained from the four images illuminated by the four different modes for the 500 runs, and subfigure b shows equivalently the  $y$  position. In subfigure c the  $y$  positions are plotted with respect to the corresponding  $x$  for all experimental runs. It can be seen that there is clearly an offset between the positions measured from the images where the nanoparticle was illuminated with elliptically polarized light. The average values of the measured apparent displacement are  $\Delta x(\text{Re}(\tilde{\epsilon}) = 1.33) = 123(1) \text{ nm}$  and  $\Delta x(\text{Re}(-\tilde{\epsilon}) = -1.33) = -110(1) \text{ nm}$ , which agrees very well with the predicted value. These values were determined by taking the mean value of the apparent displacements obtained from the images taken in the individual imaging sequences, where the apparent displacement was measured in the images of the elliptically polarized emitter with respect to the reference images in which the nanoparticle was illuminated

<sup>3</sup>In this and the following chapter the theoretical predictions of the displacement are denoted by  $\Delta x_t$ .

from the same direction in the nanofiber. The given error is the standard error of the mean value, which is caused by shot-to-shot drifts of the optical setup. Errors resulting from the error of the magnification or in the fit of the positions are about one order of magnitude smaller than the standard error, meaning that the precision of our position measurements is limited by the shot-to-shot drifts.

For the displacement along the  $y$ -axis we expect no shift. Nevertheless we observe a small offset between the  $y$  positions of the two different reference images, which can be seen in sub-figure b. The mean value of the offset between the  $y$  positions measured in the reference images using  $P_1^L$  and  $P_2^L$  is  $45(1)$  nm. This offset, as well as the asymmetry between the two measured apparent displacements  $\Delta x$  is very likely caused by a small mismatch of the polarizations of the counter propagating illumination modes. Although they are aligned using the same procedure (see 3.3.1.4) it is possible that the aligned polarizations do not match perfectly. A small mismatch between the polarizations of the modes used to take the reference images would then also effect the images of the apparently displaced particle.

While the  $x$  position of the nanoparticle is, in general, quite stable and varies only within a range of approximately 100 nm over the time of the measurements, which was about 10 minutes, the  $y$  position underlies a much larger drift in a range of approximately 700 nm. This behaviour is caused by the fact that the fiber is mounted horizontally, which features a much larger freedom of movement in the plane orthogonal to the roll axis of the fiber than along the roll axis. For instance, any temperature fluctuation of the fiber holder can change the strain of the fiber and therefore change the  $y$  position of the nanoparticle. All images taken of the nanoparticle have this long term drifts in common. Since the time scale of one imaging sequence is much smaller than the time scale of this drifts the measurement of the apparent displacement, which was always evaluated from images within the data-set of one individual imaging sequences, is not influenced.

In order to image a nanorod in addition to a nanoparticle on the surface of a nanofiber we changed the wavelength of the illuminating light and the diameter of the nanoparticle, to adapt them to the resonance frequency of the used nanorod. The wavelength corresponding to the surface plasmon resonance was much higher than the one of the 80 nm diameter particles and the 532 nm laser. The purpose of the nanorod was to have an emitter which is strictly linearly polarized. Such an emitter would, when properly focused, always reveal its real position and could be used as a position reference on the fiber.

Eventually, we did not use nanorods as position marker on the nanofiber, since it was not possible to image them properly at the same time with the nanoparticle, because the nanorods emitted far less power than the nanoparticle. Additionally, we decided that it is more interesting to measure the apparent position of a particle with respect to its real position and not the distance to some far off object. Moreover we came to the conclusion that the nanoparticle which has a ratio of diameter to length of  $1/3$  could still emit a highly elliptically polarized field, which can lead to a large apparent displacement.

Still we worked with the new particles and laser and performed a measurement in which the apparent displacement of the nanoparticle with respect to the relative focal position of the imaging system was investigated. The used fiber had a diameter of 410 nm and the deposited nanoparticle had a diameter of 125 nm. In Figure 3.5c, the corresponding absorption spectra

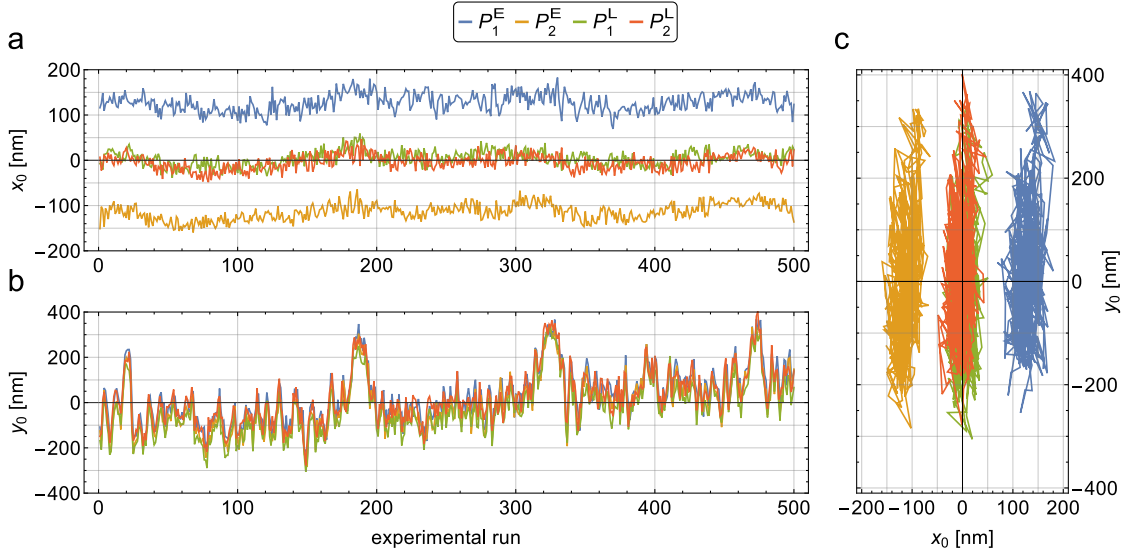


**Figure 3.9: Measured positions of the nanoparticle.** **a**, The fitted position  $x_0$  of the nanoparticle along the  $x$ -axis plotted for the effective polarization states  $\text{Re}(\pm\tilde{\epsilon}) = \pm 1.33$  (blue, yellow) and  $\tilde{\epsilon} = 0$  illuminating the particle from left and right in the nanofiber (green, red) with respect to an origin defined as the mean value of all positions measured in all reference images. An apparent displacement of the images illuminated with the modes  $P_{1,2}^E$  with respect to the reference images is clearly visible. **b**, The fitted position  $y_0$  of the nanoparticle along the  $y$ -axis plotted for all fiber modes. A small offset between the positions measured in the reference images can be seen. All images have the long term drift of the nanofiber in common. **c**, The fitted position of the nanoparticle shown in one plot.

is shown. Since a measurement to find the azimuthal position of the nanoparticle is very time consuming, it was not performed for this nanofiber - nanoparticle sample. After the deposition of the nanoparticle the fiber was rotated by  $90^\circ$  such that the nanoparticle sitting on top then face towards the imaging system.<sup>4</sup> In combination with a 685 nm laser, the evanescent field of the  $P_{1,2}^E$  mode provides a dipole polarization ratio at the position of the nanoparticle of  $\epsilon = \pm 1.75$  ( $\tilde{\epsilon} = \pm 1.42 \mp 0.50 i$ ). The theoretical predicted apparent displacement is  $\Delta x_1 = \pm 142$  nm. After a modification of the imaging system its magnification was calibrated to  $M \approx 13.92(0.1)$ . In addition to the previous presented measurement here the imaging system was scanned along the  $z$ -axis in order to investigate the effect of defocussing on the apparent displacement. Therefore the imaging system was moved along the optical axis over  $22 \mu\text{m}$  with a step size of  $1 \mu\text{m}$  across the focus region. At each relative focus position 50 measurement runs were performed. For each relative focal position the real position of the particle was obtained by taking the mean of the position measured from all reference images, in which the nanoparticle was illuminated with  $P_{1,2}^L$ . We define the focus of the imaging system as the position where the highest local

<sup>4</sup>As the nanoparticle deposition process reliably positioned the nanoparticles on top of the fiber, with only minor deviations, the time consuming azimuthal position scan was not performed for this nanofiber - nanoparticle system.

intensity was measured, which directly relates to the amplitude in the fit applied to determine the particles position, see Figure 3.10a. The different maxima of the fit amplitudes for the different illumination modes are caused by slightly different powers of the corresponding modes, which have been adjusted in the illumination setup. The average displacement in the focus is  $\Delta x(\text{Re}(\tilde{\epsilon}) = 1.42) = 135(3) \text{ nm}$  and  $\Delta x(\text{Re}(-\tilde{\epsilon}) = -1.42) = -140(3) \text{ nm}$ . This values agree very well with the theoretical predicted displacement.

Figure 3.10b shows the averaged apparent displacement  $\Delta x$  as a function of the relative focal position  $z$ , along with the standard error. It is clearly visible that the apparent displacement strongly depends on the relative focal position. At  $z = -6 \mu\text{m}$  the image of the particle shows the same displacement for both illuminating modes  $P_{1,2}^E$ . For  $z > -6 \mu\text{m}$  the displacement  $\Delta x(P_1^E)$ <sup>5</sup> increases while  $\Delta x(P_2^E)$  decreases. Surprisingly, for  $z < -6 \mu\text{m}$  it is the other way around such that  $\Delta x(P_1^E)$  and  $\Delta x(P_2^E)$  even switch signs. This behaviour stems from a directional emission of the nanoparticle which leads to an inhomogeneous illumination of the aperture of the imaging system, which in turn leads to a focus dependent apparent displacement, as described in 3.3.2. The almost linear change of the displacement with respect to the relative focal position agrees very well with other theoretical and experimental studies of this effect [118, 121].

In addition to the apparent displacement in  $x$  direction the apparent displacement in  $y$  direction is plotted in Figure 3.10b. Its standard deviation is higher than of the displacement in  $x$  direction due to larger drifts of the fiber along the vertical axis. While  $\Delta y(P_2^E)$  is almost zero in the focus region,  $\Delta y(P_1^E)$  is clearly non zero. This could stem from an imperfect alignment of the polarization of the  $P_1^{E,L}$  modes and from the possibility that the nanoparticle might not be perfectly facing towards the imaging system. Nevertheless, in the focus the apparent displacements in  $y$  direction are much smaller than the ones in  $x$  direction.

Figure 3.10c shows the waist of the image of the nanoparticle at the CCD chip obtained by the Gaussian fit for the images illuminated with the modes  $P_1^{E,L}$ . It can be seen that the waist is almost constant between the relative focus positions of  $-5 \mu\text{m}$  and  $5 \mu\text{m}$ , while the apparent position of the nanoparticle varies over 250 nm. Therefore the waist of the Gaussian fit is not a suitable parameter to identify the focus in this setup. For large negative relative focus positions, the waist is in between 25  $\mu\text{m}$  and 30  $\mu\text{m}$ , and decreases quickly for higher relative focal positions to about 12  $\mu\text{m}$ . This is due to a ring structure appearing in the defocused images (see Figure 3.11), which the Gaussian fit takes into account. An inhomogeneous brightness of such ring structures might lead to an additional apparent displacement, which is directly caused by the fit. Consequently a two dimensional Gaussian is not a proper function to fit such defocused images. Additionally it can be seen, that the waist of the reference images evolves slightly different than the one of the images illuminated with  $P_1^E$  while going through the focus region. This is very likely caused by a deformation of the point spread function of an elliptically polarized emitter, see Figure 2.8.

Figure 3.11 shows the images of the nanoparticle for  $z = -13 \mu\text{m}$  and  $z = 7 \mu\text{m}$ , which are positions far off the focus, for  $z = -6 \mu\text{m}$  which is the position where both displacements in  $x$  direction are the same and for  $z = 0 \mu\text{m}$  which is assumed to be the focus. The presented images

---

<sup>5</sup>The displacement  $\Delta x(P_1^E)$  is measured using images made when illuminating the nanoparticle with the mode  $P_1^E$  and the corresponding reference images made using the mode  $P_1^L$ .

are obtained by adding up all the corresponding individual images taken with the particular illumination mode to correct for shot to shot noise and drifts. The reference images in this plot, which indicate the real position of the nanoparticle, were obtained by averaging over both sets of reference images, taken while illuminating the nanoparticle with the  $P_{1,2}^L$  modes. The white crosses obtained from the averaged reference image indicate the estimated real position of the nanoparticle and the dashed ellipses show the apparent position as it was obtained by the Gaussian fit, where the major axes of the ellipses correspond to the fitted waist in  $x$  and  $y$  direction. The images show the evolution of the point spread function of the nanoparticle in this imaging system when scanning through the focus region and that in the focus it is not obvious visible that the displacement of the nanoparticle is only apparent. An image needs to be further analysed to find out if the position of a particle is real or apparent, see Chapter 5. At  $z = -13 \mu\text{m}$  it is visible that the image features a quite bright ring around the center spot. This ring is very problematic for the fitting process, as seen in Figure 3.10c. The big waist of the Gaussian fit shows that the ring is included in the fit. Due to inhomogeneous brightness of this ring it is possible that the displacement might be wrongly measured.

Summarizing the first experimental taken data, it can be said that we have shown that there can be clearly seen an apparent displacement in the image of a gold nanoparticle which was illuminated via the evanescent field of a nanofiber, which features local elliptical polarizations. Not only was it possible to measure this apparent displacement but also does it fit very well to the theoretical predicted values. The nanofiber - nanoparticle system turned out to be a handy tool to demonstrate that there is an apparent displacement when imaging elliptically polarized emitters. Admittedly the small uncertainty in the azimuthal position of the nanoparticle in combination with the finite precision of the polarization alignment leads to an eventual mismatch between the experimental results and the theoretical prediction. In addition it was possible to also measure the effect of an apparent displacement when defocusing the imaging system. Within this measurements the displacement due to defocusing has the same order of magnitude as the displacement due to the elliptically polarized emission of the particle.

### 3. MEASUREMENT OF APPARENT DISPLACEMENT DUE TO SOI

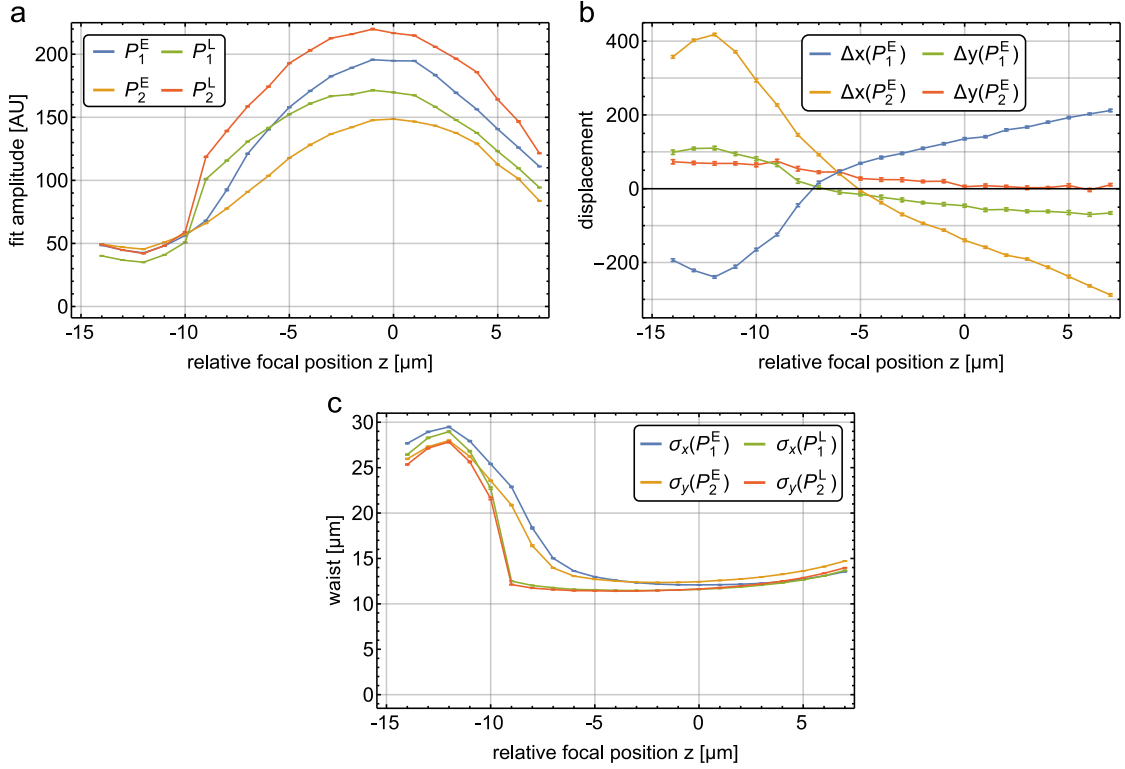


**Figure 3.10: Focus dependent displacement and fit parameters.** **a**, The fit amplitude as a function of the relative focus position  $z$ , plotted for the effective polarization states of the nanoparticle  $\text{Re}(\tilde{\epsilon}) = \pm 1.42$  (blue, yellow) and  $\tilde{\epsilon} = 0$  (green, red) illuminating the particle from left and right in the nanofiber. The different maxima in this curves are caused by different powers of the illuminating fiber modes. Statistical errors are included in this plot, but are too small to be seen properly. **b**, The apparent displacement  $\Delta x(\Delta y)$  plotted for  $\text{Re}(\tilde{\epsilon}) = \pm 1.42$  in blue and yellow (green and red) as a function of  $z$ . The change of  $\Delta x$  is almost linear for  $z > -10$   $\mu\text{m}$  and strongly non-linear for  $z < -10$   $\mu\text{m}$ . This is likely caused by the fitting process, and will be understandable in the next subfigure. While for the images illuminated from the right  $\Delta y \approx 0$  in the focus region, this is not the case for the images illuminated from the left. Nevertheless, the apparent displacement  $\Delta y$  is much smaller than  $\Delta x$  in the focus region. **c**, The waist of the two dimensional elliptical Gaussian fit at the CCD chip for  $\text{Re}(\tilde{\epsilon}) = 1.42$  along the  $x$ -axis ( $y$ -axis) in blue (yellow) and for  $\tilde{\epsilon} = 0$  (illuminated with  $P_1^L$ ) along the  $x$ -axis ( $y$ -axis) in green (red) plotted as a function of  $z$ . The difference in the evolution of the waist for  $\text{Re}(\tilde{\epsilon}) = 1.42$  and  $\tilde{\epsilon} = 0$  shows that the elliptically polarized particle features a different point spread function than the linearly polarized one. At  $z = -9$   $\mu\text{m}$  the waist for  $\tilde{\epsilon} = 0$  dropped rapidly to about one half of its value for lower relative focal positions. This is caused by a ring structure which appears in the images at lower relative focal positions and is taken into account by the Gaussian fit. A similar effect can be observed for  $\text{Re}(\tilde{\epsilon}) = 1.42$ . An inhomogeneous brightness of such ring structures might lead to a wrong estimation of the nanoparticles apparent displacement.

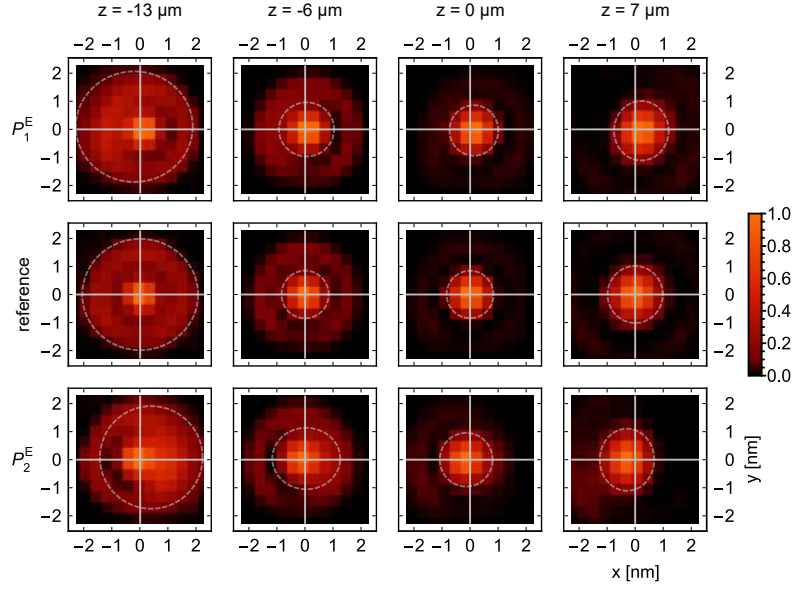


**Figure 3.11: Images of an elliptically polarized gold nanoparticle.** Images of a gold nanoparticle which is effectively elliptically polarized with  $\text{Re}(\tilde{\epsilon}) = \pm 1.42$  (upper and lower line) and linearly polarized with  $\tilde{\epsilon} = 0$  (middle line) for different relative focal positions  $z$ . The reference images are obtained by averaging over all 100 reference images illuminated with the modes  $P_{1,2}^L$  and the other images by averaging over 50 individual images to correct for shot-to-shot noise and drifts. The white cross indicates the estimated real position of the nanoparticle obtained from the reference image and the white dashed ellipses show the apparent position as it was obtained by the Gaussian fit, where the major axes of the ellipses correspond to the fitted waist in  $x$  and  $y$  direction. The images show the evolution of the point spread function along with the change of the apparent position when scanning through the focus region caused by the particles anisotropic emission. Note that the Gaussian fit includes the ring structure in the images at  $z = -13 \mu\text{m}$  which might lead to a wrong estimation of the apparent displacement due to inhomogeneous brightness of the ring.



# Measurement of polarization dependent apparent displacement

While the previous presented experimental setup allowed us to show that the apparent shift of an elliptically polarized emitter exists, it also had some drawbacks that prevented us from a precise quantitative determination of the exact polarization of the emitter. With the use of the evanescent field of the nanofiber the nanoparticle could only be illuminated by a single elliptical polarization state. Measuring the apparent position of the nanoparticle using other elliptical polarization states by using fibers with different diameter would have been a very time consuming method. Moreover, the strong anisotropic emission along the aperture results in an additional strong apparent displacement when the imaging system is not perfectly focused. Since any small drift or defocussing, which is in general not an easy task to avoid, makes it very difficult to measure the apparent shift caused by the elliptical polarization state of the imaged emitter. Therefore we decided to design a far improved experimental setup, that is not subject to these issues and effectively mimics the situation of a nanoparticle in free space. Moreover, this new setup is related to immersion microscopy, which is a widely used method in optical microscopy and is therefore a direct demonstration that emitters might appear at positions where they are actually not in common microscopy setups.

## 4.1 Experimental setup

In order to have a single gold nanoparticle at a fixed position that behaves like a particle in free space we positioned the nanofiber with the nanoparticle on it in between two half sphere lenses with a manufactured diameter of 5 mm and filled the residual gap with index matching oil, as shown in Figure 4.1. We took great care to ensure that the lenses and the nanofiber have the same refractive index (fused silica  $n = 1.458$ ) and chose the index matching fluid accordingly. This setup provides a single gold nanoparticle in the middle of a glass sphere. Due to the homogeneous refractive index around the nanoparticle and the spherical geometry with

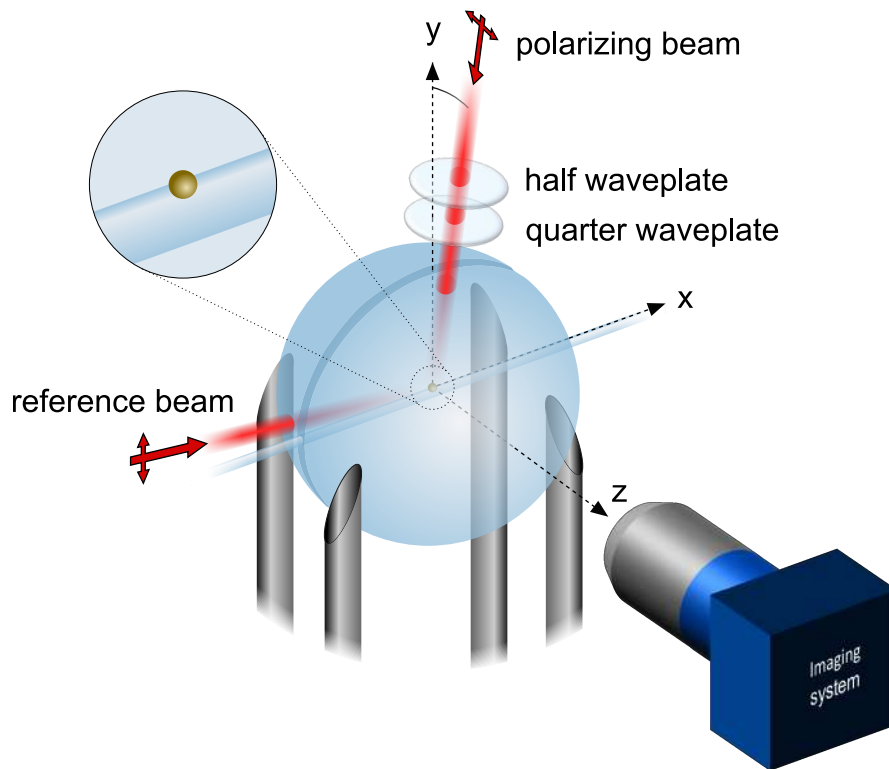


**Figure 4.1: Experimental setup.** A spherical gold nanoparticle (100 nm diameter) mounted on a nanofiber (410 nm diameter) which is positioned in the small gap ( $\sim 200 \mu\text{m}$ ) between two half sphere lenses (5 mm diameter). The opening between this two lenses is filled with index matching fluid of the same refractive index as the fiber and the lenses. The two lenses are mounted on four syringe needles, which are attached to mirror mounts and translation stages to provide a perfect alignment of the lenses with respect to each other. From the left a vertically linearly polarized beam almost parallel to the  $x$ -axis is aligned onto the nanoparticle, such that it does not pass the edge of the back half sphere lens or the surface of the index matching fluid. This beam passes the surface of the half sphere perpendicular and therefore its polarization is conserved. It polarizes the nanoparticle linearly along the vertical  $y$ -axis. Consequently images taken of the particle in this polarization state with the imaging system placed along the  $z$ -axis reveal the particle's real position. Therefore this beam is addressed as reference beam. Additionally there is a beam aligned onto the nanoparticle coming in from the top which is initially linearly polarized along the optical axis of the imaging system ( $z$ -axis). This beam is tilted by about  $7^\circ$  towards the imaging system to pass the front half sphere lens perpendicular through its surface. Via a half and a quarter wave plate it is possible to adjust any desired elliptical polarization for that beam and consequently for the nanoparticle. This beam is used to measure the apparent displacement of the particle as a function of the illuminating polarization and is therefore addressed as polarizing beam.

the particle in the center we are not subject to reflections that would result in an anisotropic emission. Since the nanoparticle is placed in the center of this glass sphere it can be imaged from the outside without any distortions and any illuminating beam aligned onto the particle coming from the outside passes the surface of the glass sphere perpendicular and its polarization is therefore not changed. Using now an illumination beam which propagates perpendicular to the optical axis, the nanoparticle can be illuminated with a wide set of polarization states. Note that this setup is similar to that of a standard immersion microscope commonly used in high precision microscopy.

Although the glass sphere does not distort the particle's image, it still needs to be taken into account when determining the magnification in the images of the nanoparticle inside the sphere. Therefore the front half sphere lens is conceptually included in the new overall imaging system. Also due to the refractive index the wavelength of the used laser is different inside the index matching fluid than in free space, which needs to be considered when determining the theoretical displacement. A closer description of the central parts of the setup will be given in the next sections.

#### 4.1.1 Half sphere lenses alignment and illumination beams

In order to mount the half sphere lenses with a maximum of optical access, they are attached to syringe needles with uv-curing adhesive.<sup>1</sup> At the front lens that faces the microscope objective the needles are placed on the side and on the back lens more in the middle of the lens, as shown in Figure 4.1. Each pair of needles is fixed on two small mirror mounts such that the lenses can be tilted with respect to the  $x$ - and  $y$ -axis. Thereby they can be precisely aligned to each other such that their plane facets facing each other are parallel. The nanoparticle - half sphere lens system is imaged with the microscope described in section 3.3.1.2. The alignment of the half sphere lenses is done by using the microscope to determine the distance between the two facets at different points at the edges. Therefore the standard microscope is moved in  $z$ -direction with a motorized translation stage from the point where the edge of one lens is in focus to the point where the edge of the other lens is in focus. With the help of the motorized translation stage this distance can be measured very precisely. Both mirror mounts holding the lenses are attached to the same motorized three axes translation stage. In addition the back lens can be moved in the  $xy$ -plane with manual translation stages and in  $z$ -direction with a motorized translation stage. In this way, it is possible to align the parallel facets of the lenses also in the  $xy$ -plane and to adjust the size of the gap as well as its position with respect to the nanofiber. All this alignment was done before a fiber was mounted in the setup. In order to prepare a single nanoparticle for imaging we deposit the particle on a nanofiber using the process discussed in section 3.2.2. This deposition is monitored with the microscope, while the half sphere lens pair is placed well below the fiber not to disturb the deposition process. After the nanoparticle is deposited on the fiber the lens system is moved upwards with the motorized translation stage. The fiber fits into the gap ( $\sim 3$  mm) between the lenses. All the further alignment now is done via motorized translation stages, since they provide a much higher accuracy. The front lens is moved close towards the fiber until the distance of the fiber and the lens is reduced to about  $100 \mu\text{m}$ . Then

<sup>1</sup>This is also used to fix nanofibers on their holders.

the lens system is aligned such that it is centered around the nanoparticle. For this purpose the nanoparticle is illuminated via the fiber and imaged through the front lens. After this alignment the index matching fluid is applied to the facet of the back lens, which is then slowly moved towards the front lens. This needs to be done very slowly in order to prevent the index matching fluid from being squeezed out between the two lenses and spilling on the front lens, which would change the spherical surface of the lens into some irregular surface through which the particle cannot be imaged properly. In this process the gap between the two lenses was reduced to about 200  $\mu\text{m}$ . Several trials showed that this process does not destroy the usually fragile nanofiber.

Until the index matching fluid is in contact with the nanofiber the particle can be easily illuminated by the fiber and therefore be observed. An illumination of the particle on the fiber with a free space beam is not possible unless the angle between the laser beam and the fiber is small. Otherwise reflections from the fiber are much brighter than the particle itself. When the index matching fluid comes in contact with the fiber, the light is no longer guided in the fiber and the particle cannot be illuminated via the fiber any longer. In order to still illuminate the nanoparticle two pre aligned free space laser beams from the outside are used. After applying the index matching fluid both beams as well as the focus need to be slightly adjusted to illuminate and observe the particle. This process has to be done very carefully since it features the possibility to lose track of the nanoparticle. The whole setup is placed in a flowbox to keep it clean. It needs to be turned off during measurements, because the flow of air causes the nanofiber to vibrate orthogonal to its roll axis. This vibration is damped by the index matching fluid, but not totally suppressed. When finally aligning the reference and polarizing beam and the focus of the imaging system this characteristic vibration is very helpful to identify the nanoparticle. In case the nanoparticle is not properly illuminated and is out of focus it is very difficult to separate it from the motionless background. The characteristic movement due to the vibration of the fiber when the flow box is turned on makes it much easier to identify the particle and align the illumination beams.

The laser beams used to illuminate the nanoparticle from the outside almost coincide with the  $x$ - and  $y$ -axis, but are slightly tilted with respect to these axes. The tilt prevents the beams from passing the edge or trough the gap between the lenses where the index matching fluid could modify the propagation direction and initial polarization of the beams, since there they would pass surfaces which are not orthogonal to their propagation direction. Instead they pass through the surface of the lenses. A horizontal beam which is linearly polarized along the  $y$ -axis is used to excite the nanoparticle with a polarization which is orthogonal to the optical axis in order to measure its real position, see Figure 4.1. This beam is called the reference beam. With a second beam which is tilted from the  $y$ -axis towards the imaging system by about  $7^\circ$  it is possible to illuminate the particle with different elliptical polarization states. This beam is called the polarizing beam. The polarization of this initially linearly polarized beam is controlled with a half and a quarter wave plate. The polarization alignment procedure is presented in section 4.1.4.

For all the measurements which were done with this setup, a single nanoparticle - nanofiber sample was used with a fiber diameter of 410 nm and a nanoparticle diameter of 100 nm. Figure 3.5b shows the corresponding absorption spectra. The used laser to illuminate the nanoparticle had a wavelength of 685 nm.

### 4.1.2 Imaging system and magnification

The overall imaging system of the setup consists of the standard optical microscope which was already introduced in the previous experimental setup 3.3.1.2 and the half sphere lens made of fused silica in front of the nanoparticle. For the experiments described in the following two objectives were used with the same magnification but different NA. The first was the already mentioned Mitutoyo objective (20X Mitutoyo Plan Apo SL Infinity-Corrected Objective) with  $NA = 0.28$ , the second one (20X Mitutoyo Plan Apo Infinity Corrected Long WD Objective) has  $NA = 0.42$ , a working distance of 20 mm and an effective focal length of 10 mm. Due to the refractive index of the half sphere lens  $n = 1.458$ , the effective numerical aperture of the overall imaging systems is increased to  $NA_{\text{eff}} = 0.41$  for the first objective and to  $NA_{\text{eff}} = 0.61$  for the second objective. The magnifications of the standard microscopes without the immersion half sphere lens were determined with the help of a surface topography standard containing a periodic pattern of elevated squares with a side length of  $(19.99 \pm 3) \mu\text{m}$  per square. To evaluate the magnification we used the data of 14 consecutive squares and obtained  $M_{0.28} = 14.8$  and  $M_{0.41} = 13.6$ .<sup>2</sup>

To determine the magnification of the overall imaging system we approximate the standard optical microscope by a single lens with a focal length of 10 mm. From the distance the optical standard microscope needs to be moved in order to get a focused image of the nanoparticle respectively the facet of the front half sphere lens, which is  $101 \mu\text{m}$ , the distance between the nanoparticle and the facet of the half sphere lens could be determined to be  $68 \mu\text{m}$ . This calculation was done using ray transfer matrix analysis [123]. Knowing this distance the magnification of the overall imaging systems could be evaluated to  $M_{0.41} = 21.9 \pm 0.1$  and  $M_{0.61} = 20.0 \pm 0.1$ . A more detailed discussion of the determination of the magnification is presented in appendix A.11.

### 4.1.3 Flat field correction

In digital imaging it is common to perform a so called flat field correction [124–126]. This correction compensates for different efficiencies and dark counts of the single pixels in a CCD chip. Thereby many sources of undesirable effects like shadowing effects from dust in the imaging system, or reflections which can lead to a variation of single pixel efficiency are neutralized. To perform the flat field correction an image without any illuminating light, a so called darkframe, and an image of a homogeneous illuminated plane surface is needed. From the dark frame the dark counts of the pixels are determined and from the homogeneous illuminated image the pixel efficiencies. In principle such a flat field correction can be done arbitrarily sophisticated, like measuring the pixel efficiencies with respect to the wavelength of the collected light.

To be able to perform a flat field correction on the taken data we averaged over several darkframes and took several homogeneous illuminated images using a diffuser which was illuminated with a white light source. Before averaging over these images we checked that there is no global gradient in the measured photon numbers.

<sup>2</sup>In the following we denote the magnification of the different imaging systems with the corresponding NA as index.

#### 4.1.4 Polarization alignment and data acquisition sequence

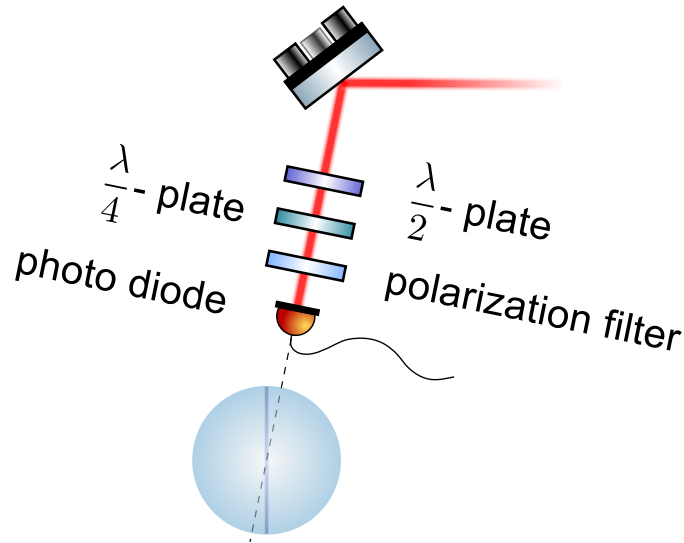


**Figure 4.2: Polarization alignment of the polarizing beam.** A laser beam which is aligned almost vertically passes a half and a quarter wave plate and a polarizer before its power is measured by a photo diode. The photo diode is used to align the optical axis of the wave plates to the transmission axis of the polarization filter.

The alignment of the polarization of the reference beam was simply done by placing a linear polarizer into the beam path in front of a photo diode. This polarizer is aligned such that the transmitted light is linearly polarized along the  $z$ -axis, other polarizations are filtered. The reference beam is out-coupled from one of the output fibers of the illumination setup presented in section 3.3.1.3. Using the Berek compensator of the illumination setup, it is very easy to align the polarization of the reference beam by minimizing the power measured with the photo diode, resulting in a linear polarization of the reference beam along the  $y$ -axis.

Aligning the polarization of the polarizing beam is more complex. The basic idea is to have the beam initially linearly polarized along the  $z$ -axis and then going through a half and a quarter wave plate to control its final polarization, see Figure 4.2. Thereby, the linear polarization is rotated by the half wave plate and then made elliptical by the quarter wave plate. In order to realize this it is required to align the initial polarization and the optical axes of the wave plates. Therefore, the particle is imaged and with the Berek compensator from the illumination setup the polarization is adjusted such that the number of photons in the image of the particle is at a minimum. This adjustment is performed without the wave plates implemented in the polarization setup. In this configuration the polarization of the beam is parallel to the optical axis. Now a polarizer and a photo diode are brought into the beam path. The polarization filter is aligned with its transmission axis oriented along the  $x$ -axis by minimizing the signal from the photo diode. Then the half wave plate is positioned in the beam path, in front of the polarization filter. It is mounted in a motorized rotation mount and its optical axis is aligned

such that the signal on the photo diode is still minimized. The same procedure is performed for the quarter wave plate which is inserted between the half wave plate and the polarization filter. Both linear polarizations, parallel and orthogonal to the optical axis of the imaging system are not changed by the quarter wave plate. When the half wave plate is rotated by  $45^\circ$  the initial linear polarization parallel to the optical axis is rotated by  $90^\circ$  and is then orthogonal to the optical axis. Correspondingly, the polarization after the quarter wave plate is with the rotation of the half wave plate going from linear and parallel to the optical axis, to elliptical with its major axis parallel to the optical axis, to circular, to elliptical with its major axis orthogonal to the optical axis, and ends up being linear and orthogonal to the optical axis. This means that the polarization ratio  $\epsilon$  of the polarizing beam passes through all values between  $\infty$  and  $0$ . When rotating the quarter wave plate again by  $45^\circ$   $\epsilon$  evolves back from  $0$  to  $-\infty$ . When the polarization alignment is completed the polarizer and the photo diode are removed.

In this experiment we also performed measurements at different focal positions. For this purpose the focus of the imaging system is scanned by moving the standard optical microscope along the optical axis with a piezo for  $20 \mu\text{m}$  with a stepsize of  $1.25 \mu\text{m}$ . To compensate for slow drifts of our experimental setup and imaging system, we alternately take images with the reference and the polarizing beam. For every relative focus position and polarization state 25 sets of images are taken, where one set contains an image in which the nanoparticle was illuminated with the polarizing beam and one with the reference beam. In this way, we get an average real and apparent position together with the apparent displacement as well as an estimate for the errors of the position measurement.

## 4.2 Experimental results

### 4.2.1 Focus determination

In order to find the focus of the imaging system we used the same method as in the previous experiment by scanning the relative focal position and choosing the one which features the highest local intensity. As a measure of the local intensity we used the photon number per pixel on the CCD chip of the camera. The corresponding data is plotted in Figure 4.3a, where every data point is averaged over 925 images. In the following the shown error bars correspond to the standard error of the mean value of the measured quantities, given by  $\sigma/\sqrt{N}$ , where  $\sigma$  is the standard deviation of the measured quantities and  $N$  the number of measurements.

To measure the position of the nanoparticle a two dimensional Gaussian function with elliptical contour was fitted to the images. The main axes of the contour ellipse are fixed on the  $x$ - and  $y$ -axis. A more detailed description and discussion of the data analysis is given section 4.3. In Figure 4.3b the two waists of the elliptical Gaussian fit, where  $\sigma_x(\sigma_y)$  denotes the waist along the  $x(y)$ -axis, obtained from the reference images on the CCD chip is plotted with respect to the relative focal position. The horizontal dashed lines give the waist which was obtained by the simulation of the images. These simulations were performed using the parameters of the imaging systems involved in the particular setup taking into account the  $7^\circ$  tilt of the polarizing beam. While the experimentally obtained waist at the focus of  $15.3 \mu\text{m}$  agrees very well with the calculated value of  $14.9 \mu\text{m}$  for the imaging system with the effective aperture  $\text{NA}_{\text{eff}} = 0.41$

#### 4. MEASUREMENT OF POLARIZATION DEPENDENT APPARENT DISPLACEMENT

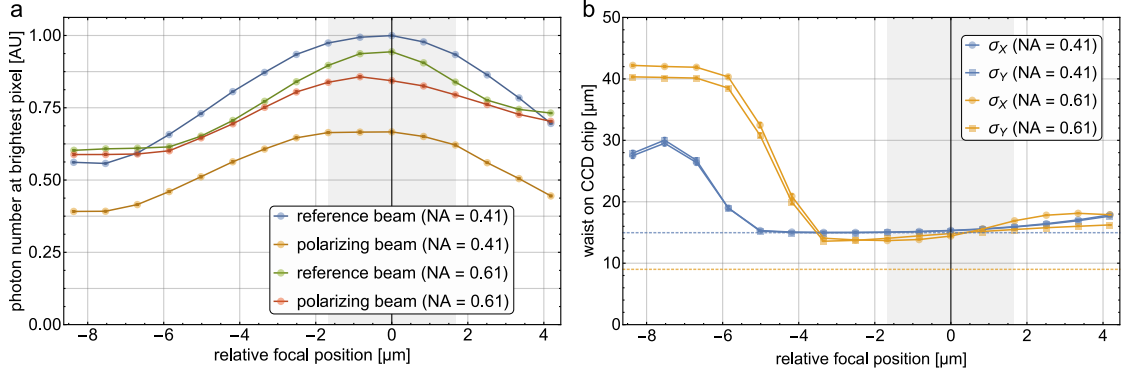


**Figure 4.3: Focus determination.** **a**, The photon number at the brightest pixel used as a measure for the local intensity in the image of the nanoparticle, plotted as a function of the relative focal position. The blue (yellow) curve shows the data measured with the imaging system with  $\text{NA}_{\text{eff}} = 0.41$  while the nanoparticle was illuminated with the reference (polarization) beam and the green (red) curve shows the data measured with the imaging system with  $\text{NA}_{\text{eff}} = 0.61$  while the nanoparticle was illuminated with the reference (polarization) beam. The fact that the maximum of the measured photon numbers have different values stems from the different powers of the reference and polarizing beam. The focus is defined as the relative focal position with the highest local intensity. The grey highlighted area indicates the data in the focal region which was used for further analysis, which also applies for the next subfigure. **b** The waist of the reference images at the CCD chip of the camera fitted with a two dimensional elliptical Gaussian plotted as a function of the relative focal position. For the imaging system with  $\text{NA}_{\text{eff}} = 0.41$  the waist along the  $x(y)$ -axis is shown as blue disks (squares) and for the imaging system with  $\text{NA}_{\text{eff}} = 0.61$  the waist along the  $x(y)$ -axis is shown as yellow disks (squares). The blue (yellow) dashed line indicates the theoretically obtained waist in the focus using the parameters of the imaging system with  $\text{NA}_{\text{eff}} = 0.41$  ( $\text{NA}_{\text{eff}} = 0.61$ ).

the experimental obtained value of  $14.6 \mu\text{m}$  is in comparison to the simulated value of  $9.2 \mu\text{m}$  noticeably higher for the imaging system with  $\text{NA}_{\text{eff}} = 0.61$ . This mismatch might stem from small aberrations in the high NA imaging system. Nevertheless, the overall good agreement of the measured waists in comparison to the calculated ones shows a good performance of the imaging system and does not indicate any alarming aberrations. One can observe that the waist is like in the previously presented experiment almost constant for a wide range of relative focal positions and cannot be used to define a precise focus. Additionally the rapid increase of the waist due to ring structures in the point spread function for large negative relative focal positions can be observed.

#### 4.2.2 Main results

The main purpose of this experiment was to measure the apparent displacement of a nanoparticle as a function of its polarization state. This is realized by rotating the half wave plate, which is assigned to adjust the polarization of the polarizing beam (see 4.1.4) from its initial position by

90° in 2.5° steps. Thereby we scan through 37 polarization states, *i.e.* 37 values of  $\epsilon$  between  $-\infty$  and  $\infty$  from which 34 values of  $\epsilon$  lie in the interval  $[-6, 6]$ . For every polarization state and every relative focal position 50 images are taken alternatingly illuminated with the polarizing and the reference beam. Consequently we can determine the apparently displaced position of the nanoparticle with respect to its real position in successively taken images. This rules out any short term drifts. In order to keep the impact of shot-to-shot noise small, we averaged the apparent displacement over the 125 measurements taken in the focus region, which involves beside the focus the four relative focal positions closest to the focus. The focus region is highlighted in grey in Figure 4.3

The corresponding data, obtained from the five datasets in the focus region, is plotted in Figure 4.4a for the setup with  $\text{NA}_{\text{eff}} = 0.41$  and in Figure 4.4b for the setup with  $\text{NA}_{\text{eff}} = 0.61$ . The solid curves show the displacement obtained from a simulated measurement. The dashed coloured curves show the displacement of the center of mass according to expression 2.51. Note that the corresponding theoretical model does not take the tilt of the polarizing beam into account. For  $|\epsilon| \leq 1$  the data agrees very well with the linear approximation  $\Delta x = \epsilon \cdot \tilde{\lambda}/(2\pi)$ , which is shown as grey dashed line. Here  $\tilde{\lambda} = \lambda/n$ , while  $\lambda$  denotes the free space wavelength of 685 nm of the laser used to illuminate the nanoparticle and  $n = 1.458$  is the refractive index of the index matching fluid. In the regime  $|\epsilon| > 1$  the center of mass prediction shows significant deviations from the experimental data which is no need to be alarmed, since the experimentally obtained position was obtained from a two dimensional Gaussian fit which is a different measurement. Instead the numerical prediction using Gaussian fitting of the calculated images using expression 2.64 agrees very well with the experimental data. These calculations were performed using the parameters of the imaging systems involved in the particular setup and take into account the 7° tilt of the polarizing beam. The maximal distance between the apparent positions of the nanoparticle is about  $0.9 \cdot \tilde{\lambda} = 423$  nm, which by far exceeds the diameter of the nanoparticle of 100 nm. For the circular polarized nanoparticle in the setup with  $\text{NA} = 0.41$  the measured displacement is  $\Delta x_t(\epsilon = -1) = -76(5)$  and  $\Delta x(\epsilon = 1) = 69(4)$  while the predicted values from the simulation are  $\Delta x_t(\epsilon = \pm 1) = \pm 72$  and from the center of mass also  $\Delta x(\epsilon = \pm 1) = \pm 72$ . In the setup with  $\text{NA} = 0.61$  the experimental obtained displacement is  $\Delta x(\epsilon = -1) = -69(3)$  and  $\Delta x(\epsilon = 1) = 73(3)$ , with the predicted values from the simulation of  $\Delta x(\epsilon = \pm 1) = \pm 72$  and from the center of mass of  $\Delta x(\epsilon = \pm 1) = \pm 69$ . Within the statistical errors our experimental obtained data agrees very well with the theoretical predictions.

Figure 4.4c shows images of the nanoparticle taken with the imaging system with  $\text{NA}_{\text{eff}} = 0.41$  for different dipole polarization ratios  $\epsilon$ . These images are averaged over the data sets in the focus, *i.e.* relative focal position equals zero. The white dashed ellipse indicate the measured real position of the nanoparticle. The plotted ellipses indicate the measured apparent positions and the major axes of the ellipse correspond to the fitted waists  $\sigma_x$  and  $\sigma_y$ . The apparent displacement is clearly visible. While for  $|\epsilon| \leq 2.1$  the point spread functions look nearly indistinguishable from each other the change of the PSFs for  $|\epsilon| \gg 1$  is visible.

In Figure 4.6a the fit amplitude with respect to the dipole polarization ratio  $\epsilon$  obtained from the images taken with the reference and polarizing beam are plotted. The presented data are averaged over the images in the focus region. While the fit amplitude and consequently the

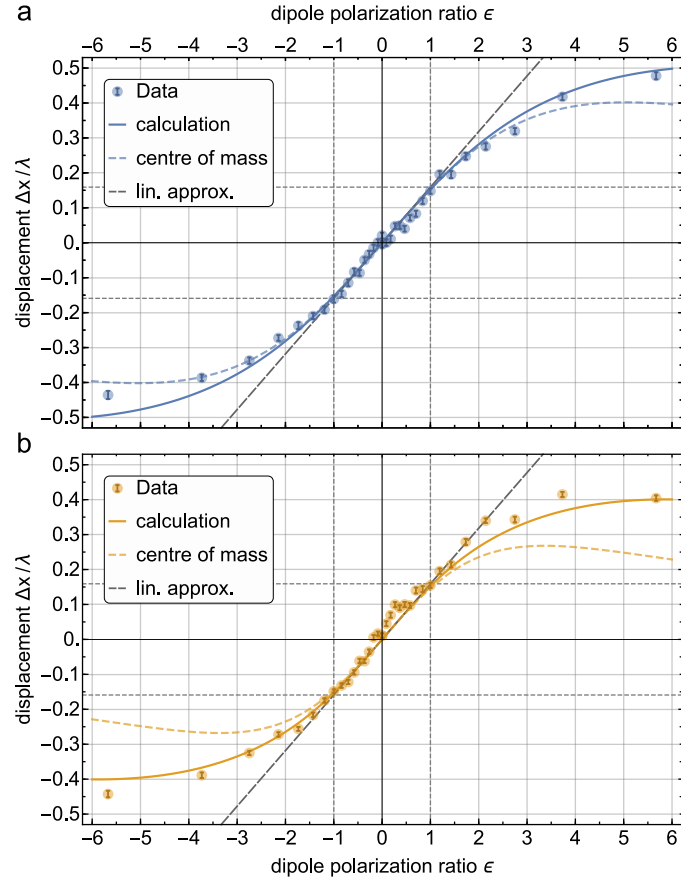


**Figure 4.4: Apparent displacement measured as function of polarization.** **a**, The measured apparent displacement  $\Delta x$  (blue disks) using the imaging system with  $\text{NA}_{\text{eff}} = 0.41$  plotted as a function of the dipole polarization ratio  $\epsilon$ . The solid blue line indicates the numerical displacement obtained from fitting the calculated images taking the tilt of the polarizing beam into account. The dashed blue curve shows the theoretically obtained center of mass displacement (see expression 2.51). The dark grey dashed line shows the linear approximation  $\Delta x = \epsilon \cdot \tilde{\lambda} / (2\pi)$  with  $\tilde{\lambda}$  the wavelength of the laser inside the index matching fluid. The light vertical grey dashed lines indicate the circular polarization state  $|\epsilon| = 1$  and the horizontal ones the displacement  $\Delta x = \pm \tilde{\lambda} / (2\pi)$ . **b**, Shows the same plot as in subfigure **a** for the imaging system with  $\text{NA}_{\text{eff}} = 0.61$ .

accumulated number of photons at the CCD chip should be constant when illuminating the nanoparticle with the reference beam, it is dependent on the polarization when illuminating with the polarizing beam. In addition to the fit amplitudes gained from the experimental data the fit amplitudes gained from theoretical images of an elliptically polarized emitter are shown in the plot. The amplitudes in the images taken with the polarizing beam agree very well with the calculated data while the fit amplitudes in the reference images, which should be constant

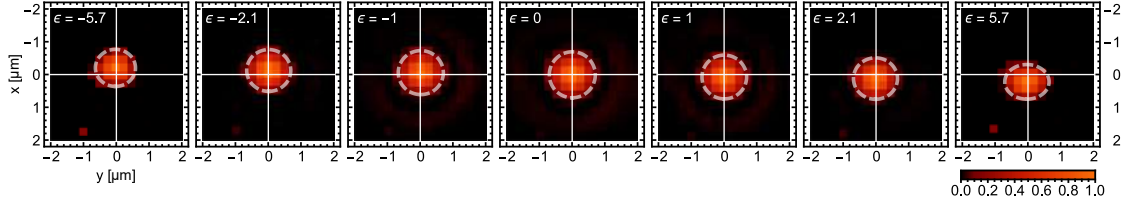


**Figure 4.5: Images of elliptically polarized dipole.** Images of the nanoparticle for different values of  $\epsilon$ . Every single image is averaged over 25 images taken for the particular polarization state in the focus. The white crosses indicate the real position of the nanoparticle obtained from the image with  $\epsilon = 0$ . The white dashed ellipse indicate the measured position of the nanoparticle and the major axes of the ellipse correspond to the waists  $\sigma_x$  and  $\sigma_y$  of the elliptical Gaussian fit. The apparent displacement is clearly visible. While for  $|\epsilon| \leq 2.1$  the images are nearly indistinguishable from each other for  $|\epsilon| \gg 1$  a change in the point spread function is visible.

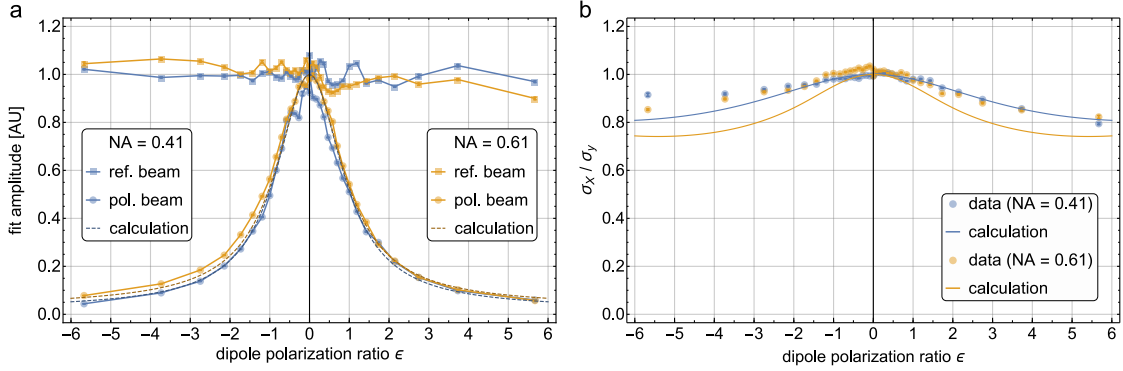


**Figure 4.6: Fit parameters.** **a**, The fit amplitude for both imaging systems and both illumination beams plotted as a function of  $\epsilon$ . The blue squares (disks) correspond to the data taken with the imaging system with  $\text{NA}_{\text{eff}} = 0.41$  from images illuminated with the reference (polarizing) beam and the yellow squares (disks) correspond to the data taken with the imaging system with  $\text{NA}_{\text{eff}} = 0.61$  from images illuminated with the reference (polarization) beam. The dashed blue (yellow) curve shows the fit amplitude of the calculated images for  $\text{NA}_{\text{eff}} = 0.41$  ( $\text{NA}_{\text{eff}} = 0.61$ ). The data obtained from the images illuminated with the polarizing beams agrees very well with the calculated data while the fit amplitude obtained from the reference images shows a fluctuation of the power of the reference beam of about 10%. **b**, The ratio  $\sigma_x/\sigma_y$  from the fitted waists plotted as a function of  $\epsilon$ . The blue (yellow) disks correspond to the data taken with the imaging system with  $\text{NA}_{\text{eff}} = 0.41$  ( $\text{NA}_{\text{eff}} = 0.61$ ) and the blue (yellow) curve shows the calculated data. The measured data shows some deviations with respect to the calculated data but follows in general the overall evolution of the latter.

in general, varies for about 10%. This variation is very likely caused by fluctuations of the laser intensity. However small fluctuations of the laser intensity have no impact on the position

determination of the nanoparticle.

The ratio  $\sigma_x/\sigma_y$  of the two waists of the images in which the nanoparticle was illuminated with the polarizing beam is plotted in Figure 4.6b along with the corresponding calculated data. The presented data is averaged over the images in the focus region. While for  $\epsilon > 0$  and  $\text{NA}_{\text{eff}} = 0.41$  the experimental data agrees very well with the simulation, there is a discrepancy for  $\epsilon < 0$  and  $\text{NA}_{\text{eff}} = 0.41$  and in general for  $\text{NA}_{\text{eff}} = 0.61$ . Nevertheless the decreasing of  $\sigma_x/\sigma_y$  with increasing  $|\epsilon|$  follows the overall behavior of the simulation. According to the calculation the ratio of the waists should be smaller than measured, which would make it easier to recognize that the particle is apparently displaced. Consequently when trying to estimate the apparent displacement from the deformation of the point spread function one would possibly underestimate the apparent displacement of the nanoparticle in this data.

### 4.2.3 Defocussing errors

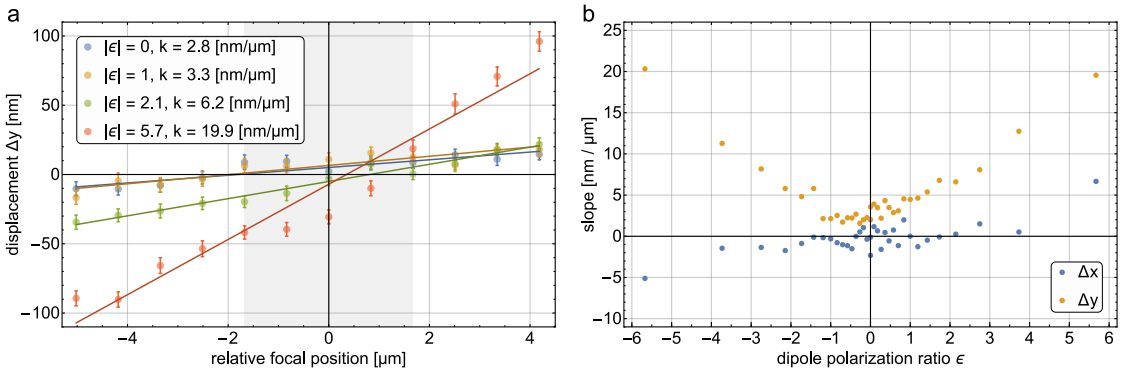


**Figure 4.7: Apparent displacement along vertical axis due to defocussing.** **a**, The displacement  $\Delta y$  as a function of the relative focal position for different values of  $|\epsilon|$  plotted with the corresponding linear approximations. The corresponding slopes are given in nanometer of displacement per microns of defocussing. The presented data was taken with the imaging system with  $\text{NA}_{\text{eff}} = 0.41$ . The increase of the slopes of the linear approximations with increasing  $|\epsilon|$  shows the increasing anisotropy of the nanoparticle's emission pattern. The grey highlighted area indicates the data in the focal region which was used for further analysis. Every data point was averaged over 25 images, which causes the statistical error to be larger than in the previous plots. **b** The slope of the focus dependent displacement  $\Delta y$  plotted (blue) as a function of  $\epsilon$ . It shows clearly the increase of the slope with increasing  $|\epsilon|$  which could already be estimated from the previous subfigure. Additionally the slopes of the displacement  $\Delta x$  are plotted (yellow) which is expected to feature no dependence on the relative focal position, meaning the slopes are expected to be zero.

In the experimental setup discussed in this chapter the superposition of the light emitted by the nanoparticle and its reflection on the nanofiber lead to an anisotropic illumination of the aperture and thus to a strong dependence of the apparent displacement on the relative focal position. The new setup was designed to minimize this effect. While for  $\epsilon = 0$  the emission pattern

of the nanoparticle should indeed be isotropic across the aperture, it starts getting anisotropic when increasing  $|\epsilon|$ . This stems from the increasing amplitude of the dipole oscillating along the optical axis. Since this oscillation axis is tilted by  $7^\circ$  it features an anisotropic emission across the aperture. However this anisotropy is along the  $y$ -axis and should therefore not influence the apparent displacement  $\Delta x$  but introduce an additional apparent displacement  $\Delta y$  along the  $y$ -axis which depends on the relative focal position and the polarization. In particular it should depend on the absolute value of  $\epsilon$ , since the anisotropy of the emission does not depend on the sign of  $\epsilon$ .

For the datasets obtained from the experimental setup with  $\text{NA}_{\text{eff}} = 0.41$  the evolution of  $\Delta y$  is plotted in Figure 4.7a with respect to the relative focal position for different values of  $|\epsilon|$ . Note that the statistical error in this plot is quite high, since in comparison to the data presented *e.g.* in Figure 4.4 only 50 images are averaged for every data point. Additionally like in the previous chapter the nanoparticle drifts stronger in  $y$  direction than in  $x$  direction, since it is mounted on a horizontally oriented nanofiber. The solid lines show linear fits to the corresponding data sets. One can see that increasing anisotropy of the emission of the nanoparticle with growing  $|\epsilon|$  results in an increasing of the slope of the apparent displacement  $\Delta y$ . For  $\epsilon = 0$  the slope is not zero as expected, but still small, which originates potentially from the finite precision of the polarization alignment of the reference and the polarizing beam. If the polarization of the reference beam is not aligned perfectly linearly along the  $y$ -axis, but slightly tilted towards the imaging system this would cause a dependency of the  $y$  position of the nanoparticle in the reference images on the relative focal position. This would then directly influence the apparent  $y$  position of the elliptically polarized particle, since this position is measured with respect to the assumed real position.

Figure 4.7b shows the slope of the focus dependent displacement  $\Delta y$  as a function of the polarization of the particle. In addition, also the slopes of the linear approximation of the apparent displacement along the  $x$ -axis are plotted. While the slopes of  $\Delta y$  increase with growing  $|\epsilon|$  the slopes of  $\Delta x$  are mainly constant and small. In an ideal aberration free optical imaging system the displacement  $\Delta y$  is zero at the focus. This condition could in principle be used to define the focus of the imaging system. Averaging over all the positions where the displacement  $\Delta y(\epsilon)$  intersects the  $x$ -axis gives a value of  $-1.1 \mu\text{m}$ , which indicates the the focus position we defined in section 4.2.1 is in good agreement with the focus one would obtain when defining it via the requirement that  $\Delta y = 0$ .

Figure 4.8a shows the displacement  $\Delta x$  plotted as a function of the relative focal position  $z$  for different values of  $\epsilon$  for the data taken with the setup with  $\text{NA} = 0.41$ . Only for the highest value of  $|\epsilon|$  a clear change of  $\Delta x$  with respect to the relative focal position is visible. Still this change is very small compared to the mean value of the corresponding displacement. In order to see, if the relative focal position effects the polarization dependent position shift of the nanoparticle, we analyzed the apparent displacement  $\Delta x$  for the two relative focal positions  $-5.0 \mu\text{m}$  and  $4.2 \mu\text{m}$ , see Figure 4.8b and c. The experimental data is in good agreement with the simulation which shows that the effect studied in this thesis is independent from the relative focal position. Additionally, it shows that the requirement on this setup to minimize any dependence on the relative focal position of  $\Delta x$  was achievable within the precision of the polarization and beam alignment.

#### 4. MEASUREMENT OF POLARIZATION DEPENDENT APPARENT DISPLACEMENT

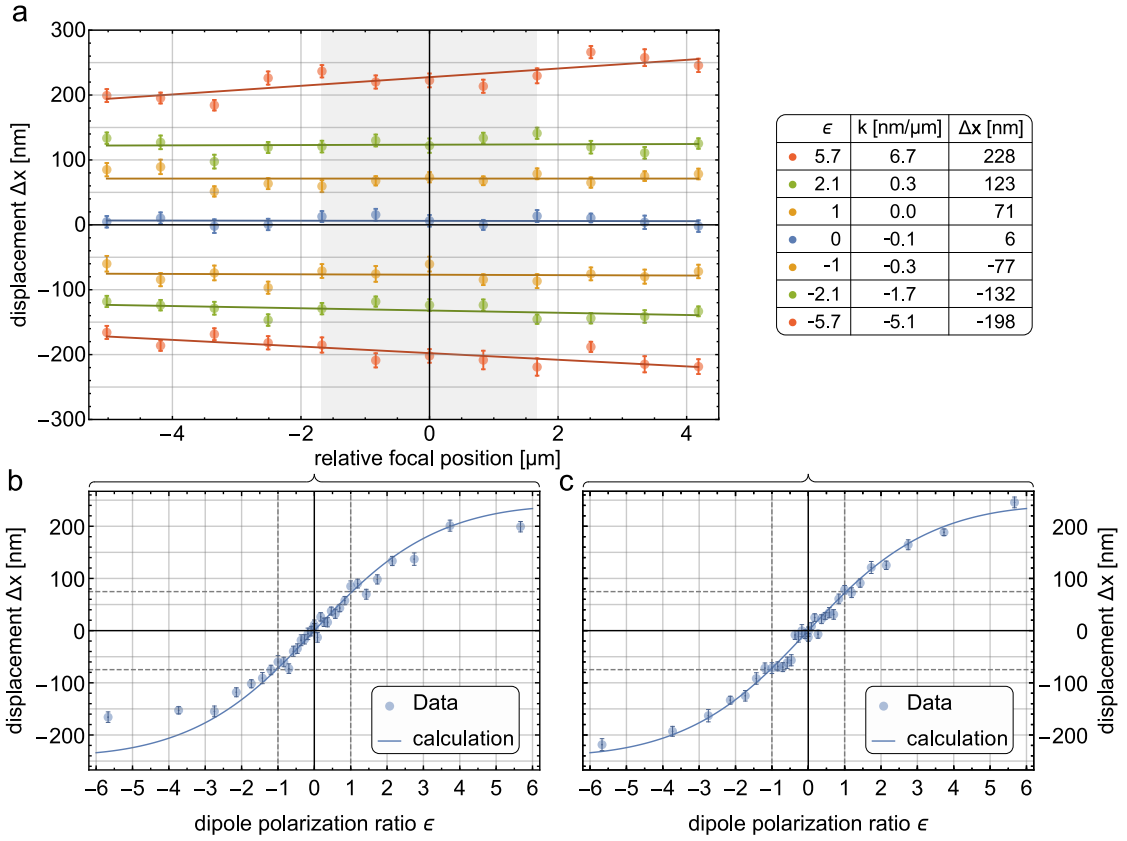


**Figure 4.8: Apparent displacement along horizontal axis due to defocussing.** **a**, The displacement  $\Delta x$  plotted as a function of the relative focal position for different values of  $\epsilon$  with the corresponding linear approximations. The presented data was taken with the imaging system with  $\text{NA}_{\text{eff}} = 0.41$ . One can see, that only for  $|\epsilon| \gg 1$  the apparent displacement shows a small dependence of the relative focal position and can be considered as constant otherwise. The grey highlighted area indicates the focal region. **b** and **c**, The apparent displacement plotted as a function of  $\epsilon$  for the data taken at the relative focal positions  $-5 \mu\text{m}$  and  $4.2 \mu\text{m}$ . Both plots show a good agreement with the calculated displacement (solid line) and underline that the apparent displacement is not dependent on the relative focal position.

Figure 4.9 shows the focus dependent displacements  $\Delta y$  and  $\Delta x$  for the imaging system with  $\text{NA}_{\text{eff}} = 0.61$  for several values of  $|\epsilon|$ , plotted as a function of the relative focal position  $z$ . In comparison to the data presented from the setup with the smaller NA (see Figure 4.7a) the slopes of  $\Delta y$  for small  $|\epsilon|$  are higher, specially the slope of  $\Delta y$  for  $\epsilon = 0$  is twice as high as for the previous presented data. This might stem from the fact that the higher NA collects a bigger part of the anisotropic emission pattern or the anisotropy was increased, caused by a not so well performed polarization alignment. Averaging these data over all the positions where the displacement  $\Delta y(\epsilon)$  intersects the x-axis gives a value of  $1.5 \mu\text{m}$  which agrees very well with the chosen focus.

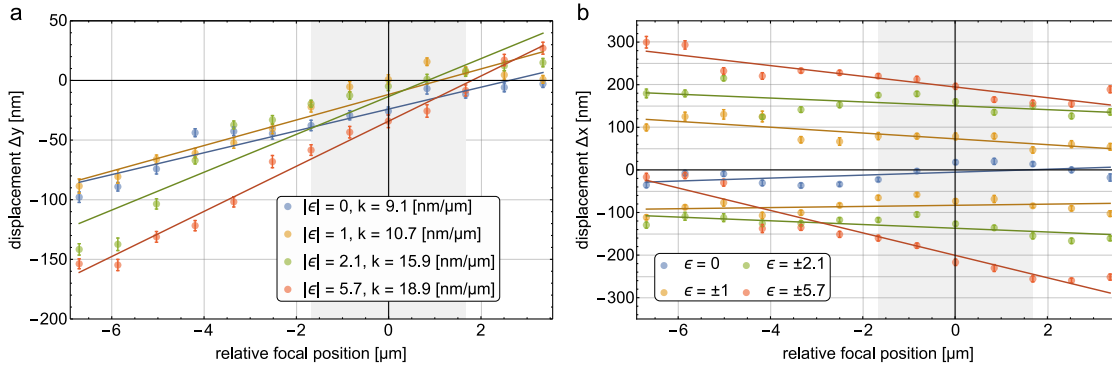


**Figure 4.9: Apparent displacement due to defocussing.** **a**, The displacement  $\Delta y$  plotted as a function of the relative focal position for different values of  $|\epsilon|$  including the corresponding linear approximations. The presented data was taken with the imaging system with  $\text{NA}_{\text{eff}} = 0.61$ . The slopes for the first three values of  $|\epsilon|$  are noticeably higher than in the previous experiment with the smaller NA which might stem from the higher NA. The grey highlighted area indicates the focal region, which also applies for the next subfigure. **b**, The displacement  $\Delta x$  plotted as a function of the relative focal position for different values of  $\epsilon$  with the corresponding linear approximations. In contrast to the same data presented for the lower NA experiment here the apparent displacement depends on the relative focal position, specially for large  $|\epsilon|$ . This behavior indicates an overall anisotropic emission of the nanoparticle which likely stems from imperfect alignment of the particle's polarization.

For the displacement along the  $x$ -axis we observe in contrast to the same plot for the data taken with the small NA a clear dependence of  $\Delta x$  on the relative focal position. When only considering the cases  $\epsilon = \pm 2.1$  and  $\epsilon = \pm 5.7$  the slopes have the same sign and approximately the same value which indicates that this behavior could stem from a dependence of the reference position on the relative focal position. This would directly impact the measured apparent position. Such an effect could appear when the reference beam is not perfectly linearly polarized along the  $y$ -axis, which would lead to an anisotropic illumination of the aperture and thus to an apparent shift of the particles position in the reference images. Although this might play a role in the presented data it cannot explain the behavior of the evolution of  $\Delta x$  for the other polarization states. Hence it is likely that not only the polarization of the reference beam is not perfectly aligned but also the polarization of the polarizing beam. Any possible misalignment does not influence the data taken with the lower NA setup, since the polarization alignment, see section 4.1.4, was redone in between the both measurements.

Summarizing the presented data shows a strong dependence of the apparent position of an emitter on its polarization state. The measured displacement from the real position is even larger than the theoretical predictions derived for the center of mass (2.51). Furthermore, the measured displacement fits very well to the values obtained from a calculation that takes the Gaussian fitting into account to obtain the apparent position of the particle. While a clear dependence of the apparent displacement of the aperture as indicated by the center of mass displacement, it could not be observed. But the calculations of the displacement including the Gaussian fitting

show, that in this position determination process the aperture does not play such a prominent role in the regime of the apertures we used. Besides the apparent displacement along the  $x$ -axis an apparent displacement along the  $y$ -axis was observed that depends on the relative focal position and originates from an intrinsic polarization dependent anisotropic emission of the nanoparticle caused by the tilt of the polarizing beam. In contrast to the experimental setup presented in the previous chapter we could show that this setup is in principle capable to show an apparent displacement ( $\Delta x$ ) which does not depend on the relative focal position. In summary, when comparing the size of the used nanoparticle to the highest measured displacements, which are close to the wavelength, it can be said, that the nanoparticle is clearly seen at a position where it is not.

### 4.3 Data analysis

There exist several methods which could be used to determine the position of the nanoparticle from the image data. Center of mass determination, cross correlation [87] and fitting of a theoretically or experimentally obtained point spread function [127] as well as fitting two dimensional Gaussian functions are commonly used to identify the position of a sub-wavelength diameter emitter. In order to check if these methods have an influence on the polarization dependent position shift we used two such methods: fitting a Gaussian function to the image data and using the experimentally obtained point spread function. In the first part of this section we discuss the results of the Gaussian fitting procedure.

To measure the position of the nanoparticle we fit a two dimensional elliptical Gaussian function to the image data, which is one of the most common methods. The fit function is given by

$$G_{2D}(x, y) = A \cdot e^{-2\left(\frac{(x-x_0)^2}{\sigma_x^2} + \frac{(y-y_0)^2}{\sigma_y^2}\right)} + O, \quad (4.1)$$

where the fit parameters  $(x_0, y_0)$  give the centroid of the Gaussian function, *i.e.* are associated with the position of the nanoparticle,  $A$  is the amplitude and  $O$  a global offset. From section 2.2.4 we know that the images taken within the presented experimental setups should approximately be elliptically symmetric with the main axis aligned along the  $x$ - and  $y$ -axis, see Figure 2.8. Consequently we did not implement an arbitrary orientation of the elliptical two dimensional Gaussian function in the  $xy$ -plane, but restricted the major axes to the  $x$ - and  $y$ -axis. The waist of the Gaussian function along the  $x$ - and  $y$ -axis is given by  $\sigma_x$  and  $\sigma_y$ .

Considering the basic idea of the presented experiments fitting a Gaussian function is considered to be an appropriate method [128] to obtain the position of the nanoparticle. Moreover it is commonly used to determine the position of nanoparticles in the super-resolution regime [98], involving also more advanced methods [129]. In principal the accuracy of the Gaussian fit is only limited by the signal to noise ratio of the given image [65, 130]. Therefore, Gaussian fitting is widely used for position estimation not only in microscopy, but also for instance in astronomy, and there are attempts to further improve its performance [131, 132].

In order to check that the particular Gaussian fit function does not introduce any bias on the measured positions, we compared the results obtained with the already mentioned fitting

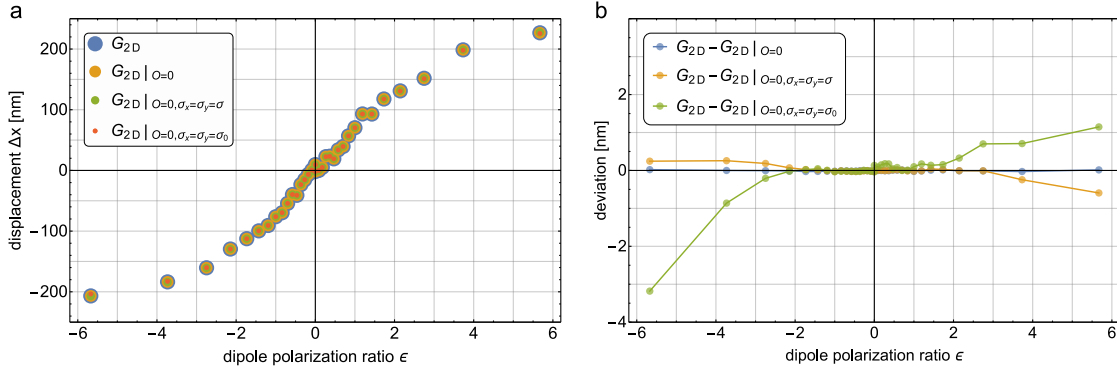


**Figure 4.10: Gaussian fitting.** **a**, The apparent displacement measured with the imaging system with  $\text{NA}_{\text{eff}} = 0.41$  plotted as a function of  $\epsilon$ . The corresponding data was analyzed with an elliptical Gaussian fit with offset (blue disks), an elliptical Gaussian fit without offset (yellow disks), a circular Gaussian fit without offset (green disks) and a circular Gaussian fit with fixed waist obtained from the reference images (red disks). **b**, The deviation of the mentioned fitting functions with respect to the elliptical Gaussian fit with offset plotted as a function of  $\epsilon$ . In general this deviation is in far the sub-nanometer regime and therefore much smaller than the statistical errors. Specially for  $|\epsilon| < 2$  the deviation is negligible.

function 4.1 to three different Gaussian based fitting functions which are:

$$G_{2D}(x, y)|_{O=0} \quad (4.2)$$

$$G_{2D}(x, y)|_{O=0, \sigma_x=\sigma_y=\sigma} \quad (4.3)$$

$$G_{2D}(x, y)|_{O=0, \sigma_x=\sigma_y=\sigma_0} \quad (4.4)$$

Here, the function 4.2 is similar to 4.1 but without a global offset. The other two expressions describe a two dimensional Gaussian with circular contour. While in 4.3 the waist  $\sigma$  is a fit parameter we used in 4.4 the fixed waist  $\sigma_0$  which was obtained from the set of focused reference images. The deviation between the different fitting functions lies within the sub-nanometer regime and is therefore, in general, smaller than the statistical error of the measured positions, see Figure 4.10. Thus no relevant error is introduced by the particular used fitting function.

### 4.3.1 Experimental point spread function fitting

Additional to the position determination by fitting a Gaussian function we also investigated if position estimation using a fit of the experimentally obtained point spread function gives rise to a different apparent displacement. This analysis was performed following the methods presented in [127]. The basic idea of this fitting process is to stepwise scan a test image of the theoretical or experimentally obtained PSF over the experimentally obtained image. For each relative position of the fit image and the experimentally obtained image, the sum of squares of the differences over all pixels is calculated. Searching the minimum of this sum then yields the best match of the two images and is associated with the emitters position, which is then given with respect to a

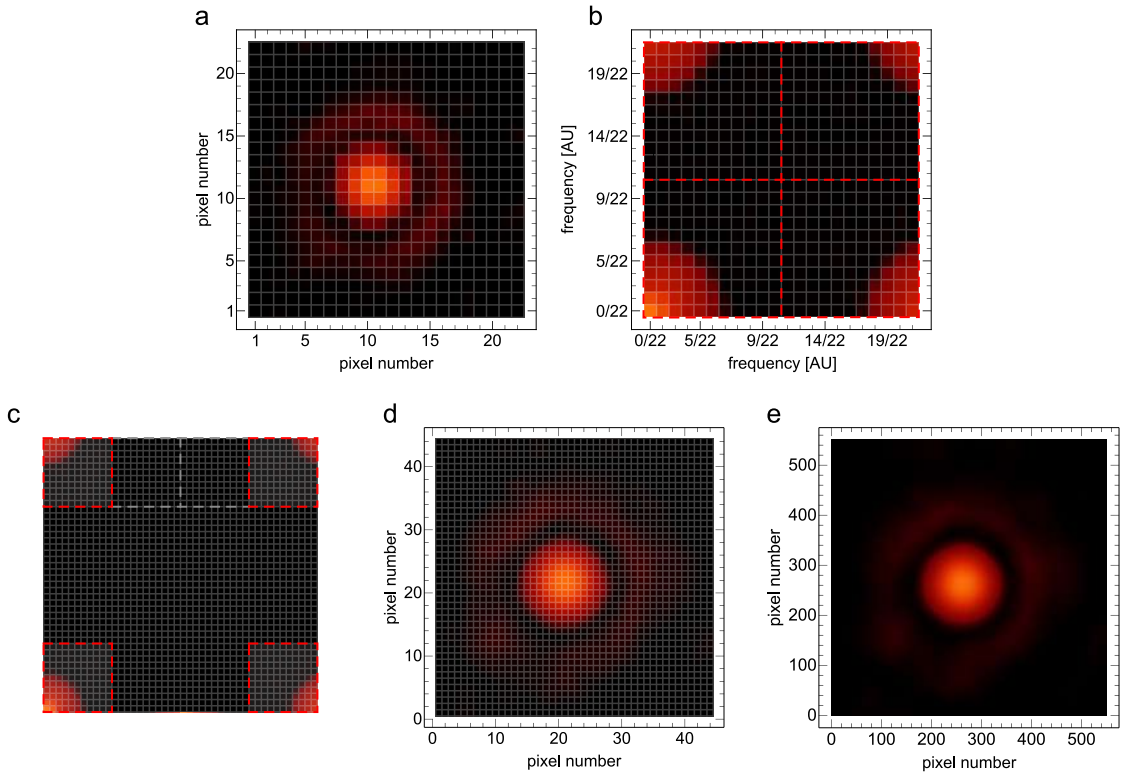


**Figure 4.11: Determining the experimental point spread function.** **a**, First guess of the PSF by averaging over several reference images which are aligned to each other with respect to the brightest pixel. **b**, Discrete Fourier transform of the first guess of the PSF (**a**). Due to the alias effect the low spatial frequency components reappear in the other edges of the image. **c**, Interpolation of the PSF by adding data points with value zero in the Fourier transform along the region of the effective highest frequencies. In this particular case the overall number of pixels is increased by a factor of four. The interpolation process is done under the assumption that the image of the PSF is not subject to fast modulations on the order of next neighbor pixels. **d**, Interpolated image by calculating the inverse Fourier transform, which now features twice the resolution as the initial PSF. **e**, Experimentally obtained PSF of the linearly along the  $y$ -axis polarized dipole, imaged with the optical setup with  $\text{NA}_{\text{eff}} = 0.41$ . The number of pixels was increased by a factor of 24 which now provides a resolution of 10 nm (in the object plane) for the fitting process.

global reference of the CCD chip. A more detailed description of such a fitting process is given in chapter 5. While in principal the used PSF could be taken from a theoretical model of the imaging system and emitter in general the PSF is not known a priori due to unknown aberrations, and not analytically reproducible. In such a chase it can be determined experimentally.

We applied this position measurement for the setup  $\text{NA}_{\text{eff}} = 0.41$ . To generate the image of a PSF which could be used to measure the position of the nanoparticle we made a first guess of the

unknown PSF by averaging over a set of reference images, which were taken in the focus region. Before averaging over all these images they were aligned with respect to each other such that the brightest pixels are at the same position. The resulting image is shown in Figure 4.11a. This test image is a two dimensional array which we now call  $PSF_0$ .<sup>3</sup> The resolution of the position measurement using  $PSF_0$  is given by the pixel size of the CCD chip, since this is the smallest step size with which  $PSF_0$  can be scanned over images in the position determination process. This leads to a stepsize in the object plane of  $5.3 \mu\text{m}/M_{0.41} = 242 \text{ nm}$ , which is by far too big to accurately measure the apparent displacement. To gain a higher resolution in this fitting process the reference image  $PSF_0$  is interpolated. Therefore the discrete Fourier transform of  $PSF_0^F$  is calculated, see Figure 4.11b. The discrete Fourier transform is given by

$$(PSF_0^F)_{kl} = \frac{1}{\sqrt{N}} \sum_{m,n} (PSF_0)_{nm} e^{2\pi i(m-1)(n-1)\frac{(k-1)(l-1)}{N}}, \quad (4.5)$$

where  $N$  is the number of pixels per side length of the quadratic two dimensional array  $PSF_0$  and  $n$  and  $m$  denote the pixel position in the image in line  $n$  and column  $m$ . The amplitude  $(PSF_0^F)_{kl}$  corresponds to a spacial frequency of  $(k-1)/N$  in  $x$ - and  $(l-1)/N$  in  $y$ -direction. In Figure 4.11b one can see that subfigure 4.11a seems to be composed of low and high frequency parts. While the lower frequency are given by  $n/N$  with  $n \ll N$  the higher frequency can be written as  $n/N = 1 - \tilde{n}/N$  with  $\tilde{n} \ll N$ . When sampling a signal with a sampling frequency which is less than half of the signal frequency the so called alias effect [133] appears. Due to this effect a signal of frequency  $1 - \tilde{n}/N$  with  $\tilde{n} < N/2$  cannot be distinguished from a signal with a much smaller frequency of about  $\tilde{n}/N$ . Therefore, the effective highest spatial frequency which can be identified from the image is approximately 0.5. Making use of the assumption that the yet unknown PSF should not be subject to fast modulations (on the size of next neighbor pixels in the image) we can now generate an interpolated image. For this purpose we insert data points with the value zero to the array  $PSF_0^F$  along the regions in the center that correspond to the highest frequencies, see Figure 4.11c. Calculating then the inverse Fourier transform, see 4.11d, we obtain an interpolated image. We call this interpolated data set  $PSF_0^{int}$ . When increasing the overall number of data points in the Fourier transform by a factor of four in the interpolation process, one ends up with twice the number of pixels along the  $x$ - and  $y$ -axis in the interpolated PSF image and has consequently gained a factor 2 higher resolution. Now we can fit the interpolated guess of the PSF to the individual and also interpolated images which were initially used to create  $PSF_0^F$ , which gives us a better estimation of the positions on a subpixel level for the centroid of these images. The already interpolated images can then be averaged to a better approximated image of the real PSF by reorganizing the images such that the just measured positions of the centroids coincide. Since the number of pixels has increased due to the interpolation the images can be aligned with respect to each other more accurately than it was possible in first place. We call this new guess of the image of the point spread function  $PSF_1$ .

<sup>3</sup>Note that the term point spread function is in general used to describe to continuous intensity distribution generated by a lens system in the imaging process in the image plane. Sometimes its also used to describe the theoretical image array this intensity distribution causes when measured theoretically with CCD screen. In the framework of this thesis we refer to the first definition of the PSF. However, in the following the experimentally obtained images of the PSF and the determined interpolated images will also be addressed as *PSF* (italic).

#### 4. MEASUREMENT OF POLARIZATION DEPENDENT APPARENT DISPLACEMENT

Using  $PSF_1$ , the positions of the centroids of all interpolated reference images can again be determined and then a new test image  $PSF_2$  can be generated, in the same way as  $PSF_1$  was obtained. This iterative process is done until  $PSF_i = PSF_{i+1} \equiv PSF_{\text{fit}}$ , meaning until this process converges. Figure 4.11d shows the  $PSF_{\text{fit}}$  that was obtained using this process for an interpolation which doubles the resolution.

Using the experimentally obtained image  $PSF_{\text{fit}}$  of the point spread function of a linearly polarized dipole ( $\epsilon = 0$ ), the position of the nanoparticle in all images taken with the experimental setup with  $NA_{\text{eff}} = 0.41$  can be measured. Therefore the point spread function  $PSF_{\text{fit}}$  is fitted to all images taken in the measurements.

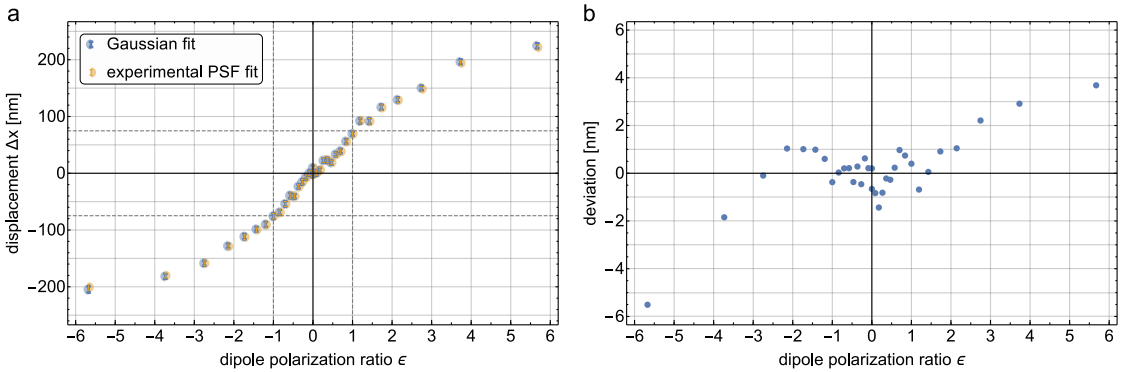


**Figure 4.12: Comparison of Gaussian and PSF fit.** **a**, The apparent displacement  $\Delta x$  plotted as a function of  $\epsilon$  where the blue (yellow) half disks correspond to the Gaussian (experimental PSF) fit. Within the statistical errors both fitting procedures provide the same results. The vertical dashed lines indicate the circular polarization state  $\epsilon = \pm 1$  and the dashed horizontal lines indicate the corresponding displacement  $\Delta x = \lambda/(2\pi)$ . **b** The difference of the measured apparent displacement of both fitting methods plotted as a function of  $\epsilon$ .

In order to gain a precision of 10 nm in the position measurement one of the original images pixel had to be interpolated by 24 subpixels. The resulting  $PSF_{\text{fit}}$  is shown in 4.11e. While the fitting of a two dimensional Gaussian function is in general done very quickly the experimental PSF fitting is very time consuming. The determination of  $PSF_{\text{fit}}$ , and the following fitting process took about one week to be computed. If this runtime could be reduced by an order of magnitude by using more sophisticated algorithms and parallelizing them it would still take half a day to compute the apparent displacements for the whole data set. In contrast, the Gaussian fitting was done on the fly while taking the data, and was redone afterwards to compare different Gaussian based fitting functions, which took less than one hour.

Figure 4.12a shows the apparent displacement  $\Delta x$  determined with the experimental PSF fit as a function of the dipole polarization ratio  $\epsilon$  and for comparison the corresponding apparent displacement determined with the Gaussian fit. The analyzed data set is the same as in section 4.2.2. The apparent displacements obtained with both methods agree very well and overlap within the corresponding statistical errors. In Figure 4.12b the deviation, *i.e.* the difference of the measured apparent displacement of both position measurements is shown. It is of the same

form as the deviation of the circular Gaussian fit with fixed waist from the elliptical Gaussian fit as shown in Figure 4.10c (green dataset). Therefore, it is likely that the dependence of the deviation on  $\epsilon$  stems from the deformation of the point spread function.

Summarizing we can conclude that within our experimental errors there is no relevant difference if the position determination of the nanoparticle is done with a Gaussian fit, or with the experimental PSF fit.

Fitting the experimentally obtained image of the PSF, which we derived from images of a linearly polarized dipole, to the images of an elliptically polarized dipole introduces for obvious reasons a systematic error. From section 2.2.4 it is known that an elliptically polarized dipole features a different PSF than a linearly polarized one, see Figure 2.8. In the next chapter we discuss in more detail the limits of position estimation when one also includes the dependence of the point spread function on the polarization in the fitting process.



# Consequences of spin-orbit interaction in super-resolution microscopy

This chapter focuses on a discussion of the impact of the polarization dependent displacement presented in this work on optical super-resolution microscopy. Appendix A.13 gives a brief introduction to other error sources in super-resolution microscopy. As already pointed out in section 2.2.4 the apparent displacement of an elliptically polarized emitter is accompanied by a distortion of the point spread function (PSF).<sup>1</sup> This distortion can in principal be used to measure the particles polarization and apparent position at the same time. With this knowledge one can compensate for the apparent shift. In this chapter we investigate the signal to noise limited position accuracy of such a measurement.

Parallel to the evolution of super-resolution microscopy a lot of work has been done to find localisation limits in position measurements. Within the related publications there exist different approaches how to model the imaged intensity distributions of the considered emitters and how to define a precision limit. Some of the studies feature numerical methods while others are done analytically, or in both ways. There are several publications directly related to the method presented in this work via least square fits, also known as sum of squared or absolute difference, see [65, 66, 87, 130, 134, 135]. Although the precise definition of the precision limit may differ within this studies, the major outcomes are very similar and are qualitatively comparable to the precision limit defined in this chapter.

One major approach to define a precision limit involves a least square fit using a theoretically obtained PSF. With this fit the position of an emitter in an image containing noise is measured. It is possible that due to noise the measured position does not coincide with the real position of the emitter. An important quantity in this process is the variance of the position measurement, which is used to define a precision limit dependent on the noise.

---

<sup>1</sup>When light of an emitter passes a lens system and is imaged onto a screen the intensity distribution on the screen is determined by the imaging system and the emission properties of the emitter. An imaging system can feature aberrations which modify the intensity distribution in the image plane. The point spread function is a noise free image of that intensity distribution.

Additionally in digital imaging the resolution of a CCD chip which is used to take images has influence on the precision of position measurements [65, 66, 130]. Therefore we will also investigate how the image resolution influences the precision limit.

## 5.1 A precision limit in position determination of elliptically polarized emitters

We now define two precision limits for position measurements of a dipole emitter. One for the case that the polarization state of the emitter is known, where only the position needs to be measured, and one for the case the polarization state of the emitter is unknown. Then the position and the polarization state needs to be measured from the image. The noise limited accuracy of the measurement of the polarization state of an emitter leads to an additional uncertainty in position, caused by the polarization uncertainty, which in turn leads to an apparent displacement.

In the derivation of the precision limits we assume elliptically polarized emitters (as defined in 2.2.1) with real valued  $\epsilon$  only. For the imaging process we assume an imaging system which is perfectly focussed and aberration free. The optical axis of the imaging system coincides with the  $y$ -axis. The image obtained from an elliptically polarized emitter in the assumed imaging system is given by the intensity distribution 2.64. We restrict the quantitative measure of the precision limits to the  $x$ -axis, since in this particular situation the apparent shift of the emitter takes place along this axis.

Digital images consist of data sets which feature an array of measured values like photon numbers or measured power. Every such value is assigned to a position in the image. In particular it is not assigned to a point-like position but to a small area which is usually referred to as pixel, which has a certain shape and size.<sup>2</sup> As the precision limit is dependent on the pixel size ( $PS$ ) and the size of the PSF in the image plane we assume in the following calculations, that these parameters are chosen to provide a minimum precision limit. The influence of  $PS$  and the size of the PSF on the precision limit are investigated in section 5.2.

In order to obtain from the function describing the intensity distribution of the imaged dipole emitters an image array, the intensity functions are integrated over the area of single pixels.<sup>3</sup> This mimics the situation how an image is taken with a CCD chip. We denote in the following an image as a set  $n = \{n_1, n_2, \dots, n_P\}$ , where  $n_i$  gives the photon number at pixel  $i$ . The total number of photons in an the image  $n$  is given by  $N = \sum_{i=1}^P n_i$ , where  $P$  is the total number of pixels in the image. Note that in the following calculations the position of the single pixels in the image is not of importance, therefore it is sufficient to address the single pixels of the image only by a single number. Since we limited the possible elliptical polarization states of the imaged emitter such that it can only cause an apparent shift along the  $x$ -axis, we only consider the situation where the emitter is placed along the  $x$ -axis. The real position of the emitter along

---

<sup>2</sup>In the following we assume an array of quadratic pixels in which every pixel measures the number of incoming photons.

<sup>3</sup>To obtain from the intensity integrated over the are of a pixel a photon number the measured power needs to be divided by  $\hbar\omega$  an multiplied by the exposure time of the imaging system. Since this is a constant factor it will be neglected in the following derivations and the integrated intensity is treated as photon numbers.

the  $x$ -axis is given by  $\delta x$ . Such an emitter is then characterized by the two parameters  $(\delta x, \epsilon)$  with the resulting image  $n(\delta x, \epsilon)$ .

### 5.1.1 Sum of squared difference - a measure to compare images

To compare two images we use the sum of squared difference of the images, which is given by

$$S(n, m) = \frac{1}{N^2} \sum_{i=1}^P (n_i - m_i)^2, \quad (5.1)$$

where  $\sum_{i=1}^P n_i = \sum_{i=1}^P m_i = N$ . This sum is normalized on the total photon number of the images. We now consider a realistic imaging situation where one tries to find the unknown position and polarization state  $(\overline{\delta x}, \overline{\epsilon})$  of an emitter from its image  $\tilde{n}(\overline{\delta x}, \overline{\epsilon})$ , which contains noise.<sup>4</sup> The position and polarization state of the imaged emitter are measured by minimizing the outcome of  $S(\tilde{n}, m(\delta x, \epsilon))$  by varying the position  $\delta x$  and polarization state  $\epsilon$  of the reference image  $m(\delta x, \epsilon)$ . This reference image is defined by the PSF of the imaged emitter. In the absence of noise the parameters  $(\overline{\delta x}, \overline{\epsilon})$  are perfectly identified by  $(\delta x, \epsilon)$  for  $S(n(\overline{\delta x}, \overline{\epsilon}), m(\delta x, \epsilon)) = 0$ .

The noise dependent precision limit will be derived from the function  $S$ . This is done using the noise dependent expectation value  $\langle S \rangle$  and the variance  $\text{Var}(S)$  of  $S$  as a function of  $N$ ,  $\epsilon$  and the real displacement  $\delta x$ . In the process of deriving  $\langle S \rangle$  and  $\text{Var}(S)$  we need to study two special cases of the function  $S$ . We start with

$$S_0(\delta x, \epsilon, \epsilon_0) = \frac{1}{N^2} \sum_{i=1}^P (n_i(0, \epsilon_0) - m_i(\delta x, \epsilon))^2. \quad (5.2)$$

This function compares the image  $n(0, \epsilon_0)$  of an emitter in polarization state  $\epsilon_0$  placed at the origin with the test image  $m(\delta x, \epsilon)$  of an emitter in polarization state  $\epsilon$  placed at the position  $\delta x \cdot e_x$ . Both images are assumed to not contain noise. The special function  $S_0^{\text{lin}}(\delta x, \epsilon) = S_0(\delta x, \epsilon, 0)$  is plotted in Figure 5.1a. The zoom of the center region of this plot is shown in Figure 5.1b. There it can be seen that  $S_0^{\text{lin}}(\delta x, \epsilon)$  has a elongated minimum along  $\epsilon_{\delta x} = -\delta x \cdot 2\pi/\lambda$  which stems from the effect that a real displacement  $\delta x$  is cancelled by the apparent displacement  $\Delta x = \epsilon_{\delta x} \cdot \lambda/(2\pi) = -\delta x$ .<sup>5</sup> This shows that the image of an elliptically polarized emitter which is suitable displaced can be very similar to the one of the solely linearly polarized emitter at the origin. Still  $S_0^{\text{lin}}$  gives a small but nonzero value due to the small deformation of the PSF stemming from the elliptical polarization. Therefore, there exists a continuous set of highly correlated parameters  $(\delta x, \epsilon)$  that creates images nearly indistinguishable from the image of the linearly polarized dipole located at the origin.

The image arrays used to determine the data shown in Figure 5.1 were obtained by integrating the intensity distribution 2.64 over the area of single pixels with the pixel size  $PS$ .<sup>6</sup> The pixel size is  $PS = 0.7 \cdot FWHM$ , where  $FWHM$  denotes the full width half maximum of the

<sup>4</sup>In the following images which are considered to contain noise are marked with a tilde.

<sup>5</sup>In the following  $\epsilon_{\delta x}$  denotes the polarization of an emitter which counters the real displacement  $\delta x$

<sup>6</sup>While the intensity distribution in 2.64 is given for an emitter located at the origin here the real displacement needs to be taken into account.

intensity distribution of a linearly polarized emitter ( $\epsilon = 0$ ). This pixel size provides the highest precision in position measurements when imaging a linearly polarized emitter (see section 5.2). The overall number of pixels per image is  $P = 121$ . The side length of an image is then about one order of magnitude larger than the *FWHM* of the image and consequently covers therefore most of the image information. This values apply to all images in section 5.1 which are used to determine any specific values.

For vanishing pixel size  $PS$  the function  $S_0$  results in an integral over the area of the image. Instead of the squared difference of the power measured at certain pixels the squared difference of the intensity functions is directly integrated. For small real displacement  $\delta x \ll 1$  the squared difference of the intensity distributions can be approximated with a Taylor series:

$$(\mathcal{I}(0, \epsilon) - \mathcal{I}(\delta x, \epsilon))^2 = a \delta x^2 \quad (5.3)$$

$$\left( \mathcal{I}(0, 0) - \mathcal{I}\left(\delta x, -\delta x \frac{2\pi}{\lambda}\right) \right)^2 = b \delta x^4, \quad (5.4)$$

where  $\mathcal{I}(\delta x, \epsilon)$  gives the intensity distribution in the image of an dipole emitter in polarization state  $\epsilon$  at position  $\delta x e_x$ . Figure 5.1c shows the same data as subfigure a and b, but here  $S_0^{\text{lin}}(\delta x, \epsilon)$  is evaluated along the line  $\epsilon = 0$  (blue points - dotted grey line in subfigure b) and  $\epsilon = \epsilon_{\delta x}$  (yellow points - dashed grey line in subfigure b). The value of  $S_0^{\text{lin}}$  increases quadratically with  $\delta x$  when comparing images of linearly polarized emitters and goes with the fourth power of  $\delta x$  when comparing the image of a linearly polarized emitter with the image of an emitter which is elliptically polarized such that the apparent shift cancels the real shift. Hence the approximations of  $S_0$  for  $\delta x \ll 1$  is also for non vanishing pixel sizes valid, as it can be seen in the plot. The factors  $a$  and  $b$  were determined by fitting the corresponding approximations to the data, providing the fit parameters  $a = 0.033$  and  $b = 0.009$ . This figure nicely illustrates that it is easier to distinguish with the help of  $S_0$  a linearly polarized emitter at the origin from a linearly polarized one which is slightly displaced than from an displaced emitter which is elliptically polarized in such a way that the apparent displacement cancels the real displacement. This fact is crucial when considering imaging with noise.

In Figure 5.2a the fit parameter  $a$  is plotted as a function of  $\epsilon$ . It was obtained by fitting the approximation  $a \delta x^2$  to the data obtained by  $S_0(\delta x, \epsilon)$  for different values of  $\epsilon$ . The fit parameter rises for  $\epsilon = 1$  to its global maxima slightly above the value for  $\epsilon = 0$  and decreases then for increasing  $\epsilon$ .

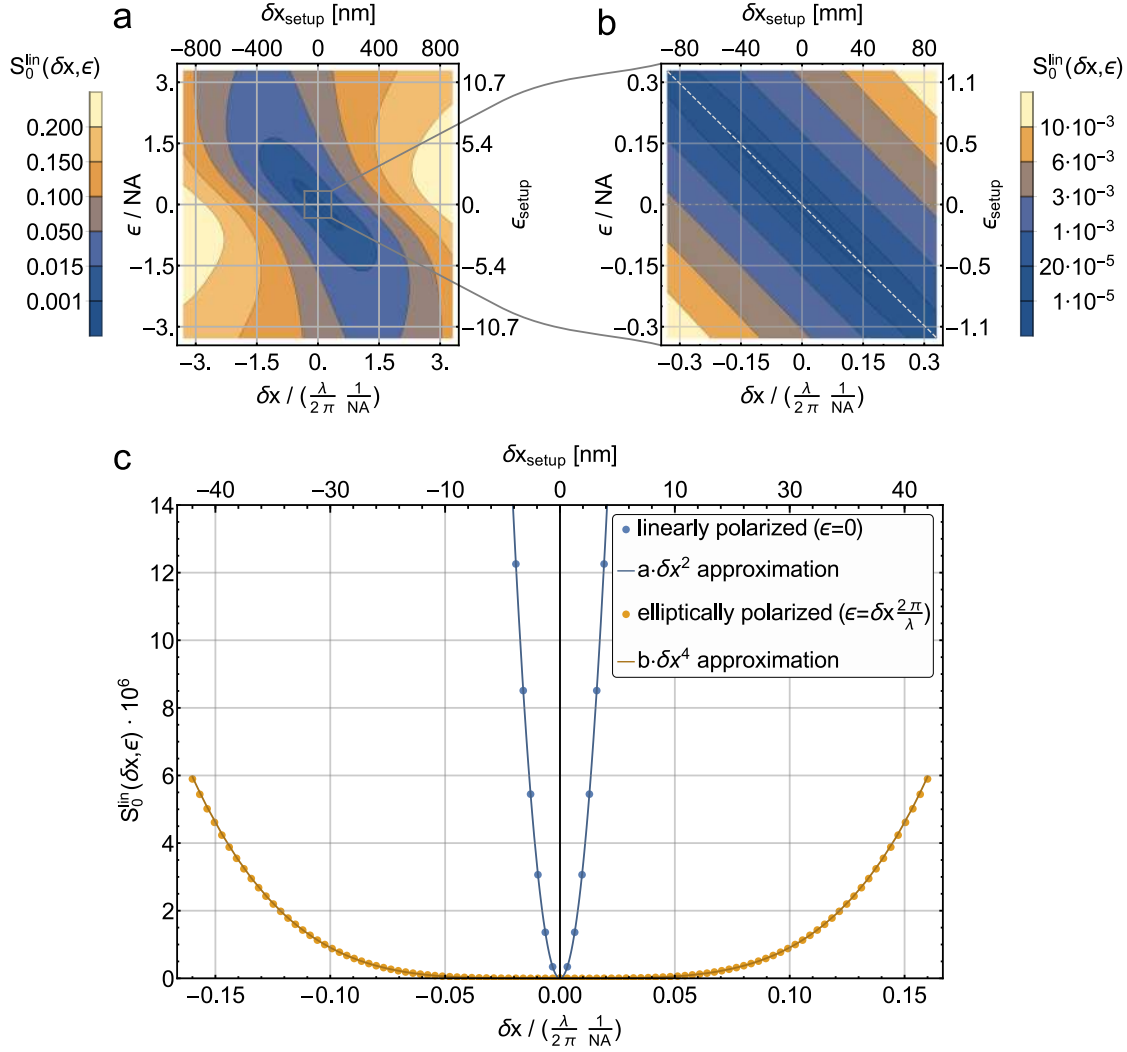


**Figure 5.1: Sum of squared difference.** **a**, Two dimensional plot of  $S_0^{\text{lin}}(\delta x, \epsilon)$ . The lower  $x$ -axis represents the real displacement  $\delta x$  normalized to the wavelength  $\lambda$  and the NA and the left  $y$ -axis represents  $\epsilon$  normalized to the NA. The upper  $x$ -axis and right  $y$ -axis correspond to the setup presented in chapter 4, with  $\lambda = 470\text{nm}$  and  $\text{NA} = 0.28$ . Note that this NA was introduced as a geometrical NA in 2.2.4. **b**, A zoom of the center region of subplot **a**. There an elongated minimum for  $\epsilon_{\delta x} = -\delta x \cdot 2\pi/\lambda$  can be seen. Along this minimum the real displacement  $\delta x$  is cancelled by the apparent displacement  $\Delta x = \epsilon_{\delta x} \cdot \lambda/(2\pi) = -\delta x$ . Still the outcome of  $S_0^{\text{lin}}$  is nonzero due to the distortion of the point spread function caused by the elliptical polarization. **c**,  $S_0^{\text{lin}}$  evaluated along  $\epsilon = 0$  (dotted grey line in **b**) as blue dots and along  $\epsilon_{\delta x}$  (dashed grey line in **b**) as yellow dots. For small  $\delta x$  the function  $S_0^{\text{lin}}$  can be approximated by  $S_0^{\text{lin}}(\delta x, \epsilon) \approx a \cdot \delta x^2$  for  $\epsilon = 0$  and  $S_0^{\text{lin}}(\delta x, \epsilon) \approx b \cdot \delta x^4$  for  $\epsilon_{\delta x}$ . The corresponding fitted parameters are  $a = 0.033$  and  $b = 0.009$ . These approximations are plotted as solid blue and yellow lines. The number of photons  $N$  used to generate this plots is  $10^6$ .

### 5.1.2 Comparing noisy images

We now consider experimentally taken images containing noise. For this we limit the following discussion to the case where the images are dominated by photon shot noise [136], since this is the most fundamental noise source. Therefore it is of major importance in high precision imaging. To study the impact of this noise on the position determination we derive the expectation value and the variance of  $S$ . This will be performed in two steps. Before deriving the expectation value and the variance of  $S$  it will be derived for the function

$$S_{\text{id}}(\delta x, \epsilon) = \frac{1}{N^2} \sum_{i=1}^P (n_i(\delta x, \epsilon) - \tilde{n}_i(\delta x, \epsilon))^2, \quad (5.5)$$

which gives a measure to compare the perfect noiseless image  $n$  of an emitter with a noisy image  $\tilde{n}$  of the same emitter. Due to the photon shot noise, the number of photons collected at a pixel follows a Poisson distribution. The expectation value of the photon number counted at a pixel is given by [137]  $\langle \tilde{n}_i \rangle = n_i$ . The higher momenta of the Poisson distribution can be written as polynomials, where the moment of grade  $k$  is given by the  $k$ th complete exponential Bell polynomial [137],  $\langle \tilde{n}_i^k \rangle = B_k(n_i, \dots, n_i)$ . In the following calculations the first four momenta of  $\tilde{n}_i$  will be used:

$$\langle \tilde{n}_i \rangle = B_1(n_i) = n_i \quad (5.6)$$

$$\langle \tilde{n}_i^2 \rangle = B_2(n_i, n_i) = n_i + n_i^2 \quad (5.7)$$

$$\langle \tilde{n}_i^3 \rangle = B_3(n_i, n_i, n_i) = n_i + 3n_i^2 + n_i^3 \quad (5.8)$$

$$\langle \tilde{n}_i^4 \rangle = B_4(n_i, n_i, n_i, n_i) = n_i + 7n_i^2 + 6n_i^3 + n_i^4. \quad (5.9)$$

Therefore the expectation value of  $S_{\text{id}}$  can be derived to

$$\begin{aligned} \langle S_{\text{id}} \rangle &= \frac{1}{N^2} \left\langle \sum_{i=1}^P (n_i - \tilde{n}_i)^2 \right\rangle \\ &= \frac{1}{N^2} \sum_{i=1}^P \langle (n_i - \tilde{n}_i)^2 \rangle \\ &= \frac{1}{N^2} \sum_{i=1}^P (n_i^2 - 2n_i \langle \tilde{n}_i \rangle + \langle \tilde{n}_i^2 \rangle) = \frac{1}{N}. \end{aligned} \quad (5.10)$$

This means that the difference  $S_{\text{id}}$  between an noisy image and its noiseless equivalent decreases with  $1/N$ . For infinite integration time the image containing noise becomes an image of the PSF given by the imaging system. In the same way the expectation value of  $S_{\text{id}}$  has been calculated,

its variance can be determined from  $\text{Var}(S_{\text{id}}) = \langle S_{\text{id}}^2 \rangle - \langle S_{\text{id}} \rangle^2$ :

$$\begin{aligned}
 \langle S_{\text{id}}^2 \rangle &= \left\langle \left( \frac{1}{N^2} \sum_{i=1}^P (n_i - \tilde{n}_i)^2 \right)^2 \right\rangle \\
 &= \frac{1}{N^4} \left\langle \sum_{i,j=1}^P (n_i - \tilde{n}_i)^2 \cdot (n_j - \tilde{n}_j)^2 \right\rangle \\
 &= \frac{1}{N^4} \left\langle \sum_{i=1}^P (n_i - \tilde{n}_i)^4 \right\rangle + \frac{1}{N^4} \left\langle \sum_{i \neq j}^P (n_i - \tilde{n}_i)^2 (n_j - \tilde{n}_j)^2 \right\rangle. \quad (5.11)
 \end{aligned}$$

With the usage of the first four momenta of  $\tilde{n}_i$ , the first part of 5.11 simplifies to

$$\left\langle \sum_{i=1}^P (n_i - \tilde{n}_i)^4 \right\rangle = N + 3 \sum_{i=1}^P n_i^2. \quad (5.12)$$

Assuming that the noise on the pixels  $i$  and  $j$  is not correlated, the second part of the expression 5.11 can be derived to

$$\sum_{i \neq j}^P \langle (n_i - \tilde{n}_i)^2 \rangle \langle (n_j - \tilde{n}_j)^2 \rangle = N^2 - \sum_{i=1}^P n_i^2. \quad (5.13)$$

Therefore the variance of  $S_{\text{id}}$  is given by

$$\begin{aligned}
 \text{Var}(S_{\text{id}}) &= \frac{1}{N^4} \left( N + 3 \sum_{i=1}^P n_i^2 + N^2 - \sum_{i=1}^P n_i^2 - N^2 \right) \\
 &= \frac{1}{N^3} + \frac{2}{N^2} \sum_{i=1}^P \left( \frac{n_i}{N} \right)^2. \quad (5.14)
 \end{aligned}$$

It is useful to make the following definition:

$$B := \left( \frac{\sum_{i=1}^P n_i^2}{N^2} \right)^{-1}. \quad (5.15)$$

Here  $B^{-1}$  is the square of the image normalized by  $N^2$ . The highest possible value for  $B$  is the number of pixels  $P$  for  $n_i = N/P$  and the lowest value is 1 in case all light is detected only with one single pixel.  $B$  can be understood as the number of bright pixels in an image.<sup>7</sup>

In any relevant imaging process  $B$  is much smaller than the overall number of collected photons. Therefore the variance of  $S_{\text{id}}$  is dominated by the  $1/N^2$  expression and we make the approximation

$$\text{Var}(S_{\text{id}}) = \frac{2}{N^2 B} \quad \text{for } B \ll N. \quad (5.16)$$

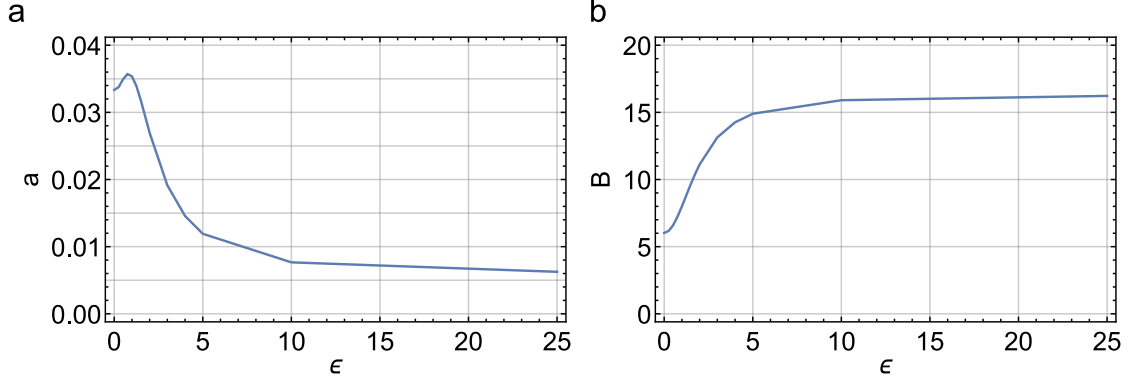


**Figure 5.2: Fit parameter and number of bright pixels.** **a**, The fit parameter  $a$  plotted for different values of  $\epsilon$ . It was obtained by fitting the approximation  $S_0 = a \delta x^2$  to the data obtained by  $S_0$ . **b**, The number of bright pixels  $B$  plotted for different values of  $\epsilon$ . In the image of an emitter which is linearly polarized along an axis orthogonal to the optical axis ( $\epsilon = 0$ ) the number of bright pixels is approximately 6. In the case of an emitter which is linearly polarized along the optical axis ( $\epsilon \gg 1$ ), where the image is given by a ring, the number of bright pixels is increases to about 16.

Figure 5.2b shows the parameter  $B$  plotted as a function of  $\epsilon$ . For the case of linearly polarized emitter  $B \approx 6$  and rises with increasing  $\epsilon$  to a value of about 16.

Now that we derived the expectation value and the variance of  $S_{\text{id}}$  we do the same for the general function  $S$ , which compares a measured image containing noise to the image of a any theoretical PSF. Therefore we rewrite  $S$  to

$$S(\tilde{n}, m) = \frac{1}{N^2} \sum_{i=1}^P (\tilde{n}_i - m_i)^2 = \frac{1}{N^2} \sum_{i=1}^P (n_i + \hat{n}_i - m_i)^2, \quad (5.17)$$

where  $m$  is the the image of theoretical fit PSF. Here  $\tilde{n}$  is the experimentally obtained image with noise and  $n$  is the noise free image of the PSF that corresponds to the emitter of which the image  $\tilde{n}$  was taken. The noise measured on pixel  $i$  is given by  $\hat{n}_i = \tilde{n}_i - n_i$ . Again, when deriving the expectation value and variance of  $S$  we require the first four momenta of  $\hat{n}$ :

$$\langle \hat{n}_i \rangle = \langle \tilde{n}_i - n_i \rangle = 0 \quad (5.18)$$

$$\langle \hat{n}_i^2 \rangle = \langle (\tilde{n}_i - n_i)^2 \rangle = n_i \quad (5.19)$$

$$\langle \hat{n}_i^3 \rangle = \langle (\tilde{n}_i - n_i)^3 \rangle = -n_i \quad (5.20)$$

$$\langle \hat{n}_i^4 \rangle = \langle (\tilde{n}_i - n_i)^4 \rangle = n_i + 3n_i^2. \quad (5.21)$$

<sup>7</sup>In a flat image where  $n_i$  is either a constant value or zero  $B$  corresponds to the number of illuminated pixels. In typical imaging conditions most of the light is distributed over a small number of pixels compared to the overall number of pixels in an image. Hence  $B$  can be understood as the number of pixels with large photon numbers.

Using this momenta the expectation value of  $S$  can be written as

$$\begin{aligned}
 \langle S \rangle &= \frac{1}{N^2} \left\langle \sum_{i=1}^P (n_i + \hat{n}_i - m_i)^2 \right\rangle \\
 &= \frac{1}{N^2} \sum_{i=1}^P (n_i^2 + \langle \hat{n}_i^2 \rangle + m_i^2 + 2n_i \langle \hat{n}_i \rangle - 2n_i m_i - 2 \langle \hat{n}_i \rangle m_i) \\
 &= \frac{1}{N^2} \left( N + \sum_{i=1}^P (n_i - m_i)^2 \right). \tag{5.22}
 \end{aligned}$$

The sum  $\sum (n_i - m_i)^2 / N^2$  can be identified as the function  $S_0$  (5.2) comparing the two noiseless images  $n$  and  $m$ . It is the comparison of the noise free part of  $\tilde{n}$  with the test image  $m$ . Consequently, the expectation value

$$\langle S \rangle = \frac{1}{N} + S_0 = \langle S_{\text{id}} \rangle + S_0, \tag{5.23}$$

is given by the sum of the expectation value of  $S_{\text{id}}$ , which represents the comparison of the noisy image  $\tilde{n}$  with the image  $n$  of the corresponding theoretical PSF, and the value  $S_0$ . This means that including photon shot noise into the imaging process adds an offset  $1/N$  to the average outcome of the function  $S_0$ .

To derive the variance of  $S$  we first start with the evaluation of  $\langle S^2 \rangle$ :

$$\begin{aligned}
 \langle S^2 \rangle &= \left\langle \left( \frac{1}{N^2} \sum_{i=1}^P (n_i + \hat{n}_i - m_i)^2 \right)^2 \right\rangle \\
 &= \frac{1}{N^4} \left\langle \sum_{i=1}^P (n_i + \hat{n}_i - m_i)^4 \right\rangle + \frac{1}{N^4} \left\langle \sum_{i \neq j}^P (n_i + \hat{n}_i - m_i)^2 (n_j + \hat{n}_j - m_j)^2 \right\rangle. \tag{5.24}
 \end{aligned}$$

Using  $(n_i - m_i)/N = \sqrt{(S_0)_i}$ <sup>8</sup> the first part of expression 5.24 can be written as

$$\left\langle \sum_{i=1}^P (\sqrt{(S_0)_i} N + \hat{n}_i)^4 \right\rangle = N + \sum_{i=1}^P \left( 3n_i^2 - 4n_i \sqrt{(S_0)_i} N + 6n(S_0)_i N^2 + (S_0)_i^2 N^4 \right), \tag{5.25}$$

while the second part of expression 5.24, assuming again that the noise measured at pixel  $i$  and

---

<sup>8</sup> $(S_0)_i = (n_i - m_i)^2$

$j$  is not correlated, can be written as

$$\begin{aligned}
 & \sum_{i \neq j}^P (n_i + N^2(S_0)_i) (n_j + N^2(S_0)_j) \\
 &= (N + N^2 S_0)^2 - \sum_i^P (n_i^2 + 2n_i(S_0)_i + (S_0)_i^2) \\
 &= N^4 \langle S \rangle^2 - \sum_i^P (n_i^2 + 2n_i(S_0)_i + (S_0)_i^2). \tag{5.26}
 \end{aligned}$$

Therefore we can now derive the variance of  $S$  to

$$\begin{aligned}
 \text{Var}(S) &= \langle S^2 \rangle - \langle S \rangle^2 \\
 &= \frac{1}{N^4} \left( N + \sum_i^P (2n_i^2 + 4n_i(S_0)_i N^2 - 4n_i \sqrt{(S_0)_i} N) \right) \\
 &= \text{Var}(S_n) + 4 \sum_i^P \left( \frac{1}{N^2} n_i(S_0)_i - \frac{1}{N^3} n_i \sqrt{(S_0)_i} \right). \tag{5.27}
 \end{aligned}$$

For  $m = n$  the expectation value and variance of  $S$  reduces to the values  $\langle S(\tilde{n}, n) \rangle = \langle S_{\text{id}} \rangle$  and  $\text{Var}(S(\tilde{n}, n)) = \text{Var}(S_{\text{id}})$ . In the following we make the assumption, that the overall number of collected photons is much larger than the number of bright pixels  $B \ll N$ , and, that the number of bright pixels is much smaller than the number of pixels  $P \gg B$ . This assumptions agree with common experimental results in microscopy imaging. Using

$$\sum_{i=1}^P \sqrt{(S_0)_i} \geq \sqrt{\sum_{i=1}^P (S_0)_i} \tag{5.28}$$

we can now make a upper estimation for the variance of  $S$ :

$$\begin{aligned}
 \text{Var}(S) &\lesssim \frac{1}{N^3} + \frac{2}{N^2 B} + 4 \sum_{i=1}^P \left( \frac{N S_0}{N^2 B} - \frac{N \sqrt{S_0}}{N^3 B} \right) \\
 &= \frac{1}{N^3} + \frac{2}{N^2 B} + 4 \left( \frac{S_0}{N} - \frac{\sqrt{S_0}}{N^2} \right). \tag{5.29}
 \end{aligned}$$

For  $N \gg B$ , the term  $1/N^3$  can be neglected. We can rewrite  $\sqrt{S_0} = \sqrt{a} \delta x$  for  $\delta x \ll 1$ . Assuming  $\delta x$  is in the nanometer regime the term  $\sqrt{S_0}/N^2$  can be neglected with respect to  $2/(N^2 B)$ . With this assumptions the variance of  $S$  is given by

$$\text{Var}(S) = \frac{2}{N^2 B} + 4 \frac{S_0}{N}. \tag{5.30}$$

### 5.1.3 The precision limit

We now want to establish a precision limit *i.e.* the expected position uncertainty in a position measurement for a given photon number  $N$ . To define the precision limit we use the expectation value and the variance of the comparing functions  $S$  and  $S_{\text{id}}$ . The function  $S_{\text{id}}$  compares a noisy image  $\tilde{n}$  with an image  $n$  of the corresponding theoretical PSF, while  $S$  compares the experimental image  $\tilde{n}$  with the image  $m$  of a theoretical PSF. In Figure 5.3 the expectation value  $\langle S(\tilde{n}, m(\delta x, \epsilon)) \rangle$  is plotted (solid curves) as a function of  $\delta x$  for  $\epsilon = 0$  (subfigure a) and  $\epsilon_{\delta x} = -\delta x 2\pi/\lambda$  (subfigure b). At  $\delta x = 0$  the expectation values in this plots are given by  $\langle S_{\text{id}} \rangle = 1/N$ . In addition to the expectation value the standard deviation  $\sigma_S = \sqrt{\text{Var}(S)}$  is shown in both subfigures. In particular the borders of the one  $\sigma_S$  interval  $[\langle S \rangle - \sigma_S, \langle S \rangle + \sigma_S]$  are plotted (dashed lines) as a function of  $\delta x$ . These plots were generated using the approximations 5.3 and 5.4 of  $S_0$  with  $a = 0.033$  and  $b = 0.009$ . These values were obtained from fits to  $S_0$  using images with a number of bright pixels  $B \in [6, 16]$  and an overall number of pixels per image of  $P = 121$ . The used number of photons was  $N = 10^6$ . This parameters suit the assumptions made to obtain the variance of  $S$  as given in 5.30 where it was assumed that  $N \gg B$  and  $B \ll P$ .

We now define the precision limit  $Dx$  as the position at which

$$\langle S(Dx) \rangle - \sigma_S(Dx) = \langle S_{\text{id}} \rangle + \sigma_{S_{\text{id}}}. \quad (5.31)$$

The precision limit  $Dx$  corresponds to the real displacement for which the value of the lower boarder of the one  $\sigma_S$  interval rises above the value of the upper boarder of the one  $\sigma_{S_{\text{id}}}$  interval. This intersections of  $\langle S \rangle - \sigma_S$  with  $\langle S_{\text{id}} \rangle + \sigma_{S_{\text{id}}}$  are highlighted in Figure 5.3 as red circles. The precision limit shown in subfigure a, which corresponds to the case that we have prior knowledge, that the imaged emitter is in the polarization state  $\epsilon = 0$ , is about one order of magnitude smaller than the precision limit in subfigure b. There the situation corresponds to the case were we have no prior knowledge of the polarization state of the emitter.<sup>9</sup>

From

$$\langle S(Dx) \rangle - \sigma_S(Dx) = \langle S_{\text{id}} \rangle + \sigma_{S_{\text{id}}} \quad (5.32)$$

$$\frac{1}{N} + S_0(Dx) - \sqrt{\frac{2}{N^2 B} + 4 \frac{S_0}{N}} = \frac{1}{N} + \sqrt{\frac{2}{N^2 B}}, \quad (5.33)$$

we can derive analytic expressions for  $Dx$  for the case that the polarization state of the imaged emitter is known

$$Dx^{\text{np}} = \left( \frac{2 \left( 2 + \sqrt{\frac{2}{B(\epsilon)}} \right)}{a(\epsilon) N} \right)^{\frac{1}{2}} \quad (5.34)$$

<sup>9</sup>At this point one might ask why one should use the PSF of an emitter in polarization state  $\epsilon = 0$  to fit the position of an emitter of unknown polarization. This is a suitable choice assuming the imaged emitters are only slightly elliptically polarized ( $\epsilon \ll 1$ ). For different imaging scenarios one could adapt the definition of the precision limit or extend the derivation of the precision limit to even more general cases.

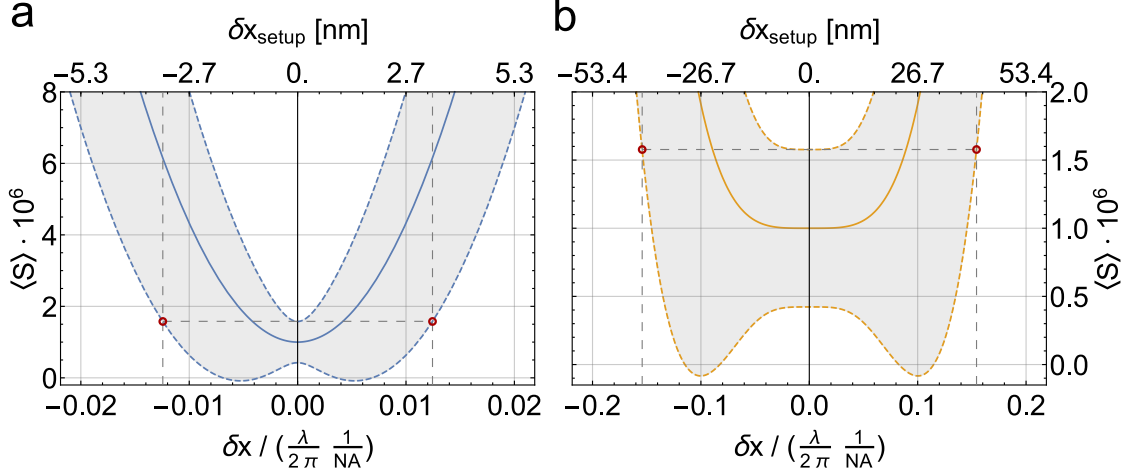


**Figure 5.3: Definition of the precision limit.** **a**, The expectation value  $\langle S(\tilde{n}, m(\delta x, \epsilon = 0)) \rangle$  plotted as solid line versus the real displacement  $\delta x$  normalized on the wavelength  $\lambda$  and the numerical aperture NA. This corresponds to the case where the imaged emitter is linearly polarized orthogonal to the optical axis. The dashed blue lines indicate the boarder of the one  $\sigma_S$  interval  $[\langle S \rangle - \sigma_S, \langle S \rangle + \sigma_S]$  (grey area). The precision limit (red dots) is defined as the  $\delta x$  for which the lower boarder of the one sigma interval around  $S$  rises above the upper boarder of the one sigma interval at  $\delta x = 0$ , which is indicated by the grey dashed horizontal lines. The photon number  $N$  of the images used to create this plot is  $10^6$ . The upper  $x$ -axis corresponds to  $\delta x$  for the experimental setup presented in chapter 4, with  $\lambda = 470\text{nm}$  and  $NA = 0.28$  **b**, The same plot for the expectation value  $\langle S(\tilde{n}^k, m(\delta x, \epsilon_{\delta x} = -\delta x \cdot 2\pi/\lambda)) \rangle$ . This corresponds to the case where we assume to have no prior knowledge of the emitters polarization. The corresponding precision limit is about one order of magnitude larger than the one for a solely linearly polarized dipole.

using the approximation  $S_0(\delta x) = a(\epsilon) \delta x^2$  for  $\delta x \ll 1$  and for the case of an emitter with unknown polarization state

$$Dx^{\text{up}} = \left( \frac{2 \left( 2 + \sqrt{\frac{2}{B}} \right)}{b N} \right)^{\frac{1}{4}} \quad (5.35)$$

using  $S_0(\delta x) = b \delta x^4$ .<sup>10</sup> When evaluating the precision limit  $Dx^{\text{up}}(\epsilon)$  for different values of  $a(\epsilon)$  and  $B(\epsilon)$  one finds that the smallest precision limit appears when imaging an emitter which is circularly polarized ( $\epsilon = \pm 1$ ). This precision limit is about 5% smaller than the one in the imaging process of linearly polarized emitters, which is a very interesting finding. However, since the difference is so small and it is more common to assume linearly polarized emitters in high resolution imaging we restrict the discussion in the following to  $Dx^{\text{up}}(\epsilon = 0)$

<sup>10</sup>Note that  $a$  has the unit length squared and  $b$  length to fourth power.

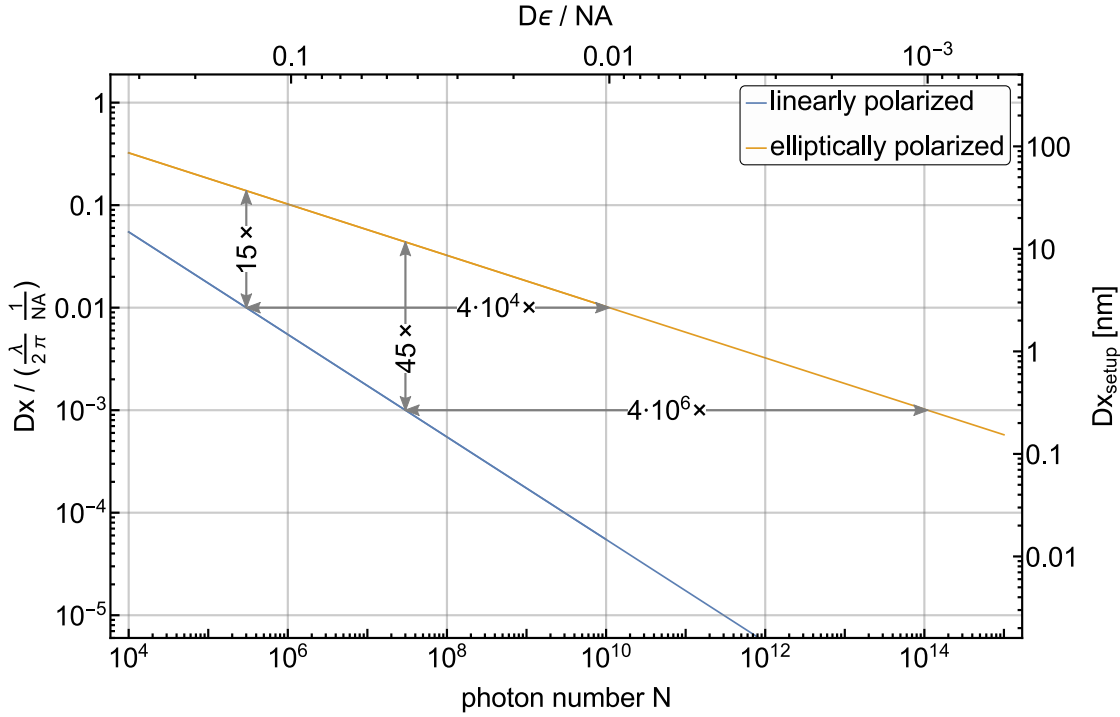


**Figure 5.4: Precision limit.** The precision limits  $Dx^{\text{np}}(\epsilon = 0)$  and  $Dx^{\text{up}}$  for position measurements resulting from photon shot noise plotted as a function of the total photon number  $N$ . The left  $y$ -axis corresponds to  $Dx$  normalized to the wavelength  $\lambda$  emitted by the imaged dipole and the numerical aperture NA of the imaging system. The right  $y$ -axis corresponds to  $Dx$  for the experimental setup presented in chapter 4, with  $\lambda = 470\text{nm}$  and  $\text{NA} = 0.28$ . The upper  $x$ -axis corresponds to the polarization uncertainty  $D\epsilon$  normalized by the NA, which needs to be present in order to cause the apparent displacement which leads in turn to the precision decrease. It can also be understood as the necessary elliptical polarizability of the imaged emitters, which they need to feature in order to cause the corresponding apparent shift. The precision increases much faster with respect to  $N$  for a linearly polarized emitter than it does for one with unknown polarization. Therefore the latter requires orders of magnitude larger photon numbers, *i.e.* exposure time to gain the same precision, which is indicated by the horizontal dashed lines. The decrease in precision between the case of a linearly polarized dipole and the case of a dipole of unknown polarization is indicated with the vertical dashed lines for two photon numbers.

The precision limits  $Dx^{\text{np}}(\epsilon = 0)$  and  $Dx^{\text{up}}$  are plotted in Figure 5.4 as a function of the photon number  $N$ . Over the whole range of the plot the precision limit for the imaging process where the polarization of the emitter is unknown is approximately one to three orders of magnitude larger than for the case where the polarization state of the imaged emitter is known. It is still possible to gain the same precision when imaging an emitter of unknown polarization state by increasing the photon integration time in the imaging process. However it requires within the data shown in the plot at least two orders of magnitude longer integration time.

For instance when imaging an emitter with  $\text{NA} = 1$  at a wavelength of about 628 nm the precision given by  $Dx^{\text{np}}(\epsilon = 0)$  is 1 nm for a total photon number  $N = 10^6$ . For the same parameters  $Dx^{\text{up}}$  gives a precision of approximately 15 nm. To gain the same precision as in the case of the emitter with known polarization state the overall number of measured photons needs to be increased by a factor  $4 \cdot 10^4$ , which directly links to the measurement time. Alternatively one needs to know the polarization uncertainty better than  $D\epsilon = 0.01$  which corresponds to an polarization overlap with linear polarization better than  $\eta = 1/(1 + D\epsilon^2) = 99.99\%$ . The polarization overlap  $\eta$  is determined via

$$\eta = \left| E_{D^x} \cdot \frac{1}{\sqrt{1 + \epsilon^2}} (E_{D^x} + i \cdot \epsilon \cdot E_{D^y}) \right|^2 = \frac{1}{1 + \epsilon^2}. \quad (5.36)$$

Summing up, this section shows that even in perfect imaging systems, which only feature photon shot noise as an error source, the uncertainty of the outcome of a position measurement is strongly dependent on the presence of longitudinal field components (with respect to the optical axis) in the light field emitted by the imaged emitter. With the presented estimation of the precision limit it can be seen that for similar experimental situations the position error is orders of magnitude smaller for the case where the polarization state of the emitter is known with respect the case where it is not. This is a very important finding. To compensate for this effect one has either to increase the measurement time by several orders of magnitude in combination with the use of a more complex fitting algorithm or obtain very precise knowledge of the polarization state of the imaged emitters. In appendix A.12 the possible presence of local elliptically polarization of the illuminating light in microscopy setups is briefly discussed. While the presented method to compare two images might considered to be not optimal it is commonly used. More sophisticated algorithms should on one hand provide in general a higher precision, but we expect them to show a similar discrepancy for the two cases of known and unknown polarization of the emitter. The derivation of the precision limit can be easily generalized to two dimensions, which will lead to similar findings.

## 5.2 Optimal pixel size

As mentioned in the beginning of this chapter, the achievable precision in a given imaging setup is dependent on the pixel size  $PS$ . In general there exists an optimal pixel size which provides the highest precision in position measurements, depending on the imaging setup, imaged emitter and localization method. Related results can be found in [130] and [66]. In particular the pixel size depends on the PSF of the used imaging system.<sup>11</sup> We focus on the case of an emitter which is linearly polarized along an axis orthogonal to the optical axis ( $\epsilon = 0$ ). The intensity distribution of such an emitter in the image plane is rotationally symmetric. A suitable quantity

<sup>11</sup>We assume in the following that the emitter is smaller than the diffraction limit.

to describe such a PSF is the full width half maximum  $FWHM$  approximately given by<sup>12</sup>

$$FWHM = 3.23 \cdot \lambda / (2\pi) \cdot M/NA. \quad (5.37)$$

In the following we study the precision limits given in the previous section with respect to ratio  $PS/FWHM$ .

We do this with the same assumptions concerning the imaged emitters and the imaging process as in section 5.1. The precision limits presented in equation 5.34 and 5.35 are dependent on the overall number of photons  $N$ , the number of bright pixels  $B$  in the image's PSF and on the values  $a(\epsilon = 0)$  and  $b$  from the approximations 5.3 and 5.4. The values  $B$ ,  $a$  and  $b$  are dependent on the ratio  $PS/FWHM$ . Figure 5.5a shows how  $a$  and  $b$  change with  $PS/FWHM$ . They do not reach their maximum at the same pixel size. This means that the optimal pixel size to gain the smallest precision limit is for linearly polarized emitters different than for the measurement of the position of an emitter with unknown polarization. The evolution of  $B$  with respect to  $PS/FWHM$  is shown in Figure 5.5b. For  $PS/FWHM < 1$  it is proportional to  $1/PS^2$  since the area in the image plane, which exhibits large intensities is constant. This area is given by  $B \cdot PS^2$ .

The resulting consequence for the precision limits is shown in Figure 5.5c, where  $Dx^{np}(\epsilon = 0)$  and  $Dx^{up}$  are plotted in blue and yellow as a function of  $PS/FWHM$ . This is done using the numerical obtained values of  $a$ ,  $b$  and  $B$ . For a linearly polarized emitter ( $\epsilon = 0$ ) the highest precision can be reached for  $PS/FWHM \approx 0.7$ , which means that the  $FWHM$  is about 1.4 pixels wide. In the case of an emitter with unknown polarization state the highest precision is reached for  $PS/FWHM \approx 1.2$ , but the precision limit changes only slowly near its minima. When imaging emitters of unknown polarization state with the optimal pixel size for linearly polarized ones the precision is only decreased by about 15%.

This study shows that it is useful and necessary to adapt in digital imaging the CCD screen to the PSF of the imaging system when doing high precision position measurements. While it is quite intuitive that large pixel sizes limit the accuracy of position measurements, since in the limiting case all light is measured at only one pixel, the fact that to small pixel sizes decrease the precision limit might not be commonly known.

---

<sup>12</sup>Note that this  $FWHM$  can not be perfectly converted to the waist of the measured images in chapter 3 and 4 since the waist there was measured using a Gaussian fit. The PSFs studied in this chapter can not be perfectly approximated by a two dimensional Gaussian function. Therefore there is a small difference between the  $FWHM$  of a Gaussian and the  $FWHM$  given here.

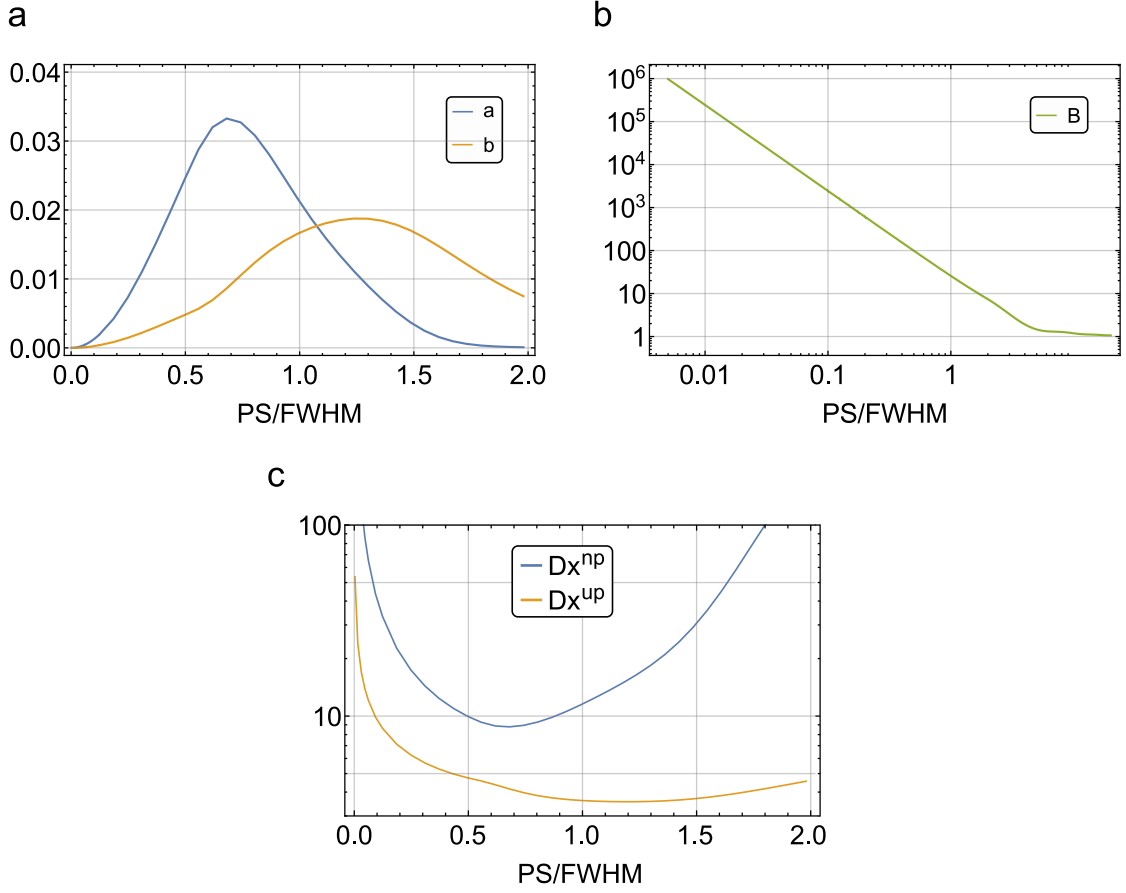


**Figure 5.5: Optimal pixel size.** **a**, The fit parameters  $a$  and  $b$  obtained by fitting the approximations 5.3 and 5.4 to the data given by the comparing function  $S_0$ . They are plotted versus the ratio  $PS/FWHM$ . **b**, The number of bright pixels  $B$ , as defined in 5.15 plotted versus  $PS/FWHM$ . For  $PS/FWHM < 1$  it is proportional to  $1/PS^2$  since the area featuring the highest intensities in the image is constant and is given by  $B \cdot PS^2$ . For  $PS/FWHM > 1$  it approaches 1. For large pixel sizes the strongly illuminated area in the image plane is then covered by one pixel only. **c**, The precision limits  $Dx^{np}(\epsilon = 0)$  (blue) and  $Dx^{up}$  (yellow) plotted versus the ratio  $PS/FWHM$ . The plot shows that the ratio  $PS/FWHM \approx 0.7$  provides the highest precision when determining the position of a linearly polarized dipole. In contrast the highest precision for an emitter of unknown polarization state is reached for  $PS/FWHM \approx 1.2$ . When imaging emitters of unknown polarization with the optimal pixel size for linearly polarized ones the precision is only decreased by about 15%. The two precision limits are normalized by  $Dx^{np}/(\sqrt{2/N}\lambda/(2\pi NA))$  and  $Dx^{up}/(\sqrt[4]{2/N}\lambda/(2\pi NA))$ .

# Summary and Outlook

## 6.1 Summary

In this thesis I investigated spin-orbit interaction of light in a free-space setting and showed that it can cause in an optical imaging process a displacement of the emitter's image. This in return leads to the assumption that the emitter is at a position where it is actually not. The resulting apparent displacement is determined by the presence of linear transverse momentum from which an analytic expression for the apparent displacement can be derived. Studying the displacement as a function of the polarization of the imaged emitter reveals that in the case of small numerical aperture of the imaging system, a circularly polarized emitter appears to be displaced by  $\lambda/(2\pi)$ . Compared to the current commonly reached precisions in position measurements in super-resolution microscopy this is already a large deviation from the actual position. Furthermore, it is possible to enhance the apparent displacement to exceed the optical wavelength by preparing the imaged emitter in a highly elliptical polarization state. For vanishing aperture it can even be arbitrarily large. A major finding of this theoretical study is that even in a perfectly focussed aberration free imaging system the centroid of the image of a nanoscale emitter does in general not correspond to the emitters position.

The apparent displacement of a single gold nanoparticle was measured in two related but different experimental setups. In both experiments good agreement with the theoretical predictions was observed and an overall displacement of about one optical wavelength measured, which exceeds four times the particle's diameter. The particle was clearly seen at a position where it was in fact not.

Since the apparent displacement is usually in the order of the optical wavelength I also studied its possible effect on the signal to noise limited position accuracies in super-resolution microscopy. I defined precision limits for the two situations with and without prior knowledge of the imaged emitter's polarization. Considering only fundamental photon shot noise the position of an emitter of known polarization can be determined orders of magnitude more precise than for an emitter of unknown polarization. One can compensate for this effect by extending the photon

integration time in the imaging process. However, the exposure time needs to be increased by several orders of magnitude which can be challenging in an realistic imaging process.

## 6.2 Outlook

The presented apparent displacement introduces a new source of possible errors in super-resolution microscopy, which pushed optical imaging to the nanoscale [52]. While some of the used novel methods can in principle not be subject to the apparent displacement presented in this work, like STED [62], other methods could possibly be exposed to this systematic error which can exceed the established accuracies by up to two orders of magnitude [52,53]. The majority of the emitters used in super-resolution microscopy are fluorescent molecules which are considered to strictly feature linearly polarized transitions [138] and should therefore only emit light which does not feature orbital angular momentum. But being immersed in a gaseous, liquid, or solid medium causes temperature- and/or strain-induced vibrations or static distortions which possibly lead to spectral overlap of transitions of different polarizations. In such an environment the considered strictly linear polarizability should be critically challenged. So far it was not possible to find any detailed studies on the polarizability properties of these commonly used emitters. With the publication of the effects presented in this thesis in [139] we hope to encourage corresponding investigations. In order that any finite elliptical polarizability of fluorescent molecules can lead to errors in position measurements the presence of elliptical polarization at the position of the molecule is necessary. Spurious reflection in or near an imaged sample can easily result in local elliptically polarizations and are in general difficult to be absolutely suppressed.

Since the apparent displacement can occur for any kind of wave carrying orbital angular momentum it is relevant beyond optical imaging. The fact that the apparent displacement can get arbitrary large for vanishing NA is not of importance for super-resolution microscopy, since there the low NA regime is not of interest. But it should be kept in mind for other localization techniques like radar [140–142] or sonar imaging [143,144]. It could even influence the apparent position of astronomical objects which are detected through their emission of gravitational waves [145,146].

Certainly, the polarization dependent shift of an emitters image can be used for new applications. As for example it offers useful implementations in arrays of particles, like for instance optically trapped particle arrays [147]. There it could be applied to measure the local polarization of illuminating light at the position of the particles using their apparent displacement, assuming their real positions are precisely determined. With such a setup a polarization probe could be realized. The other way around, when illuminating such a particle array with light of precisely known polarization, apparent shifts in an image would provide insight to local physical parameters which affect the polarizability or the apparent displacement of the particles. The apparent displacement measured in an image of a nano-structure smaller than the diffraction limit as a function of the polarization and wavelength of the illuminating light could reveal important information of the spatial orientation of the nano-structure. With this method one could determine the orientation of nanorods. Furthermore, this method could be used to measure defects or irregularities in the structure.

## Appendix

### A.1 Induced resonant dipole as momentum probe

In this section we will shortly discuss what kind of particle is a suitable probe to sense the momentum of light fields. To check if an emitter is a useful momentum probe we investigate its behavior in the simplest electromagnetic field, a plane wave. In a plane wave the propagation direction is obvious and at every point the same. Consequently, a test emitter onto which only momentum is transferred from the wave needs to move in propagation that direction.

In the simplest approach one could think of a single charged particle, which we assume to be much smaller than the wavelength of the plane wave. This particle needs to be considered locked in place, otherwise it can not probe the mean local momentum transfer averaged over one oscillation period of the field. The force acting on this particle vanishes when averaging over one oscillation period of the light field, meaning it does not gain any momentum by the field. Consequently it can not be used as a momentum probe.

The next logical approach would be to think of a dipolar particle of which the overall charge is zero. Such a particle can be realized by a static or permanent dipole or by an induced dipole. A static dipole can be considered as the extreme case of a far detuned induced dipole, which feels a force parallel or anti-parallel to the field gradient. This force is called the gradient force [71, 72], which is used for instance in optical tweezers. An induced dipole which is resonant to the exciting light field however does not feel this gradient force and is only subject to the radiation pressure [70]. Therefore it is the proper choice as a momentum probe in a light field.

### A.2 Momentum density of light fields - details

This section provides several details and mathematical proofs which were used in section 2.1.1 to determine the momentum density of light fields.

### A.2.1 Center of mass and relative coordinates

The positions  $\mathbf{r}_\pm$  of two charges  $\pm Q$  with the masses  $m_\pm$  can be expressed using the centre of mass coordinate

$$\mathbf{R} = \frac{m_+}{m} \mathbf{r}_+ + \frac{m_-}{m} \mathbf{r}_- \quad (\text{A.1})$$

and the relative coordinate

$$\mathbf{r}_d = \mathbf{r}_+ - \mathbf{r}_-, \quad (\text{A.2})$$

where  $m = m_+ + m_-$  denotes the overall mass of the dipole. Using this coordinates the positions of the charges can be written as

$$\begin{aligned} \mathbf{r}_\pm &= \frac{m_+ + m_-}{m_+ + m_-} \mathbf{r}_\pm = \frac{m_+}{m} \mathbf{r}_\pm + \frac{m_-}{m} \mathbf{r}_\pm + \frac{m_\mp}{m} \mathbf{r}_\mp - \frac{m_\mp}{m} \mathbf{r}_\mp = \\ &= \left( \frac{m_\pm}{m} \mathbf{r}_\pm + \frac{m_\mp}{m} \mathbf{r}_\mp \right) + \frac{m_\mp}{m} (\mathbf{r}_\pm - \mathbf{r}_\mp) = \\ &= \mathbf{R} \pm \frac{m_\pm}{m} \mathbf{r}_d. \end{aligned} \quad (\text{A.3})$$

### A.2.2 Vector identities I

The Jacobi matrix  $J_f$  of a vector valued function  $\mathbf{f} : \mathbb{R}^3 \rightarrow \mathbb{R}^3$  is given by

$$J_f(\mathbf{r}_0) = \left( \vec{\nabla} \otimes \mathbf{f} \right)^T (\mathbf{r}_0) = \begin{pmatrix} \frac{\partial f_x}{\partial x}(\mathbf{r}_0) & \frac{\partial f_x}{\partial y}(\mathbf{r}_0) & \frac{\partial f_x}{\partial z}(\mathbf{r}_0) \\ \frac{\partial f_y}{\partial x}(\mathbf{r}_0) & \frac{\partial f_y}{\partial y}(\mathbf{r}_0) & \frac{\partial f_y}{\partial z}(\mathbf{r}_0) \\ \frac{\partial f_z}{\partial x}(\mathbf{r}_0) & \frac{\partial f_z}{\partial y}(\mathbf{r}_0) & \frac{\partial f_z}{\partial z}(\mathbf{r}_0) \end{pmatrix}, \quad (\text{A.4})$$

where  $\otimes$  denotes the outer product [69] and  $\mathbf{f}^T$  is the transpose of  $\mathbf{f}$ . The expression  $J_f(\mathbf{r}_0)\mathbf{r}$  can be rewritten as

$$\begin{aligned} J_f(\mathbf{r}_0)\mathbf{r} &= \begin{pmatrix} \frac{\partial f_x}{\partial x}(\mathbf{r}_0) & \frac{\partial f_x}{\partial y}(\mathbf{r}_0) & \frac{\partial f_x}{\partial z}(\mathbf{r}_0) \\ \frac{\partial f_y}{\partial x}(\mathbf{r}_0) & \frac{\partial f_y}{\partial y}(\mathbf{r}_0) & \frac{\partial f_y}{\partial z}(\mathbf{r}_0) \\ \frac{\partial f_z}{\partial x}(\mathbf{r}_0) & \frac{\partial f_z}{\partial y}(\mathbf{r}_0) & \frac{\partial f_z}{\partial z}(\mathbf{r}_0) \end{pmatrix} \begin{pmatrix} r_x \\ r_y \\ r_z \end{pmatrix} = \\ &= \begin{pmatrix} r_x \frac{\partial f_x}{\partial x}(\mathbf{r}_0) + r_y \frac{\partial f_x}{\partial y}(\mathbf{r}_0) + r_z \frac{\partial f_x}{\partial z}(\mathbf{r}_0) \\ r_x \frac{\partial f_y}{\partial x}(\mathbf{r}_0) + r_y \frac{\partial f_y}{\partial y}(\mathbf{r}_0) + r_z \frac{\partial f_y}{\partial z}(\mathbf{r}_0) \\ r_x \frac{\partial f_z}{\partial x}(\mathbf{r}_0) + r_y \frac{\partial f_z}{\partial y}(\mathbf{r}_0) + r_z \frac{\partial f_z}{\partial z}(\mathbf{r}_0) \end{pmatrix} = \\ &= \left( r_x \frac{\partial}{\partial x} + r_y \frac{\partial}{\partial y} + r_z \frac{\partial}{\partial z} \right) \begin{pmatrix} f_x(\mathbf{r}_0) \\ f_y(\mathbf{r}_0) \\ f_z(\mathbf{r}_0) \end{pmatrix} = \left( \mathbf{r} \cdot \vec{\nabla} \right) \mathbf{f}(\mathbf{r}_0) \end{aligned} \quad (\text{A.5})$$

### A.2.3 Momentum absorbed by a dipole

In this section the derivation of the momentum  $\mathbf{P}$  absorbed by a resonant Lorentz oscillator from a light field is performed in detail. We assume the center of mass of the dipole to be spatially

fixed at the position  $\mathbf{R}$ . The light field is described by the monochromatic electric and magnetic fields

$$\begin{aligned}\mathcal{E}(\mathbf{r}, t) &= \frac{1}{2} (\mathbf{E}(\mathbf{r}, t) + \mathbf{E}^*(\mathbf{r}, t)) = \frac{1}{2} (\mathbf{E}_0(\mathbf{r}) e^{-i\omega t} + \mathbf{E}_0^*(\mathbf{r}) e^{i\omega t}), \\ \mathcal{B}(\mathbf{r}, t) &= \frac{1}{2} (\mathbf{B}(\mathbf{r}, t) + \mathbf{B}^*(\mathbf{r}, t)) = \frac{1}{2} (\mathbf{B}_0(\mathbf{r}) e^{-i\omega t} + \mathbf{B}_0^*(\mathbf{r}) e^{i\omega t}),\end{aligned}\quad (\text{A.6})$$

where  $\mathbf{E}^*$  is the complex conjugate of  $\mathbf{E}$ . The momentum is derived via the integral of the overall force  $\mathbf{F}_0$  (see 2.15), acting on the dipole, over one oscillation period of the light field<sup>1</sup>,

$$\begin{aligned}\mathbf{P}(\mathbf{R}) &= \int_0^{\frac{2\pi}{\omega}} \left[ \left( \bar{\boldsymbol{\mu}}_{\text{L}} \cdot \vec{\nabla} \right) \mathcal{E}(\mathbf{R}, t) + \dot{\boldsymbol{\mu}}_{\text{L}} \times \mathcal{B}(\mathbf{R}, t) \right. \\ &\quad \left. + \dot{\boldsymbol{\mu}}_{\text{L}} \times \left( \left( \bar{\boldsymbol{\mu}}_{\text{L}} \cdot \vec{\nabla} \right) \mathcal{B}(\mathbf{R}, t) \right) \frac{m_-^2 - m_+^2}{Qm^2} \right] dt,\end{aligned}\quad (\text{A.7})$$

where the dipole moment of the resonant Lorentz oscillator is given by [68]

$$\bar{\boldsymbol{\mu}}_{\text{L}} = \frac{i}{2} \text{Im}(\alpha) (\mathbf{E} - \mathbf{E}^*). \quad (\text{A.8})$$

In order to solve this integral we treat the first two terms separately from the third. To integrate the first two terms we make use of the following identity:  $z - z^* = (a + ib) - (a - ib) = 2ib = 2i \text{Im}(z)$ , with  $z \in \mathbb{C}$  and  $a, b \in \mathbb{R}$ . Further more we make use of the Maxwell–Faraday equation

$$\vec{\nabla} \times \mathcal{E} = -\frac{\partial}{\partial t} \mathcal{B}, \quad (\text{A.9})$$

which we decompose to

$$\vec{\nabla} \times \mathcal{E} = (\vec{\nabla} \times \mathbf{E}) + (\vec{\nabla} \times \mathbf{E}^*) = (\vec{\nabla} \times \mathbf{E}_0) e^{-i\omega t} + (\vec{\nabla} \times \mathbf{E}_0^*) e^{i\omega t} \quad (\text{A.10})$$

and

$$-\frac{\partial}{\partial t} \mathcal{B} = -\frac{\partial}{\partial t} (\mathbf{B}_0 e^{-i\omega t} + \mathbf{B}_0^* e^{i\omega t}) = i\omega (\mathbf{B}_0 e^{-i\omega t} - \mathbf{B}_0^* e^{i\omega t}) = i\omega (\mathbf{B} - \mathbf{B}^*). \quad (\text{A.11})$$

Identifying the terms with the same oscillation behaviour leads to

$$\vec{\nabla} \times \mathbf{E} = i\omega \mathbf{B}, \quad (\text{A.12})$$

$$\vec{\nabla} \times \mathbf{E}^* = -i\omega \mathbf{B}^*. \quad (\text{A.13})$$

---

<sup>1</sup>Note that  $\mathbf{P}$  is a function of the position  $\mathbf{R}$  and  $\bar{\boldsymbol{\mu}}_{\text{L}}$  is a function of the position  $\mathbf{R}$  and time  $t$ . These dependencies are not always mentioned in the following in order to increase the readability. The same applies to the different components of the electrical and magnetic field.

Now we perform the integral of the first two terms of A.7:

$$\begin{aligned}
& \int_0^{\frac{2\pi}{\omega}} \left[ \left( \vec{\mu}_L \cdot \vec{\nabla} \right) \mathcal{E}(\mathbf{R}, t) + \dot{\vec{\mu}}_L \times \mathcal{B}(\mathbf{R}, t) \right] dt = \tag{A.14} \\
&= \frac{i}{4} \text{Im}(\alpha) \int_0^{\frac{2\pi}{\omega}} \left[ \left( (\mathbf{E} - \mathbf{E}^*) \cdot \vec{\nabla} \right) (\mathbf{E} + \mathbf{E}^*) + (\dot{\mathbf{E}} - \dot{\mathbf{E}}^*) \times (\mathbf{B} + \mathbf{B}^*) \right] dt = \\
&= \frac{i}{4} \text{Im}(\alpha) \int_0^{\frac{2\pi}{\omega}} \left[ (\mathbf{E} \cdot \vec{\nabla}) \mathbf{E} - (\mathbf{E}^* \cdot \vec{\nabla}) \mathbf{E}^* + (\mathbf{E} \cdot \vec{\nabla}) \mathbf{E}^* - (\mathbf{E}^* \cdot \vec{\nabla}) \mathbf{E} + \right. \\
&\quad \left. + \left( -i\omega (\mathbf{E} + \mathbf{E}^*) \times \left( -\frac{i}{\omega} \vec{\nabla} \times \mathbf{E} + \frac{i}{\omega} \vec{\nabla} \times \mathbf{E}^* \right) \right) \right] dt = \\
&= \frac{i}{4} \text{Im}(\alpha) \underbrace{\int_0^{\frac{2\pi}{\omega}} e^{-2i\omega t} dt}_{=0} \left[ (\mathbf{E}_0 \cdot \vec{\nabla}) \mathbf{E}_0 - \mathbf{E}_0 \times (\vec{\nabla} \times \mathbf{E}_0) \right] - \\
&- \frac{i}{4} \text{Im}(\alpha) \underbrace{\int_0^{\frac{2\pi}{\omega}} e^{+2i\omega t} dt}_{=0} \left[ (\mathbf{E}_0^* \cdot \vec{\nabla}) \mathbf{E}_0^* - \mathbf{E}_0^* \times (\vec{\nabla} \times \mathbf{E}_0^*) \right] - \\
&- \frac{i}{4} \text{Im}(\alpha) \underbrace{\int_0^{\frac{2\pi}{\omega}} dt}_{= \frac{2\pi}{\omega}} \left[ (\mathbf{E}_0^* \cdot \vec{\nabla}) \mathbf{E}_0 - \left( (\mathbf{E}_0^* \cdot \vec{\nabla}) \mathbf{E}_0 \right)^* + \mathbf{E}_0^* \times (\vec{\nabla} \times \mathbf{E}_0) - \left( \mathbf{E}_0^* \times (\vec{\nabla} \times \mathbf{E}_0) \right)^* \right] = \\
&= \frac{\pi}{\omega} \text{Im}(\alpha) \text{Im} \left( (\mathbf{E}_0^* \cdot \vec{\nabla}) \mathbf{E}_0 + \mathbf{E}_0^* \times (\vec{\nabla} \times \mathbf{E}_0) \right) \tag{A.15}
\end{aligned}$$

The third term of the integral A.7 can be derived to

$$\begin{aligned}
& \int_0^{\frac{2\pi}{\omega}} \dot{\vec{\mu}}_L \times \left( (\vec{\mu}_L \cdot \vec{\nabla}) \mathcal{B}(\mathbf{R}, t) \right) \frac{(m_-^2 - m_+^2)}{Qm^2} dt = \\
&= \frac{1}{8} \text{Im}(\alpha)^2 \frac{(m_-^2 - m_+^2)}{Qm^2} \left[ h_1(\mathbf{E}_0, \mathbf{B}_0) \underbrace{\int_0^{\frac{2\pi}{\omega}} e^{-3i\omega t} dt}_{=0} + h_2(\mathbf{E}_0, \mathbf{B}_0) \underbrace{\int_0^{\frac{2\pi}{\omega}} e^{-i\omega t} dt}_{=0} + \right. \\
&\quad \left. + h_3(\mathbf{E}_0, \mathbf{B}_0) \underbrace{\int_0^{\frac{2\pi}{\omega}} e^{i\omega t} dt}_{=0} + h_4(\mathbf{E}_0, \mathbf{B}_0) \underbrace{\int_0^{\frac{2\pi}{\omega}} e^{3i\omega t} dt}_{=0} \right] = 0. \tag{A.16}
\end{aligned}$$

Finally the momentum absorbed by a resonant Lorentz oscillator with fixed center of mass at a position  $\mathbf{R}$  is given by

$$\mathbf{P} = \frac{\pi}{\omega} \text{Im}(\alpha) \text{Im} \left( (\mathbf{E}_0^* \cdot \vec{\nabla}) \mathbf{E}_0 + \mathbf{E}_0^* \times (\vec{\nabla} \times \mathbf{E}_0) \right). \tag{A.17}$$

### A.2.4 Vector identities II

This section provides a proof to the vector identity

$$(\mathbf{a} \cdot \vec{\nabla})\mathbf{b} + \mathbf{a} \times (\vec{\nabla} \times \mathbf{b}) = (\vec{\nabla} \otimes \mathbf{b}) \mathbf{a}, \quad (\text{A.18})$$

where  $\mathbf{a}$  and  $\mathbf{b}$  are vector valued functions with  $\mathbf{a}, \mathbf{b} : \mathbb{R}^3 \rightarrow \mathbb{R}^3$ , where  $\mathbf{b}$  is at least once totally continuously differentiable and  $\vec{\nabla}$  acts only on  $\mathbf{b}$ . The vector identity can be proofed by rewriting it in its components:

$$\begin{aligned} & (\mathbf{a} \cdot \vec{\nabla}) \mathbf{b} + \mathbf{a} \times (\vec{\nabla} \times \mathbf{b}) = \\ & = \left( a_x \frac{\partial}{\partial x} + a_y \frac{\partial}{\partial y} + a_z \frac{\partial}{\partial z} \right) \begin{pmatrix} b_x \\ b_y \\ b_z \end{pmatrix} + \begin{pmatrix} a_x \\ a_y \\ a_z \end{pmatrix} \times \left[ \begin{pmatrix} \frac{\partial}{\partial x} \\ \frac{\partial}{\partial y} \\ \frac{\partial}{\partial z} \end{pmatrix} \times \begin{pmatrix} b_x \\ b_y \\ b_z \end{pmatrix} \right] = \\ & = \begin{pmatrix} a_x \frac{\partial}{\partial x} b_x + a_y \frac{\partial}{\partial y} b_x + a_z \frac{\partial}{\partial z} b_x \\ a_x \frac{\partial}{\partial x} b_y + a_y \frac{\partial}{\partial y} b_y + a_z \frac{\partial}{\partial z} b_y \\ a_x \frac{\partial}{\partial x} b_z + a_y \frac{\partial}{\partial y} b_z + a_z \frac{\partial}{\partial z} b_z \end{pmatrix} + \begin{pmatrix} a_y \frac{\partial}{\partial x} b_y - a_y \frac{\partial}{\partial y} b_x - a_z \frac{\partial}{\partial z} b_x + a_z \frac{\partial}{\partial x} b_z \\ a_z \frac{\partial}{\partial y} b_z - a_z \frac{\partial}{\partial z} b_y - a_x \frac{\partial}{\partial x} b_y + a_x \frac{\partial}{\partial y} b_x \\ a_x \frac{\partial}{\partial z} b_x - a_x \frac{\partial}{\partial x} b_z - a_y \frac{\partial}{\partial y} b_z + a_y \frac{\partial}{\partial z} b_y \end{pmatrix} = \\ & = \begin{pmatrix} a_x \frac{\partial}{\partial x} b_x + a_y \frac{\partial}{\partial x} b_y + a_z \frac{\partial}{\partial x} b_z \\ a_x \frac{\partial}{\partial y} b_x + a_y \frac{\partial}{\partial y} b_y + a_z \frac{\partial}{\partial y} b_z \\ a_x \frac{\partial}{\partial z} b_x + a_y \frac{\partial}{\partial z} b_z + a_z \frac{\partial}{\partial z} b_z \end{pmatrix} = \\ & = \begin{pmatrix} a_x & a_y & a_z \\ \frac{\partial}{\partial x} b_x & \frac{\partial}{\partial y} b_x & \frac{\partial}{\partial z} b_x \\ \frac{\partial}{\partial x} b_y & \frac{\partial}{\partial y} b_y & \frac{\partial}{\partial z} b_y \\ \frac{\partial}{\partial x} b_z & \frac{\partial}{\partial y} b_z & \frac{\partial}{\partial z} b_z \end{pmatrix}^T = (\mathbf{a}^T J_{\mathbf{b}})^T = \\ & = (\mathbf{a}^T (\vec{\nabla} \otimes \mathbf{b})^T)^T = (\vec{\nabla} \otimes \mathbf{b}) \mathbf{a}, \quad (\text{A.19}) \end{aligned}$$

where  $J_{\mathbf{b}}$  is the Jacobi matrix of  $\mathbf{b}$ .

## A.3 Decomposition of the Poynting vector

In this section the decomposition of the Poynting vector [68] into the orbital and spin part will be presented [75, 76]. The orbital part is proportional to the momentum density of a light field and the spin part is proportional to the curl of the spin density. In order to identify the spin density as part of the Poynting vector we first need to derive this vector quantity.

### A.3.1 Spin density of a light field

In order to determine the spin density of a light field we start in the same way as to calculate the momentum density in section 2.1.1, by assuming a small induced electric dipole with a charge

$Q$  of mass  $m_+$  at position  $\mathbf{r}_+$  and a charge  $-Q$  of mass  $m_-$  at position  $\mathbf{r}_-$ , see Figure 2.1. The torque on this electric dipole is given by

$$\mathbf{T} = \mathbf{r}_+ \times \mathbf{F}_+ + \mathbf{r}_+ \times \mathbf{F}_d + \mathbf{r}_- \times \mathbf{F}_- - \mathbf{r}_- \times \mathbf{F}_d, \quad (\text{A.20})$$

where  $\mathbf{F}_\pm$  is the sum of the Coulomb and Lorentz force acting on each charge and  $\mathbf{F}_d$  is the binding force between the two charges. Using the center of mass and relative coordinates introduced in section A.2.1 we can rewrite the overall torque as

$$\mathbf{T} = \mathbf{r}_+ \times \mathbf{F}_+ + \mathbf{r}_- \times \mathbf{F}_- + \underbrace{\mathbf{r}_d \times \mathbf{F}_d}_{=0}, \quad (\text{A.21})$$

where the last part vanishes since the binding force  $\mathbf{F}_d$  acts parallel to the relative coordinate  $\mathbf{r}_d$ . Since we assume the distance  $r_d$  between the two charges of the dipole to be much smaller than the wavelength of its emitted light, we can do a linear approximation to the remaining force, as presented in section 2.1.1, see expressions 2.9 and 2.10. Using the electric dipole moment  $\boldsymbol{\mu} = Q \cdot \mathbf{r}_d$ , the torque can then be written as

$$\begin{aligned} \mathbf{T} &= \left( \mathbf{R} + \frac{m_-}{m} \mathbf{r}_d \right) \times Q \left( \boldsymbol{\mathcal{E}} + \dot{\mathbf{R}} \times \boldsymbol{\mathcal{B}} + \frac{m_-}{m} \dot{\mathbf{r}}_d \times \boldsymbol{\mathcal{B}} \right) \\ &\quad - \left( \mathbf{R} - \frac{m_+}{m} \mathbf{r}_d \right) \times Q \left( \boldsymbol{\mathcal{E}} + \dot{\mathbf{R}} \times \boldsymbol{\mathcal{B}} - \frac{m_+}{m} \dot{\mathbf{r}}_d \times \boldsymbol{\mathcal{B}} \right) = \\ &= Q \left[ \mathbf{r}_d \times \boldsymbol{\mathcal{E}} + \mathbf{R} \times (\dot{\mathbf{r}}_d \times \boldsymbol{\mathcal{E}}) + \mathbf{r}_d \times (\dot{\mathbf{R}} \times \boldsymbol{\mathcal{B}}) + \mathbf{r}_d \times (\dot{\mathbf{r}}_d \times \boldsymbol{\mathcal{B}}) \frac{(m_-^2 - m_+^2)}{Qm^2} \right] = \\ &= \boldsymbol{\mu} \times \boldsymbol{\mathcal{E}} + \mathbf{R} \times (\dot{\boldsymbol{\mu}} \times \boldsymbol{\mathcal{E}}) + \boldsymbol{\mu} \times (\dot{\mathbf{R}} \times \boldsymbol{\mathcal{B}}) + \boldsymbol{\mu} \times (\dot{\boldsymbol{\mu}} \times \boldsymbol{\mathcal{B}}) \frac{(m_-^2 - m_+^2)}{Qm^2}. \end{aligned} \quad (\text{A.22})$$

The second term in this expression is dependent on the choice of the origin of the coordinate system and vanishes if the origin is set to be the center of mass of the dipole. This term will therefore not be taken into account for the intrinsic torque of the dipole. The third term is dependent on the speed of the dipole and vanishes for the case of a spatially fixed position of the dipole. Using the dipole moment  $\bar{\boldsymbol{\mu}}_L$  of the resonant Lorentz oscillator (see expression 2.14) the intrinsic torque  $\mathbf{T}_0$  of a spatially fixed resonant dipole oscillator is given by

$$\mathbf{T}_0 = \bar{\boldsymbol{\mu}}_L \times \boldsymbol{\mathcal{E}} + \bar{\boldsymbol{\mu}}_L \times (\dot{\bar{\boldsymbol{\mu}}}_L \times \boldsymbol{\mathcal{B}}) \frac{(m_-^2 - m_+^2)}{Qm^2}. \quad (\text{A.23})$$

Now the angular momentum  $\mathbf{L}$  of the spatially fixed resonant driven dipole after one oscillation period of the external light field is given by

$$\begin{aligned} \mathbf{L} &= \int_0^{\frac{2\pi}{\omega}} \mathbf{T}_0 dt \\ &= \int_0^{\frac{2\pi}{\omega}} \bar{\boldsymbol{\mu}}_L \times \boldsymbol{\mathcal{E}} dt + \frac{(m_-^2 - m_+^2)}{Qm^2} \underbrace{\int_0^{\frac{2\pi}{\omega}} \bar{\boldsymbol{\mu}}_L \times (\dot{\bar{\boldsymbol{\mu}}}_L \times \boldsymbol{\mathcal{B}}) dt}_{=0}, \end{aligned} \quad (\text{A.24})$$

where the second part vanishes<sup>2</sup> for the same reason as in equation A.16. The intrinsic angular momentum can now be evaluated to

$$\begin{aligned}
\mathbf{L} &= \int_0^{\frac{2\pi}{\omega}} \bar{\boldsymbol{\mu}}_{\perp} \times \boldsymbol{\mathcal{E}} dt = \\
&= \frac{i}{4} \text{Im}(\alpha) \left[ (\mathbf{E}_0 \times \mathbf{E}_0) \underbrace{\int_0^{\frac{2\pi}{\omega}} e^{-2i\omega t} dt}_{=0} - (\mathbf{E}_0^* \times \mathbf{E}_0^*) \underbrace{\int_0^{\frac{2\pi}{\omega}} e^{2i\omega t} dt}_{=0} \right. \\
&\quad \left. - \underbrace{((\mathbf{E}_0^* \times \mathbf{E}_0) - (\mathbf{E}_0^* \times \mathbf{E}_0)^*)}_{2i \text{Im}(\mathbf{E}_0^* \times \mathbf{E}_0)} \underbrace{\int_0^{\frac{2\pi}{\omega}} dt}_{=\frac{2\pi}{\omega}} \right] = \\
&= \frac{\pi}{\omega} \text{Im}(\alpha) \text{Im}(\mathbf{E}_0^* \times \mathbf{E}_0). \tag{A.25}
\end{aligned}$$

From the angular momentum which is absorbed by the dipole we can determine the spin density  $\boldsymbol{\rho}_S$  using the absorption cross section  $\sigma_{\text{Abs}}$  of the Lorentz oscillator, see expression 2.19. The spin density evaluates to

$$\boldsymbol{\rho}_S = \frac{\mathbf{L}}{\lambda\sigma} = \frac{\epsilon_0}{2\omega} \text{Im}(\mathbf{E}_0^* \times \mathbf{E}_0). \tag{A.26}$$

### A.3.2 Orbit and spin part of the Poynting vector

We start with the time dependent Poynting vector

$$\boldsymbol{\mathcal{S}} = \boldsymbol{\mathcal{E}} \times \boldsymbol{\mathcal{H}}, \tag{A.27}$$

with the electric field strength

$$\boldsymbol{\mathcal{E}} = \frac{1}{2} (\mathbf{E} + \mathbf{E}^*) = \frac{1}{2} (\mathbf{E}_0 e^{-i\omega t} + \mathbf{E}_0^* e^{i\omega t}) \tag{A.28}$$

and the magnetic field strength

$$\boldsymbol{\mathcal{H}} = \frac{1}{2} (\mathbf{H} + \mathbf{H}^*) = \frac{1}{2} (\mathbf{H}_0 e^{-i\omega t} + \mathbf{H}_0^* e^{i\omega t}). \tag{A.29}$$

Using  $\boldsymbol{\mathcal{H}} = \epsilon_0 c^2 \boldsymbol{\mathcal{B}}$ , the magnetic field strength can be rewritten as the magnetic flux density

$$\boldsymbol{\mathcal{B}} = \frac{1}{2} (\mathbf{B} + \mathbf{B}^*) = \frac{1}{2} (\mathbf{B}_0 e^{-i\omega t} + \mathbf{B}_0^* e^{i\omega t}). \tag{A.30}$$

<sup>2</sup>After expanding the expression all the integrands are proportional to  $\epsilon^n e^{i\omega t}$  with  $n \in \{-3, 1, 1, 3\}$ . Every single one of this integrals evaluates to zero.

The time average of the Poynting vector over one oscillation period of the light field is given by

$$\begin{aligned}
\mathcal{S}_0 &= \frac{\omega}{2\pi} \int_0^{\frac{2\pi}{\omega}} \mathcal{S} dt = \\
&= \frac{\omega}{8\pi} \left( (\mathbf{E}_0 \times \mathbf{H}_0) \underbrace{\int_0^{\frac{2\pi}{\omega}} e^{-2i\omega t} dt}_0 + (\mathbf{E}_0^* \times \mathbf{H}_0^*) \underbrace{\int_0^{\frac{2\pi}{\omega}} e^{2i\omega t} dt}_0 + 2 \operatorname{Re}(\mathbf{E}_0^* \times \mathbf{H}_0) \int_0^{\frac{2\pi}{\omega}} dt \right) = \\
&= \frac{1}{2} \operatorname{Re}(\mathbf{E}_0^* \times \mathbf{H}_0) = \frac{\epsilon_0 c^2}{2} \operatorname{Re}(\mathbf{E}_0^* \times \mathbf{B}_0). \tag{A.31}
\end{aligned}$$

Using again the identity  $(\vec{\nabla} \times \mathbf{E}_0) = i\omega \mathbf{B}_0$ , which stem from the Maxwell-Faraday equation, see A.2.3, we can rewrite the time averaged Poynting vector as

$$\begin{aligned}
\mathcal{S}_0 &= \frac{\epsilon_0 c^2}{2\omega} \operatorname{Re}(\mathbf{E}_0^* \times (i\vec{\nabla} \times \mathbf{E}_0)) = \\
&= -\frac{\epsilon_0 c^2}{2\omega} \operatorname{Im}(\mathbf{E}_0^* \times (\vec{\nabla} \times \mathbf{E}_0)) = \\
&= \frac{\epsilon_0 c^2}{2\omega} \operatorname{Im}((\vec{\nabla} \otimes \mathbf{E}_0) \mathbf{E}_0^*) + \frac{\epsilon_0 c^2}{2\omega} \operatorname{Im}((\mathbf{E}_0^* \cdot \vec{\nabla}) \mathbf{E}_0). \tag{A.32}
\end{aligned}$$

Here we first used with  $z \in \mathbb{C}$  and  $z = a + ib$ , with  $a, b \in \mathbb{R}$  the identity  $\operatorname{Re}(i \cdot z) = \operatorname{Re}(ia + i^2 b) = \operatorname{Re}(-b + ia) = -b = -\operatorname{Im}(z)$  and then the vector identity presented in A.2.4. We now make use of the vector identity [69]

$$(\mathbf{b} \cdot \vec{\nabla}) \mathbf{a} - (\mathbf{a} \cdot \vec{\nabla}) \mathbf{b} + \mathbf{a} (\vec{\nabla} \cdot \mathbf{b}) - \mathbf{b} (\vec{\nabla} \cdot \mathbf{a}) = \vec{\nabla} \times (\mathbf{a} \times \mathbf{b}), \tag{A.33}$$

where  $\mathbf{a}$  and  $\mathbf{b}$  are vector valued functions with  $\mathbf{a}, \mathbf{b} : \mathbb{R}^3 \rightarrow \mathbb{R}^3$ , which are at least once totally continuously differentiable. In the charge free space<sup>3</sup> the divergence of the electric field strength is zero, leading to

$$\vec{\nabla} \cdot \mathcal{E} = e^{-i\omega t} \vec{\nabla} \cdot \mathbf{E}_0 + e^{i\omega t} \vec{\nabla} \cdot \mathbf{E}_0^* = 0, \tag{A.34}$$

which is in general only valid if  $\vec{\nabla} \cdot \mathbf{E}_0 = \vec{\nabla} \cdot \mathbf{E}_0^* = 0$ . With this we can make use of the vector identity A.33 for  $\mathbf{E}_0$  and  $\mathbf{E}_0^*$ :

$$\begin{aligned}
\vec{\nabla} \times (\mathbf{E}_0^* \times \mathbf{E}_0) &= (\mathbf{E}_0 \cdot \vec{\nabla}) \mathbf{E}_0^* - (\mathbf{E}_0^* \cdot \vec{\nabla}) \mathbf{E}_0 + \underbrace{\mathbf{E}_0^* (\vec{\nabla} \cdot \mathbf{E}_0)}_{=0} - \underbrace{\mathbf{E}_0 (\vec{\nabla} \cdot \mathbf{E}_0^*)}_{=0} = \\
&= (\mathbf{E}_0 \cdot \vec{\nabla}) \mathbf{E}_0^* - ((\mathbf{E}_0 \cdot \vec{\nabla}) \mathbf{E}_0^*)^* = 2i \operatorname{Im}((\mathbf{E}_0 \cdot \vec{\nabla}) \mathbf{E}_0^*). \tag{A.35}
\end{aligned}$$

---

<sup>3</sup>The situation described in section 2.1.1, where we study the momentum density of the light field emitted by a electric dipole which is much smaller than the wavelength of its emitted light, is at a distance exceeding several wavelengths of the dipole well described by a charge free space.

We then find

$$\begin{aligned}
\underbrace{\operatorname{Im}((\mathbf{E}_0 \cdot \vec{\nabla}) \mathbf{E}_0^*)}_{\in \mathbb{R}} &= -\frac{i}{2} \underbrace{\vec{\nabla} \times (\mathbf{E}_0^* \times \mathbf{E}_0)}_{\in \mathbb{R}} = \\
&= -\frac{i}{2} \left( \underbrace{\operatorname{Re}(\vec{\nabla} \times (\mathbf{E}_0^* \times \mathbf{E}_0))}_{\text{needs to be 0}} + i \operatorname{Im}(\vec{\nabla} \times (\mathbf{E}_0^* \times \mathbf{E}_0)) \right) = \\
&= \frac{1}{2} \operatorname{Im}(\vec{\nabla} \times (\mathbf{E}_0^* \times \mathbf{E}_0)). \tag{A.36}
\end{aligned}$$

Finally we can write the time averaged Poynting vector as

$$\mathcal{S}_0 = \underbrace{\frac{\epsilon_0 c^2}{2\omega} \operatorname{Im}((\vec{\nabla} \otimes \mathbf{E}_0) \mathbf{E}_0^*)}_{\mathcal{S}_0^{\text{Orb}}} + \underbrace{\frac{\epsilon_0 c^2}{2\omega} \operatorname{Im}(\vec{\nabla} \times (\mathbf{E}_0^* \times \mathbf{E}_0))}_{\mathcal{S}_0^{\text{Spin}}}. \tag{A.37}$$

We denote the first part as the orbital part of the Poynting vector, since is proportional to the momentum density  $\rho_P$  of the light field, as it was determined in section 2.1.1,

$$\mathcal{S}_0^{\text{Orb}} = c^2 \cdot \rho_P. \tag{A.38}$$

The second part is called the spin part of the Poynting vector, which is proportional to the curl of the spin density  $\rho_S$  of the light field,

$$\mathcal{S}_0^{\text{Spin}} = \frac{c^2}{2} \cdot (\vec{\nabla} \times \rho_S). \tag{A.39}$$

### A.3.3 Consistency check of momentum and spin density

Using a circularly polarized plane wave propagating along the  $z$ -axis

$$\mathcal{E}_{\text{PW}} = \frac{1}{2} \left( A e^{-ikz} \frac{1}{\sqrt{2}} (\mathbf{e}_x + i\mathbf{e}_y) + A^* e^{ikz} \frac{1}{\sqrt{2}} (\mathbf{e}_x - i\mathbf{e}_y) \right), \tag{A.40}$$

we can quickly check the consistency of the determined momentum density  $\rho_P$  (2.20) and spin density  $\rho_S$  (A.26). The momentum density of this light field is given by

$$\rho_P = \frac{\pi}{\omega} \operatorname{Im}(\alpha) |A|^2 k \mathbf{e}_z \tag{A.41}$$

and the spin density by

$$\rho_S = \frac{\pi}{\omega} \operatorname{Im}(\alpha) |A|^2 \mathbf{e}_z. \tag{A.42}$$

The ratio of the momentum and spin density is then in fact

$$\frac{\|\rho_P\|}{\|\rho_S\|} = k, \tag{A.43}$$

as one would await.

## A.4 The dipole polarization ratio

It is possible to decompose the electric field of any elliptically polarized dipole, as defined in 2.2.1, into two fields emitted by two linearly polarized dipoles which feature orthogonal polarization axes and which are phase shifted by  $\pi/2$ . The ratio of the absolute value of the amplitudes of this two fields correspond to the principal axes of the so called polarization ellipse. If  $\epsilon$  is real valued, the principal axes of the polarization ellipse coincide with the  $x$ - and  $y$ -axis. Figure A.1a shows the polarization ellipse for  $\epsilon = 0.25$ . If  $\epsilon$  is purely imaginary with  $0 < |\epsilon| < \infty$ , the corresponding dipole field is linearly polarized along an axis which does not coincide with the  $x$ - or  $y$  axis, see Figure A.1d.

Using the further decomposition

$$\mathbf{E}_{\text{ell}} = \frac{1}{N_\epsilon} (\mathbf{E}_{\text{D}^x} + i \operatorname{Re}(\epsilon) \mathbf{E}_{\text{D}^y} - \operatorname{Im}(\epsilon) \mathbf{E}_{\text{D}^y}) \quad \text{with} \quad N_\epsilon = \sqrt{1 + |\epsilon|^2} \quad (\text{A.44})$$

shows, that the field of any elliptically polarized dipole given by a complex valued  $\epsilon$  can be decomposed into the field of an elliptically polarized dipole of which the major axes of the polarization ellipse coincide with the  $x$ - and  $y$ -axis, given by  $(\mathbf{E}_{\text{D}^x} + i \cdot \operatorname{Re}(\epsilon) \mathbf{E}_{\text{D}^y})/N_\epsilon$ , plus the field of a linearly polarized dipole oscillating along the  $y$ -axes. Figure A.1b and c shows the original polarization ellipse and the polarization ellipse of the described decomposition for two complex values of  $\epsilon$ . This shows that in general, when imaging an arbitrarily elliptically polarized dipole it is possible to decompose its emitted field into a part emitted by an elliptically polarized dipole of which the major or minor axis of the polarization ellipse coincides with the optical axis of the imaging system, which we address as optical-axis-oriented elliptically polarized dipole, plus a residual part caused by a linearly polarized dipole which oscillates orthogonal to the optical axis and is  $\pi/2$  phase shifted with respect to its counterpart in the optical-axis-oriented elliptically polarized dipole.

It is shown in section 2.2.3.3 and 2.2.4.1, that when imaging an elliptically polarized emitter with  $\epsilon \in \mathbb{C}$  along the  $y$ -axis, the apparent displacement is only caused by the field component  $(\mathbf{E}_{\text{D}^x} + i \cdot \operatorname{Re}(\epsilon) \mathbf{E}_{\text{D}^y})/N_\epsilon$ , while the residual field component  $\operatorname{Im}(\epsilon) \mathbf{E}_{\text{D}^y}/N_\epsilon$  decreases the apparent displacement.

## A.5 Wave fronts

In this section the wave fronts in the  $xy$ -plane of an elliptically polarized emitter, as defined in section 2.2.1, will be derived. We make use of the fact that the light emitted by the elliptically polarized dipole, which is rotating in the  $xy$ -plane, is in the  $xy$ -plane solely linearly polarized (see 2.2.2). This means that the real valued local field vector has a time independent direction and an oscillating amplitude. Within one oscillation period of the electric field the field amplitude has two zero crossings. We now determine the the phase fronts of the amplitude oscillation. One way to do so is to determine the paths where the field  $\mathcal{E}_{\text{ell}} = \mathcal{E}_{\text{ell}} + \mathcal{E}_{\text{ell}}^*$  from 2.29 is zero and then generalizing this solutions. The paths of equal phase are given by

$$\mathbf{R}_{\text{ell}}(\phi, t, \epsilon, \phi_0) = R_{\text{ell}}(\phi, t, \epsilon, \phi_0) \begin{pmatrix} -\operatorname{sgn}(\epsilon) \cos(\phi) \\ \sin(\phi) \end{pmatrix} \quad (\text{A.45})$$

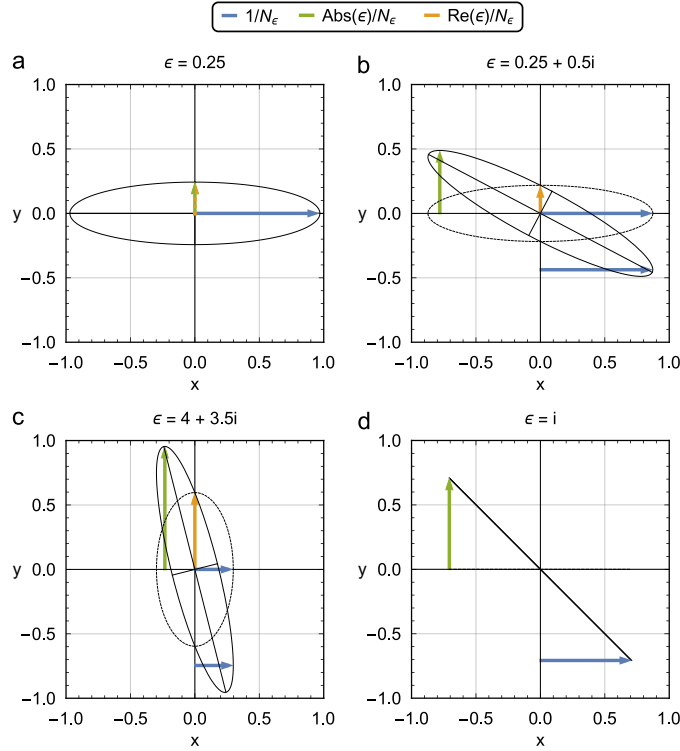


**Figure A.1: Dipole polarization ratio.** **a**, The polarization ellipse of an elliptically polarized dipole for a solely real valued dipole polarization ratio of  $\epsilon = 0.25$ . The major (minor) axis of the ellipse is given by  $1/N_\epsilon$  ( $\text{Re}(\epsilon)/N_\epsilon$ ). **b** and **c**, The polarization ellipse (solid) of an elliptically polarized dipole field for two complex valued dipole polarization ratios. Additionally the polarization ellipse (dashed) of the elliptically polarized dipole field described by  $\text{Re}(\epsilon)$  is shown. It is possible to decompose the field emitted by the dipole in polarization state  $\epsilon$  into the field of a dipole in polarization state  $\text{Re}(\epsilon)$  and the residual field of a linearly polarized dipole with described by  $\text{Im}(\epsilon)$ , see next subfigure. **d**, For  $\epsilon$  being solely complex valued the polarization ellipse reduces to a line coinciding with the axis along which the corresponding field of a linearly polarized dipole is polarized.

with

$$R_{\text{ell}}(\phi, t, \epsilon, \phi_0) = \frac{\lambda}{2\pi} \left( \text{sgn}(\epsilon)\phi_0 + \text{sgn}(\epsilon)\frac{2\pi}{\lambda}ct + \arctan\left(\frac{1}{\epsilon}\tan(\phi)\right) + \text{sgn}(\epsilon)n\pi \right) \quad (\text{A.46})$$

where  $\text{sgn}(\epsilon)$  gives the sign of  $\epsilon$  and  $n \in \mathbb{N}_0$ . The parameter  $\phi_0 \in (0, 2\pi]$  defines the phasing of the wave front within one oscillation period of the light field, where the cases  $\phi_0 = 0$  and  $\phi_0 = \pi$  correspond to zero amplitude and the cases  $\phi_0 = \pi/2$  and  $\phi_0 = 3\pi/2$  to the positive respectively the negative amplitude maxima. To obtain a continuous curve from this expression several cases of  $n$  and the domain of  $\phi$  need to be considered and are dependent on  $t$  and  $\phi_0$ .

We defined the wave fronts in section 2.2.2 as the surface of which the tangential plane is in every point orthogonal to the linear momentum density of the field. To find out if the path given

by  $\mathbf{R}_{\text{ell}}$  is a wave front according to our definition we need to check if the tangent of the curve is in every point orthogonal to the momentum density. The tangent  $\mathbf{T}$  of  $\mathbf{R}_{\text{ell}}$  is given by

$$\mathbf{T} = \frac{d}{dt} \mathbf{R}_{\text{ell}}. \quad (\text{A.47})$$

Indeed the product

$$\mathbf{T}(\phi, t, \epsilon, \phi_0) \cdot \rho_{\mathcal{P}}(\mathbf{R}_{\text{ell}}(\phi, t, \epsilon, \phi_0)) = 0, \quad (\text{A.48})$$

where  $\rho_{\mathcal{P}}$  gives the momentum density as defined in 2.20.<sup>4</sup>

While it is in general difficult to write down the path of a wave front for arbitrary  $t$  and  $\phi_0$  as a continuous curve from the origin to infinity this is much easier for the special case  $t = 0$  and  $\phi_0 = n_\phi \pi/2$  with  $n_\phi \in \{1, 2, 3\}$ . The continuous wave front is then given by

$$\begin{aligned} \mathbf{R}_{\text{ell}}^0(\epsilon, n_\phi) = & \left\{ R_{\text{ell}}^0(\phi, n, n_\phi, \epsilon) \begin{pmatrix} -\text{sgn}(\epsilon) \cos(\phi + \frac{n\pi}{2}) \\ \sin(\phi + \frac{n\pi}{2}) \end{pmatrix} \middle| n \in \mathbb{N}_0, \phi \in \left(0, \frac{\pi}{2}\right] \right\} \cup \\ & \cup \left\{ \tilde{R}_{\text{ell}}^0(\phi, n, n_\phi, \epsilon) \begin{pmatrix} -\text{sgn}(\epsilon) \cos(\phi - \frac{n\pi}{2}) \\ \sin(\phi - \frac{n\pi}{2}) \end{pmatrix} \middle| n \in \mathbb{N}, n \leq n_\phi, \phi \in \left(0, \frac{\pi}{2}\right] \right\} \end{aligned} \quad (\text{A.49})$$

with

$$R_{\text{ell}}^0(\phi, n, n_\phi, \epsilon) = \frac{\lambda}{2\pi} \left[ \text{sgn}(\epsilon) \frac{n_\phi \pi}{2} + \arctan\left(\frac{\tan(\phi + \frac{n\pi}{2})}{\epsilon}\right) \right] + \frac{\text{sgn}(\epsilon)}{2} \text{ip}\left(\frac{n+1}{2}\right) \lambda \quad (\text{A.50})$$

and

$$\tilde{R}_{\text{ell}}^0(\phi, n, n_\phi, \epsilon) = \frac{\lambda}{2\pi} \left[ \text{sgn}(\epsilon) \frac{n_\phi \pi}{2} + \arctan\left(\frac{\tan(\phi - \frac{n\pi}{2})}{\epsilon}\right) \right] - \frac{\text{sgn}(\epsilon)}{2} \text{ip}\left(\frac{n}{2}\right) \lambda, \quad (\text{A.51})$$

where the function  $\text{ip} : \mathbb{R} \rightarrow \mathbb{N}_0$  gives the integer part of a real number and  $n_\phi \in \{1, 2, 3\}$ .

## A.6 Displacement determined from wave fronts

The the apparent displacement can be determined directly from the local tilt of the normal vector to wave fronts with respect to the radial direction, given by the angle  $\alpha$ . We demonstrate this for the case of a circularly polarized dipole, see Figure A.2. The parametric expression for the spiral wave front of a  $\sigma^+$  polarized dipole is given by

$$\mathbf{R}(t) = \frac{\lambda}{2\pi} \omega t \begin{pmatrix} \cos(\omega t) \\ \sin(\omega t) \end{pmatrix}, \quad (\text{A.52})$$

---

<sup>4</sup>Note that the momentum density given in 2.20 is a function of  $\mathbf{r} \in \mathbb{R}^3$ , while  $\mathbf{R}_{\text{ell}}$  is a two dimensional path. In order to calculate the product in A.48 the  $z$ -coordinate in the momentum density needs to be set zero

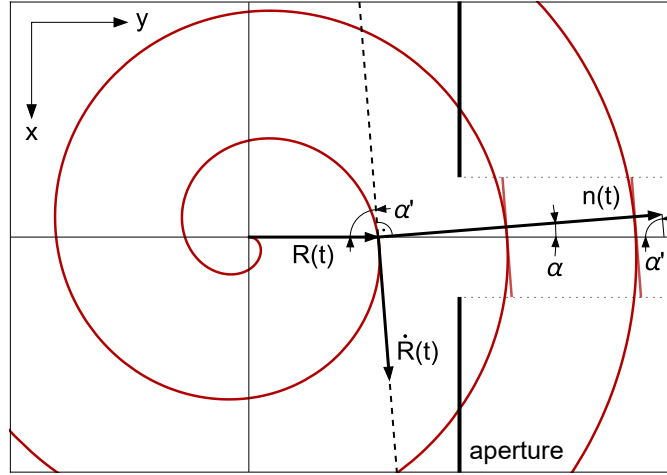


**Figure A.2: Spiral wave front.** The spiral wave front of the light emitted by a  $\sigma^+$  polarized dipole, which is given by the parametric expression  $R(t)$ . The angle  $\alpha'$  between the vector  $\dot{R}(t)$ , which is parallel to the tangent on the wave fronts, can be used to determine the angle  $\alpha$  between the normal vector  $n(t)$  on the wave fronts and the radial direction, given by  $R(t)$ . The wave fronts of the light passing an aperture can be approximated by plane waves which are tilted by  $\alpha$ , giving the impression that the light originates from a position which is not the position of the emitter.

with  $R(t) = \omega t \lambda / (2\pi)$ . The tangent of this spiral is given by

$$\dot{R}(t) = \frac{\lambda}{2\pi} \omega \begin{pmatrix} \cos(\omega t) - \omega t \sin(\omega t) \\ \sin(\omega t) + \omega t \cos(\omega t) \end{pmatrix}, \quad (\text{A.53})$$

with  $\dot{R}(t) = \sqrt{1 + (\omega t)^2} \cdot \lambda / (2\pi)$ . Now the angle  $\alpha'$  between  $R(t)$  and  $\dot{R}(t)$  can be determined via

$$\cos(\alpha') = \frac{R(t) \cdot \dot{R}(t)}{R(t) \dot{R}(t)} = \frac{1}{\sqrt{1 + (\omega t)^2}}. \quad (\text{A.54})$$

Since  $\alpha$  and  $\alpha'$  lie within an rectangular triangle we can get the following expression for  $\alpha$  :

$$\sin(\alpha) = \frac{1}{\sqrt{1 + t^2}}. \quad (\text{A.55})$$

With  $t = R \cdot 2\pi / (\lambda \omega)$  and assuming  $\alpha$  being small and  $R$  large we can make the approximation  $\alpha \approx \lambda / (2\pi R)$ .

We now assume the situation were an aperture with diameter  $D$  is placed along the  $y$ -axis at a distance  $R \gg D$  from a  $\sigma^\pm$  polarized dipole and it is imaged onto a screen at a distance  $d$  from the aperture. The local wave fronts at the position of the aperture can be approximated by plane waves which are tilted by the angle  $\alpha$  with respect to the optical axis. This tilt leads to a

displacement of the center of mass of the image of a  $\sigma^\pm$  polarized dipole at the screen of

$$\bar{q}_x = \mp \frac{d}{R} \frac{\lambda}{2\pi}. \quad (\text{A.56})$$

From this center of mass position along the  $x$ -axis one draws the conclusion, that the emitter is displaced by

$$\Delta x = \pm \frac{\lambda}{2\pi}. \quad (\text{A.57})$$

## A.7 Modification of dipole fields by a lens

We now assume a dipole emitter which is placed in the focus of a lens at the optical axis. In order to describe the electric field of an elliptically polarized dipole after the lens we use the decomposition of the field introduced in 2.31. The field of the elliptically polarized dipole rotating around the  $z$ -axis is given by

$$\mathbf{E}_{\text{ell}} = \frac{1}{N_\epsilon} (\mathbf{E}_{D^x} + \epsilon \cdot i \cdot \mathbf{E}_{D^y}), \quad (\text{A.58})$$

where  $\mathbf{E}_{D^x}$  and  $\mathbf{E}_{D^y}$  are the fields emitted by dipoles oscillating along the  $x$ - and  $y$ -axis. Applying their corresponding dipole momenta  $\boldsymbol{\mu}_{D^x} = \mathbf{e}_x$  and  $\boldsymbol{\mu}_{D^y} = \mathbf{e}_y$  to equation 2.29 leads to the following expressions for the far field:

$$\mathbf{E}_{D^x}^{\text{ff}}(\rho, \phi, y) = \frac{e^{ik\sqrt{y^2+\rho^2}}}{(y^2 + \rho^2)^{3/2}} \begin{pmatrix} y^2 + \rho^2 \sin^2(\phi) \\ -y\rho \cos(\phi) \\ -\rho^2 \sin(\phi) \cos(\phi) \end{pmatrix} C_E \quad (\text{A.59})$$

$$\mathbf{E}_{D^y}^{\text{ff}}(\rho, \phi, y) = \frac{e^{ik\sqrt{y^2+\rho^2}}}{(y^2 + \rho^2)^{3/2}} \begin{pmatrix} -y\rho \cos(\phi) \\ \rho^2 \\ -y\rho \sin(\phi) \end{pmatrix} C_E. \quad (\text{A.60})$$

Here  $\mathbf{r} = (x, y, z)$  denotes the Cartesian coordinates with respect to the origin and  $(\rho, \phi)$  are polar coordinates within the plane orthogonal to the imaging axis ( $y$ -axis) with  $x = \rho \cos(\phi)$  and  $z = \rho \sin(\phi)$ .  $C_E$  is constant in  $\mathbf{r}$  but includes the time dependence of the field. With  $D \ll f$  follows at the position of the aperture  $\rho \ll f$ , leading to

$$\frac{1}{(f^2 + \rho^2)^{3/2}} \approx \frac{1}{f^3}. \quad (\text{A.61})$$

By only taking the lowest order of  $f^{-n}$  into account and neglecting the higher orders we can approximate the fields at the aperture in front of the lens to

$$\mathbf{E}_{D^x}^{\text{ap.}}(\rho, \phi, f) = \frac{1}{f} \mathbf{e}_x e^{ik\sqrt{f^2+\rho^2}} C_E \quad (\text{A.62})$$

$$\mathbf{E}_{D^y}^{\text{ap.}}(\rho, \phi, f) = -\frac{\rho}{f^2} \mathbf{e}_\rho e^{ik\sqrt{f^2+\rho^2}} C_E, \quad (\text{A.63})$$

where  $\mathbf{e}_\rho$  is given by

$$\mathbf{e}_\rho = \begin{pmatrix} \cos(\phi) \\ 0 \\ \sin(\phi) \end{pmatrix}. \quad (\text{A.64})$$

The lens now modifies the phase of the fields passing through with the phase transfer function [83]

$$l(\rho) = e^{-ik\frac{\rho^2}{2f}} \cdot e^{ik(y+y_0)}, \quad (\text{A.65})$$

where  $y_0$  is a constant phase shift. The phase of the fields right after the lens is given by

$$l(\rho) \cdot e^{ik\sqrt{f^2+\rho^2}} = e^{ik\left(\sqrt{f^2+\rho^2}-\frac{\rho^2}{2f}\right)} \cdot e^{ik(y+y_0)} = e^{ikf\left(\sqrt{1+\frac{\rho^2}{f^2}}-\frac{\rho^2}{2f^2}\right)} \cdot e^{ik(y+y_0)}. \quad (\text{A.66})$$

Here we can make the following approximation

$$ikf\left(\sqrt{1+\frac{\rho^2}{f^2}}-\frac{\rho^2}{2f^2}\right) \approx ikf\left(1+\frac{\rho^2}{2f^2}-\frac{\rho^2}{2f^2}\right) = ikf, \quad (\text{A.67})$$

for  $\rho \ll f$ . This leads to a phase  $e^{iky} \cdot e^{ik(y_0+f)}$  of the field after the lens, meaning that the field after the lens is a spatially limited plane wave. The constant part of this phase shift will in the further calculations be included in  $C_E$ . Now the fields after the lens can be written as

$$\mathbf{E}_{D^x}^{\text{lens}}(\rho, \phi) = \frac{1}{f} \mathbf{e}_x e^{iky} C_E \quad (\text{A.68})$$

$$\mathbf{E}_{D^y}^{\text{lens}}(\rho, \phi) = -\frac{\rho}{f^2} \mathbf{e}_\rho e^{iky} C_E. \quad (\text{A.69})$$

Finally the field of the elliptically polarized dipole after the lens is given by

$$\mathbf{E}_{\text{ell}}^{\text{lens}} = \frac{1}{N_\epsilon} (\mathbf{E}_{D^x}^{\text{lens}} + \epsilon i \mathbf{E}_{D^y}^{\text{lens}}) \quad (\text{A.70})$$

## A.8 Determination of mean momentum

In this section the mean momentum  $\bar{\mathbf{p}}$  of light emitted by an elliptically polarized dipole, which passed the first lens of an imaging system will be derived. We assume an imaging system as it is shown in Figure 2.6, where the first lens of focal length  $f$  and aperture diameter  $D$  is placed at distance  $f$  from the emitter, which is located at the origin. The optical axis of the imaging system is set to be the  $y$ -axis. The light field of the elliptically polarized emitter after the first

lens is given by

$$\begin{aligned} \mathbf{E}_{\text{ell}}^{\text{lens}} &= \frac{1}{\sqrt{1+|\epsilon|^2}} (\mathbf{E}_{D^x}^{\text{lens}} + i\epsilon \mathbf{E}_{D^y}^{\text{lens}}) = \\ &= \frac{1}{\sqrt{1+|\epsilon|^2}} \begin{pmatrix} \frac{1}{f} - i\epsilon \frac{\rho}{f^2} \cos(\phi) \\ 0 \\ -i\epsilon \frac{\rho}{f^2} \sin(\phi) \end{pmatrix} e^{iky} C_E, \end{aligned} \quad (\text{A.71})$$

using the fields  $\mathbf{E}_{D^x}^{\text{lens}}$  and  $\mathbf{E}_{D^y}^{\text{lens}}$  which are derived in section A.7. Here  $(\rho, \phi)$  are polar coordinates within the plane orthogonal to the imaging axis, with  $x = \rho \cos(\phi)$  and  $z = \rho \sin(\phi)$ .

The mean momentum of the light after the lens is given by the integral of the linear momentum density  $\rho_{\mathbf{p}}$  over the volume of the lens,

$$\bar{\mathbf{p}} = \int_f^{f+d_y} \int_0^{2\pi} \int_0^{D/2} \underbrace{\frac{\epsilon_0}{2\omega} \text{Im} \left( (\vec{\nabla} \otimes \mathbf{E}_{\text{ell}}^{\text{lens}}) (\mathbf{E}_{\text{ell}}^{\text{lens}})^* \right)}_{\rho_{\mu}} \rho \, d\rho \, d\phi \, dy. \quad (\text{A.72})$$

With the expression

$$\vec{\nabla} \otimes \mathbf{E}_{\text{ell}}^{\text{lens}} = \frac{1}{\sqrt{1+|\epsilon|^2}} \frac{1}{f^2} \begin{pmatrix} -i\epsilon & 0 & 0 \\ k(if + \epsilon\rho \cos(\phi)) & 0 & k\epsilon\rho \sin(\phi) \\ 0 & 0 & -i\epsilon \end{pmatrix} e^{iky} C_E, \quad (\text{A.73})$$

the linear momentum density of the field of the elliptically polarized emitter after the lens can be written as

$$\begin{aligned} \rho_{\mathbf{p}} &= \frac{\epsilon_0 |C_E|^2}{2\omega f^4 \sqrt{1+|\epsilon|^2}} \text{Im} \left( \left( \begin{pmatrix} |\epsilon|^2 \rho \cos(\phi) - i\epsilon f \\ i \left( kf^2 + |\epsilon|^2 k\rho^2 + 2 \text{Im}(\epsilon) kf\rho \cos(\phi) \right) \\ |\epsilon|^2 \rho \sin(\phi) \end{pmatrix} \right) \right) = \\ &= \frac{\epsilon_0 |C_E|^2}{2\omega f^4 \sqrt{1+|\epsilon|^2}} \begin{pmatrix} -\text{Re}(\epsilon) f \\ kf^2 + |\epsilon|^2 k\rho^2 + 2 \text{Im}(\epsilon) kf\rho \cos(\phi) \\ 0 \end{pmatrix}. \end{aligned} \quad (\text{A.74})$$

It is then possible to evaluate the integral A.72 to

$$\bar{\mathbf{p}} = \frac{e_0 C_E}{2\omega} \frac{D^2}{4f^2} \frac{d_y}{(1+|\epsilon|^2)} \begin{pmatrix} -\frac{1}{f} \pi \text{Re}(\epsilon) d_y \\ k\pi (1+|\epsilon|^2) \frac{D^2}{8f^2} d_y \\ 0 \end{pmatrix}. \quad (\text{A.75})$$

In the approximation  $D \ll f$  we can identify  $D/(2f)$  with the numerical aperture NA of the imaging system. Note that this aperture is the geometrical aperture and thus does not depend on the refractive index. The mean momentum is then finally given by

$$\bar{\mathbf{p}} = \frac{\epsilon_0 C_E}{2\omega} \frac{\text{NA}^2 d_y}{(1 + |\epsilon|^2)} \begin{pmatrix} -\frac{1}{f} \pi \text{Re}(\epsilon) d_y \\ k\pi(1 + |\epsilon|^2 \frac{\text{NA}^2}{2}) d_y \\ 0 \end{pmatrix}. \quad (\text{A.76})$$

The mean linear momentum density of the light that passed the lens and was emitted by linearly polarized emitters oscillating along the  $x$ - and  $y$ -axis is given by

$$\rho_{\mathbf{P}}(\boldsymbol{\mu}_{\text{D}^x}) = \frac{\epsilon_0 |C_E|^2 k}{2\omega f^2} \mathbf{e}_y \quad (\text{A.77})$$

and

$$\rho_{\mathbf{P}}(\boldsymbol{\mu}_{\text{D}^y}) = \frac{\epsilon_0 |C_E|^2 k \rho^2}{2\omega f^4} \mathbf{e}_y. \quad (\text{A.78})$$

The mean linear momentum density of this two dipole emitters does not feature any transverse components and thus no displacement of the center of mass of the image at the screen can be observed. This can also be seen in expression A.76, for  $\epsilon = 0$ , which corresponds to a linearly polarized dipole oscillating along the  $x$ -axis and  $\epsilon = \infty$ , which corresponds to a linearly polarized dipole oscillating along the  $y$ -axis. In both cases the transverse linear momentum component vanishes.

## A.9 Angular momentum of photons

The effect that an emitter which is elliptically polarized appears to be at a position where it is in fact not, was determined in section 2.2.3, using the classical linear momentum density of a light field. However, it is possible to explain and quantitatively study this effect in a quantum mechanically approach using the angular momentum of the photons emitted by the dipole emitter. This derivation will be presented in this section.

In general an arbitrary polarized dipole emits photons with an non-zero angular momentum. The angular momentum carried by the photons can be decomposed into the orbital and the spin angular momentum, which are represented by the operators  $\hat{\mathbf{L}}$  and  $\hat{\mathbf{S}}$ , with

$$\hat{\mathbf{L}} = \mathbf{r} \times \hat{\mathbf{p}}, \quad (\text{A.79})$$

and  $\hat{\mathbf{p}} = -i\hbar\vec{\nabla}$ . A  $\sigma^\pm$  polarized dipole, rotating in the  $xy$ -plane, emits photons with a total angular momentum of  $\pm\hbar$ . It was already pointed out in 2.2.2 that the decomposition of this overall angular momentum into orbital and spin angular momentum is dependent on the propagation direction of the emitted photons. While photons emitted along the  $z$ -axis feature solely spin angular momentum the photons in the  $xy$ -plane carry only orbital angular momentum.

### A.9.1 Weak value of orbital angular momentum

In order to determine the displacement of the center of mass of the intensity distribution in the image of an elliptically polarized emitter, we want to measure locally the orbital angular momentum. This seems to be somehow contradictory to Heisenberg's uncertainty principle. But, using an operational approach, the local orbital angular momentum of the photons emitted by the dipole is measured by cutting off a part of the photon wave function  $\Psi(\mathbf{r}, t)$ , using an aperture. This is known as a measurement of the so called weak value of the overall orbital angular momentum of the photon wave function at the position of the aperture. The concept of weak values was first introduced in [84]. In the following we define the weak value of the photon's orbital angular momentum by [85, 86]

$$\langle \hat{p}_j \rangle_A = \frac{\langle \Psi_A | \hat{p}_j | \Psi \rangle}{\langle \Psi_A | \Psi \rangle}, \quad (\text{A.80})$$

where  $\Psi$  is the original photon wave function and  $\Psi_A$  the post-selected wave function which defines the part of the photon that passes the aperture. In the following we use the notation

$$\langle \Psi_A | \hat{p}_j | \Psi \rangle := \langle \Psi | \hat{p}_j | \Psi \rangle_A \quad (\text{A.81})$$

and

$$\langle \Psi_A | \Psi \rangle := \langle \Psi | \Psi \rangle_A. \quad (\text{A.82})$$

A weak value does not need to lie within the range of eigenvalues of the measured observable and can even be complex valued. Consequently the local angular momentum of the photons can exceed  $\hbar$  by far and is an example for a so called 'supermomentum' [148].

Following the procedure in 2.2.3 we assume an emitter at the origin emitting photons with non-zero angular momentum. Without limitation of generality we set the axis along which we image the emitter as  $y$ -axis. An aperture with diameter  $D$  is placed at a distance  $r_0$  from the origin and the part of the emitted light passing the aperture, is imaged onto a screen in the far field at a distance  $d$  to the aperture. The presence of orbital angular momentum in the light at the aperture then gives rise to a linear transverse momentum  $\langle \hat{p}_j \rangle_A$ , with  $j \in \{x, z\}$ , which is given by

$$\langle \hat{p}_x \rangle_A = -\frac{1}{r_0} \langle \hat{L}_z \rangle_A \quad (\text{A.83})$$

$$\langle \hat{p}_z \rangle_A = \frac{1}{r_0} \langle \hat{L}_x \rangle_A. \quad (\text{A.84})$$

The presence of the linear transverse momentum in addition to the linear longitudinal momentum  $\langle \hat{p}_y \rangle_A$  causes a tilt of the mean propagation direction of the photons which passed the aperture, see Figure A.3. The tilt of the mean propagation direction with respect to the optical axis is the reason why the photons seem to originate from a position which is offset to the emitter [49, 50, 79, 81, 82]. Along their way from the aperture to the screen the photons increase their distance to the optical axis, forming an image at the screen of which the center of mass does not

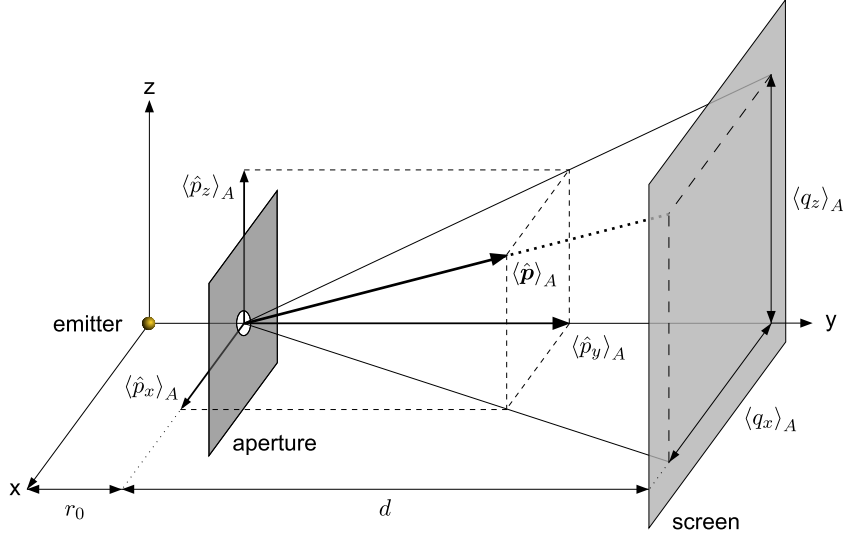


**Figure A.3: Transverse linear momentum.** The orbital angular momentum of the light emitted by an arbitrary polarized dipole leads to linear transverse momenta  $\langle \hat{p}_x \rangle_A$  and  $\langle \hat{p}_z \rangle_A$  of the photons that pass an aperture at a distance  $r_0$  from the emitter. This linear transverse momentum leads in turn to a tilt of the local propagation direction. Along the way to a screen at a distance  $d$  from the aperture the photons which passed the aperture increase their distance to the optical axis due to the tilt of the local propagation direction. This results in a displacement of the center of mass of the image on the screen.

coincide with the optical axis. The expectation value of the shift  $\langle q_j \rangle_A$  of the center of mass of the far field image with respect the optical axis can be determined via the relations

$$\frac{\langle \hat{p}_x \rangle_A}{\langle \hat{p}_y \rangle_A} = \frac{\langle q_x \rangle_A}{d} \quad (\text{A.85})$$

$$\frac{\langle \hat{p}_z \rangle_A}{\langle \hat{p}_y \rangle_A} = \frac{\langle q_z \rangle_A}{d}. \quad (\text{A.86})$$

Consequently the shift of the center of mass can be written as

$$\langle q_x \rangle_A = d \frac{\langle \hat{p}_x \rangle_A}{\langle \hat{p}_y \rangle_A} = d \frac{\langle \Psi | \hat{p}_x | \Psi \rangle_A}{\langle \Psi | \hat{p}_y | \Psi \rangle_A} \quad (\text{A.87})$$

$$\langle q_z \rangle_A = d \frac{\langle \hat{p}_z \rangle_A}{\langle \hat{p}_y \rangle_A} = d \frac{\langle \Psi | \hat{p}_z | \Psi \rangle_A}{\langle \Psi | \hat{p}_y | \Psi \rangle_A} \quad (\text{A.88})$$

Determining the center of mass in the far field image can therefore be considered as a measurement of the weak value of the orbital angular momentum of the photons passing the aperture.

### A.9.2 Displacement and momentum density

In order to determine the displacement of the center of mass of the image of an elliptically polarized dipole we need to find the wave function  $\Psi$  of the photons emitted by the dipole. In general the photon wave function can be written as

$$|\Psi\rangle = \sum_{k=1}^3 \int \Psi(\mathbf{r}, \chi_k) a_{\mathbf{r}, \chi_k}^\dagger |0\rangle d^3r, \quad (\text{A.89})$$

where  $\Psi(\mathbf{r}, \chi_k)$  gives the probability to find the photon at the position  $\mathbf{r}$  in one of the three orthogonal polarization states  $\chi_k$  with  $k \in \{1, 2, 3\}$ . Using this wave function we can determine the expectation values of the position of the center of mass in the image plane, given by the expressions A.87 and A.88. The un-normalized expectation value  $\langle \Psi | \hat{p}_j | \Psi \rangle_A$  can be written as

$$\begin{aligned} \langle \Psi | \hat{p}_j | \Psi \rangle_A &= -i\hbar \int \int_A \sum_l \sum_k \Psi^*(\mathbf{r}', \chi_l) \partial x_j \Psi(\mathbf{r}, \chi_k) \underbrace{\langle 0 | a_{\mathbf{r}', \chi_l} a_{\mathbf{r}, \chi_k}^\dagger | 0 \rangle}_{\delta_{\mathbf{r}\mathbf{r}'} \delta_{kl}} d^3r' d^3r \\ &= -i\hbar \int_A \sum_k \Psi^*(\mathbf{r}, \chi_k) \partial x_j \Psi(\mathbf{r}, \chi_k) d^3r. \end{aligned} \quad (\text{A.90})$$

Here  $\int_A d^3r'$  indicates the integral over the aperture. For the considered emitter the probability  $\Psi(\mathbf{r}, \chi_{e_k})$  to find at position  $\mathbf{r}$  a photon in the polarization state  $\chi_{e_k}$  is proportional to the corresponding component of the classical electric field  $e_k \cdot \mathbf{E}_{\text{ell}}(\mathbf{r})$ , with  $k \in \{x, y, z\}$ . Therefore, the expression A.90 can be written as

$$\begin{aligned} \langle \Psi | \hat{p}_j | \Psi \rangle_A &= -i\hbar |C_\Psi|^2 \int_A \sum_k E_k^*(\mathbf{r}) \partial x_j E_k(\mathbf{r}) d^3r \\ &= -i\hbar |C_\Psi|^2 \cdot e_j \int_A \left( \vec{\nabla} \otimes \mathbf{E}_{\text{ell}}(\mathbf{r}) \right) \mathbf{E}_{\text{ell}}^*(\mathbf{r}) d^3r. \end{aligned} \quad (\text{A.91})$$

We already know the expression  $\left( \vec{\nabla} \otimes \mathbf{E}_{\text{ell}} \right) \mathbf{E}_{\text{ell}}^*$ , since its imaginary part is the momentum density  $\rho_P$  2.20. The un-normalized expectation value  $\langle \Psi | \hat{p}_j | \Psi \rangle_A$  can in the framework of this derivation in principle be a complex number. The weak value of the linear momentum is given by the just derived expression divided by  $\langle \Psi | \Psi \rangle_A$ , which is real valued. In order to obtain a physical meaningful expectation value of the momenta we take the real part of the un-normalized expectation value A.91,

$$\begin{aligned} \text{Re} \left( \langle \Psi | \hat{p}_j | \Psi \rangle_A \right) &= -\hbar |C_\Psi|^2 \cdot e_j \int_A \text{Re} \left( i \left( \vec{\nabla} \otimes \mathbf{E}_{\text{ell}}(\mathbf{r}) \right) \mathbf{E}_{\text{ell}}^*(\mathbf{r}) \right) d^3r \\ &= \hbar |C_\Psi|^2 \cdot e_j \int_A \rho_P(\mathbf{r}) d^3r. \end{aligned} \quad (\text{A.92})$$

Consequently the expectation value of the center of mass of the image is given by ratio of the mean linear transverse momentum to the mean linear longitudinal momentum, averaged over

the aperture,

$$\langle q_x \rangle_A = d \frac{\int_A \mathbf{e}_x \cdot \boldsymbol{\rho P}(\mathbf{r}) d^3}{\int_A \mathbf{e}_y \cdot \boldsymbol{\rho P}(\mathbf{r}) d^3} \quad (\text{A.93})$$

$$\langle q_z \rangle_A = d \frac{\int_A \mathbf{e}_z \cdot \boldsymbol{\rho P}(\mathbf{r}) d^3}{\int_A \mathbf{e}_y \cdot \boldsymbol{\rho P}(\mathbf{r}) d^3}, \quad (\text{A.94})$$

which is the same result as obtained in 2.2.3. When applying to this expectation values the field emitted by an elliptically polarized emitter, which passed a lens, one gets exactly the same result for the displacement of the center of mass of the image, and the consequently assumed apparent displacement, as determined in 2.2.3.3. Not only does one get the same result as in the classical determination, it would also be possible to identify in this derivations the momentum density.

## A.10 Polarization of the evanescent field

When sending quasi linearly polarized light through a nanofiber there exist local elliptical polarizations, which can be in some cases almost circular [14]. While standard circularly polarized light rotates in a plane which is perpendicular to the direction of propagation, the strong transverse field gradients in the nanofiber give rise to elliptically polarized light fields rotating in a plane of which the surface normal is fully perpendicular to the propagation direction. Considering the case of a nanofiber mode propagating along the  $z$ -axis which is quasi linearly polarized along the horizontal  $x$ -axis, the evanescent field in the  $yz$ -plane is also solely linearly polarized along the  $x$ -axis. However the field in the  $xz$ -plane exhibits local elliptical polarization close to the fiber surface (inside the fiber as well as in the evanescent field). This local elliptical polarization is of the form

$$\mathbf{E}_{\text{fib}}(x, y = 0, z) \propto \frac{1}{\sqrt{1 + |\chi(x)|^2}} (\mathbf{e}_x + i \chi(x) \mathbf{e}_z), \quad (\text{A.95})$$

where  $\mathbf{E}_{\text{fib}}$  is the electric field of the light propagating in the nanofiber. Consequently the major axis of the local polarization ellipse (see section 2.2.1) are equal to the  $x$ - and  $z$ -axis.

In order to compare the light field in and outside of the fiber to linearly or circularly polarized fields we use the polarization overlap which is defined as

$$\eta = \frac{\mathbf{E}_{\text{fib}}^* \cdot \mathbf{e}_p}{|\mathbf{E}_{\text{fib}}|^2}, \quad (\text{A.96})$$

where  $\mathbf{e}_p$  is a normalized polarization vector.

Figure A.4a shows the intensity distribution of the light field in a nanofiber [14] with a diameter of 320 nm, plotted along the cross section of the nanofiber. The light field is quasi linearly polarized along the  $x$ -axis and has a wavelength of 532 nm. Subfigure b shows the polarization overlap of the same fiber field in the  $xz$ -plane with  $\sigma^\pm$  polarization, plotted as a function of the  $x$ -position, with  $\mathbf{e}_p(\sigma^\pm) = (\mathbf{e}_x \pm i \mathbf{e}_z)/\sqrt{2}$ . While this overlap has a strong variation inside of the nanofiber it is almost constant in the evanescent field, with a value of

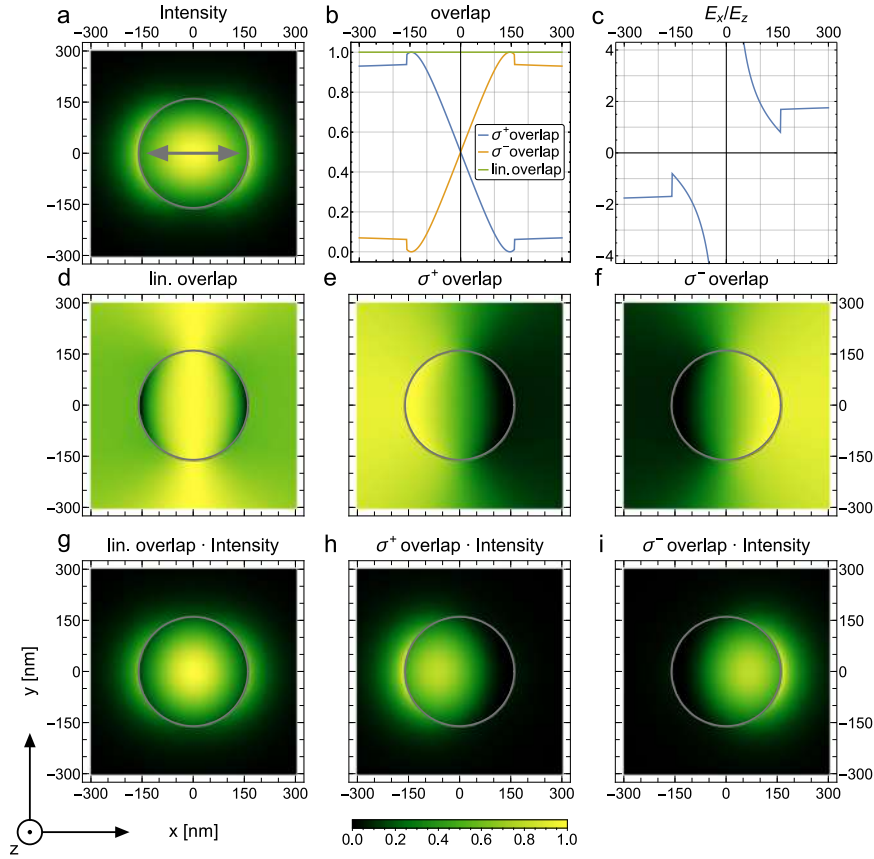


**Figure A.4: Fiber field and polarization overlap.** **a**, The intensity distribution in the cross section of a nanofiber with a diameter of 320 nm, guiding light at a wavelength of 532 nm which is quasi linearly polarized along the  $x$ -axis. **b**, The polarization overlap of the fiber field in the  $xz$ -plane with  $\sigma^\pm$  polarization (blue, yellow) plotted as a function of the  $x$ -position with respect to the center of the fiber. Additionally, the overlap of the fiber field in the  $yz$ -plane with linear polarization (along  $x$ -axis) (green) is plotted as a function of the  $y$ -position. **c**, The ratio of the  $z$  and  $x$  components of the field in the  $xz$ -plane, plotted as a function of the  $x$ -position. This ratio corresponds to the dipole polarization ratio  $\epsilon$  with respect to an observer which observes the fiber along the  $x$ -axis. **d**, **e** and **f**, Density plots along the fiber cross section showing the overlap with linear (along  $x$ -axis),  $\sigma^+$  and  $\sigma^-$  polarization. **g**, **h** and **i**, Density plots along the fiber cross section showing the overlap with linear (along  $x$ -axis),  $\sigma^+$  and  $\sigma^-$  polarization, multiplied with the local intensity.

$\pm 0.93$ . Additionally the polarization overlap of the fiber field in the  $yz$ -plane with  $e_p = e_x$  (linear polarization along the  $x$ -axis) is plotted as a function of the  $y$ -position. It can be seen, that along the  $y$ -axis the fiber field is solely linearly polarized along the horizontal axis. In subfigure **c** the ratio between the  $z$ - and  $x$ -component of the electric field in the  $xz$ -plane, plotted as a function of the  $x$ -position. This ratio corresponds to the dipole polarization ratio  $\epsilon$  (see section

2.2.1) with respect to an observer which observes the fiber along the  $x$ -axis. Here  $\epsilon \approx -1.7$  on the left side of the fiber and  $\epsilon \approx 1.7$  on the right side of the fiber. From these values it is possible to estimate the offset between the apparent position and the real position when imaging a nanoparticle which is illuminated by the local elliptically polarized light in the evanescent field of the nanofiber. However, one has to take a modification of the field emitted by the nanoparticle into account which is caused by the reflection on the fiber, see 3.3.2. The subfigures d, e and f show the polarization overlap with linear (along  $x$ -axis) and  $\sigma^\pm$  polarization along the fiber cross-section and the subfigures g, h, and i show the same overlap multiplied with the local intensity.

Due to the polarization properties of the evanescent field nanofibers are not only useful tools to mount and detect individual nanoparticles. Moreover they provide polarization states which are either linearly or almost perfectly circularly polarized. Therefore, nanofibers were excellent tools for a first proof that the position of a single gold nanoparticle seems to depend on the polarization of the illuminating light.

## A.11 Determining the magnification of the immersion microscope

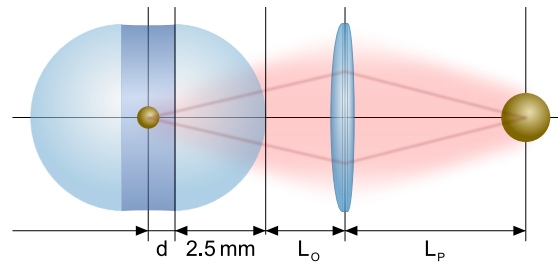


**Figure A.5: simplified sketch of the imaging system.** The microscope of the imaging system is modelled by a single lens which is placed at distance  $L_O$  from the front half sphere lens. It forms an image at the CCD chip of the camera which has a fixed distance  $L_P$  to the lens. In order to obtain a focussed image of the nanoparticle, which is at a distance  $d$  from the plane facet of the front half sphere lens only the distance  $L_O$  can be changed.

To determine the magnification of the overall imaging system we approximate the standard optical microscope by a single lens with a focal length of 10 mm, as shown in Figure A.5. Usually in an imaging system the distance between the object and the whole imaging system is changed to obtain a focused image of the object, while the composing components of the imaging system have fixed distances. In our imaging system only the rear part, consisting of the standard optical microscope can be moved to scan for the focus. The fixed distance  $L_P$  between the lens approximating the standard optical microscope and the image plane is determined via the magnification of the standard microscope. It was measured using a surface topography standard. Then the distance  $L_O$  between the half sphere lens and the lens representing the standard optical microscope is evaluated using ray transfer matrix analysis [123]. This is done under the condition that light which is emitted at the optical axis at a distance  $d$  with respect to the facet

of the half sphere lens, is imaged at a distance  $L_P$  after the microscope lens again on the optical axis. While the real distance  $d$  between the gold nanoparticle and the facet of the half ball lens could not be measured directly it was possible to measure the distance  $d' = (101 \pm 15) \mu\text{m}$  for which the standard optical microscope needed to be moved in order to show a focused image of the nanoparticle, respectively of scatterers on the facet of the half sphere lens. The error of this measured length is given by the distance the standard optical microscope can be moved while the image of the nanoparticle respectively the facet of the half sphere lens might still be considered focused. However, this error is likely to be overestimated. Using  $d'$  the position of the nanoparticle with respect to the facet of the half sphere lens can be determined to  $d = (68 \pm 10) \mu\text{m}$ . With this parameters we now evaluate the magnification of the overall imaging system to  $M_{0.41} = 21.9 \pm 0.1$  and  $M_{0.61} = 20.0 \pm 0.1$ .

## A.12 Linear polarization under imaging conditions

The presented apparent displacement introduces a new source of possible errors in superresolution microscopy. While some of the novel methods used in this very active field can not be subject to the apparent displacement presented in this work, like STEP [62] other methods could in principle be subject to systematic errors which exceeds the established accuracies by up to two orders of magnitude [52, 53]. The majority of the emitters used in super-resolution microscopy are fluorescent molecules. A major assumption concerning this molecules is that they are considered to strictly feature linearly polarized transitions [138]. If this would be an accurate assumption, such molecules could not emit fields containing orbital angular momentum and therefore do not feature any apparent position when the used imaging system is properly focused.

But this assumption should be critically challenged. Even for a molecule of which the internal geometry would fulfil the requirement the assumption of a strictly linearly polarized transition seems un-physical under experimental conditions. Being immersed in a gaseous, liquid, or solid medium, temperature- and/or strain-induced vibrations or static distortions will lead to spectral overlap of transitions of different polarizations. Thus it is likely that molecules can feature a finite elliptical polarization of transitions which would be perfectly linearly polarized without such perturbations. The question is how strong the perturbation and the consequent elliptical polarization is in a given experimental situation.

In order that such a finite elliptically polarized transitions of fluorescent molecules can lead to errors in position measurements the presence of elliptical polarization at the position of the molecule is necessary. Such an elliptical field component can in principal occur initially in the illuminating beam, or arise in the imaging system. An example is a strongly focused beam, which is initially perfectly linearly polarized, but shows in the focus region local elliptical polarization [8, 9], see Figure A.6a. Another example is the interference of the initial illuminating light with some spurious reflection. Figure A.6b shows a substrate containing emitters of which the positions should be measured. The top and bottom surface of the substrate are considered to be not perfectly parallel, but being tilted with respect to each other by an angle  $\alpha$ . The initial illumination light is linearly polarized. Now the superposition of the illuminating light and its reflection generates a periodic pattern of local elliptical polarizations. The corresponding apparent

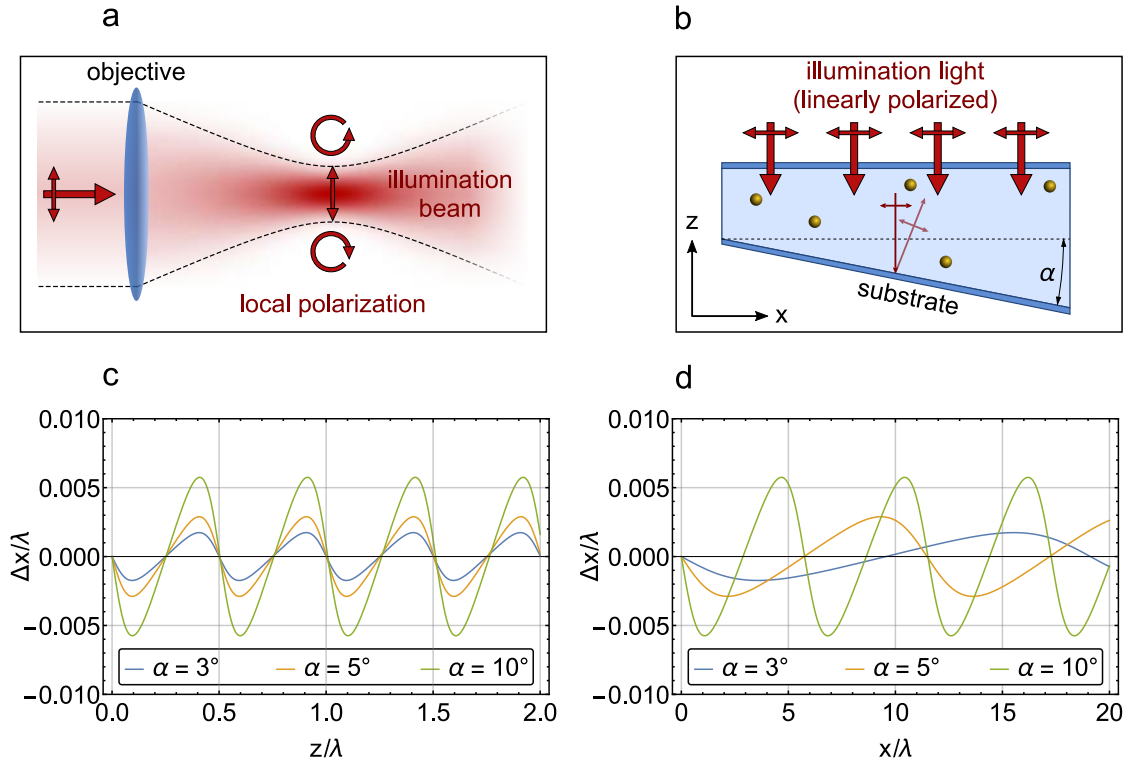


**Figure A.6: Sources of local elliptical polarization.** **a**, An initially linearly vertically polarized collimated beam is focused by a lens. Near the focus region there exist local elliptical polarizations. **b**, An along the  $x$ -axis linearly polarized beam illuminates emitters within a substrate. The bottom surface of the substrate is tilted with respect to the top surface by an angle  $\alpha$ . The superposition of the incoming illuminating light with the light reflected by the bottom surface leads to local elliptical polarization at the position of the emitters. **c**, The displacement  $\Delta x$  of an emitter with scalar polarizability resulting from the situation shown in subfigure **b** plotted as a function of the  $z$  position, for three different angles  $\alpha$ . The reflectivity of the bottom surface is assumed to be 4%. The emitters are considered to feature any polarization state. Both axes are given in units of  $\lambda$ . **d**, The displacement  $\Delta x$  resulting from the situation shown in subfigure **b** plotted as a function of the  $x$  position, for three different angles  $\alpha$ .

displacement one would measure when imaging an emitter which features a scalar polarizability, *e.g.* a gold nanoparticle, are shown in Figure A.6c as a function of the  $z$ -position (along the optical axis) and in subfigure d as a function of the  $x$ -position (along an axis, parallel to the polarization of the illumination light) of the emitter. The aperture used to calculate the plot data is  $\text{NA} = 1$  and the reflectivity of the substrate was considered to be 4%. A crucial behaviour of local elliptical polarizations generated by superposition is, that they occur in a periodic pattern. Therefore the apparent shift of the imaged emitters depends on their position. Consequently the error when measuring the distance between two emitters can be either zero, or twice the apparent displacement. In general it is not an easy task to rule out any spurious reflection in or near the

sample to be imaged.

To estimate a possible error in an individual position measurement one needs to investigate the polarizability properties of the imaged emitters into account, as well as the potential presence of local elliptical polarization. Any detailed study has to be done for individual experimental realisations.

### **A.13 Other error sources in super-resolution microscopy**

Beside this so far more or less unknown effect presented in this thesis, there are a lot of other error sources in super-resolution microscopy which can influence the outcome of position determination measurements. While playing a minor role in traditional microscopy, were they are negligible, they now start to play a key role in super-resolution microscopy limiting the achievable resolution. This by now well known effects were subject to many studies to investigate their origin and to develop methods for correcting the outcome of position measurements. Such possible error sources can be categorized in three major fields: technical limitations and issues of the imaging setup itself, undesired behaviour of the imaged samples and the usage of inappropriate methods to determine positions [149]. Most methods to avoid or minimize the resulting errors are not implemented in only one of three named fields but take action in the overall imaging and analysing process. A prominent example for technical issues is the fact that an inhomogeneous illumination of the optical aperture leads to systematic errors in position determination when the imaged sample is out of focus [118, 150]. This effect is well known and there are numerous of studies which provide methods to avoid the caused errors. The majority of this methods work on the analysis involved in the position determination process to achieve high precisions [119, 120, 151, 152]. But there are also approaches which take action at the setup, like adding additional optical elements to the used microscope [121]. Some of the innovative methods used in super-resolution microscopy take advantage of the fundamental properties of nano-scale emitters, which are used to improve the obtainable resolution. This is the case for the methods PALM [63] and dSTORM [64], which are representatives of fluorescence microscopy and are based on photoswitchable fluorescent molecules. Beside the advantages of this kind of emitters their stochastic behaviour can give rise to misinterpretation of the produced images [153]. There are numerous of other methods to go beyond the standard resolution limit. Some of them make the imaging and position determination process much more complex as it was in traditional microscopy, see for example [154]. In general, the super-resolution microscopy is a very active field in science, used to study and being studied. A lot of effort has been put into holding the newly acquired resolution and not to lose it again to effects which were former considered to be negligible or not known at all [130, 155]. The effect presented in this work will add a very fundamental error source in super-resolution position determination and should be kept in mind when designing and performing position measurements in the sub wavelength regime.

# Bibliography

- [1] J. C. Maxwell, “A treatise on electricity and magnetism, vol. 2,” *At the Clarendon press*, 1873.
- [2] F. J. Belinfante, “On the current and the density of the electric charge, the energy, the linear momentum and the angular momentum of arbitrary fields,” *Physica*, vol. 7, no. 5, pp. 449–474, 1940.
- [3] A. I. Bishop, T. A. Nieminen, N. R. Heckenberg, and H. Rubinsztein-Dunlop, “Optical application and measurement of torque on microparticles of isotropic nonabsorbing material,” *Physical Review A*, vol. 68, 2003.
- [4] L. Allen, S. M. Barnett, and M. J. Padgett, *Optical Angular Momentum, 1st Edition*. CRC Press, 2003.
- [5] J. H. Poynting, “The wave motion of a revolving shaft, and a suggestion as to the angular momentum in a beam of circularly polarised light,” *Proceedings of the Royal Society of London. Series A*, vol. 82, pp. 560–567, July 1909.
- [6] Z. Bomzon, M. Gu, and J. Shamir, “Angular momentum and geometrical phases in tight-focused circularly polarized plane waves,” *Applied Physics Letters*, vol. 89, no. 24, 2006.
- [7] Y. Zhao, J. S. Edgar, G. D. M. Jeffries, D. McGloin, and D. T. Chiu, “Spin-to-orbital angular momentum conversion in a strongly focused optical beam,” *Physical Review Letters*, vol. 99, 2007.
- [8] T. A. Nieminen, A. B. Stilgoe, N. R. Heckenberg, and H. Rubinsztein-Dunlop, “Angular momentum of a strongly focused gaussian beam,” *Journal of Optics A*, vol. 10, 2008.
- [9] P. B. Monteiro, P. A. Maia Neto, and H. M. Nussenzveig, “Angular momentum of focused beams: Beyond the paraxial approximation,” *Physical Review A*, vol. 79, 2009.
- [10] A. Y. Bekshaev, “A simple analytical model of the angular momentum transformation in strongly focused light beams,” *Central European Journal of Physics*, vol. 8, no. 6, pp. 947–960, 2010.
- [11] L. Marrucci, E. Karimi, S. Slussarenko, B. Piccirillo, E. Santamato, E. Nagali, and F. Sciarrino, “Spin-to-orbital conversion of the angular momentum of light and its classical and quantum applications,” *Journal of Optics*, vol. 13, 2011.

- [12] K. Y. Bliokh and F. Nori, “Transverse spin of a surface polariton,” *Physical Review A*, vol. 85, 2012.
- [13] K.-Y. Kim, I.-M. Lee, J. Kim, J. Jung, and B. Byoung-ho Lee, “Time reversal and the spin angular momentum of transverse-electric and transverse-magnetic surface modes,” *Physical Review A*, vol. 86, 2012.
- [14] F. Le Kien, J. Liang, K. Hakuta, and V. Balykin, “Field intensity distributions and polarization orientations in a vacuum-clad subwavelength-diameter optical fiber,” *Optics Communications*, vol. 242, no. 6-8, pp. 445–455, 2004.
- [15] C. N. Alexeyev, A. N. Alexeyev, N. A. Boklag, and M. A. Yavorskiy, “Effect of the spin-orbit interaction on polarization conversion in coupled waveguides,” *Journal of Optics A*, vol. 11, 2009.
- [16] A. Espinosa-Soria and A. Martinez, “Transverse spin and spin-orbit coupling in silicon waveguides,” *Photonics Technology Letters*, vol. 28, no. 14, 2016.
- [17] Z. Shao, J. Zhu, Y. Chen, Z. Yanfeng, and S. Yu, “Spin-orbit interaction of light induced by transverse spin angular momentum engineering,” *Nature Communications*, vol. 9, no. 926, 2018.
- [18] A. Aiello, P. Banzer, M. Neugebauer, and G. Leuchs, “From transverse angular momentum to photonic wheels,” *Nature Photonics*, vol. 9, Nov. 2015.
- [19] K. Y. Bliokh, F. J. Rodriguez-Fortuno, F. Nori, and A. V. Zayats, “Spin-orbit interactions of light,” *Nature Photonics*, vol. 9, pp. 796–808, Dec. 2015.
- [20] P. Lodahl, S. Mahmoodian, S. Stobbe, A. Rauschenbeutel, P. Schneeweiss, J. Volz, H. Pichler, and P. Zoller, “Chiral quantum optics,” *Nature*, vol. 541, pp. 473–480, Jan. 2017.
- [21] A. Kavokin, G. Malpuech, and M. Glazov, “Optical spin hall effect,” *Physical Review Letters*, vol. 5, no. 95, 2005.
- [22] K. Y. Bliokh, Y. Gorodetski, V. Kleiner, and E. Hasman, “Coriolis effect in optics: Unified geometric phase and spin-hall effect,” *Physical Review Letters*, vol. 8, July 2008.
- [23] O. Hosten and P. Kwiat, “Observation of the spin hall effect of light via weak measurements,” *Science*, vol. 319, pp. 787–790, Feb. 2008.
- [24] O. G. Rodríguez-Herrera, D. Lara, K. Y. Bliokh, E. A. Ostrovskaya, and C. Dainty, “Optical nanoprobng via spin-orbit interaction of light,” *Physical Review Letters*, vol. 10, June 2010.
- [25] N. Bokor, Y. Iketaki, T. Watanabe, and M. Fujii, “Investigation of polarization effects for high-numerical-aperture first-order laguerre-gaussian beams by 2d scanning with a single fluorescent microbead,” *Optics Express*, vol. 13, no. 26, 2005.

- 
- [26] P. Banzer, M. Neugebauer, A. Aiello, C. Marquardt, N. Lindlein, T. Bauer, and G. Leuchs, “The photonic wheel - demonstration of a state of light with purely transverse angular momentum,” *J. Europ. Opt. Soc. Rap. Public.*, vol. 8, 2013.
- [27] Y. Zhao, D. Shapiro, D. McGloin, D. T. Chiu, and S. Marchesini, “Direct observation of the transfer of orbital angular momentum to metal particles from a focused circularly polarized gaussian beam,” *Optics Express*, vol. 17, no. 25, 2009.
- [28] F. Le Kien, V. I. Balykin, and K. Hakuta, “Atom trap and waveguide using a two-color evanescent light field around a subwavelength-diameter optical fiber,” *Phys. Rev. A*, vol. 70, Dec 2004.
- [29] G. Sague, B. A., and A. Rauschenbeutel, “Blue-detuned evanescent field surface traps for neutral atoms based on mode interference in ultrathin optical fibres,” *New Journal of Physics*, vol. 10, 2008.
- [30] A. Goban, K. S. Choi, D. J. Alton, D. Ding, C. Lacroûte, M. Pototschnig, T. Thiele, N. P. Stern, and H. J. Kimble, “Demonstration of a state-insensitive, compensated nanofiber trap,” *Phys. Rev. Lett.*, vol. 109, Jul 2012.
- [31] I. J. Luxmoore, N. A. Wasley, A. J. Ramsay, A. C. T. Thijssen, R. Oulton, M. Hugues, S. Kasture, V. G. Achanta, A. M. Fox, and M. S. Skolnick, “Interfacing spins in an InGaAs quantum dot to a semiconductor waveguide circuit using emitted photons,” *Phys. Rev. Lett.*, vol. 110, Jan 2013.
- [32] C. Junge, D. O’Shea, J. Volz, and A. Rauschenbeutel, “Strong coupling between single atoms and nontransversal photons,” *Phys. Rev. Lett.*, vol. 110, May 2013.
- [33] I. Luxmoore, N. Wasley, A. Ramsay, A. Thijssen, R. Oulton, M. Hugues, A. Fox, and M. Skolnick, “Optical control of the emission direction of a quantum dot,” *Applied Physics Letters*, vol. 103, 12 2013.
- [34] M. Neugebauer, T. Bauer, P. Banzer, and L. Gerd, “Polarization tailored light driven directional optical nanobeacon,” *Nano Letters*, vol. 14, no. 5, pp. 2546–2551, 2014.
- [35] J. Petersen, J. Volz, and A. Rauschenbeutel, “Chiral nanophotonic waveguide interface based on spin-orbit interaction of light,” *Science*, vol. 346, pp. 67–71, Oct. 2014.
- [36] F. J. Rodríguez-Fortuño, I. Barber-Sanz, D. Puerto, A. Griol, and A. Martínez, “Resolving light handedness with an on-chip silicon microdisk,” *ACS Photonics*, vol. 1, no. 9, pp. 762–767, 2014.
- [37] Y. Lefier and T. Grosjean, “Unidirectional sub-diffraction waveguiding based on optical spin-orbit coupling in subwavelength plasmonic waveguides,” *Optics Letters*, vol. 40, no. 12, 2015.

- [38] I. Shomroni, S. Rosenblum, Y. Lovsky, O. Bechler, G. Guendelman, and B. Dayan, “All-optical routing of single photons by a one-atom switch controlled by a single photon,” *Science*, vol. 345, no. 6199, pp. 903–906, 2014.
- [39] R. R. Mitsch, C. C. Sayrin, B. B. Albrecht, P. P. Schneeweiss, and A. Rauschenbeutel, “Quantum state-controlled directional spontaneous emission of photons into a nanophotonic waveguide,” *Nature Communications*, vol. 5, no. 5713, 2014.
- [40] I. Söllner, S. Mahmoodian, S. Lindskov Hansen, L. Midolo, A. Javadi, G. Kirsanske, T. Pregnolato, H. El-Ella, E. Hye Lee, J. Dong Song, S. Stobbe, and P. Lodahl, “Deterministic photon–emitter coupling in chiral photonic circuits,” *Nature nanotechnology*, vol. 10, 07 2015.
- [41] B. le Feber, N. Rotenberg, and L. Kuipers, “Nanophotonic control of circular dipole emission,” *Nature communications*, vol. 6, 2015.
- [42] R. Coles, D. Price, J. Dixon, B. Royall, E. Clarke, P. Kok, M. Skolnick, A. Fox, and M. Makhonin, “Chirality of nanophotonic waveguide with embedded quantum emitter for unidirectional spin transfer,” *Nature Communications*, vol. 7, March 2016.
- [43] S.-Y. Lee, I.-M. Lee, J. Park, S. Oh, W. Lee, K.-Y. Kim, and B. Lee, “Role of magnetic induction currents in nanoslit excitation of surface plasmon polaritons,” *Phys. Rev. Lett.*, vol. 108, May 2012.
- [44] J. Lin, J. P. B. Mueller, Q. Wang, G. Yuan, N. Antoniou, X.-C. Yuan, and F. Capasso, “Polarization-controlled tunable directional coupling of surface plasmon polaritons,” *Science*, vol. 340, no. 6130, pp. 331–334, 2013.
- [45] F. J. Rodriguez-Fortuno, G. Marino, P. Ginzburg, D. O’Connor, A. Martinez, G. A. Wurtz, and A. V. Zayats, “Near-field interference for the unidirectional excitation of electromagnetic guided modes,” *Science*, vol. 340, pp. 328–330, Apr. 2013.
- [46] C. Sayrin, C. Junge, R. Mitsch, B. Albrecht, D. O’Shea, P. Schneeweiss, J. Volz, and A. Rauschenbeutel, “Nanophotonic optical isolator controlled by the internal state of cold atoms,” *Phys. Rev. X*, vol. 5, Dec 2015.
- [47] M. Scheucher, A. Hilico, E. Will, J. Volz, and A. Rauschenbeutel, “Quantum optical circulator controlled by a single chirally coupled atom,” *Science*, vol. 354, no. 6319, pp. 1577–1580, 2016.
- [48] O. Bechler, A. Borne, S. Rosenblum, G. Guendelman, O. Ezra Mor, M. Netser, T. Ohana, Z. Aqua, N. Drucker, R. Finkelstein, Y. Lovsky, R. Bruch, D. Gurovich, E. Shafir, and B. Dayan, “A passive photon–atom qubit swap operation,” *Nature Physics*, 08 2018.
- [49] H. F. Arnoldus, X. Li, and J. Shu, “Subwavelength displacement of the far-field image of a radiating dipole,” *Opt. Lett.*, vol. 33, pp. 1446–1448, Jul 2008.

- 
- [50] X. Li and H. F. Arnoldus, *Computational Studies of New Materials II*, ch. Nanoscale Resolution in the Near and Far Field Intensity Profile of Optical Dipole Radiation, Chapter 14, pp. 379–404. World Scientific, 2011.
- [51] D. Haefner, S. Sukhov, and A. Dogariu, “Spin hall effect of light in spherical geometry,” *Phys. Rev. Lett.*, vol. 102, Mar. 2009.
- [52] S. W. Hell, “Far-field optical nanoscopy,” *Science*, vol. 316, pp. 1153–1158, May 2007.
- [53] E. Betzig, G. H. Patterson, R. Sougrat, O. Wolf Lindwasser, S. Olenych, J. S. Bonifacino, M. W. Davidson, J. Lippincott-Schwartz, and H. F. Hess, “Imaging intracellular fluorescent proteins at nanometer resolution,” *Science*, vol. 313, pp. 1642–1654, Sept. 2006.
- [54] T. A. Klar, “Optical nanoscopy turns coherent,” *Nature Photonics*, vol. 12, pp. 63–65, 2018.
- [55] B. O. Leung and K. C. Chou, “Review of super-resolution fluorescence microscopy for biology,” *Applied Spectroscopy*, vol. 65, p. 9, 2011.
- [56] B. Huang, M. Bates, and X. Zhuang, “Super-resolution fluorescence microscopy,” *Annual Review of Biochemistry*, vol. 78, no. 1, pp. 993–1016, 2009. PMID: 19489737.
- [57] B. Huang, “Super-resolution optical microscopy: multiple choices,” *Current Opinion in Chemical Biology*, vol. 14, no. 1, pp. 10–14, 2010.
- [58] J. Reymann, D. Baddeley, M. Gunkel, P. Lemmer, W. Stadter, T. Jegou, K. Rippe, C. Cremer, and U. Birk, “High-precision structural analysis of subnuclear complexes in fixed and live cells via spatially modulated illumination (smi) microscopy,” *Chromosome Research*, vol. 16, pp. 367–382, May 2008.
- [59] G. Shtengel, J. Galbraith, C. Galbraith, J. Lippincott-Schwartz, J. Gillette, S. Manley, R. Sougrat, C. Waterman-Storer, P. Kanchanawong, M. Davidson, R. Fetter, and H. F. Hess, “Interferometric fluorescent super-resolution microscopy resolves 3d cellular ultrastructure,” *Proceedings of the National Academy of Sciences of the United States of America*, vol. 106, pp. 3125–30, 2009.
- [60] C.-L. Hsieh, S. Spindler, J. Ehrig, and V. Sandoghdar, “Tracking single particles on supported lipid membranes: Multimobility diffusion and nanoscopic confinement,” *The Journal of Physical Chemistry B*, vol. 118, pp. 1545–1554, 2014.
- [61] C. R. Copeland, J. Geist, C. D. McGray, V. A. Aksyuk, J. A. Liddle, B. R. Ilic, and S. M. Samuel M. Stavis, “Subnanometer localization accuracy in widefield optical microscopy,” *Light: Science & Applications*, vol. 7, no. 1, 2017.
- [62] S. W. Hell and J. Wichmann, “Breaking the diffraction resolution limit by stimulated emission: stimulated-emission-depletion fluorescence microscopy,” *Optics Letters*, vol. 19, pp. 780–782, Jun 1994.

- [63] S. T. Hess, T. P. K. Girirajan, and M. D. Mason, "Ultra-high resolution imaging by fluorescence photoactivation localization microscopy," *Biophysical Journal*, vol. 91, pp. 4258–4272, 2006.
- [64] M. J. Rust, M. Bates, and X. Zhuang, "Sub-diffraction-limit imaging by stochastic optical reconstruction microscopy (storm)," *Nature Methods*, vol. 3, pp. 793–796, 2006.
- [65] N. Bobroff, "Position measurement with a resolution and noise-limited instrument," *Review of Scientific Instruments*, vol. 57, pp. 1152–1157, Feb. 1986.
- [66] R. J. Ober, S. Ram, and S. E. Ward, "Localization accuracy in single-molecule microscopy," *Biophysical Journal*, vol. 86, pp. 1185–1200, Feb. 2004.
- [67] S. Stenholm, "The semiclassical theory of laser cooling," *Reviews of Modern Physics*, vol. 58, pp. 699–739, July 1986.
- [68] M. Born and E. Wolf, *Principles of Optics 7th Edition*. Cambridge University Press, 1999.
- [69] G. B. Arfken and H. J. Weber, *Mathematical methods for physicists, 6th Edition*. Elsevier Academic Press, 2005.
- [70] E. Hecht, *Optics 5th Edition*. Pearson, 2016.
- [71] A. Ashkin, "Acceleration and trapping of particles by radiation pressure," *Physical Review Letters*, vol. 24, pp. 156–159, Jan. 1970.
- [72] A. Ashkin, J. M. Dziedzic, J. E. Bjorkholm, and S. Chu, "Observation of a single-beam gradient force optical trap for dielectric particles," *Optics Letters*, vol. 11, no. 5, pp. 288–290, 1986.
- [73] L. Novatny and B. Hecht, *Principles of Nano-Optics*. Cambridge University Press, 2006.
- [74] C. F. Bohren and D. R. Huffman, *Absorption and Scattering of Light by Small Particles*. Wiley, 1983.
- [75] M. V. Berry, "Optical currents," *J. Opt. A: Pure Appl. Opt.*, vol. 11, Aug. 2009.
- [76] F. Le Kien and A. Rauschenbeutel, "Negative azimuthal force of nanofiber-guided light on a particle," *Physical Review A*, vol. 88, Dec. 2013.
- [77] J. D. Jackson, *Classical Electrodynamics. 3rd ed.* Wiley, 1998.
- [78] G. Moe and W. Hapner, "Conservation of angular momentum for light propagating in a transparent anisotropic medium," *J. Phys. B: At. Mol. Phys.*, vol. 10, no. 7, pp. 1191–1208, 1977.
- [79] C. Schwartz and A. Dogariu, "Conservation of angular momentum of light in single scattering," *Optics Express*, vol. 14, pp. 8425–8433, July 2016.

- 
- [80] C. D. Darwin, “Notes on the theory of radiation,” *The Royal Society*, pp. 36–52, May 1932.
- [81] X. Li, J. Shu, and H. F. Arnoldus, “Far-field detection of the dipole vortex,” *Opt. Lett.*, vol. 33, pp. 2269–2271, Oct 2008.
- [82] X. Li and H. F. Arnoldus, “Macroscopic far-field observation of the sub-wavelength near-field dipole vortex,” *Physics Letters A*, vol. 374, pp. 1063–1067, 2010.
- [83] J. W. Goodman, *Introduction to Fourier Optics. 3rd ed.* McGraw Hill Higher Education, 1996.
- [84] Y. Aharonov, D. Z. Albert, and V. Lev, “How the result of a measurement of a component of the spin of a spin- 2 particle can turn out to be 100,” *Physical Review Letters*, vol. 60, pp. 1351–1354, Apr. 1988.
- [85] R. Jozsa, “Complex weak values in quantum measurement,” *Physical Review A*, vol. 76, 2007.
- [86] B. E. Y. Svensson, “Pedagogical review of quantum measurement theory with an emphasis on weak measurements,” *Quanta*, vol. 1, pp. 18–49, May 2013.
- [87] M. K. Cheezum, W. F. Walker, and W. H. Guilford, “Quantitative comparison of algorithms for tracking single fluorescent particles,” *Biophysical Journal*, vol. 81, pp. 2378–2388, Oct. 2001.
- [88] V. Amendola, R. Pilot, M. Frasconi, O. M. Marago, and M. A. Iati, “Surface plasmon resonance in gold nanoparticles: a review,” *Journal of Physics: Condensed Matter*, vol. 29, Feb. 2017.
- [89] S. Eustis and M. A. El-Sayed, “Why gold nanoparticles are more precious than pretty gold: Noble metal surface plasmon resonance and its enhancement of the radiative and nonradiative properties of nanocrystals of different shapes,” *Chemical Society Reviews*, vol. 35, pp. 209–217, 2006.
- [90] S. Jain, D. Hirst, and J. O’Sullivan, “Gold nanoparticles as novel agents for cancer therapy,” *The British Journal of Radiology*, vol. 85, pp. 101–113, 2012.
- [91] T. K. Sau, A. L. Rogach, F. Jäckel, T. A. Klar, and J. Feldmann, “Properties and applications of colloidal nonspherical noble metal nanoparticles,” *Advanced Materials*, vol. 22, no. 16, pp. 1805–1825, 2010.
- [92] V. Myroshnychenko, J. Rodriguez-Fernandez, I. Pastoriza-Santos, A. M. Funston, C. Novo, P. Mulvaney, L.-M. L. M., and F. Javier Garcia de Abajo, “Modelling the optical response of gold nanoparticles,” *Chemical Society Reviews*, vol. 37, pp. 1792–1805, 2008.

- [93] B. Thomas, S. Orlov, U. Peschel, and G. Leuchs, "Nanointerferometric amplitude and phase reconstruction of tightly focused vector beams," *Nature Photonics*, vol. 8, 2014.
- [94] T. A. Klar and J. Feldmann, *Complex-Shaped Metal Nanoparticles: Bottom-Up Syntheses and Applications*, ch. Fluorophore-Metal Nanoparticle Interactions and Their Applications in Biosensing, Chapter 12, pp. 395–427. Wiley, 2012.
- [95] Y.-C. Yeh, B. Creran, and V. M. Rotello, "Gold nanoparticles: preparation, properties, and applications in bionanotechnology," *Nanoscale*, vol. 4, no. 1871, 2012.
- [96] M. Das, K. H. Shim, S. S. A. An, and D. K. Yi, "Review on gold nanoparticles and their applications," *Toxicology and Environmental Health Sciences*, vol. 3, no. 4, pp. 193–205, 2011.
- [97] P. D. Howes, R. Chandrawati, and M. M. Stevens, "Colloidal nanoparticles as advanced biological sensors," *Science*, vol. 346, no. 6205, 2014.
- [98] P. Zhang, S. Lee, H. Yu, N. Fang, and S. H. Kang, "Super-resolution of fluorescence-free plasmonic nanoparticles using enhanced dark-field illumination based on wavelength-modulation," *Scientific Reports*, vol. 5, June 2015.
- [99] P. Zhang, K. Kim, S. Lee, S. K. Chakkarapani, N. Fang, and S. H. Kang, "Augmented 3d super-resolution of fluorescence-free nanoparticles using enhanced dark-field illumination based on wavelength-modulation and a least-cubic algorithm," *Scientific Reports*, vol. 6, Sept. 2016.
- [100] Y. Gu, X. Di, W. Sun, G. Wang, and N. Fang, "Three-dimensional super-localization and tracking of single gold nanoparticles in cells," *Analytical Chemistry*, pp. 4111–4117, Mar. 2012.
- [101] P. Bon, N. Bourg, S. Lécart, S. Monneret, E. Fort, J. Wenger, and S. Lévêque-Fort, "Three-dimensional nanometre localization of nanoparticles to enhance super-resolution microscopy," *Nature Communications*, July 2015.
- [102] M. Haruta, "When gold is not noble: Catalysis by nanoparticles," *The Chemical Record*, vol. 3, pp. 75–87, Nov. 2003.
- [103] M. Ramos, L. Ortiz-Jordan, A. Hurtado-Macias, S. Flores, J. T. Elizalde-Galindo, C. Rocha, B. Torres, M. Zarei-Chaleshtori, and R. R. Chianelli, "Hardness and elastic modulus on six-fold symmetry gold nanoparticles," *Materials*, vol. 6, pp. 198–205, Jan. 2013.
- [104] P. Buffat and J.-P. Borel, "Size effect on the melting temperature of gold particles," *Physical Review A*, vol. 13, pp. 2287–2298, June 1976.
- [105] A. Kuhlicke, S. Schietinger, C. Matyssek, K. Busch, and O. Benson, "In situ observation of plasmon tuning in a single gold nanoparticle during controlled melting," *Nano Letters*, vol. 13, pp. 2041–2046, Apr. 2013.

- 
- [106] J. Petersen, *Interfacing Trapped Ions and Plasmonic Particles with Optical Nanofibers*. Phd thesis, Technische Universität Wien, 2015.
- [107] F. A. Warken, *Ultradünne Glasfasern als Werkzeug zur Kopplung von Licht und Materie*. PhD thesis, Rheinische Friedrich-Wilhelm Universität, 2007.
- [108] A. Stiebeiner, R. Garcia-Fernandez, and A. Rauschenbeutel, “Design and optimization of broadband tapered optical fibers with a nanofiber waist,” *Optics Express*, vol. 18, pp. 22677–22685, Sept. 2010.
- [109] A. Stiebeiner, O. Rehband, R. Garcia-Fernandez, and A. Rauschenbeutel, “Ultra-sensitive fluorescence spectroscopy of isolated surface-adsorbed molecules using an optical nanofiber,” *Optics Express*, vol. 17, pp. 21704–21711, Nov. 2009.
- [110] W. Garcia-Fernandez, Rand Alt, F. Bruse, C. Dan, K. Karapetyan, O. Rehband, A. Stiebeiner, U. Wiedemann, D. Meschede, and A. Rauschenbeutel, “Optical nanofibers and spectroscopy,” *Applied Physics B*, vol. 105, Sept. 2011.
- [111] G. d. P. Mie, “Beiträge zur optik trüber medien, speziell kolloidaler metallösungen,” *Annalen der Physik*, vol. 330, no. 3, pp. 377–445, 1908.
- [112] H. Wolfram and T. Wriedt, *The Mie Theory Basics and Applications*. Springer, 2012.
- [113] C. F. Bohren and D. R. Huffman, *Absorption and Scattering of Light by Small Particles*. Wiley, 1983.
- [114] F. Le Kien, S. Dutta Gupta, V. I. Balykin, and K. Hakuta, “Spontaneous emission of a cesium atom near a nanofiber: Efficient coupling of light to guided modes,” *Physical Review A*, vol. 72, no. 032509, 2005.
- [115] P. W. Barber and S. C. Hill, *Light scattering by particles: computational methods, Volume 2*. World Scientific, 1990.
- [116] S. Scheel, S. Y. Buhmann, C. Clausen, and P. Schneeweiss, “Directional spontaneous emission and lateral casimir-polder force on an atom close to a nanofiber,” *Physical Review A*, vol. 92, 2015.
- [117] A. P. Bartko and R. M. Dickson, “Imaging three-dimensional single molecule orientations,” *The Journal of Physical Chemistry B*, vol. 103, no. 51, pp. 11237–11241, 1999.
- [118] J. Engelhardt, J. Keller, P. Hoyer, M. Reuss, T. Staudt, and S. W. Hell, “Molecular orientation affects localization accuracy in superresolution far-field fluorescence microscopy,” *Nano Letters*, vol. 11, pp. 209–213, June 2011.
- [119] M. P. Backlund, M. D. Lew, A. S. Backer, S. J. Sahl, G. Grover, A. Agrawal, R. Piestun, and W. E. Moerner, “Simultaneous, accurate measurement of the 3d position and orientation of single molecules,” *PNAS*, vol. 109, p. 19087–19092, Nov. 2012.

- [120] S. Stallinga and B. Rieger, "Position and orientation estimation of fixed dipole emitters using an effective hermite point spread function model," *Optics Express*, vol. 20, pp. 5896–5921, Mar. 2012.
- [121] M. D. Lew and W. E. Moerner, "Azimuthal polarization filtering for accurate, precise, and robust single-molecule localization microscopy," *Nano Letters*, vol. 14, pp. 6407–6413, Oct. 2014.
- [122] M. P. Backlund, A. Arbabi, P. N. Petrov, E. Arbabi, S. Saurabh, A. Faraon, and W. E. Moerner, "Removing orientation-induced localization biases in single-molecule microscopy using a broadband metasurface mask," *Nature Photonics*, vol. 10, pp. 459–462, 2016.
- [123] B. E. A. Saleh and M. C. Teich, *Fundamentals of Photonics 2nd Edition*. Wiley-Interscience, 2007.
- [124] J. A. Seibert, J. M. Boone, and K. K. Lindfors, "Flat-field correction technique for digital detectors," *Proceedings of SPIE*, vol. 7, pp. 348–354, Feb. 1998.
- [125] M. Model, "Intensity calibration and flat-field correction for fluorescence microscopes," *Curr Protoc Cytom*, vol. 68, Apr. 2014.
- [126] J. Manfroid, "Stellar claibration of ccd flat fielding," *Astronomy and Astrophysics Supplement Series*, vol. 113, Nov. 1995.
- [127] A. Alberti, C. Robens, W. Alt, S. Brakhane, M. Karski, R. Reimann, A. Widera, and D. Meschede, "Super-resolution microscopy of single atoms in optical lattices," *New Journal of Physics*, vol. 18, 2016.
- [128] S. Stallinga and B. Rieger, "Accuracy of the gaussian point spread function model in 2d localization microscopy," *Optics Express*, vol. 18, Nov. 2010.
- [129] L. Gardini, M. Capitanio, and F. S. Pavone1, "3d tracking of single nanoparticles and quantum dots in living cells by out-of-focus imaging with diffraction pattern recognition," *Scientific Reports*, vol. 5, Apr. 2015.
- [130] R. E. Thompson, D. R. Larson, and W. W. Webb, "Precise nanometer localization analysis for individual fluorescent probes," *Biophysical Journal*, vol. 82, pp. 2775–2783, May 2002.
- [131] J. Condon, "Errors in elliptical gaussian fits," *Astronomical Society of the Pacific*, vol. 109, pp. 166–172, 1997.
- [132] H. Guo, "A simple algorithm for fitting a gaussian function," *IEEE Signal Processing Magazine*, vol. 134, Sept. 2011.
- [133] I. Bilinskis, *Digital Alias-free Signal Processing*. John Wiley & Sons Ltd, 2007.

- 
- [134] A. V. Abraham, S. Ram, J. Chao, E. Ward, and R. J. Ober, “Quantitative study of single molecule location estimation techniques,” *Optics Express*, vol. 17, no. 26, pp. 23352–23373, 2009.
- [135] R. N. Ghosh and W. W. Webb, “Automated detection and tracking of individual and clustered cell surface low density lipoprotein receptor molecules,” *Biophysical Journal*, vol. 66, pp. 1301–1318, 1994.
- [136] D. L. Fried, “Noise in photoemission current,” *Appl. Opt.*, vol. 4, pp. 79–80, Jan 1965.
- [137] A. Papoulis and S. U. Pillai, *Probability, Random Variables, and Stochastic Processes 4th edition*, ch. Poisson Points and Shot Noise. McGraw-Hill, 2002.
- [138] M. P. Backlund, M. D. Lew, A. S. Backer, S. J. Sahl, and W. E. Moerner, “The role of molecular dipole orientation in single-molecule fluorescence microscopy and implications for super-resolution imaging,” *Chemphyschem*, vol. 15, pp. 587–599, Mar. 2014.
- [139] G. Araneda, S. Walser, Y. Colombe, D. B. Higginbottom, J. Volz, R. Blatt, and A. Rauschenbeutel, “Wavelength-scale errors in optical localization due to spin–orbit coupling of light,” *Nature Physics*, 2018.
- [140] J.-S. Lee and E. Pottier, *Polarimetric Radar Imaging: From Basics to Applications, 1st Edition*. CRC Press, 2009.
- [141] M. Cheney and B. Borden, “Problems in synthetic-aperture radar imaging,” *Inverse Problems*, vol. 25, Nov. 2009.
- [142] M. Peichl, E. Schreiber, A. Heinzl, and S. Dill, “Novel imaging radar technology for detection of landmines and other unexploded ordnance,” *European Journal for Security Research*, vol. 2, pp. 23–37, Nov. 2016.
- [143] M. P. Hayes and P. T. Gough, “Synthetic aperture sonar: A review of current status,” *IEEE Journal of Oceanic Engineering*, vol. 34, pp. 207–224, 2009.
- [144] S. Caporale and Y. Petillot, “A new framework for synthetic aperture sonar microneavigation,” *arxiv*, 2017.
- [145] I. Bialynicki-Birula and Z. Bialynicka-Birula, “Gravitational waves carrying orbital angular momentum,” *New Journal of Physics*, vol. 18, no. 2, 2016.
- [146] B. P. Abbott et al, “Search for post-merger gravitational waves from the remnant of the binary neutron star merger gw170817,” *The Astrophysical Journal Letters*, vol. 851, no. 1, 2017.
- [147] W. Bakr, J. Gillen, A. Peng, S. Fölling, and M. Greiner, “A quantum gas microscope for detecting single atoms in a hubbard-regime optical lattice,” *Nature*, vol. 462, pp. 74–77, Nov. 2009.

- [148] A. Y. Bekshaev, K. Y. Bliokh, and F. Nori, “Transverse spin and momentum in two-wave interference,” *Physical Review X*, vol. 5, Mar. 2015.
- [149] M. Erdélyi, J. Sinkó, R. Kákonyi, A. Kelemen, E. Rees, D. Varga, and G. Szabó, “Origin and compensation of imaging artefacts in localization-based super-resolution microscopy,” *Methods*, vol. 88, p. 122–132, May 2015.
- [150] J. Enderlein, E. Toprak, and P. R. Selvin, “Polarization effect on position accuracy of fluorophore localization,” *Optics Express*, vol. 14, Sept. 2006.
- [151] K. I. Mortensen, L. Stirling Churchman, J. A. Spudich, and H. Flyvbjerg, “Optimized localization-analysis for single-molecule tracking and super-resolution microscopy,” *Nature Methods*, vol. 7, no. 5, pp. 377–381, 2010.
- [152] S. Quirin, S. R. Prasanna Pavani, and R. Piestun, “Optimal 3d single-molecule localization for superresolution microscopy with aberrations and engineered point spread functions,” *PNAS*, vol. 109, pp. 675–679, Jan. 2012.
- [153] A. Burgert, S. Letschert, S. Doose, and M. Sauer, “Artifacts in single-molecule localization microscopy,” *Histochem Cell Biol*, vol. 144, pp. 123–131, 2015.
- [154] S. R. Prasanna Pavani, M. A. Thompson, J. S. Biteen, S. J. Lord, N. Liuc, R. J. Twieg, R. Piestun, and W. E. Moerner, “Three-dimensional, single-molecule fluorescence imaging beyond the diffraction limit by using a double-helix point spread function,” *PNAS*, vol. 106, no. 9, p. 2995–2999, 2009.
- [155] S. Culley, D. Albrecht, C. Jacobs, P. Matos Pereira, C. Leterrier, J. Mercer, and R. Henriques, “Quantitative mapping and minimization of super-resolution optical imaging artifacts,” *Nature Methods*, 2018.

# Acknowledgements, ein Dankeschön

Now, at the very end of this thesis, I would like to use the opportunity to thank all the people who contributed to my thesis and the presented results and supported me during my time as a PhD student.

Jetzt, am Ende dieser Arbeit möchte ich die Gelegenheit nutzen mich bei allen zu bedanken, die zu dieser Arbeit und den präsentierten Resultaten beigetragen haben und mich während meiner Zeit als Doktoratsstudent unterstützt haben.

First and foremost I want to thank Arno Rauschenbeutel for the opportunity to be part of his group and for the confidence he placed in me as a physicist and a person. He is an incredible discussion partner with a seemingly infinite knowledge, not afraid to challenge anything critically. His optimistic point of view and enthusiasm for the project I had the chance to work on, played a key role in the hard work which culminated in a Nature Physics publication.

I want to thank Jürgen Volz for the many inspiring and amusing discussions, which pushed my experimental and theoretical work forward. He took his time to answer any question I addressed to him and has an enviable intuition how physics works. Thank you very much for all the proof reads of my thesis.

On this occasion I also want to thank Arno and Jürgen and our collaborators at the University of Innsbruck, Gabriel Araneda-Machuca, Daniel Higginbottom, Yves Colombe and Rainer Blatt, for the fascinating physics we did together and the resulting publication. Working on this paper together was an awesome experience.

Many thanks are addressed to the many (former) members of the Rauschenbeutel group: Adarsh, Adele, Aisling, Alexandre, Bernhard, Christoph, Clement, Daniel, David, Elisa, Hardy, Jakob, Jan, Luke, Martin, Michi, Pham, Philipp, Rudi, Sam, Sarah, Sebastian, Sofia, Thomas, Yijian and Zaneta (please forgive me if I forgot any of you!). You are an awesome group of people and I have enjoyed working with you, to be on conferences with you and to party with you! Additionally, I want to thank all the people from the ATI for the familiar atmosphere.

Ganz herzlich bedanken möchte ich mich auch bei meinen Freunden in Tirol, die mir durch meinen Umzug nach Wien nicht verloren gegangen sind. Ganz besonders hervorheben möchte ich hier die Dreschis. Jedes Wochenende mit euch war ein besonderes Erlebnis zum Kraft Tanken und jeder Besuch bei Freunden in Tirol ein kleiner Erholungsurlaub. Der Wert dieser

gemeinsamen Tage lässt sich nicht in Worte fassen. Besonders bedanken möchte ich mich auch bei meinen ehemaligen Studienkollegen und jetzigen Freunden Daniel und Laurin.

Natürlich möchte ich mich auch bei all jenen Freunden bedanken, die ich in Wien dazu gewonnen habe. Liebe Nachbarinos und liebe Brandstätters, es war wirklich eine Bereicherung euch durch meine Anstellung in Wien kennen gelernt zu haben!

Ein ganz spezieller Dank gilt meiner Familie, die mich von meinem ersten Tag im Studium bis zum letzten, mit allen ihr zur Verfügung stehenden Mitteln unterstützt hat! Ohne diese moralische und finanzielle Unterstützung, ohne das Bestärken meinen Weg und meine Ziele zu verfolgen wäre ich nicht an diesen Punkt gekommen.

In einer neuen und fremden Stadt einen seit Schultagen währenden Freund zur Seite zu haben war sehr wertvoll für mich. Danke Martin, für die historischen Debatten im Graff!

Stefan, vielen Dank für jeden Satz und jeden Gedanken den ich mit dir bidirektional teilen durfte, egal ob physikalischer, weltanschaulicher oder ganz privater Natur.

Pob, danke!

Abschließend möchte ich mich bei dir bedanken liebe Sina. Die vielen Stunden die ich an Wochenenden und Abenden gearbeitet habe waren für mich nicht leicht, für dich nicht leicht, für uns nicht leicht. Deine fortwährende und bedingungslose Unterstützung hat mir den Abschluss dieser Arbeit sehr erleichtert. Du hast mir an jedem Tag an dem ich keine Kraft mehr hatte noch die Reste deiner gegeben, und dafür kann ich dir gar nicht genug danken!